NOTE TO USERS

DISSERTATION

KINEMATIC, MICROPHYSICAL, AND ELECTRICAL STRUCTURE AND EVOLUTION OF THUNDERSTORMS DURING THE SEVERE THUNDERSTORM ELECTRIFICATION AND PRECIPITATION STUDY (STEPS)

Submitted by

KYLE CAMERON WIENS

Department of Atmospheric Science

In Partial Fulfillment

of the Requirements for the Degree of

Doctor of Philosophy in Atmospheric Science

with Dissertation in Radar Meteorology

Colorado State University

Fort Collins, Colorado

Spring 2005

COLORADO STATE UNIVERSITY

January 21, 2005

WE HEREBY RECOMMEND THAT THE DISSERTATION PREPARED UNDER OUR SUPERVISION BY KYLE CAMERON WIENS ENTITLED KINEMATIC, MICROPHYSICAL, AND ELECTRICAL STRUCTURE AND EVOLUTION OF THUNDERSTORMS DURING THE SEVERE THUNDERSTORM ELECTRIFICATION AND PRECIPITATION STUDY (STEPS) BE ACCEPTED AS FULFILLING IN PART REQUIREMENTS FOR THE DEGREE OF DOCTOR OF PHILOSOPHY.

Committee on Graduate Work

William R. Cotton

Richard T. [illegible]

Raymond L. Johnson

Paul R. Krehbiel

S. A. R.

Steven A. Rutledge, Advisor

[illegible]

Department Head

ABSTRACT

KINEMATIC, MICROPHYSICAL, AND ELECTRICAL STRUCTURE AND EVOLUTION OF THUNDERSTORMS DURING THE SEVERE THUNDERSTORM ELECTRIFICATION AND PRECIPITATION STUDY (STEPS)

Doppler-polarimetric radar and state-of-the-art lightning mapping measurements are used for detailed investigations of the kinematic, microphysical, and electrical evolution of several storms observed during the Severe Thunderstorm Electrification and Precipitation Study (STEPS). The focus is on determining what is different and/or unique about those storms that are dominated by positive cloud-to-ground (+CG) flashes. The set of case studies includes a +CG-dominant supercell, multicellular storms of varying severity that experienced a shift from −CG-dominance to +CG-dominance, and an isolated storm that produced no CG flashes of either polarity despite frequent intra-cloud (IC) lightning.

The parent charge structure of −CG-dominated storms differed significantly from that of +CG-dominated storms. In general, −CG-dominated storms exhibited the commonly observed normal tripole charge structure (positive over negative over positive charge), while the +CG-dominated storms exhibited what could be roughly described as an inverted tripole structure (negative over positive over negative charge). Neither polarity of ground flash occurred without the presence of a lower charge re-

gion (lower positive charge in the case of –CG flashes, and lower negative charge in the case of +CG flashes). The one storm that produced no CG flashes exhibited an inverted dipole charge structure consisting of a vertically thin upper negative charge region and a deep lower positive charge region. The absence of a lower negative charge in this latter storm is likely the reason for its lack of +CG flashes.

The total (IC plus CG) flash rate was found to be well-correlated with the convective development of each of the storms, with a particularly robust correlation between total flash rate and echo volume of radar-inferred graupel. Dramatic increases in total flash rate and vertical extent of the lightning flashes often accompanied strong surges in updraft and hail growth aloft, showing that total lightning measurements are a reliable proxy for convective intensity of thunderstorms and may have some utility as a indicator/predictor of severe weather.

Kyle Cameron Wiens
Department of Atmospheric Science
Colorado State University
Fort Collins, CO 80526
Spring 2005

Adviser: Dr. Steven A. Rutledge

ACKNOWLEDGMENTS

I thank my advisor, Prof. Steve Rutledge, for his advice and encouragement. I was always more motivated and focused after our meetings. Thanks to my graduate committee members: Drs. William Cotton, Richard Johnson, Paul Krehbiel, and R. S. Robinson. Special thanks to Paul Krehbiel for being a great friend and mentor for many years.

All the members of the CSU Radar Meteorology Group have been helpful and supportive. Special thanks to Sarah Tessendorf for both her friendship and collaboration on this research. Thanks to Paul Hein for his tireless technical support and friendship. Special thanks to Margi Cech for doing everything in her power to make my stay here at CSU (and travels elsewhere) as enjoyable and smooth as possible. I and the rest of the group would not survive without Margi.

Thanks to all the CSU Atmospheric Science administrative staff (especially Melissa Tucker, Marilyn Hanson, and Jen Weingardt) for all their friendly help and for showing me which forms to fill out.

Thanks to everyone involved in the STEPS campaign. Special thanks to the CHILL radar staff (Pat Kennedy, Dave Brunkow, Bob Bowie), to the ballooning crew of OU/NSSL (especially to Drs. Don MacGorman and Dave Rust for providing me with the balloon data), and to the NCAR S-pol staff (especially to L. Jay Miller for stimulating discussions and invaluable assistance with the radar data). A very big thank you to the NMT LMA folks (Drs. Paul Krehbiel, Bill Rison, Ron Thomas, Tim Hamlin, Mr. Jeremiah Harlin, and Jarrod Lombardo). Without the LMA and the associated software, this disseration would not exist.

This research was supported by NSF grants ATM-9912051 and ATM-0309303. The CSU-CHILL radar facility is sponsorted by the NSF cooperative agreement ATM-0118021 and Colorado State University. The S-Pol radar, operated by NCAR, is funded by the NSF.

This DISSERTATION was typeset with LaTeX[1] by the author.

[1]LaTeX document preparation system was developed by Leslie Lamport as a special version of Donald Knuth's TeX program for computer typesetting. TeX is a trademark of the American Mathematical Society. The LaTeX macro package for the Colorado State University DISSERTATION format was adapted from Gerald Arnold's modification of the LaTeX macro package for The University of Texas at Austin by Khe-Sing The.

I dedicate this work to my wife, Julie. You are my everything.

KYLE CAMERON WIENS

Colorado State University

Spring 2005

TABLE OF CONTENTS

LIST OF TABLES

LIST OF FIGURES

CHAPTER 1

INTRODUCTION

The majority of cloud-to-ground (CG) lightning flashes produced by warm-season thunderstorms lower negative charge to ground (–CGs; Fig. 1.1a). However, some severe thunderstorms often produce copious positive cloud-to-ground flashes (+CGs), with little if any –CGs (MacGorman and Burgess, 1994; Stolzenburg, 1994; Carey and Rutledge, 1998; Lang and Rutledge, 2002). In addition, +CG-dominated severe storms are frequent within a corridor extending northward from the Colorado-Kansas border into Canada (see Fig. 1.1b,c, and also Orville and Huffines, 2001; Zajac and Rutledge, 2001; Carey et al., 2003a). The Severe Thunderstorm Electrification and Precipitation Study (STEPS: Lang et al., 2004a) was conducted in this +CG corridor during the summer of 2000.

The objective of this dissertation is to investigate the kinematic, microphysical and electrical characteristics of several storms observed during STEPS. The focus will be on determining what is different and/or unique about those storms which are dominated by +CG flashes. The set of case studies includes a +CG-dominant supercell on 29 June that produced large hail and an F1 tornado, multicellular storms of varying severity on 23 June that experienced a shift from –CG-dominance to +CG-dominance, and an isolated storm on 3 June that produced no CG flashes of either polarity despite frequent intra-cloud lightning. Specific questions to be addressed include:

- What are the charge structures of these storms and how do these structures develop, evolve, and differ?

- Do +CG-dominated storms have charge structure that is consistently different from –CG-dominated storms?
- What are the source charge regions of +CG and –CG flashes and how do these source regions compare with the overall charge structure?
- Are there any kinematic/microphysical differences between +CG-dominated and –CG-dominated storms, and if so, can these differences explain the differing CG production?
- To what extent do the observations of charge structure agree with laboratory charging studies?
- To what extent do the observations agree with hypothesized explanations for +CG-dominated storms?
- Do total lightning flash rate and CG-polarity have any utility as indicators or predictors of severe weather?

Using the unique combination of instrumentation in STEPS, this research makes significant progress toward answering these questions.

1.1 Background and Motivation

1.1.1 Thunderstorm Charge Structure

As reviewed in Williams (1989; 2001), thunderstorms commonly have a tripole charge structure consisting of a dominant negative charge region between –10°C and –25°C, a positive charge region above the negative, and an additional (usually small) positive charge near the 0°C level (see Fig. 1.2a). The negative charge is termed "dominant" because it typically dominates the electric field measured at the ground and is the source region of the predominantly negative polarity CGs produced by warm-season thunderstorms (e.g., Krehbiel et al., 1979). Intra-cloud (IC) lightning flashes typically occur between the dominant negative and upper positive charge regions. Numerous laboratory studies (e.g., Takahashi, 1978; Saunders and Peck, 1998;

Berdeklis and List, 2001) have shown that rebounding collisions between ice particles undergoing growth by riming (i.e., graupel or hail) and smaller ice crystals act to separate charge, imparting one sign of charge on the rimer and the opposite sign of charge on the ice crystals. This non-inductive ice-ice collision (NIC) mechanism operates independently of ambient electric field and is thought to be primarily responsible for the formation of thunderstorm charge structure. The physical mechanism of this charge transfer is still uncertain (Baker and Dash, 1994; Mason and Dash, 2000; Dash et al., 2001); however, the current consensus is that the particle growing faster by vapor deposition gains positive charge in the collision (e.g., Baker et al., 1987; Jayaratne, 1993). Though the results from the various laboratory studies differ to some degree, they consistently show that the polarity and amount of the charge transferred is dependent on temperature, supercooled liquid water content, and impact velocity (Fig. 1.3), or, equivalently, on temperature and rime accretion rate (Fig. 1.4). For a representative effective liquid water content of 1 g m^{-3}, the rimer gains negative charge at temperatures colder than about –10°C, and gains positive charge at warmer temperatures and/or greater effective liquid water content. The temperature or height where the rimer charge switches from negative to positive has often been termed a charge reversal level. Following gravitational sedimentation and associated size-sorting of the hydrometeors, the NIC mechanism may produce the dominant tripole structure commonly observed in thunderstorms. For example, the main negative charge region may be carried by graupel and/or hail while the upper positive charge may be carried by smaller ice crystals. The lower positive charge may be carried by graupel and/or hail that experienced charge-separating collisions near and/or below the charge reversal level.

In situ measurements of electric field and particle charge in thunderstorms (e.g., Marshall and Winn, 1982; Marsh and Marshall, 1993; Marshall and Marsh, 1993) generally support the NIC mechanism and the tripole model. However, there are certainly observed deviations from this basic structure. For example, Stolzenburg et al. (1998a, 1998b, 1998c) analyzed a large set of balloon-borne electric field soundings

through thunderstorms. The updraft region of most of these storms consisted of the tripole structure with an additional negative charge region at the top, likely a screening layer. The heights of all the tripole charge regions were well-correlated with the strength of the updraft, with stronger updrafts associated with more elevated charge structures. The charge structures in the "non-updraft" regions of these storms were consistently more complex and variable, with additional alternating charge regions below the lower positive. The magnitude of the electric field was also consistently greater in the non-updraft regions. Stolzenburg et al.(1998c) suggest that the NIC mechanism could explain the tripole structure in the updraft, but that additional processes (e.g., inductive charging, deposition of charge by lightning, screening layer production) might be more efficient in the strong electric field of the non-updraft regions and could contribute to the more complex structure observed there.

Analyses of lightning mapping (Krehbiel et al., 2000b; Zhang et al., 2001; Hamlin, 2004) and vertical electric field profiles (Rust and MacGorman, 2002; MacGorman et al., 2004) suggest that the thunderstorms in the STEPS region are sometimes inverted in polarity. That is, the inferred charge structure of these storms consists of a main mid-level positive charge and upper negative charge, and, in some cases additional lower negative charge –essentially the inverse of the more typically observed normal tripole structure (See Fig. 1.2b). *One of the goals of this dissertation is to determine if STEPS storms do indeed exhibit inverted charge structure and if these storms are different dynamically and microphysically from storms that exhibit 'normal' charge structure.* Such an inverted structure would explain the high percentage of +CG flashes in the STEPS region.

1.1.2 Total Lightning and Storm Severity

As reviewed by Williams (2001), lightning activity in mid-latitude storms dramatically increases with thunderstorm size, with the total flash rate (IC plus CG) roughly proportional to the fifth power of cloud top height. This lightning/cloud height relationship is attributable to the strength and depth of the updraft. A stronger, deeper

updraft creates a deeper cloud and also allows for greater production of ice in and above the mixed-phase region of the cloud. This ice production is crucial to the NIC mechanism described above. Several studies have shown that total lightning flash rate is also well correlated with the volume of 30-40 dBZ radar reflectivity within the mixed-phase region, where collisional charging is thought to occur (e.g., Larson and Stansbury, 1974; Carey and Rutledge, 1996; MacGorman et al., 1989). This mixed-phase reflectivity volume is ultimately fed by the storm updraft. Hence, a greater volume of strong updraft leading to a greater volume of ice should result in more collisional charging and increased lightning flash rates. Conversely, since storms with stronger updrafts are more likely to produce larger hail and hence severe weather at the ground, the lightning itself may be a useful predictor of storm severity. Indeed, the very nice study by Williams et al. (1999) noted a flash rate threshold (60 flashes min^{-1}) between ordinary and severe storms. In addition, they often found that the total flash rate would "jump" dramatically during explosive vertical development of the radar echo. These lightning jumps were typically followed tens of minutes later by severe weather at the ground in the form of hail and down-bursts. Other studies (e.g., Hamlin, 2004) have noted similar lightning jumps preceding severe weather. *Another, somewhat secondary, goal of this proposed research is to further examine these relationships among updraft, ice echo volume, total flash rate, and hail production; and to determine what utility total lightning measurements have for severe weather indication/prediction.*

1.1.3 +CG Flashes and Storm Severity

The usual dominance of –CG flashes and relative sparsity of +CG flashes (see, e.g., Fig. 1.1) is consistent with the normal tripole charge configuration discussed above; the main negative charge is the source of the –CG flashes. +CG-dominated storms, on the other hand, are somewhat contrary to the tripole model, and several studies have indicated that +CG-dominated storms are often severe. For example, in their investigation of 15 severe storms, MacGorman and Burgess (1994) found that

storms with frequent +CG flashes often produced large hail during times when +CGs dominated the ground flash activity. Furthermore, if the dominant polarity of CG flashes switched to negative in these storms, the frequency of large hail reports and diameter of the reported hail usually decreased. In a survey of severe +CG-dominated storms, Stolzenburg (1994) also found that large hail was often reported in the vicinity of dense +CG activity. It's important to keep in mind that –CG-dominated storms can also be severe, which leads to a one-way correlation: +CG-dominated storms are often severe, but not all severe storms are +CG-dominant. As discussed above, +CG-dominated severe storms are frequent within a corridor extending northward from the Colorado-Kansas border into Canada (Fig. 1.1b,c; see also Orville and Huffines, 2001; Zajac and Rutledge, 2001; Carey et al., 2003a). The STEPS campaign (Lang et al., 2004a) was conducted on the southwest end of this +CG corridor. *One of the primary goals of STEPS (and of this dissertation) is to understand why the storms (especially severe ones) in this region are often dominated by +CG lightning.*

As recently reviewed by Williams (2001), several hypotheses have been put forth to explain the charge structure leading to +CG-dominated thunderstorms.

1. **Tilted dipole** (e.g., Brook et al., 1982; Curran and Rust, 1992): A typical dipole or tripole is assumed. The shearing of the updraft by strong mid-to-upper-level horizontal winds laterally displaces upper-positive charge. This decreases the shielding effect of the main mid-level negative charge, thus exposing the upper positive charge to ground. The +CGs could then originate from this displaced upper positive charge.

2. **Precipitation unshielding**: A typical dipole or tripole is assumed. Much of the main negative charge is removed by descending precipitation during storm collapse, leaving the upper positive charge "unshielded" from the ground and more able to produce +CG flashes. Carey and Rutledge (1998) proposed this to explain the maximum +CG flash rates that trailed maximum hail rates by tens of minutes in the storm they studied.

3. **Tripole with enhanced lower positive charge**: Here, the lower positive charge of the "typical" tripole structure is enhanced and becomes a dominant charge region. As described by Williams (2001), this charge structure may occur due to extraordinarily broad, undiluted updrafts. This would allow for enhanced formation of hail, enhanced positive charging of larger hydrometeors by the NIC mechanism, and hence a larger reservoir of lower positive charge which could lead to +CG-domination of ground flashes. In addition, –CG flashes would be reduced because of the shielding effect of the enhanced lower positive charge and also because a broader, stronger updraft would further elevate the main negative charge region.

4. **Inverted dipole**: The charge structure is essentially reversed, with negative charge aloft and positive charge in the place of the usual main negative charge region (Fig. 1.2b). The +CGs could then originate from the "main" positive charge region of this inverted structure. As noted in Williams (2001), such a structure would be expected to produce IC flashes that are also inverted relative to those in a normal tripole configuration. As discussed above, preliminary analyses of lightning mapping (Krehbiel et al., 2000b; Zhang et al., 2001) and balloon-borne electric field soundings (Rust and MacGorman, 2002; MacGorman et al., 2004) suggest that the thunderstorms in the STEPS region are sometimes inverted in polarity.

Another goal of this dissertation is to determine which, if any, of these hypotheses is most consistent with the charge structure of the +CG-dominated storms in STEPS.

These hypotheses do not explicitly address an additional element of +CG lightning production; namely, a lower negative charge region. In a normal tripole configuration, the presence of the lower positive charge beneath the main negative charge is thought to locally enhance the electric field which provides the impetus for the negative discharge to ground (e.g., Williams, 1989, 2001; Williams et al., 1989b). For the case of +CGs, a lower negative charge would provide a similar impetus for

a "main" positive charge. Furthermore, Marshall and Stolzenburg (2002) used an idealized one-dimensional charge model to demonstrate that –CG (+CG) flashes are more energetically favorable if the lower positive (negative) charge is involved in the flash. In their more more elaborate modeling studies, Mansell et al. (2002) found that CG flashes do not occur without such a lower charge region. *Another goal of this dissertation is to determine what charge structures support CG flashes (of either polarity), and how these charge structures develop and evolve within the kinematic and microphysical context of their parent storms.*

1.1.4 Enter STEPS

Most of the above studies and hypotheses are based on limited observational data. They generally lack the comprehensive time-resolved measurements of the microphysical, kinematic, and electrical structure necessary even to begin to unravel the complexities of thunderstorm electrification. As stated by Williams (2001): "Urgently needed are observations that constrain the location of the positive charge region participating in the anomalous [positive] ground flashes." With the combination of Doppler-polarimetric radar, lightning mapping, and in-situ observations, these "urgently needed observations" were made during STEPS. Given the unique combination of instrumentation and storm activity, this dissertation provides new insight into the hypotheses and pressing scientific questions outlined above.

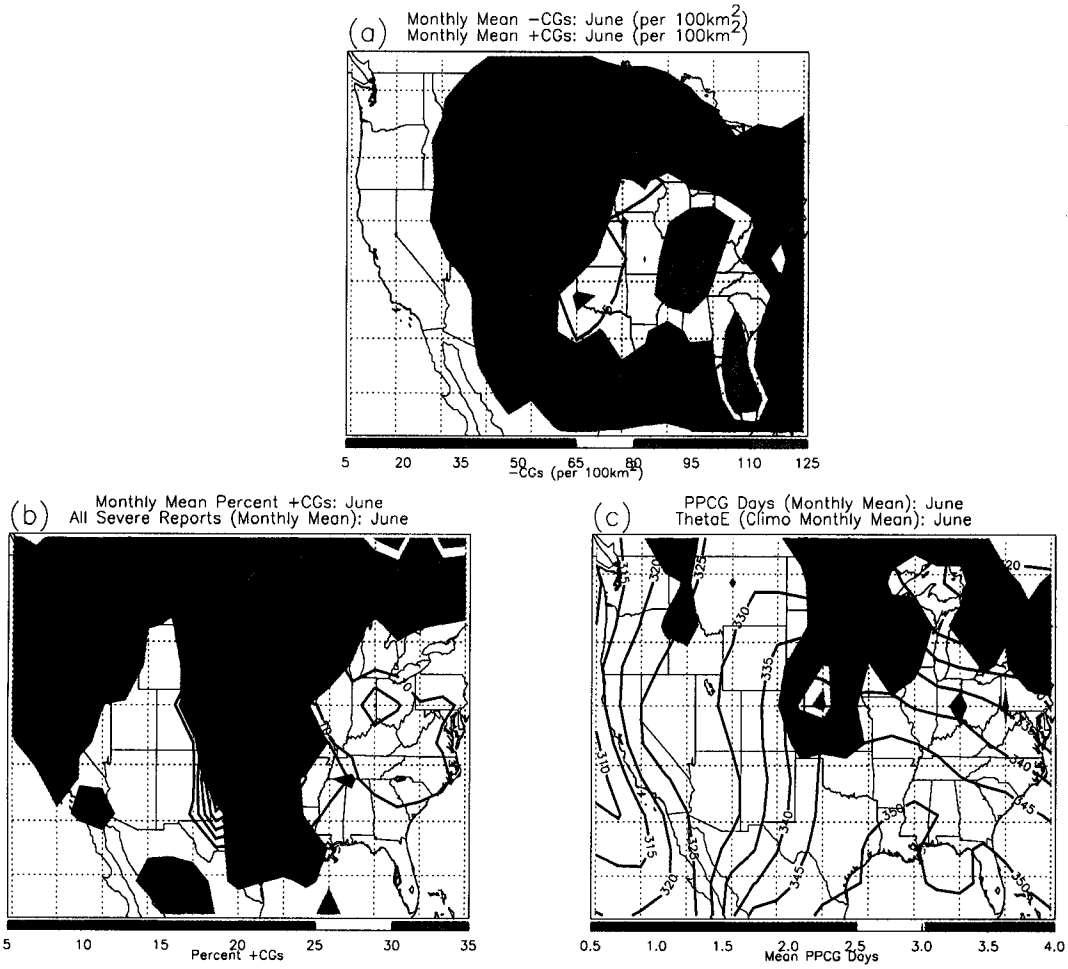

Figure 1.1: Climatological (1989–1997) mean values for June. (a) −CG flash density (color-filled according to color bar) and +CG flash density (black contours with intervals of 5 flashes per 100 km^2). (b) Percentage of +CGs (color-filled according to color bar) and severe storm reports (black contours with intervals of 10 reports). (c) Predominantly positive CG (PPCG) days (color-filled according to color bar) and surface θ_e (black contours with 5K intervals). A PPCG day is defined as a day (at each grid point) in which there were more +CGs than −CGs, with the additional constraint that there were at least 10 +CGs that day at that grid point.

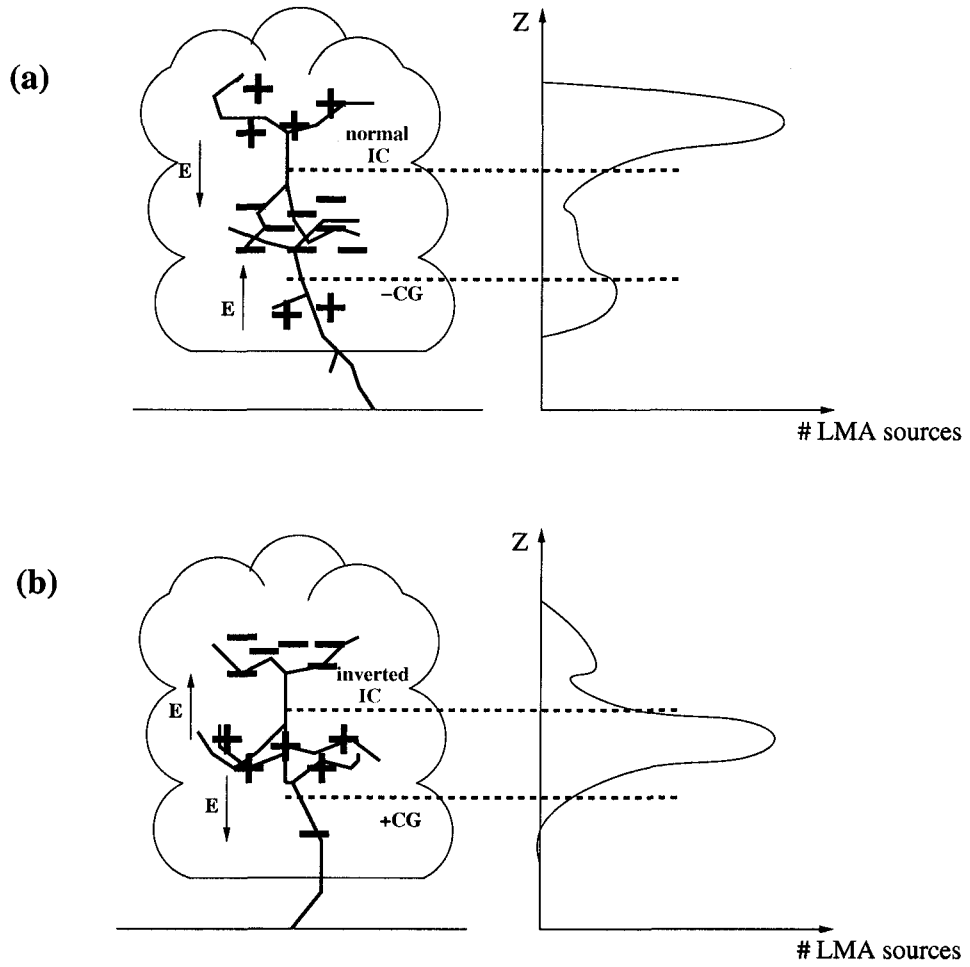

Figure 1.2: Schematics of thunderstorm charge structure and lightning for (a) normal tripole and (b) inverted tripole, with representative IC (red) and CG (blue) discharges for each case and representative altitude histograms of LMA sources. The dotted horizontal lines indicate initiation altitudes of the flashes. See Section 2.2.3 for further explanation.

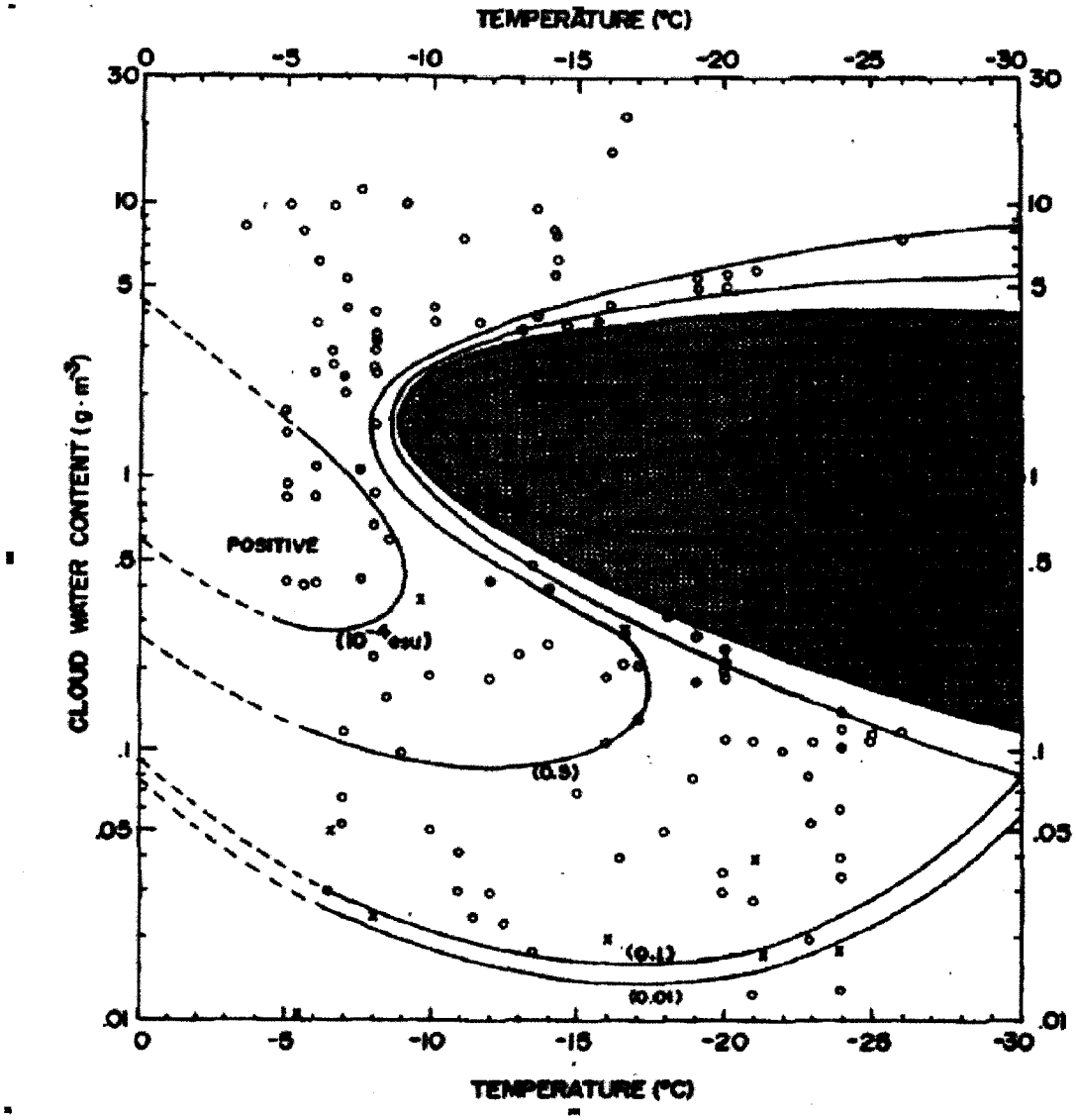

Figure 1.3: Sign and magnitude of charge imparted to riming particle in collisions as a function of temperature and liquid water content. Open circles show positive charge, solid circles show negative charge and crosses represent uncharged cases. The electric charge of rime per ice crystal collision is shown in units of 10^{-4} esu. Adapted from Fig. 8 of Takahashi (1978).

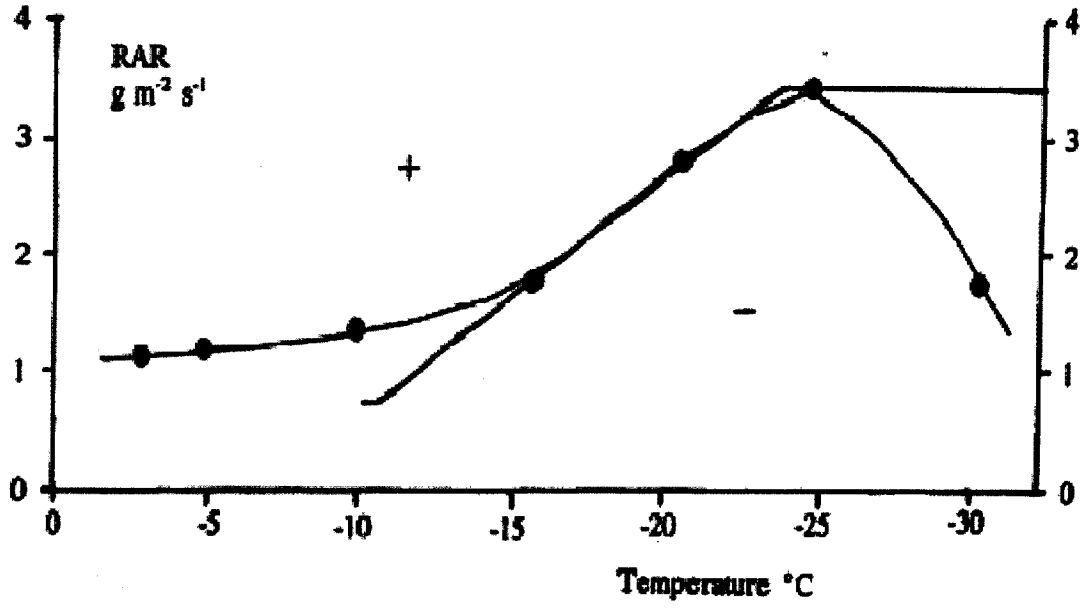

Figure 1.4: Critical rime accretion rate (RAR) for charge sign [imparted to the riming particle) reversal as a function of temperature from experiments conducted in the velocity range 4 to 11 m s^{-1}, mean velocity 7.5 m s^{-1}, drawn as a smooth curve through the data circles. Also shown is the result obtained by Saunders et al. (1991) at 3 m s−1. Rime accretion rate is simply the liquid water content multiplied by collision efficiency and impact velocity. Adapted from Fig. 6 of Saunders and Peck (1998).

CHAPTER 2

DATA AND METHODOLOGY

All times are referenced to universal time (UTC; local time=UTC–6 hours). All altitudes are referenced to mean sea level (MSL; ground level = 1.1 km MSL).

2.1 Radar

The Colorado State University CSU-CHILL and National Center for Atmospheric Research (NCAR) S-Pol polarimetric research radars, along with the KGLD National Weather Service (NWS) radar in Goodland, Kansas, comprised the triple-Doppler network during the STEPS campaign. Fig. 2.1 shows the locations of these radars along with their associated Doppler coverage areas. Table 2.1 lists the specifications for each radar.

2.1.1 Processing

The CHILL and S-Pol data files were obtained in Universal Format (UF: Barnes, 1980). Initial processing and quality control was performed while preserving the radar-centric spherical coordinate system of these UF files. The CHILL and S-Pol data were first "cleaned" of second-trip echo and other artifacts (including ground-clutter) by thresholding the data on the propagation differential phase and correlation coefficient (see description of the polarimetric variables in Section 2.1.3) using methodology similar to that of Ryzhkov and Zrnic (1998). The specific differential phase (K_{DP}) was then computed along each radar ray using a finite impulse response filter method based on Hubbert and Bringi (1995). These first two processing steps

were combined in an automated routine written by Dr. Larry Carey. Radial velocities from the CHILL and S-Pol radars were manually removed (i.e., flagged as bad data) from each ray where side-lobe contamination was suspected.

These cleaned data, along with data from the KGLD radar, were then routinely interpolated onto a Cartesian grid using NCAR's Sorted Position Radar INTerpolator (SPRINT: Mohr and Vaughn, 1979; Miller et al., 1986). For each of the case studies in the following chapters, this Cartesian grid is centered on the KGLD radar, and grid altitudes are relative to mean sea level (MSL). The horizontal resolution of these gridded data is 0.5 km for the 3 June and 29 June cases and 1.0 km for the 23 June cases. The vertical resolution is fixed at 0.5 km for all cases.

2.1.2 Doppler Synthesis

After interpolation, the velocity data were globally unfolded using NCAR's Custom Editing and Display of Reduced Information in Cartesian Space (CEDRIC; Mohr et al., 1986). If the storms were within the STEPS multi-Doppler coverage area, their three-dimensional winds were computed using the radial velocities from all three radars (when possible) or from two of the radars. This Doppler synthesis process closely followed the methodology of Tessendorf (2003) and Tessendorf et al. (2004a) and is described only briefly here. The multi-Doppler synthesis was obtained (again using CEDRIC) by vertically integrating the mass continuity equation,

$$\frac{\delta(\rho u)}{\delta x} + \frac{\delta(\rho v)}{\delta y} + \frac{\delta(\rho w)}{\delta z} = 0 \tag{2.1}$$

using the variational method for the boundary conditions (O'Brien, 1970). Coordinated volume scans, i.e., multiple radars scanning the same sectors at the same time, were not perfectly coordinated. Depending on the location of the echo relative to the radars, and depending on the scanning coverage pattern, one of the radars typically finished its volume scan sooner than another. This was especially true for coordinated scans involving the KGLD radar. The KGLD radar followed a very specific and regular 360° volume scan coverage pattern which typically took 5–6 minutes to complete.

The two research radars, on the other hand, typically restricted their coverage to smaller sectors and finished their volume scans more quickly. In attempts to account for this during the synthesis process, the velocity data from each radar were advected along the direction of storm motion (Gal-Chen, 1982). The synthesized winds were then shifted to the mean start time of each coordinated radar volume scan to account for storm advection during the sampling interval.

The resultant three-dimensional Cartesian gridded data for each volume scan were then converted to Net Common Data Format (NetCDF) which proved to be a very useful and efficient format for further processing, analysis, and display.

2.1.3 Polarimetric Radar and Hydrometeor Identification

All three of the radars in the STEPS network measure horizontal reflectivity and radial velocity. The two polarimetric research radars (CHILL and S-Pol) measure additional quantities that allow for improved discrimination of the shape, size, and phase of hydrometeors (e.g., Jameson, 1985; Bringi et al., 1986; Aydin et al., 1990; Herzegh and Jameson, 1992; Conway and Zrnic, 1993; Lopez and Aubagnac, 1997; Carey and Rutledge, 1998; Zrnic and Ryzhkov 1999; Liu and Chandrasekar, 2000; Straka et al., 2000; Lim, 2001; Scott et al., 2001; Zrnic et al., 2001). These polarimetric measurements were combined with air temperature (from nearby soundings) to infer bulk hydrometeor types within the storms of this study. To provide some background for the techniques used in this study, the following is a brief review of the definitions and physical interpretations of the five polarimetric radar measurements commonly used for hydrometeor classification. Bringi and Chandrasekar (2001) and Straka et. al (2000) (and others) provide more thorough treatments.

Horizontal Reflectivity

The horizontal reflectivity (hereafter abbreviated as Z_H) is the most commonly used and familiar of radar variables. It is proportional to the power returned in the horizontal polarization state (H received) due to scattering of a horizontally polarized

(H transmit) wave:

$$Z_H = \frac{4\lambda^4}{\pi^4}|K|^2 \langle |s_{HH}|^2 \rangle \propto \frac{|K|^2 D^6}{\lambda^2} \tag{2.2}$$

where λ is the wavelength of the transmitted wave, K is the dielectric factor, D is the mean diameter of the particles in the resolution volume, and $< |s_{HH}|^2 >$ is the squared ensemble average of the first element of the Jones scattering matrix, i.e., backscattered power in the horizontal from the ensemble of targets in the radar resolution volume. The vertical reflectivity Z_V is similarly defined for vertical transmit and receive:

$$Z_V = \frac{4\lambda^4}{\pi^4}|K|^2 \langle |s_{VV}|^2 \rangle \propto \frac{|K|^2 D^6}{\lambda^2} \tag{2.3}$$

Z_H is often expressed as the general radar reflectivity,

$$Z = \int_0^\infty N(D) D^6 dD \tag{2.4}$$

in units of mm^6 m^{-3}. The latter form more explicitly shows the dependence on number concentration $N(D)$ of targets in the radar resolution volume. However, the form of Equation 2.3 more explicitly shows the dependence on the dielectric factor and orientation of the polarized wave.

Due to its proportionality to the sixth power of the diameter, Z_H provides information about the size of the hydrometeors. In addition, liquid water has a much higher dielectric factor than ice. Thus, a water target would produce a greater Z_H than an ice target of the same size. Due to the huge measured range of Z_H, it is typically expressed in logarithmic units (or dBZ), i.e., $dBZ = 10log_{10}(Z_H)$.

Differential Reflectivity

The differential reflectivity (hereafter abbreviated as Z_{DR}) is the log of the ratio of horizontal to vertical backscattered power:

$$Z_{DR} = 10log\left[\frac{\langle|s_{VV}|^2\rangle}{\langle|s_{HH}|^2\rangle}\right] \tag{2.5}$$

Differential reflectivity should be interpreted as the reflectivity-weighted axis ratio, though this interpretation of Z_{DR} is not readily apparent in the short-hand form of Equation 2.5. That is, Z_{DR} is a measure of the mean axis ratio (horizontal dimension to vertical dimension) of the hydrometeors weighted by their reflectivity. Z_{DR} thus gives information about the shape and size of the hydrometeors in the resolution volume. Horizontally-oriented hydrometeors (e.g., large oblate rain drops) have large Z_{DR} values, while quasi-spherical hydrometeors (e.g., drizzle, dry graupel, and tumbling hail) have Z_{DR} near zero.

Aydin et al. (1986) combined Z_H and Z_{DR} to form a composite hail variable they called H_{DR}. They defined this variable by first using measured and modeled liquid drop size distributions to define a piecewise "rain line" function of Z_H in terms of Z_{DR}:

$$f(Z_{DR}) = \begin{cases} 27, & Z_{DR} \leq 0 \text{ (dB)} \\ 19Z_{DR} + 27, & 0 \leq Z_{DR} \leq 1.74 \text{ (dB)} \\ 60, & Z_{DR} > 1.74 \text{ (dB)} \end{cases} \tag{2.6}$$

Figure 2.2 illustrates this schematically. The segments of this $f(Z_{DR})$ function form an upper bound to Z_H measurements due only to rain echo. For a given pair of Z_H, Z_{DR} measurements, a Z_H that exceeds the rain line value indicates the presence of ice. The H_{DR} is defined as the deviation from the rain line:

$$H_{DR} = Z_H - f(Z_{DR}) \tag{2.7}$$

where Z_H is in dBZ and H_{DR} is in dB. "When $H_{DR} > 0$, the radar observables (Z_H, Z_{DR}) lie in the region above $f(Z_{DR})$ in the Z_H–Z_{DR} plane and are taken to signify the presence of hail. Also, the larger H_{DR}, the greater the certainty that the radar reflectivities are not due to raindrops" (Aydin et al., 1986).

Specific Differential Phase

The differential propagation phase ϕ_{DP} is the difference in the propagation phase delay for horizontally (ϕ_H) and vertically (ϕ_V) polarized waves,

$$\phi_{DP} = \phi_H - \phi_V \tag{2.8}$$

The phase delays (ϕ_H, ϕ_V) would differ if the propagation medium consisted of oriented hydrometeors. For example, a rain shaft composed of oblate rain drops would have a longer propagation path in the horizontal than in the vertical. Thus, due to a greater path length through the liquid water in the rain shaft, a horizontally polarized wave would experience greater phase delay than would a vertically polarized wave.

The specific differential phase (hereafter abbreviated as K_{DP}) is the change in ϕ_{DP} with range r, and is given by:

$$K_{DP} = \frac{1}{2}\frac{\partial \phi_{dp}}{\partial r} \tag{2.9}$$

In practice, K_{DP} is approximated by a finite difference calculation. Ice targets (especially hail) are typically quasi-spherical such that ϕ_{DP} can be approximated as the difference between the phase delays due only to liquid water, i.e.,

$$\begin{aligned} \phi_{DP} &= (\phi_{H,water} + \phi_{H,ice}) - (\phi_{V,water} + \phi_{V,ice}) \\ &\approx \phi_{H,water} - \phi_{H,water} \end{aligned} \tag{2.10}$$

We can then interpret K_{DP} as the range derivative of ϕ_{DP} due only to liquid water. Though it's not apparent in the above equation, K_{DP} is proportional to the liquid water mass in the radar resolution volume and thus very useful for quantitative rainfall estimation. For the purposes of hydrometeor classification, K_{DP} is useful for discriminating between hail and rain and for determining rain drop size. Larger K_{DP} is generally indicative of heavier rain and/or larger liquid drops.

Linear Depolarization Ratio

The linear depolarization ratio (hereafter abbreviated as LDR) is the logarithm of the ratio of received cross-polar to co-polar power. That is, given a horizontally transmitted wave, LDR gives the ratio of power received in the vertical to power received in the horizontal:

$$LDR = 10log\left[\frac{\langle|s_{VH}|^2\rangle}{\langle|s_{HH}|^2\rangle}\right] \tag{2.11}$$

LDR increases due to scattering from irregularly shaped or canted radar targets. It also increases with increased dielectric of the target. LDR is most often used to locate hail (especially wet hail) and has been used in concert with Z_{DR} to infer hail size. Kennedy et al. (2001) and Depue (2003) combined LDR with Aydin's H_{DR} to define another composite variable called the Hail Quadrature Parameter (HQP). This is constructed by normalizing the measured LDR over the range (–25 to –10 dB) and normalizing H_{DR} over the range (5 to 50 dB). The HQP is defined as the length of the (LDR, H_{DR}) vector in this normalized space. For example, an LDR of –10 dB and H_{DR} of 50 would give an HQP of $\sqrt{2}$, i.e., the maximum value. Only positive HQP values are considered. Depue (2003) evaluated the utility of HQP for several Colorado hailstorms by actually going out and measuring the hail that fell and/or getting hail size information from people who measured the hail. She found some evidence that HQP does indeed increase with hail diameter. Further testing, refinement, and interpretation of HQP is ongoing. So far the results suggest that HQP does not provide more information about hail and hail size than does H_{DR} (S. A. Rutledge, personal communication).

Correlation Coefficient at Zero Lag

The correlation coefficient at zero lag (hereafter abbreviated as ρ_{HV}) is defined by,

$$|\rho_{HV}| = \frac{< s_{VV} s_{VV}^* >}{(< s_{VV}^2 >^{1/2} < s_{VV}^2 >^{1/2})} \tag{2.12}$$

It is a measure of the randomness and heterogeneity of targets in the resolution volume. In a radar resolution volume composed of a single hydrometeor type (e.g., all drizzle or all graupel), ρ_{HV} should be near unity. The value of ρ_{HV} is expected to decrease from unity in a region of mixed hydrometeors. It is useful as an indicator of the melting level and other regions of mixed phase. As described in Scott et al. (2001), LDR and ρ_{HV} are not independent measured quantities; they give redundant information. Hence, in truth, polarimetric radar gives only four independent measurements.

Fuzzy Logic Hydrometeor Classification (FHC)

The five polarimetric variables plus temperature can be thought of as comprising a six-dimensional (6D) space, one dimension for each of the radar variables plus one for temperature (Recall that only four of the radar variables are independent measurements since LDR and ρ_{HV} are related.) Due to the size, shape, phase and orientation of bulk hydrometeors in the radar resolution volume, the radar echoes from specific hydrometeor types are expected lie within specific regions of this 6D space. Straka et al. (2000) and Zrnic et al (2001) provide detailed boundaries and thresholds for each dominant hydrometeor type in this space. For example, large hail is expected to be constrained to $Z_h > 55dBZ$, $-1 < Z_{dr} < 0.5$, $-0.5 < K_{dp} < 1$, etc. One could thus take a set of radar measurements and, in a lookup table fashion, determine which hydrometeor type best matches the measurements. An example of this would be something like the following:

```
IF Z_h>55
AND (-1<Z_dr<0.5)
AND (-0.5<K_dp<1)
AND(LDR>-24)
```

...

```
THEN Hydrometeor = Large Hail.
```

Several studies (e.g., Lopez and Aubagnac, 1997; Carey and Rutledge, 1998) have done hydrometeor classification in this way. However, this lookup table method is not always reliable because it imposes "hard" boundaries between the radar variable sub-spaces of each hydrometeor type. As noted in Liu and Chandrasekar (2000): "the radar signature for different hydrometeors is not mutually exclusive and unique," and the boundaries in the 6D space overlap, such that more than one hydrometeor could occupy the same space in the lookup process. Fuzzy logic hydrometeor classification (hereafter abbreviated as FHC) mitigates this problem by essentially making the boundaries softer.

In technical terms, the FHC process consists of four simple steps : (1) Fuzzification, (2) Inference, (3) Aggregation, and (4) Defuzzification. See the block diagram in Fig. 2.4. In simple terms, this means take the crisp (i.e, not fuzzy) inputs, perform some physically-based logic on them, and produce a crisp output. In terms of hydrometeor classification, the crisp inputs are the radar measurements and temperature, and the crisp output is the hydrometeor type (Fig. 2.5). The FHC method used in this dissertation is based on that of Liu and Chandrasekar (2000), with some significant differences.

The fuzzification steps converts the six input variables to fuzzy sets with corresponding membership degrees, or truth values. The fuzzy sets correspond to the hydrometeor types like drizzle, rain, hail, etc. The truth values are simply numbers between 0 and 1 which indicate how well the input variables fit each of the fuzzy sets. For our purposes, each of these truth values is the returned value of a membership beta function (MBF) of the form:

$$\beta(x, m, a, b) = \frac{1}{1 + \left[\left(\frac{x-m}{a}\right)^2\right]^b} \tag{2.13}$$

where x is the input variable (e.g., Z_H, Z_{DR}, etc.), m is the center of the function, a is the width, and b is the slope. For a given hydrometeor type, this function is defined to be near unity in the region where there is confidence that the value of x is due to that hydrometeor type. Outside this region, the function falls off asymptotically at a rate defined mainly by its slope, b, but never reaches zero. The value of each MBF may be thought of as a probability or "truth value" that the measurement x is due to a particular hydrometeor type j. For the most part, these MBFs were constructed based on the radar variable threshold tables in Straka et al. (2000). Tables 2.3–2.13 summarize these thresholds and compare them to thresholds used in other studies. Figs. 2.6–2.16 show plots of the actual MBFs for each hydrometeor type.

The inference step consists of taking the "fuzzy" outputs of each MBF and combining them to give a total truth value for each hydrometeor type. For example, in a manner analogous to computing a joint probability, the MBFs could be combined as a product:

$$\begin{aligned} \mu_j &= \beta_{Z_H,j} * \beta_{Z_{DR},j} * \cdots * \beta_{T,j} \\ &= \prod_{i=1}^{6} \beta_{i,j} \end{aligned} \tag{2.14}$$

Fig. 2.3 illustrates the portion of the two-dimensional space of Z_H and Z_{DR} expected to be occupied by rain. Extension of this product to six dimensions (which is, obviously, not possible to illustrate graphically) gives the total truth value for rain. Liu and Chandrasekar (2000) used this product method with good results. However, as noted by Zrnic et al.(2001), there can be difficulties with this method. A single bogus measurement could conceivably lead to misclassification. For instance, if the LDR value were contaminated by noise, this product method may combine the accurate MBF output from Z_H, Z_{DR}, K_{DP}, ρ_{HV}, and temperature with inaccurate MBF output from LDR. If the MBF output from LDR were near zero, this could lead to misclassification despite the good fit to the other measurements. Instead of a product,

Zrnic et al.(2001) employed a weighted sum scheme in which all of their membership functions were trapezoidal (not beta functions) and were two-dimensional with Z_H. The FHC in this dissertation uses one-dimensional MBFs (not trapezoids) for all the variables and combines the MBFs in a hybrid weighted sum scheme similar to that in Lim (2001). The output of the MBFs for Z_{DR}, K_{DP}, LDR and ρ_{hv} are combined as a weighted sum like this:

$$\begin{aligned}\mu'_j &= W_{Z_{DR},j} * \beta_{Z_{DR},j}(Z_{DR}) \\ &\quad + W_{K_{DP},j} * \beta_{K_{DP},j}(K_{DP}) \\ &\quad + W_{LDR,j} * \beta_{LDR,j}(LDR) \\ &\quad + W_{\rho_{HV},j} * \beta_{\rho_{HV},j}(\rho_{HV}) \\ &= \sum_{i=1}^{4} W_{i,j} * \beta_{i,j}(x_i) \end{aligned} \tag{2.15}$$

This weighted sum is normalized by the sum of the weight factors then multiplied by the MBFs for Z_H and temperature to give the total truth value for each hydrometeor type:

$$\mu_j = \beta_{T,j}(T) * \beta_{Z_H,j}(Z_H) * \mu'_j \tag{2.16}$$

The weighting factors $W_{i,j}$ allow for more importance to be placed on each variable for each hydrometeor type. Multiplication of the weighted sum by the MBFs for Z_H and temperature effectively gives more importance to these two variables. As we gain better knowledge and in situ validation of this hydrometeor identification, we could use this framework to define unique weighting factors for each variable and each hydrometeor type. However, for this dissertation, one weighting factor was used for each polarimetric variable for all hydrometeor types. That is, the weighting factor for, say, LDR was different from the weighting factor for Z_{DR}, but all hydrometeor types used the same set of weighting factors. These weighting factors are the same ones suggested by Zrnic et al. (2001) and are listed in Table 2.14.

The aggregation step simply compares the total truth values μ_j from each hydrometeor type, and defuzzification consists of returning the hydrometeor type with the maximum μ_j. The index j is then defined as the dominant bulk hydrometeor type at each grid point. If none of the hydrometeor types gets a total truth value greater than 0.001, then the grid box is assigned to the unclassified category. The resultant three-dimensional grid of hydrometeor types can then be analyzed, manipulated, and plotted like any of the other radar variables.

Table 2.2 lists the hydrometeor types used in the FHC. Essentially, these FHC types apply a physical description (e.g., graupel, rain, hail) to each radar volume based on where the measurements fall within the theoretically expected ranges for each measurement and hydrometeor type. It should be noted that FHC gives the *dominant* hydrometeor species in each radar resolution volume, with little or no information about the size distribution of the dominant species, or relative presence and concentration of other less dominant species in the same volume. For example, a grid point classified as hail may also contain significant amounts of rain, graupel, etc. The number and description of the hydrometeor types can be changed or modified by omitting some of them or combining categories with similar threshold ranges. For example, the "high density graupel" category could be combined with the similar "small hail" category by combining their respective MBFs into one MBF that encompasses both categories. Reducing the number of possible outputs forces the FHC algorithm to choose from the reduced number of hydrometeor types.

When examining individual radar cross-sections, hydrometeor classification provides a useful and physically consistent summary of the polarimetric radar and temperature measurements. For example, Figs. 2.17 and 2.18 show comparisons of the polarimetric measurements to the FHC for the case of the 29 June 2000 supercell. Here a so-called 'Z_{DR} column' (Hall et al., 1984; Illingworth et al., 1987) has formed near a strong updraft, indicating ingestion of large liquid drops. Atop the Z_{DR} column is a so-called 'LDR cap' (Bringi et al., 1997) indicating wet/melting hail or drops in the process of freezing. The interpretation is that big drops in the Z_{DR} column

served as effective embryos for rapid hail growth. The large drops themselves may have resulted from melting hail and/or graupel. As shown in the bottom panel, the FHC captures this process quite well. Note also the strong downward gradient in Z_{DR} in Fig. 2.17b. This clearly illustrates how the quasi-spherical ice particles become oblate liquid drops as they descend past the melting level. The very large Z_{DR} values (>2 dB) near the precipitation core indicate larger rain drops there, as apparently the hail growing aloft has not yet descended to the surface. Again, the FHC result summarizes all this information very well. Fig. 2.18 shows the same storm, but 20 minutes later. (The color-shading for Z_{DR} in Fig. 2.18 is different from Fig. 2.17.) The hail growth had obviously accelerated over this time period, as the precipitation core has very large Z_H but near-zero Z_{DR}. This is a very robust indication of a large hail shaft extending to the surface. However, the large values of K_{DP} in Fig. 2.18 indicate significant liquid water mass in the hail core as well, suggesting that the precipitation core had hail mixed with rain and/or hail with a thick water coating. Panels (c) and (d) of Fig. 2.18 show the FHC results in which hail/rain mixtures are excluded and included, respectively. The two results look very similar, but have some differences below the melting level. In general, the hail/rain mixture result shows mixed phase precipitation right where there is elevated K_{DP}, while the mixture-free result categorizes the "small hail mixed with rain" area as pure rain and the "large hail mixed with rain area" as pure large hail. As a final example, Fig. 2.19 compares near-surface horizontal cross-sections of Z_H, H_{DR}, HQP, and the FHC. The agreement of the FHC to the other hail metrics is very good. Hence, overall the FHC seems to do a good job.

For this dissertation, the two "hail mixed with rain" categories were omitted, forcing grid points that would have been classified as rain/hail mixtures to be classified as either hail or rain. As illustrated above, it's possible to discriminate pure hail or pure rain from a hail/rain mix; however, the FHC was used in this dissertation primarily for computing time series of echo volumes of the various hydrometeor types (particularly hail, see Section 2.1.4). These time series are more physically consistent

and useful for interpretation if the rain mixed with hail categories are removed from consideration.

2.1.4 Echo Volume Computations

Using the three-dimensional Cartesian-gridded radar volume scans, "echo volumes" of specific quantities were computed for the purposes of constructing time series and time-height contour of these specific quantities. These "echo volumes" were computed by isolating the echo of interest, counting up the the number of Cartesian grid boxes that satisfied certain criteria (e.g., $Z_H > 30$ dBZ, updraft > 10 ms^{-1}, or classified as hail by the FHC), then multiplying this number by the volume of the grid box. Such time series are useful as gross representations of storm evolution and for investigating temporal relationships among precipitation, updraft, and lightning.

2.2 Lightning Mapping Array (LMA)

The New Mexico Tech Lightning Mapping Array (LMA: Rison et al., 1999; Krehbiel et al., 2000a; Hamlin, 2004; Thomas et al., 2004) is a Global Positioning System (GPS)-based time of arrival (TOA) system that locates very high frequency (VHF) radiation sources emitted by lightning discharges. For a given lightning flash, the LMA may locate hundreds to thousands of such VHF sources, resulting in detailed maps of the total lightning activity. The LMA sources can be grouped into discrete flashes for computing total (IC+CG) flash rates (see Section 2.2.2), and analysis of the individually mapped lightning flashes can be used to determine qualitative thunderstorm charge structure (see Section 2.2.3).

2.2.1 How the LMA Works

Hamlin (2004) gives a very detailed description of the LMA, which is summarized here. During STEPS, the LMA consisted of an array of 13 stations centered within the Doppler radar network and extending 57.2 km along N–S and 76.6 km along E–W (Fig. 2.20; see also Thomas et al., 2004). As shown in Fig. 2.21, each LMA station

included:

- An antenna to detect the VHF radiation from lightning,
- A GPS antenna to provide very accurate position of the station and time of arrival (TOA) of the radiation,
- A personal computer (PC) and associated custom-made electronics to process, time-tag, and archive the TOA of the radiation,
- A communications antenna for remote control of the station and for transmission of the TOA measurements for near real-time processing.

The LMA receives lightning radiation signals in a locally unused TV channel (in this case, Channel 3 at 60-66 MHz).

The LMA maps lightning by accurate TOA of VHF radiation emitted by impulsive accelerations of charge during lightning discharges. Each of these impulsive accelerations is termed an event or a source. At each LMA station, the VHF antenna measures the radiation from each source, and an analog to digital (A/D) converter digitizes the logarithmically amplified antenna output . The peak power event (above a defined threshold) is saved in successive discrete 80 (or 100) μs windows, and the time of each peak power event is saved at a timing resolution defined by the digitization rate of the A/D converter (see Fig. 2.22). The timing is done this way since it's assumed that the peak power associated with a given lightning event will produce the the peak power received at each antenna in the array. However, there is sometimes local noise (corona discharges from sharp objects and power line noise) that may exceed the received power of the lightning event at a given station. During STEPS, the LMA used two types of A/D converters with digitization rates of 20 and 25 MHz, with respective timing window sizes of 100 and 80 μ. At full duty cycle, each LMA station in this configuration would save an event in each 100 (80) μs window, resulting in 10,000 (12,500) recorded events s^{-1} at each station. Processing of the LMA data

to determine lightning source location and time (described below) is not dependent on the window size. As described in Thomas et al. (2004), the LMA during STEPS had a nominal timing uncertainty of 40-50 ns.

As illustrated in Fig. 2.23, for a lightning event that occurs in space and time at (x, y, z, t), and is recorded at each LMA station located at (x_i, y_i, z_i), the TOA of the event at each station is given by

$$t_i = t + \frac{1}{c}\sqrt{(x - x_i)^2 + (y - y_i)^2 + (z - z_i)^2} \tag{2.17}$$

where c is the speed of light. Square this, expand, and rearrange to get,

$$c^2 t_i^2 - r_i^2 = r^2 - c^2 t^2 - 2(x_i x + y_i y + z_i z - c^2 t_i t) \tag{2.18}$$

where $r_i^2 = x_i^2 + y_i^2 + z_i^2$.

If four other stations record an event within a physically possible time[1] of the first one, we get four more equations like the one above:

$$\begin{aligned}
c^2 t_j^2 - r_j^2 &= r^2 - c^2 t^2 - 2(x_j x + y_j y + z_j z - c^2 t_j t) \\
c^2 t_k^2 - r_k^2 &= r^2 - c^2 t^2 - 2(x_k x + y_k y + z_k z - c^2 t_k t) \\
c^2 t_l^2 - r_l^2 &= r^2 - c^2 t^2 - 2(x_l x + y_l y + z_l z - c^2 t_l t) \\
c^2 t_m^2 - r_m^2 &= r^2 - c^2 t^2 - 2(x_m x + y_m y + z_m z - c^2 t_m t)
\end{aligned} \tag{2.19}$$

Each equation in (2.19) is then subtracted from Equation (2.18) to get rid of the quadratic terms, r^2 and $c^2 t^2$. This gives four differenced linear equations that are solved analytically for the event location. To simplify the notation, let $x_{ij} \equiv x_i - x_j$, $y_{ij} \equiv y_i - y_j$, etc., and let

$$K_{ij} \equiv \frac{(r_i^2 - r_j^2) - c^2(t_i^2 - t_j^2)}{2}. \tag{2.20}$$

[1]Since the spatial separation between two LMA stations was at most 60 km during STEPS, this physically possible time is generally 200 μs.

In matrix form, then, we have the system of equations:

$$\begin{pmatrix} x_{ij} & y_{ij} & z_{ij} & -ct_{ij} \\ x_{ik} & y_{ik} & z_{ik} & -ct_{ik} \\ x_{il} & y_{il} & z_{il} & -ct_{il} \\ x_{im} & y_{im} & z_{im} & -ct_{im} \end{pmatrix} \cdot \begin{pmatrix} x \\ y \\ z \\ ct \end{pmatrix} = \begin{pmatrix} K_{ij} \\ K_{ik} \\ K_{il} \\ K_{im} \end{pmatrix} \tag{2.21}$$

The solution from this system of equations gives a first guess at the event location, $m_0 = (x_0, y_0, z_0, ct_0)$. This first guess is further refined by adding measurements from as many additional stations that recorded the same event[2]. The positions and TOAs of all these stations along with the first guess m_0 from the linear solution are used to solve for the event location using an iterative process called the Levenberg Marquardt method (see, e.g, Bevington, 1969). That is, m_0 from the differenced linear equations serves as the the initial input into the modified Newton's method root finding algorithm, expressed in classical inverse problem form as:

$$m_{next} = m_0 - (J(m_0)^T J(m_0) + \lambda I)^{-1}(J(m_0)^T F(m_0)) \tag{2.22}$$

where J is the Jacobian of the forward model G matrix,

$$G(m_0)_i = t_0 + \frac{1}{c}\sqrt{(x_0 - x_i)^2 + (y_0 - y_i)^2 + (z_0 - z_i)^2} \tag{2.23}$$

and F is the vector of residuals,

$$F(m_0)_i = \frac{G(m_0)_i - t_i}{\sigma_i} \tag{2.24}$$

Equation 2.22 is iterated until it converges, that is, until the difference in residuals from one iteration to another

$$\frac{\|F_{old}\|_2 - \|F_{new}\|_2}{\|F_{old}\|_2} \leq \epsilon \tag{2.25}$$

[2]Theoretically, one could analytically solve for the four unknowns (x, y, z, t) of the lightning event with just four stations giving four equations like Equation 2.18. However, the 4×4 matrix in Equation 2.21 is ill-conditioned because the lack of a vertical baseline results in near-zero values of the elements $z_{i,*}$. Hence, more stations are included in the solution to provide redundancy and to discriminate against inclusion of noise.

changes by a very small amount, ϵ.

In mathematical terms, this method finds the root of the gradient of the residual vector, i.e., the minimum of the residual vector. Essentially, this amounts to finding the best fit (i.e., minimal error) between the matrix of observed TOAs (t_i^{obs}) and the matrix of TOA solutions from each iteration (t_i^{fit}). This error or goodness of fit can be quantified in terms of the χ^2:

$$\chi^2 = \sum_{i=1}^{N} \frac{\left(t_i^{obs} - t_i^{fit}\right)^2}{\Delta t_{rms}^2} \tag{2.26}$$

where N is the number of stations in the solution, and Δt_{rms} is the known (or assumed) uncertainty of the measured TOAs. As detailed in Hamlin (2004) and Thomas (2004), the reduced χ^2 value ($\chi_\nu^2 = \chi^2/\nu$, where $\nu = (N-4)$ is the number of degrees of freedom) is used to define a metric for the quality of the iterative solution. If the χ_ν^2 is low enough (typically ≤ 5), then the iterative solution is good enough, and the event is considered located. In practice, solutions for each event are found with all reasonable combinations of stations (Fig. 2.22), and only the solution giving the lowest χ_ν^2 for each event is kept.

Thomas et al. (2004) performed a detailed analysis of the accuracy of the LMA in general, and for the STEPS configuration in particular. For lightning sources within the LMA network, they found that the effective timing errors (Δt_{rms} in Equation 2.26) were $\approx$ 50 ns, with location accuracies of 6–12 m in the horizontal and 20–30 m in the vertical. This accuracy was degraded for lightning sources very low to the ground. Location accuracy for lightning sources outside the network decreased with distance and scaled with range. Based on model results and very reasonable physical interpretations, they expressed the location uncertainties in azimuth (Δy), range (Δr), and height (Δz) for sources outside the network as:

$$\Delta y = \left(\frac{r}{D}\right) c\Delta T \quad (2.27)$$

$$\Delta r = \left(\frac{r^2}{D^2}\right) c\Delta T \quad (2.28)$$

$$\Delta z = \left(\frac{r^2}{Dz}\right) c\Delta T \quad (2.29)$$

where r is the slant range to the radiation source, D is the effective diameter of the network, $\Delta T \approx \sqrt{2}\Delta t$ is the uncertainty in the TOA difference at a given pair of stations, and Δt is the root-mean-square timing uncertainty at each station. Thomas et al. also found that the timing errors did follow a χ^2 distribution, suggesting that these errors are indeed Gaussian. The χ^2 statistics are such that a restriction of $\chi^2_\nu \leq 2$ passes about 90% of valid (i.e., well-located) sources (e.g., Bevington, 1969).

New Mexico Tech (NMT) processed all the LMA data used in this dissertation. That is, NMT took the data from each individual station and performed the iterative solution algorithm (described above) for each event. The resulting processed data consist of just the time, location, and χ^2 value of each recorded lightning event. NMT have these processed data available in the public domain, but at decimated data rates. The decimation effectively reduces the number of events to ~10% of "full-rate" data. For this dissertation, however, only the full-rate data were used.

Fig. 2.24 shows an example of how the LMA data are typically displayed and analyzed. This figure shows 10 minutes of LMA data from one of the storms on 23 June 2000. There will be many plots like this one in this dissertation, so some description of the layout of these plots is in order. The top panel shows the altitude of the LMA sources versus time. In this case, the sources are color-coded with time, blue to red. The lower panels shows three two-dimensional projections of the LMA sources, counterclockwise from the top-left: altitude versus east-west distance, north-south distance versus east-west distance, and north-south distance versus altitude. The color-coding is the same in all panels. It may be useful to think of the projections in the three lower panels as the bottom and lateral surfaces of a box. The LMA sources

within the box are projected onto these surfaces, then the lateral surfaces are folded down. The histogram near the top right shows the number of sources as a function of altitude. The LMA sources can also be plotted in terms of LMA source density (as in Fig. 2.25), which highlights the more lightning-active regions of the storm.

Note the discrete appearance of the LMA sources in the upper altitude versus height panel in Fig. 2.24. The sources are grouped into what look like vertical streaks. These groupings of LMA sources are individual lightning flashes, each one composed of up to hundreds or thousands of sources. They are very compressed in the figure because of the large time range (10 minutes) shown. Zooming in on one of these flashes (Fig. 2.26) allows for inspection of the temporal and spatial development of the flash. This development is much clearer when the the sources are viewed in a time-animated fashion. Obviously such animations are not possible in the static images like in Fig. 2.26, but color-coding the sources by time gives some sense of the development.

2.2.2 Flash Counting

Total flash rates (IC plus CG) are determined by applying an algorithm developed by Thomas et al. (2003) which sorts the LMA sources into isolated groups. If an individual source is separated by less than 150 ms in time and 3 km in horizontal distance from another source, then the sources are put into the same group. Each group is deemed a "flash". All such flashes are then simply binned into each UTC minute to arrive at a total flash count for each minute. Only those sources with $\chi^2_\nu \leq 1$ were used in the flash rate computations. Williams et al. (1999) and Williams (2001; see his Table 13.2) used a similar method to deduce flash counts from the LDAR system at Kennedy Space Center. Flashes with fewer than ten sources were excluded in an attempt to eliminate noise sources and single-source "flashes" that could give artificially (and unphysically) large flash rates (see, e.g., Fig. 2.27). Though this 10-source threshold is somewhat arbitrary, it seems large enough to ensure that those flashes with ten or more sources are not noise. This sorting algorithm has been tested

on storms with low to moderate lightning activity by simply visually counting distinct groupings of LMA points and then comparing the visual count with the output of the sorting algorithm. For these low to moderate cases, the sorting algorithm works very well. However, for more intense storms when the lightning activity is almost continuous (like in the severe stages of the 29 June supercell), it is often impossible to visually discern distinct flashes in the LMA data. Given that there is some uncertainty in the sorting algorithm and some subjectivity in the additional 10-source criterion, there is some concern about the validity of these flash rates. However, for the purposes of this study, the interest is primarily in the *trends*. Fig. 2.27 compares the lightning activity of the 29 June storm in terms of overall LMA sources, total flash rates including all groups of sources (including single-event "flashes"), and total flash rates that include only those groups of sources with at least 10, 50, and 100 sources. As is evident in this figure, the trends are much the same regardless of how the LMA sources are partitioned into flashes. Imposing the 10-source criterion reduces the non-thresholded total flash rates by a factor of 2–5, while further restricting the flashes to $\geq$50 or $\geq$100 sources leads to less severe reduction but very good preservation of the trends. In this dissertation, however, the 10-source threshold is used for the total flash rate because it seems like a more physically representative metric that is most directly comparable to other flash rates reported in the literature.

2.2.3 Charge Structure Determination

Analysis of LMA data on a flash-by-flash basis is an interpretative process guided by a realistic physical model of the lightning discharge. Recent interferometer measurements (Rhodes et al., 1994; Shao and Krehbiel, 1996) and LMA measurements (Rison et al., 1999; Krehbiel et al., 2000a, Hamlin, 2004; Thomas et al., 2004) support the bi-directional model which was originally proposed by Kasemir (1960) and more recently advocated and described by Mazur and Ruhnke (1993). In this model, the lightning discharge initiates in the strong electric field between regions of net positive and negative charge. The discharge then propagates in opposite directions from the

discharge origin with one direction advancing negative charge (called negative breakdown or negative leaders) and the other direction advancing positive charge (positive breakdown or positive leaders). The charge block experiments of Williams et al. (1985) and modeling studies of Mansell et al. (2002) showed that discharges preferentially propagate into regions of higher charge density, with much denser branching in these regions.

Using this bi-directional model as a basis for physical interpretation, the temporal and spatial development of each flash is examined in a time-animated sense to infer locations of the charge regions involved in the flashes. As described in Rison et al. (1999): "Positive charge regions are penetrated by negative polarity breakdown which is inherently noisier [at the 60–66 MHz frequencies used by the LMA] than positive breakdown into negative charge regions. The difference is sufficiently pronounced that one can usually determine the polarity of the breakdown and the sign of the charge region from the relative number of sources." Thus, for a given flash, a region of relatively greater number of sources is generally indicative of a positive charge region (e.g., see the schematic of Fig. 1.2). In addition, partial mapping of negative charge regions is possible when negative leaders retrace the path of the quieter positive leader. This retracing of the positive channel by negative breakdown seems to correspond to the "recoil streamers" described by Mazur and Ruhnke (1993). For a typical IC flash between two charge regions, the lightning mapping generally reveals a stratified bi-level structure. Since the LMA primarily detects negative polarity breakdown, and since the negative breakdown proceeds through positive charge, the region (or height range) with a greater number of LMA sources typically corresponds to the positive charge region and the region (or height range) with fewer LMA sources corresponds to the negative charge region. The relative number of LMA sources in each inferred charge region gives a rough idea of the charge structure, though the spatial and temporal development of each flash is a more useful and reliable way to determine the charge region involved in the flash. Since the LMA primarily detects negative breakdown, the propagation direction of the first several sources of a flash are assumed

to correspond to negative breakdown that propagates in a direction opposite that of the electric field vector, i.e., the lightning mapping of each flash is assumed to initially progress toward positive charge and away from negative charge. The recent study by Coleman et al. (2003) found good agreement between LMA-inferred charge structure and balloon soundings of electric field. The location of LMA-inferred flash initiation agreed well with the balloon-inferred heights of maximum electric field, and the lightning preferentially branched into "wells" of electrostatic potential, which are typically coincident with regions of large net charge density.

To illustrate the LMA-inferred charge structure methodology, Fig. 2.28 shows lightning mapping of a five-flash sequence during the 29 June 2000 storm which reveals five vertically stacked charge regions, alternating in polarity with positive the lowest. The sources are color-coded by inferred charge to highlight the stratified structure. Fig. 2.29 shows the second flash of the five-flash sequence, with the sources color-coded by time. This flash initiated at 9.5 km, with negative breakdown initially proceeding *downward* and through an inferred stratified positive charge region at 8–9 km. A distinct and more sparse grouping of sources above the initiation point mapped out the inferred negative charge at 10–11 km. Additionally, some of the red-colored points late in the flash indicate a retracing of the breakdown through both charge regions. Such flashes are termed "inverted" IC flashes because they reveal an inverted dipole structure. Fig. 2.30 shows the third flash of the five-flash sequence and shares many of the features of the previous flash, but flipped in the vertical. This flash initiated *upward* from 8 km into the same stratified positive charge region at 8–9 km that was revealed by the previous inverted flash. The sparse grouping of sources at 6–7 km maps out the inferred negative charge below the positive. Such flashes are termed "normal" IC flashes as they reveal a normal dipole structure. Hence, the location of the positive charge was consistently revealed by both of these flashes. The remaining flashes were similarly clear, with each showing distinct bi-level structure. When put together, they reveal a very clear and consistent picture of the charge structure (Fig. 2.28). This sort of flash-by-flash analysis is performed on

literally hundreds to thousands of flashes throughout the duration of each storm to obtain a qualitative picture of the gross charge structure as a function of time. For example, Fig. 2.31 shows the same ten minutes of LMA data as Fig. 2.24, but with the sources color-coded by inferred charge instead of by time. Here all the lightning flashes showed a very consistent normal tripole charge structure. Finally, Fig. 2.32 shows the same ten minutes of LMA data color-coded by charge "density", in which the redder (bluer) colors indicate relatively greater number of LMA sources in inferred positive (negative) charge regions and the altitude histogram shows separate histograms for the inferred positive and negative charge. This latter plot more clearly shows the vertical separation of the charge regions and illustrates how the upper-positive charge region dominates the lightning activity of this storm (at least in terms of the LMA sources).

[In the body of this dissertation, concise descriptions of the development of lightning flashes presents a challenge in terms of nomenclature. For clarification, "upward initiating" ("downward initiating") flash means that the first several LMA sources show the initial negative breakdown proceeding upward (downward). In general, a given "upward" ("downward") flash indicates a positive-over-negative (negative-over-positive) dipole charge structure mapped out by the flash. For brevity, the "upward initiating" or just "upward" flash terminology will be used interchangeably with "normal", and "downward initiating" or "downward" will be used interchangeably with "inverted" in the remainder of this dissertation. It's important to keep in mind, however, that even a normally electrified storm (i.e., a storm with normal tripole charge structure) may produce "inverted" IC flashes. For example, flashes between the mid-level negative and lower positive charge regions initiate downward but are not indicative of an overall "inverted" charge structure.]

LMA determination of charge structure on a flash-by-flash basis certainly has drawbacks, including:

1. It is a very labor-intensive process, and, unfortunately, resists automation.

2. There is no quantitative information about the magnitudes of the charge. However, distributions of the density of LMA sources can reveal relatively more or less electrically active regions.

3. During very intense (i.e., frequent) lightning activity in severe storms, the lightning is more amorphous and distinct charge regions are not always clear.

4. The LMA cannot reveal charge regions that are not involved in lightning.

It's important to keep in mind that, despite these drawbacks, LMA inference of charge structure gives a basic picture of the fully *three-dimensional and time-evolving* charge structure. Without the LMA charge inference, information about the charge structure is limited to in situ measurements by balloons and/or aircraft which give, at best, a one-dimensional profile through only one part of the storm for only a brief period of time.

Another somewhat more objective means of determining the gross vertical charge structure is by inspecting altitude histograms of the LMA sources in comparison with altitude histograms of flash initiation heights (see the bottom-right panel of Fig. 2.33). As mentioned above, the altitude histograms of LMA sources give a general sense of the vertical charge structure since the positive charge regions are expected to contain relatively more LMA sources. The flash initiation heights add another piece to the puzzle. These flash heights are a nice by-product of the sorting algorithm used to compute total flash rates. The algorithm keeps track of which sources correspond to each flash. One can then take the sources from each flash, sort them in chronological order, and determine at what height each flash originated and what direction it initially traveled. The origin height is just the height of the first source of the flash, and the initiation direction can be determined by regressing the altitude of the first several sources onto the time of the first several sources. If the regression coefficient is positive (negative), then the flash initiated upward (downward). If we interpret these initial flash heights and directions according to

the bi-directional discharge model, then flashes that initiate upward (downward) are heading toward positive charge above (below) the initiation height.

Fig. 2.33 shows an example of these histograms in comparison with vertical cross-sections of radar reflectivity and LMA source density. The LMA data used in this figure are the same as what's plotted in Fig. 2.31. In this case, the distributions in the LMA sources in the flash start heights are entirely consistent with the manual flash-by-flash charge structure determination. The prominent upper-level peak in the LMA source altitude histogram and LMA density cross-section strongly indicates the upper positive charge at 8–10 km altitude, while the smaller lower-level peak gives some indication of lower positive charge near 4–5 km altitude. As indicated by the red curve in the histogram plot of Fig. 2.33, most of the flashes initiated upward near 7 km, while a second distinct population of flashes initiated downward from 5 km. Hence, the upper population of upward flashes indicates the boundary between the mid-level negative charge and upper positive charge, while the lower population of downward flashes indicates the boundary between the mid-level negative charge and lower positive charge. The heights of these two flash start maxima may also be interpreted as the locations of maximum vertical electric field (e.g., Coleman et al., 2003).

Finally, note that there are significant numbers of flashes exterior to the maxima in the histogram of Fig. 2.33, and there are significant numbers of downward flashes in the same height range as the maxima of upward flashes. These features are not consistent with a simple tripole structure nor with the manual flash-by-flash charge determination of Fig. 2.31. Clearly, the objective determination of flash start heights and flash initiation directions is not always correct and not always a reliable indicator of the vertical charge structure. The root of this problem is the algorithm which sorts the LMA sources into flashes. For example:

- If the sorting algorithm places noise sources into a flash, and if these noise sources are among the first several sources, then the initiation altitude and

propagation direction would be in error.

- If the sorting algorithm incorrectly groups sources from more than one flash into the same flash, then the initiation altitude and propagation direction will not be representative of the all the flashes grouped into the single flash identified by the sorting algorithm.

- If the sorting algorithm incorrectly breaks what is really a single flash into more than one flash, the altitude and propagation direction of some sub-set of sources in the middle of the real flash will be incorrectly identified as the initial altitude and propagation of a flash.

In an attempt to mitigate these problems, only those sorted flashes with at least ten sources were used in the objective flash start height and flash direction computations. This restriction should reduce the effects of noise to some degree.

Lightning mapping (and LMA charge determination) cannot replace in situ measurements of thunderstorm charge regions, such as those obtained from balloons and aircraft. However, it does provide a fully three-dimensional qualitative picture of the charge structure throughout the evolution of the storm to complement the quantitative information gained from in situ measurements. Furthermore, with lightning mapping, the development and evolution of charge regions can then be investigated relative to concurrent dynamical and microphysical evolution of thunderstorms.

2.2.4 CG Origin Determination

In order to reveal the relationships between storm structure and CG production (and CG polarity), we need to know not just when and where the CGs strike ground, but also where they originate. To this end, the LMA data were also used to extract the origin location of each CG flash. Following a method similar to that of Proctor (1991), the origin of the flash is defined as the centroid of the first ten LMA sources associated with the flash (there are typically 100s–1000s of sources in each CG flash).

Origin locations for each CG were computed only if the LMA sources of the parent flash that produced the CG strike could be confidently isolated and identified as being distinct from other surrounding lightning flashes. For example, Fig. 2.34 shows shows ten seconds of LMA data centered on the time of a +CG flash at 2244:52 during the 29 June supercell. The parent flash for this +CG was distinct from other lightning. It could thus be isolated (Fig. 2.35) for computation of its origin location. In contrast, Fig. 2.36 shows ten seconds of LMA data centered on another +CG flash from the same storm, this one at 2340:19. Though the +CG appears somewhat isolated, zooming in on it (Fig. 2.37) shows that there is simultaneous lightning at two separate altitudes. This one could not be isolated for computation of its origin location.

One reason for computing these CG origin locations is to see if they are consistent with a storm's overall charge structure. As shown by the filled diamond symbols on the vertical cross-sections in Fig. 2.33, the –CG origin heights are generally consistent (at least for this case). Another more important reason for computing these CG origin locations is to shed more light on the theories for their production, especially for +CG production. For example, do most +CGs for a given storm originate from the anvil, as would be predicted by the tilted normal dipole hypothesis? Or do they mostly originate at mid-levels in the core of the storm, as would be more consistent with any of the other hypotheses? Are origin altitudes for +CGs in a given storm consistently different from those of –CGs? Do +CGs (–CGs) require the presence of a lower negative (positive) charge?

2.3 National Lightning Detection Network (NLDN)

The National Lightning Detection Network (NLDN; Cummins et al., 1998) provides measurements of the time, strike location, polarity, and peak current of CG flashes. The NLDN does not measure (or at least doesn't archive) intra-cloud flashes. According to Cummins et al., the NLDN detection efficiency is 80–90% in the STEPS region. For this research, the NLDN data are used primarily to calculate CG flash

rates, to identify those LMA sources associated with CG flashes, and to place the strike points of CGs within the context of the radar observations. The NLDN data were provided courtesy of NASA Marshall Space Flight Center.

2.4 EFM Balloons

The National Severe Storms Laboratory launched balloons carrying electric field meters (EFMs: Winn and Byerly, 1975; see also Chapter 6 of MacGorman and Rust, 1998) through many of the storms during STEPS, including the 3 and 29 June storms of this study. These balloons measure in-situ temperature, relative humidity, and electric field along their flight path. Historically, these EFM balloon measurements have been the primary source of information about thunderstorm charge structure (e.g., Winn et al., 1978, 1981; Marshall and Winn, 1982; Marshall et al., 1989; Rust, 1989; Stolzenburg et al., 1998a, 1998b, 1998c; Stolzenburg and Marshall, 2002). There are also a few published studies of the balloon-inferred charge structure of storms during STEPS (Rust and MacGorman, 2002, MacGorman et al., 2004, Rust et al., 2004). Charge structure information is gleaned from these EFM soundings mainly by examination of the vertical profile of the electric field vector (**E**), specifically the vertical component of **E**. Assuming the charge regions are horizontally infinite (and thus vertically layered), taking a one-dimensional approximation of Gauss' Law,

$$\nabla \cdot \mathbf{E} = \frac{\rho_c}{\epsilon} \tag{2.30}$$

gives the charge density ρ_c as a function of the gradient of the vertical electric field:

$$\rho_c \approx \epsilon \frac{\Delta E_z}{\Delta z} \tag{2.31}$$

The modeling studies by Stolzenburg and Marshall (1994) have shown that this approximation is accurate to within 10% if the charge regions are at least 6×6 km in areal extent. They state that "[A] layered charge structure is a good first approximation of the actual vertical structure in the thunderstorm." Recent improvements to these EFMs (and increased sophistication in the signal processing of their measure-

ments) have permitted extraction of the full three-dimensional electric field vector along the balloon's flight path (e.g., MacGorman et al., 2004).

For the purposes of this dissertation, the EFM balloons' temperature soundings are used as input into the FHC algorithm on the 3 June and 29 June cases, and the charge structure inferred from the balloons' electric field measurements are used as a supplement to (and comparison with) the LMA-inferred charge structure.

2.5 Software

A tremendous amount of time and work went into developing the methodology and analysis software to bring the enormous variety and quantity of the STEPS observations together into a common analytical framework. This is probably true of most research projects, Master's theses, and Ph.D. dissertations. However, the effort was so great in this case that a brief description of the effort deserves a place in this dissertation.

New Mexico Tech developed a software package for the graphical analysis of LMA data. This software package (called XLMA) was written in the Interactive Data Language (IDL), and it proved to be an indispensable tool. XLMA was used for charge structure analysis, computation of flash rates and for making all the conventional lightning mapping style plots (e.g, Fig. 2.24). I (Kyle Wiens) developed another software package in IDL called CDF_WIDGET[3] in order to ingest and manipulate essentially all the STEPS data sets (radar, LMA, NLDN, balloons, etc.) and to display and overlay them onto each other in order to see each storm from the perspective of all the different measurement platforms, simultaneously. CDF_WIDGET was used for the time series computations, correlation analysis, fuzzy logic hydrometeor identification, and almost every other form of analysis. Nearly every plot in this dissertation (other than the conventional LMA plots) was produced using CDF_WIDGET. Oth-

[3]This CDF_WIDGET software was inspired by, and is an outgrowth of, a similar program called UF_RADAR which was developed at New Mexico Tech. UF_RADAR was originally written by Demian Shown, and has been modified and improved by many persons including me (Kyle Wiens).

ers have already made use of CDF_WIDGET (e.g., Tessendorf, 2003; Dolan, 2004; Hamlin, 2004; Kuhlman, 2004, Lang et al., 2004a, 2004b). Hopefully, it will continue to be used (and continue to be useful) in the future.

Radar	Latitude	Longitude	Altitude (km)	Wavelength (cm)
CHILL	39.235	–102.278	1.285	11.01
KGLD	39.367	–101.700	1.123	10.0
S-Pol	39.761	–102.093	1.103	10.71

Table 2.1: Radar locations and specifications

Hydrometeor type	Classifier output index
Unclassified	0
Drizzle	1
Rain	2
Dry snow	3
Wet snow	4
Vertically oriented ice crystals	5
Low density graupel	6
High density graupel	7
Small hail	8
Large hail	9
Small hail mixed with rain	10
Large hail mixed with rain	11

Table 2.2: Hydrometeor types used in the FHC.

Drizzle

Source	Z_H	Z_{DR}	K_{DP}	LDR	ρ_{HV}	T
S(2000)	< 28	0–0.07	0–0.03	< -32	> 0.97	> 0
LC(2000)	< 25	0–1.1	–0.1 to 0.1	< -34	> 0.98	NA
Lim(2001)	< 20	0–0.7	0–0.1	< -33	> 0.97	> 0
FHC	< 28	0–0.7	–0.1 to 0.1	< -32	> 0.97	> 0

Table 2.3: Radar variable threshold ranges for selected hydrometeor types. This table is for drizzle. Tables 2.4–2.13 show similar information for other hydrometeor types. Each of these tables lists the thresholds from the following sources: Straka et al. (2000), S(2000); Liu and Chandrasekar (2000), LC(2000); Carey and Rutledge (1998), CR(2000); Lopez and Aubagnac (1997), LA(1997); Lim (2001); and the thresholds used in the fuzzy logic hydrometeor classification for this dissertation, FHC. An 'NA' entry indicates that variable was not used or its thresholds were not clearly stated.

Rain

Source	Z_H	Z_{DR}	K_{DP}	LDR	ρ_{HV}	T
S(2000)	28–60	> 0.7	> 0.03	–34 to –25	> 0.95	> -10
LC(2000)	25–60	2-D	> 0	–33 to –27	> 0.97	NA
CR(1998)	< 60	> 0.5	> 0.5	< -27	> 0.97	> 0
LA(1997)	25–60	0.5–4	0–10	NA	NA	NA
Lim(2001)	15–60	2-D	2-D	–36 to –17	> 0.95	NA
FHC	25–60	> 0.7	0.03–6	–33 to –27	> 0.95	> -10

Table 2.4: As in Table 2.3 but for rain. LC(2000) and Lim(2001) used two-dimensional MBFs with Z_H for Z_{DR} and K_{DP}.

Dry snow

Source	Z_H	Z_{DR}	K_{DP}	LDR	ρ_{HV}	T
S(2000)	< 35	$0 - 6$	$0 - 0.6$	< -25	> 0.95	< 0
LC(2000)	< 35	$0 - 5$	0–1	< -25	> 0.95	NA
Lim(2001)	10–35	–0.1 to 1	–0.1 to 0.2	< -24	> 0.95	NA
FHC	< 35	> -0.1	0–0.6	< -25	> 0.95	< 0

Table 2.5: As in Table 2.3 but for dry snow.

Wet snow

Source	Z_H	Z_{DR}	K_{DP}	LDR	ρ_{HV}	T
S(2000)	< 45	0.5–3	0–0.5	–10 to –20	0.5–0.9	> 0
LC(2000)	< 45	0–3	0–2	–18 to –15	0.82–0.95	NA
Lim(2001)	28–25	–0.1 to 3	–0.1 to 0.5	> -23	< 0.9	NA
FHC	< 45	0–3	0–2	–18 to –13	0.82–0.95	–2 to 4

Table 2.6: As in Table 2.3 but for wet snow.

Vertically oriented ice crystals

Source	Z_H	Z_{DR}	K_{DP}	LDR	ρ_{HV}	T
S(2000)	< 35	–0.5 to 0.5	–0.6 to 0	< -24	> 0.95	< 0
CR(1998)	< 40	NA	< -0.25	NA	NA	< -20
FHC	< 35	–0.5 to 0.5	< -0.25	< -25	> 0.95	< 0

Table 2.7: As in Table 2.3 but for vertically oriented ice crystals.

Low density graupel

Source	Z_H	Z_{DR}	K_{DP}	LDR	ρ_{HV}	T
S(2000)	20–35	–0.5 to 1	0–0.5	< -25	> 0.95	< 0
LC(2000)	40–50	–0.5 to 1	–0.5 to 0.5	< -30	> 0.96	NA
LA(1997)	40–50	–0.5 to 1	–0.5 to 0.5	NA	NA	NA
Lim(2001)	20–45	2-D	2-D	–30 to –25	> 0.95	NA
FHC	30–45	–0.5 to 1	–0.5 to 0.5	< -30	> 0.97	< 0

Table 2.8: As in Table 2.3 but for low density graupel. Lim(2001) used two-dimensional MBFs with Z_H for Z_{DR} and K_{DP}.

High density graupel

Source	Z_H	Z_{DR}	K_{DP}	LDR	ρ_{HV}	T
S(2000)	30–50	–0.5 to 2	0–1.5	–30 to –20	> 0.95	> -15
LC(2000)	40–55	–0.5 to 3	–0.5 to 2	–25 to –20	> 0.95	NA
LA(1997)	40–55	–0.5 to 3	–0.5 to 2	NA	NA	NA
Lim(2001)	30–52	2-D	2-D	–27 to –18	> 0.94	NA
FHC	40–55	–0.5 to 3	–0.5 to 2	–25 to –20	> 0.95	–15 to 10

Table 2.9: As in Table 2.3 but for high density graupel. Lim(2001) used two-dimensional MBFs with Z_H for Z_{DR} and K_{DP}.

Small hail

Source	Z_H	Z_{DR}	K_{DP}	LDR	ρ_{HV}	T
S(2000)	45–60	–0.5 to 0.5	–0.5 to 0.5	–26 to –20	0.92–0.97	> -15
LC(2000)	50–60	–0.5 to 0.5	–0.5 to 0.5	< -20	NA	NA
CR(1998)	> 50	< 0.5	< 0.5	< -18	> 0.96	> 0
	> 55			> -26	> 0.97	< 0
LA(1997)	50–60	–0.5 to 0.5	–0.5 to 0.5	NA	NA	NA
Lim(2001)	50–60	–1 to 0.5	–0.5 to 0.5	> -25	0.91–0.98	NA
FHC	50–60	–0.5 to 0.5	–0.5 to 0.5	–24 to –18	0.92–0.98	NA

Table 2.10: As in Table 2.3 but for small (d<2 cm) hail. CR(1998) used different thresholds above and below the freezing level.

Small hail mixed with rain

Source	Z_H	Z_{DR}	K_{DP}	LDR	ρ_{HV}	T
S(2000)	45–60	–0.5 to 6	> 0	> –25	< 0.95	> –5
LC(2000)	> 50	–1 to 1	> 0	–20 to –10	> 0.9	NA
CR(1998)	> 50	< 1	> 0.5	–27 to –20	< 0.98	> 0
LA(1997)	50–70	–1 to 1	0–10	NA	NA	NA
Lim(2001)	> 45	2-D	2-D	–24 to –14	< 0.94	NA
FHC	45–60	> –0.5	0.5–6.5	–26 to –19	< 0.95	> –5

Table 2.11: As in Table 2.3 but for small hail mixed with rain. Lim(2001) used two-dimensional MBFs with Z_H for Z_{DR} and K_{DP}.

Large hail

Source	Z_H	Z_{DR}	K_{DP}	LDR	ρ_{HV}	T
S(2000)	> 55	–2 to 0.5	–0.5 to 1	> –20	< 0.92	> –25
LC(2000)	> 55	< –0.5	–1 to 1	–15 to –10	> 0.96	NA
CR(1998)	> 55	< 0.5	< 0.5	> –18	< 0.96	> 0
				> –26	> 0.97	< 0
LA(1997)	55–70	< 0.5	–1 to 1	NA	NA	NA
Lim(2001)	> 55	< 0.5	–0.5 to 1	> –20	0.84 to 0.92	NA
FHC	> 55	< 0.5	–0.5 to 1	> –20	0.85 to 0.92	NA

Table 2.12: As in Table 2.3 but for large (d>2 cm) hail. CR(1998) used different thresholds above and below the freezing level.

Large hail mixed with rain

Source	Z_H	Z_{DR}	K_{DP}	LDR	ρ_{HV}	T
S(2000)	> 55	–0.5 to 3	> 0	> –22	< 0.92	> –10
LC(2000)	> 50	–1 to 1	> 0	–20 to –10	> 0.9	NA
CR(1998)	> 55	< 1	> 0.5	> –20	< 0.96	> 0
LA(1997)	50–70	–1 to 1	0–10	NA	NA	NA
Lim(2001)	> 45	2-D	2-D	–24 to –14	< 0.94	NA
FHC	> 55	0.5–3	0.5–6.5	–20 to –10	< 0.93	> –10

Table 2.13: As in Table 2.3 but for large hail mixed with rain. Lim(2001) used two-dimensional MBFs with Z_H for Z_{DR} and K_{DP}.

Variable	Weight Factor
$\mathbf{Z_{DR}}$	1.0
$\mathbf{K_{DP}}$	0.8
$\rho_{\mathbf{HV}}$	0.5
LDR	0.5

Table 2.14: Weight factors used in the FHC. The same factors are used for each hydrometeor type.

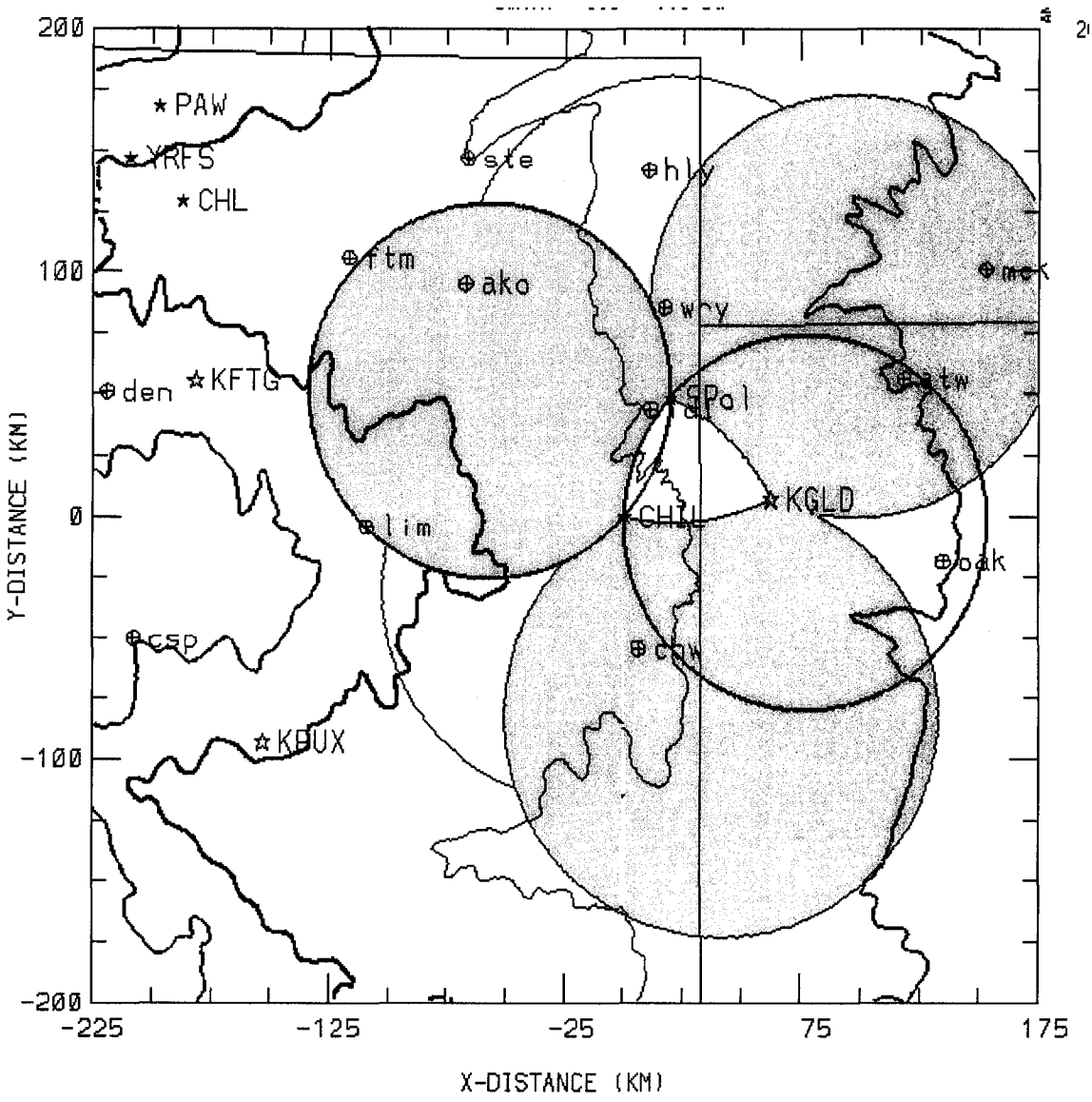

Figure 2.1: Nominal areas of coverage (gray shading outlined with thick black lines) by the STEPS radar network (CHILL, S-Pol, KGLD) for triple- and dual-Doppler (inter-radar beam angles greater than 25 degrees) winds. Topographic height contours (black lines) are at 3,4,5, and 6 kft. The straight, thin black lines are the Colorado-Kansas, Colorado-Nebraska, and Kansas-Nebraska borders. NWS WSR-88D radars are shown for Denver, CO (KFTG), Pueblo, CO (KPUX), and Goodland, KS (KGLD), along with the Yucca Ridge Field Station (YFRS). Landmarks are shown at Denver, CO (den), Colorado Springs, CO (csp), Limon, CO (lim), Akron, CO (ako), McCook, NE (mck), Atwook, KS (atw), and Oakley, KS (oak). All distances are East-West (X) and North-South (Y) from the the KGLD radar. From Tessendorf et al. (2004a).

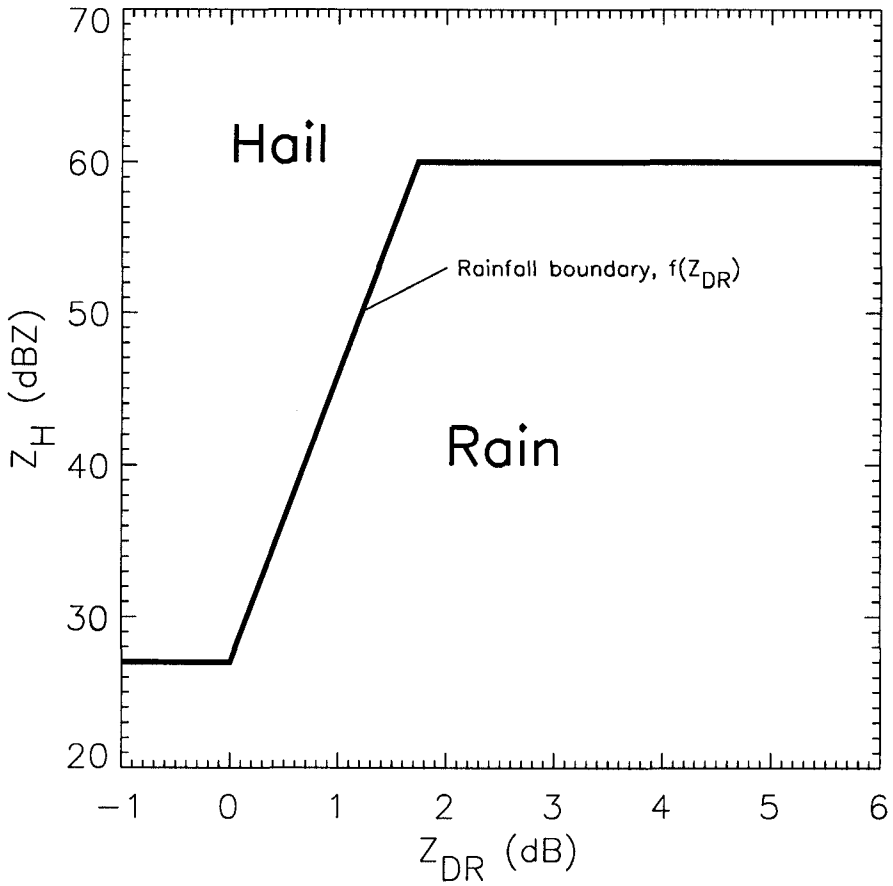

Figure 2.2: Plot of Z_H vs Z_{DR} with the line illustrating the rainfall boundary line defined by $f(Z_{DR})$ in Equation 2.6.

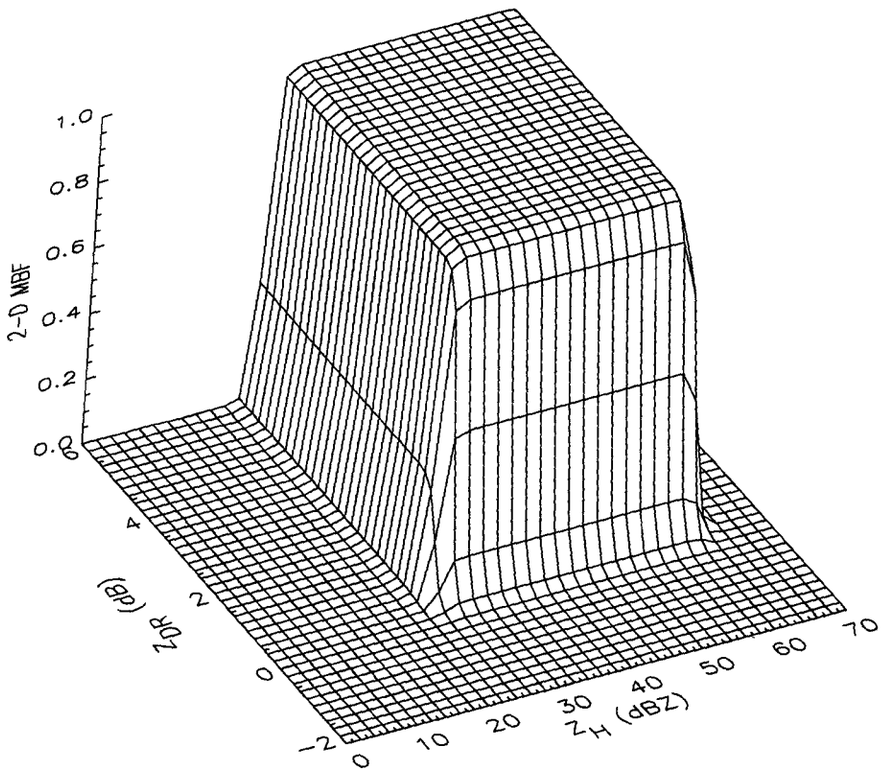

Figure 2.3: Two-dimensional (Z_H and Z_{DR}) MBF for rain. The "height" of the surface is the product of the 1-D MBFs of Z_H and Z_{DR}.

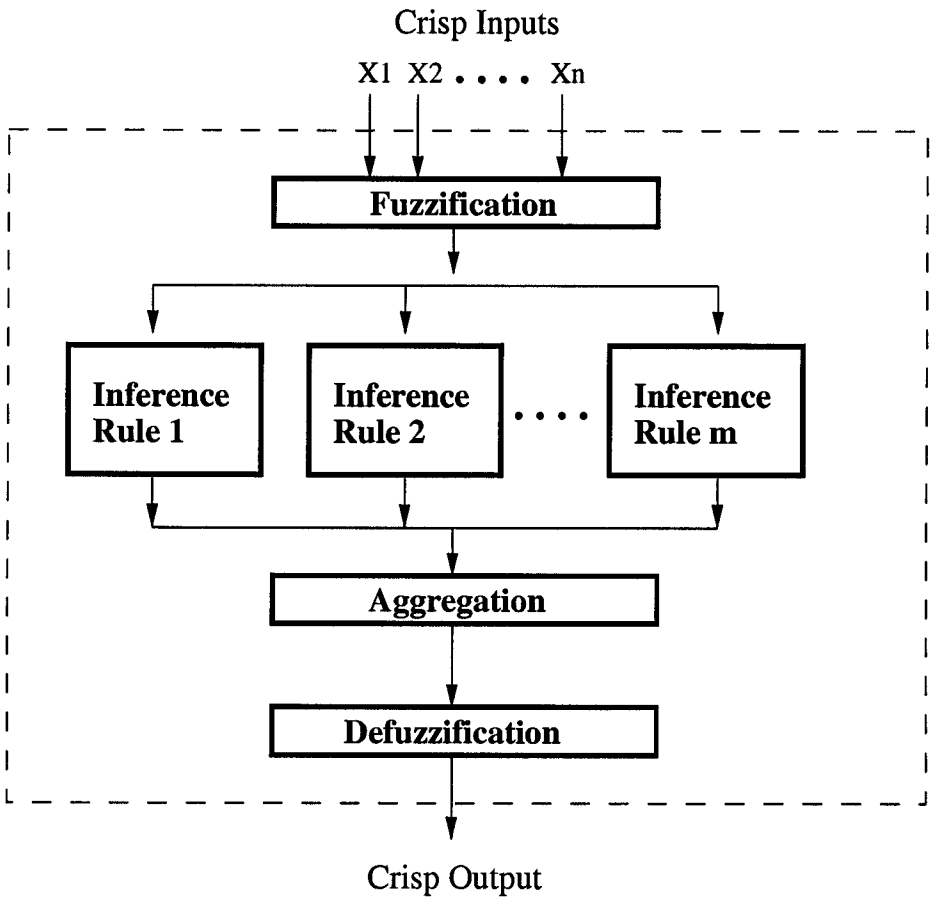

Figure 2.4: Block diagram of a general fuzzy logic system. After Liu and Chandrasekar (2000).

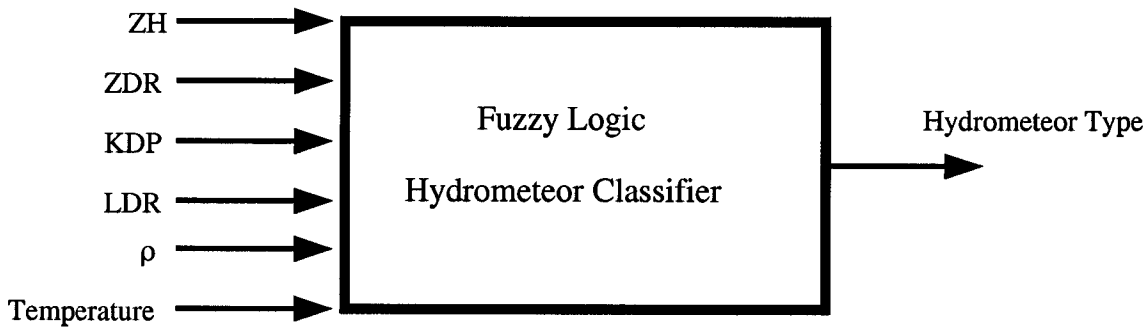

Figure 2.5: Block diagram of the fuzzy logic hydrometeor classifier (FHC). After Liu and Chandrasekar (2000)

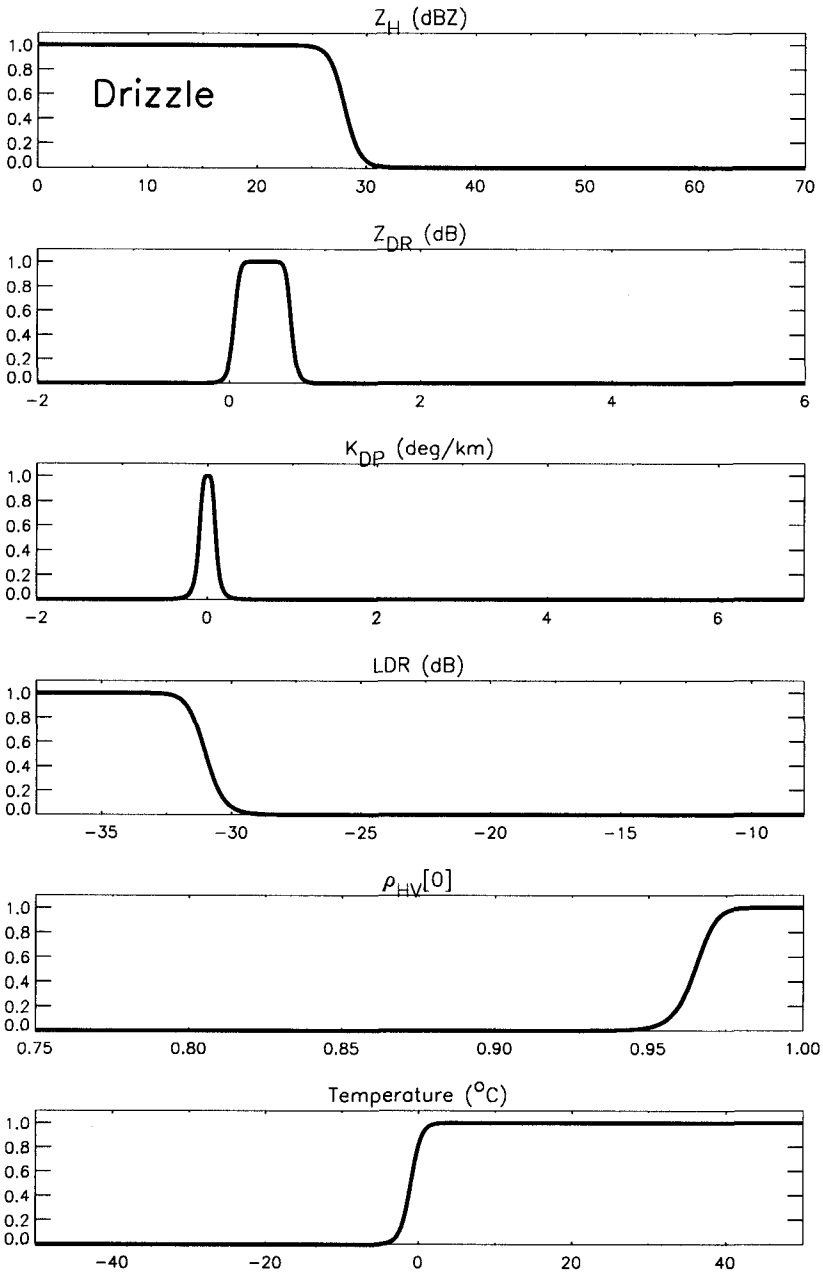

Figure 2.6: MBF for drizzle.

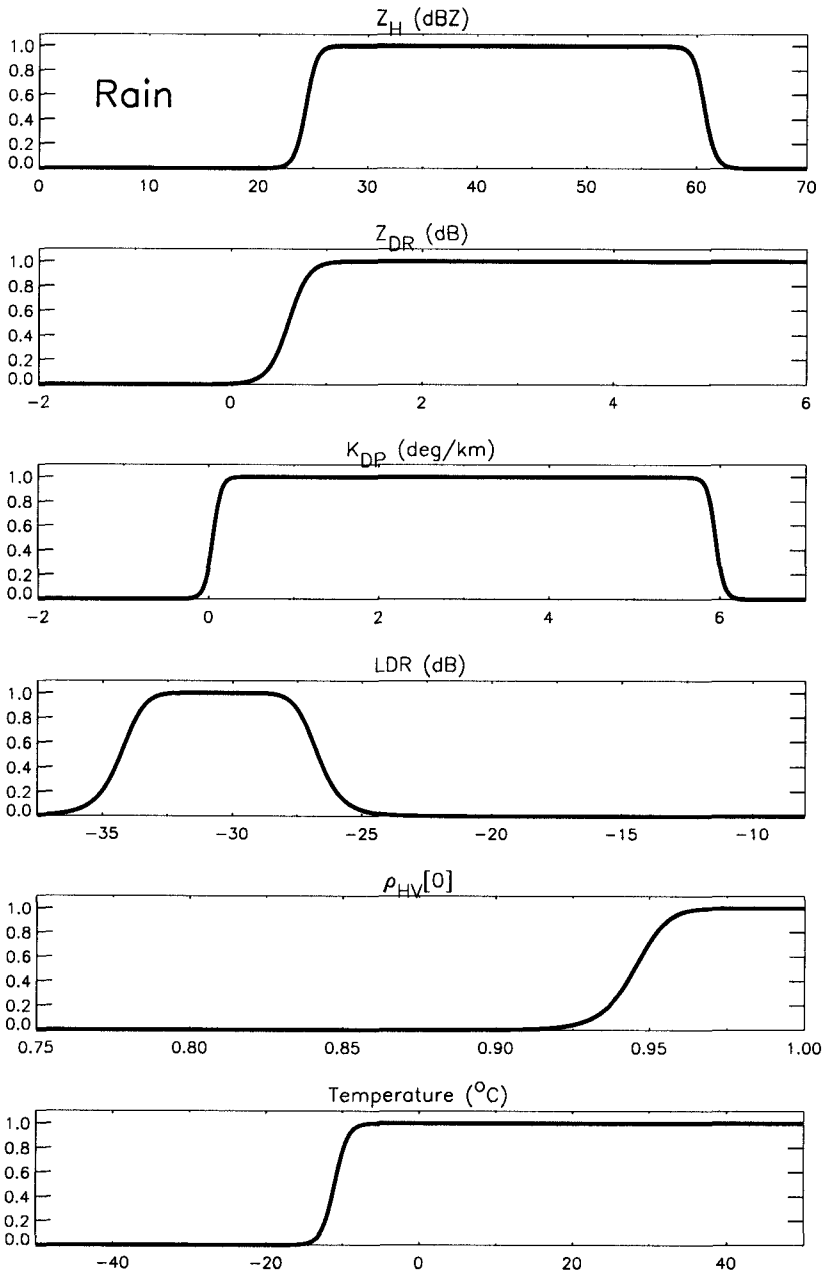

Figure 2.7: MBF for rain.

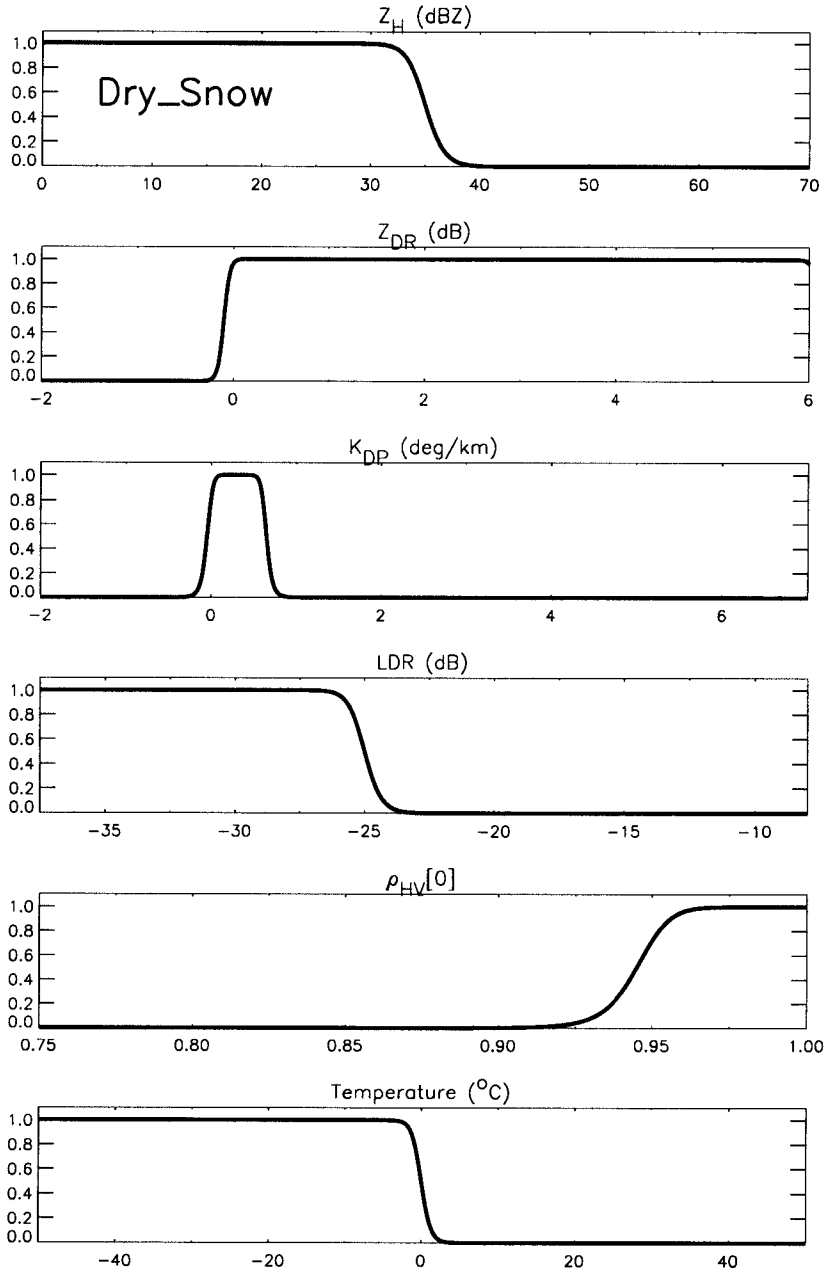

Figure 2.8: MBF for dry snow.

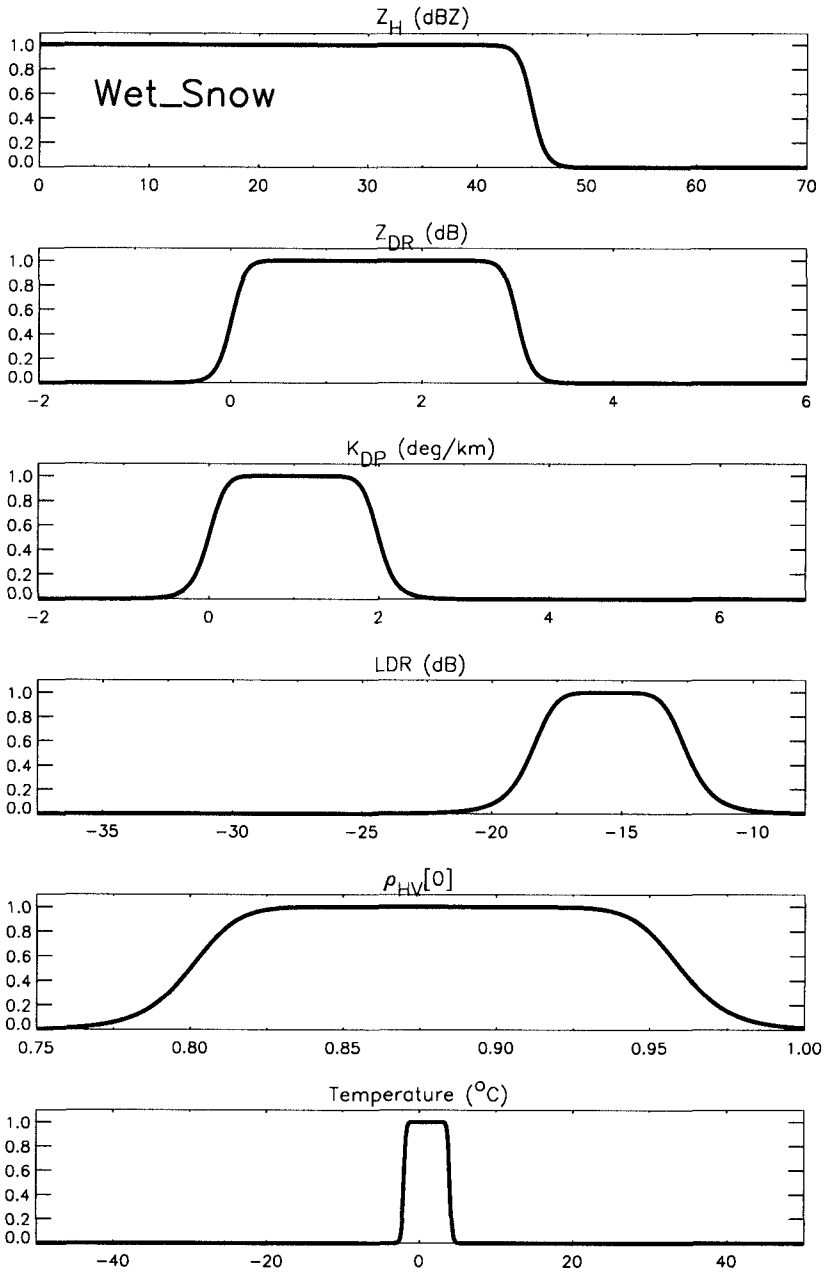

Figure 2.9: MBF for wet snow.

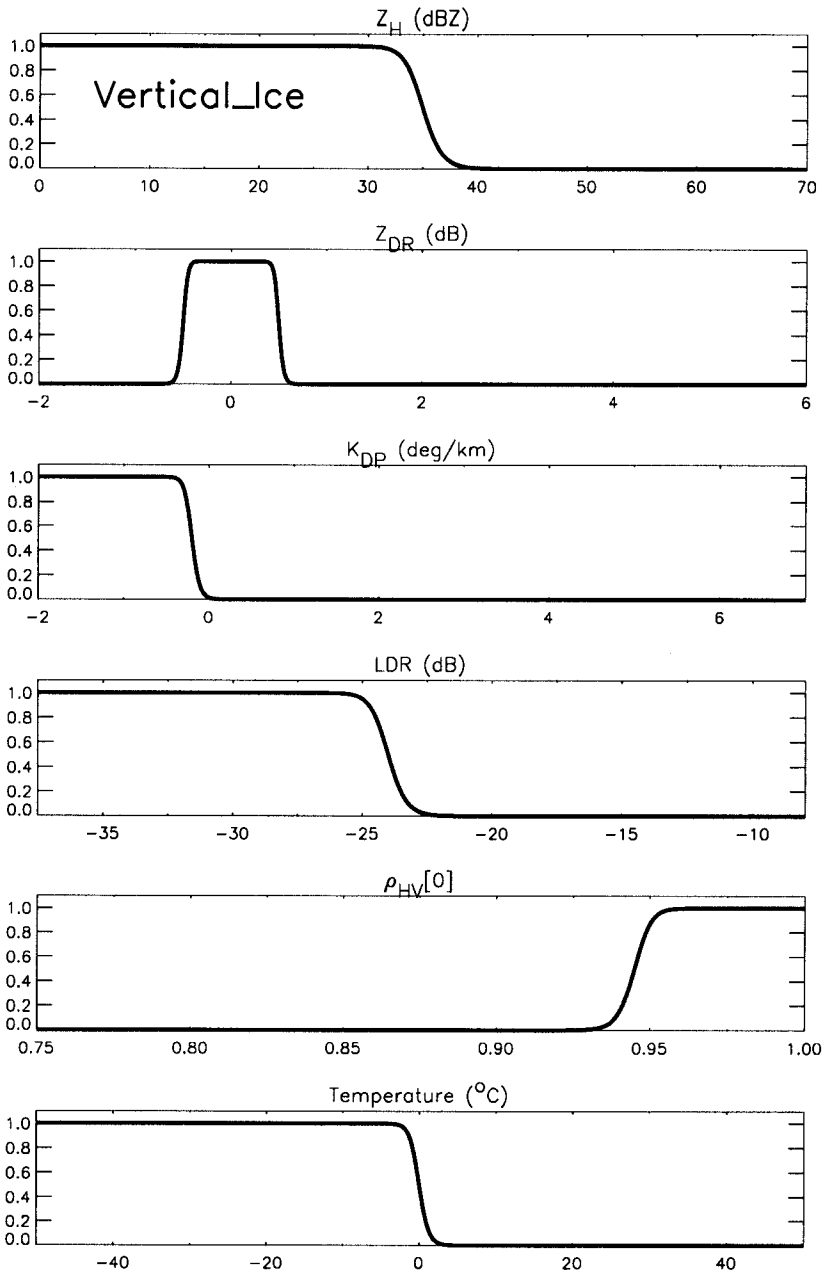

Figure 2.10: MBF for vertically oriented ice crystals.

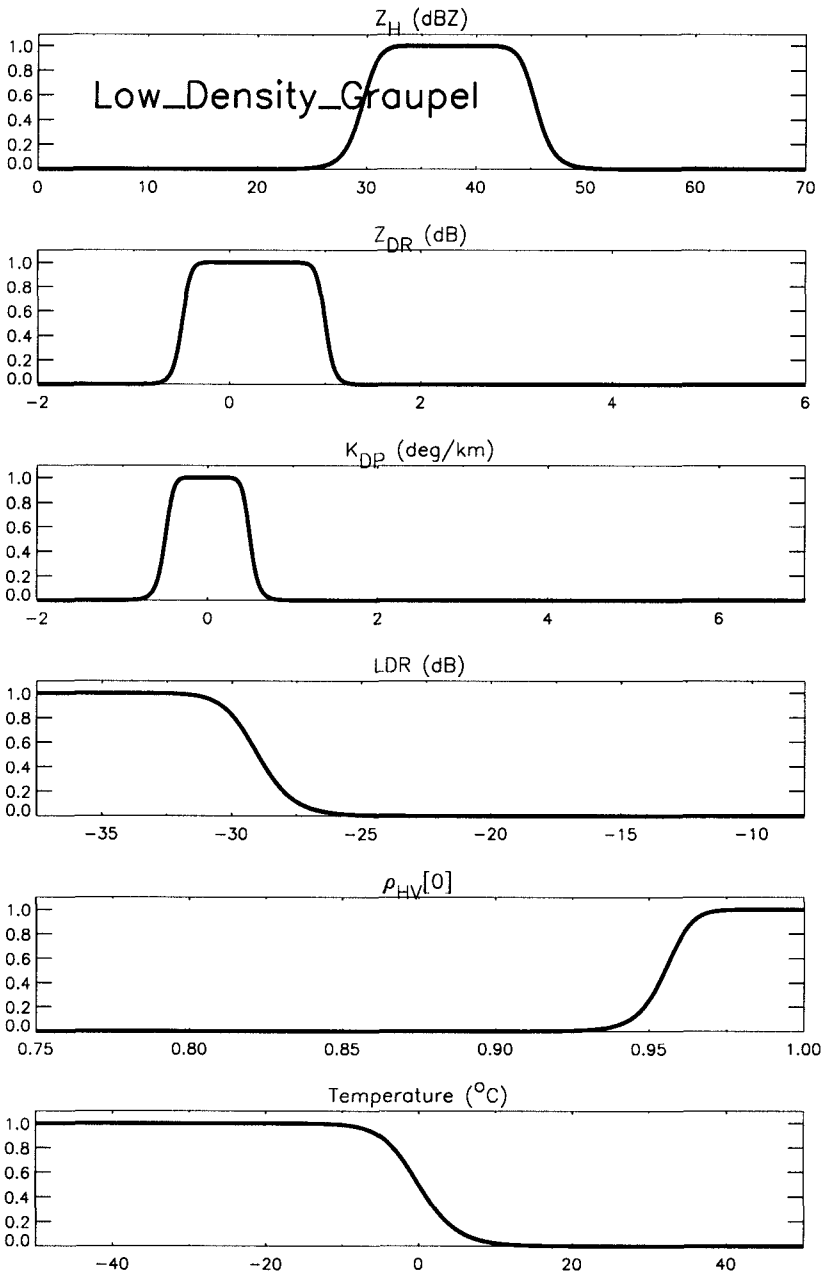

Figure 2.11: MBF for low density graupel.

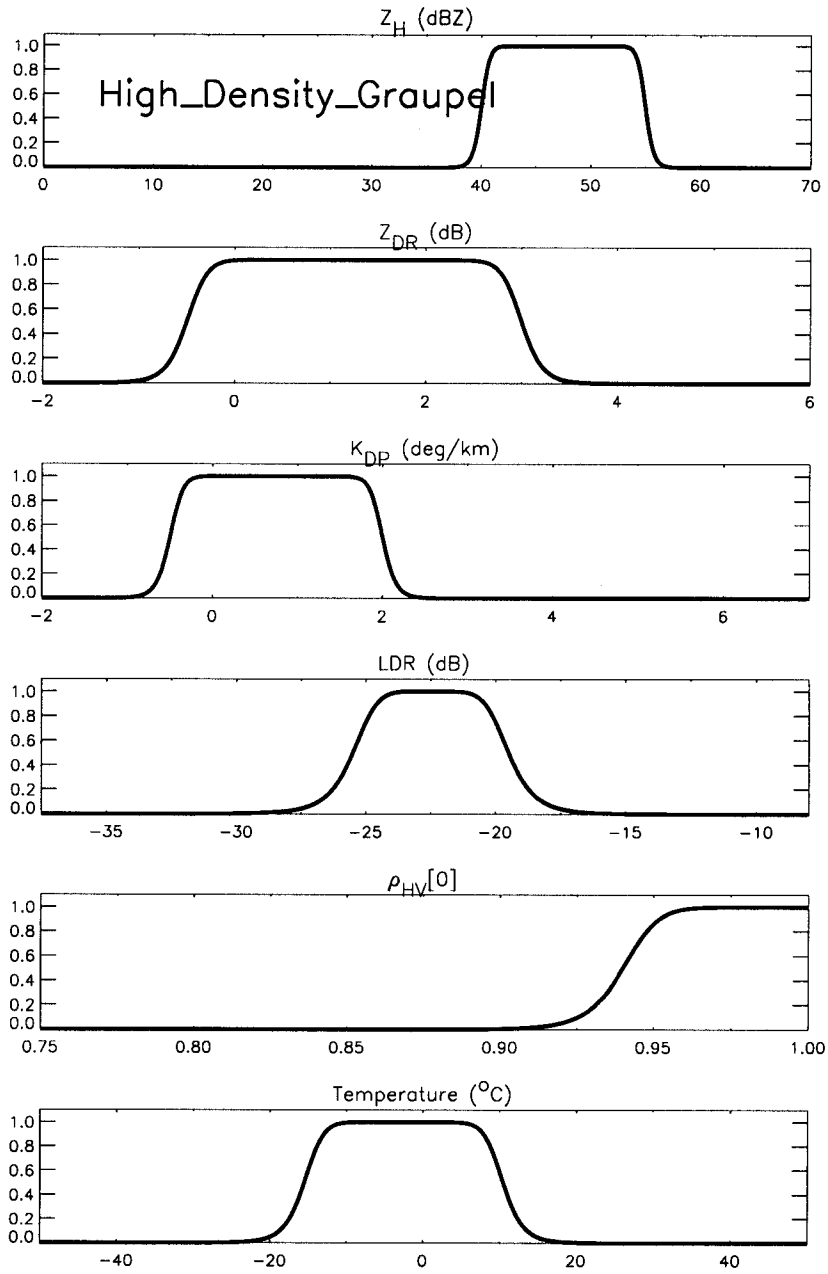

Figure 2.12: MBF for high density graupel.

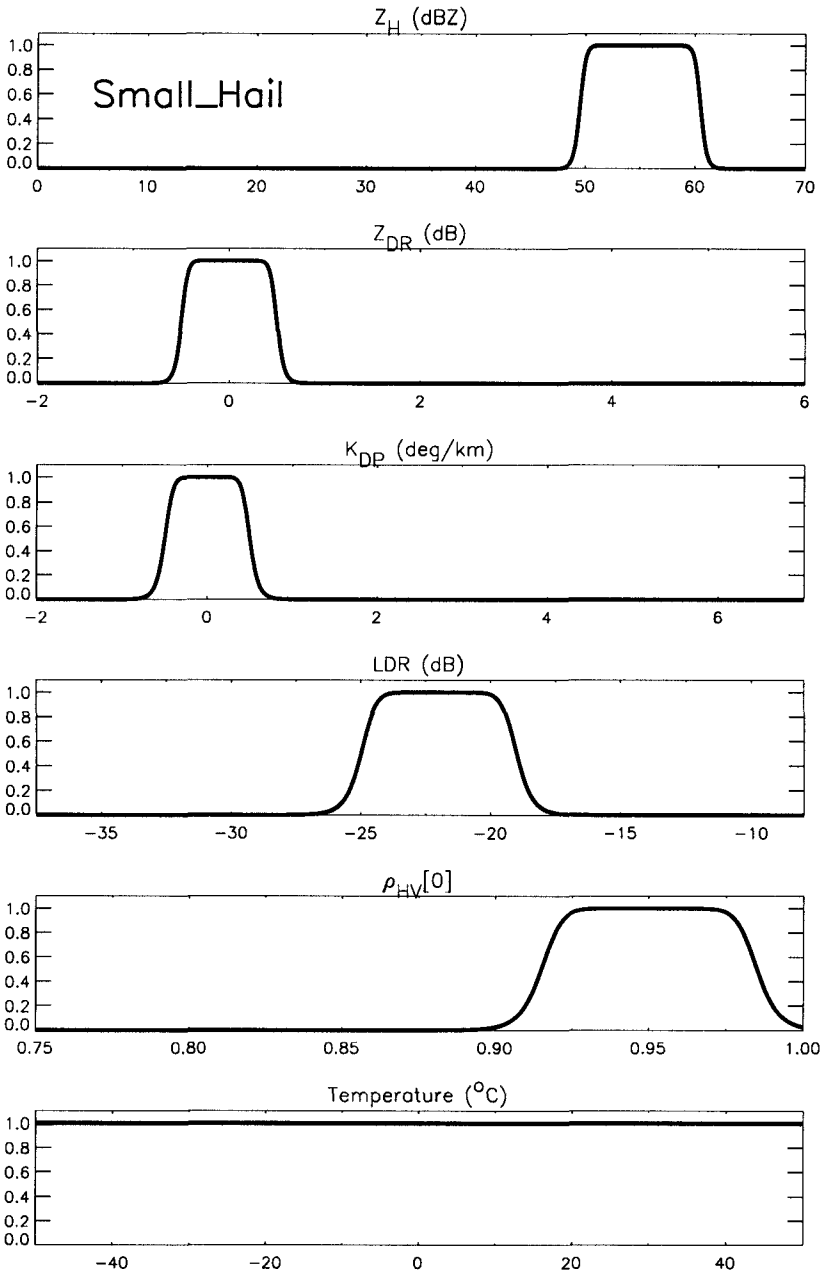

Figure 2.13: MBF for small (d<2 cm) hail.

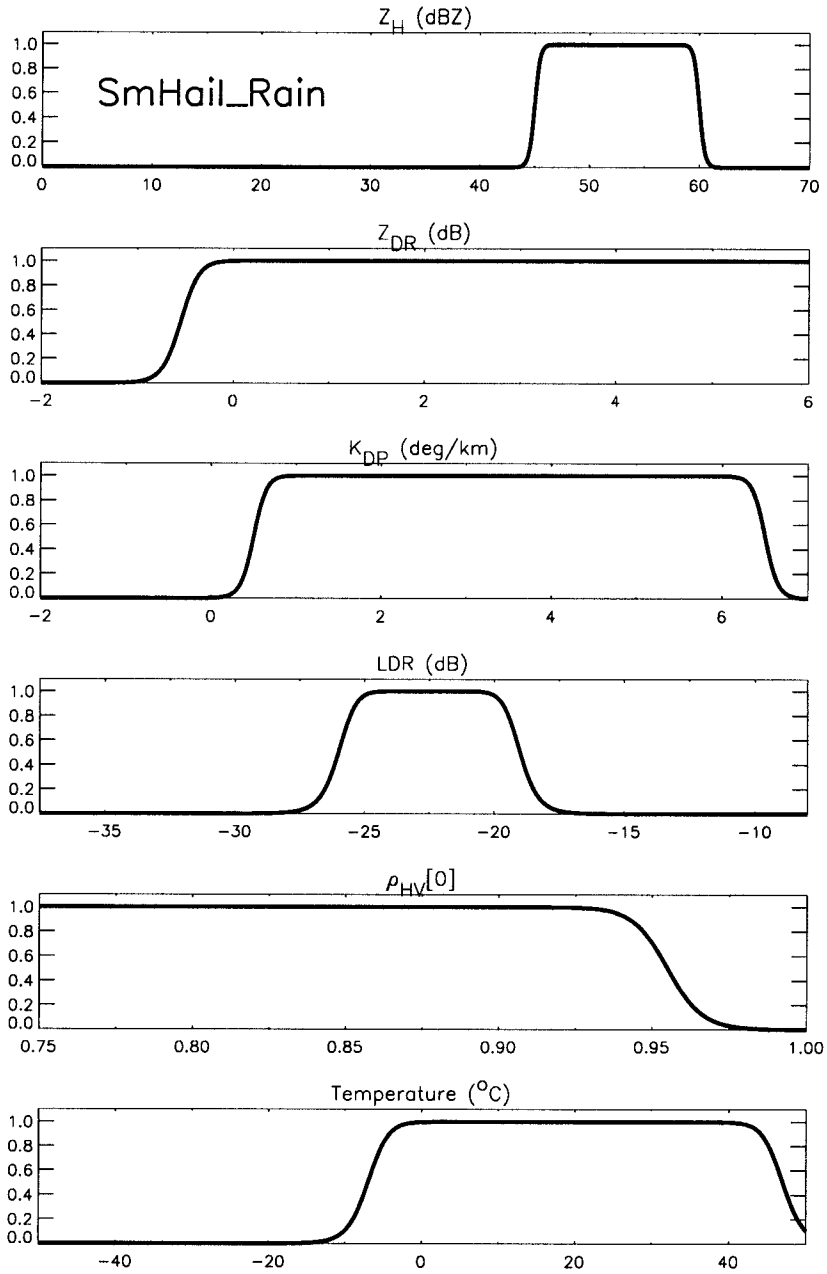

Figure 2.14: MBF for small hail mixed with rain

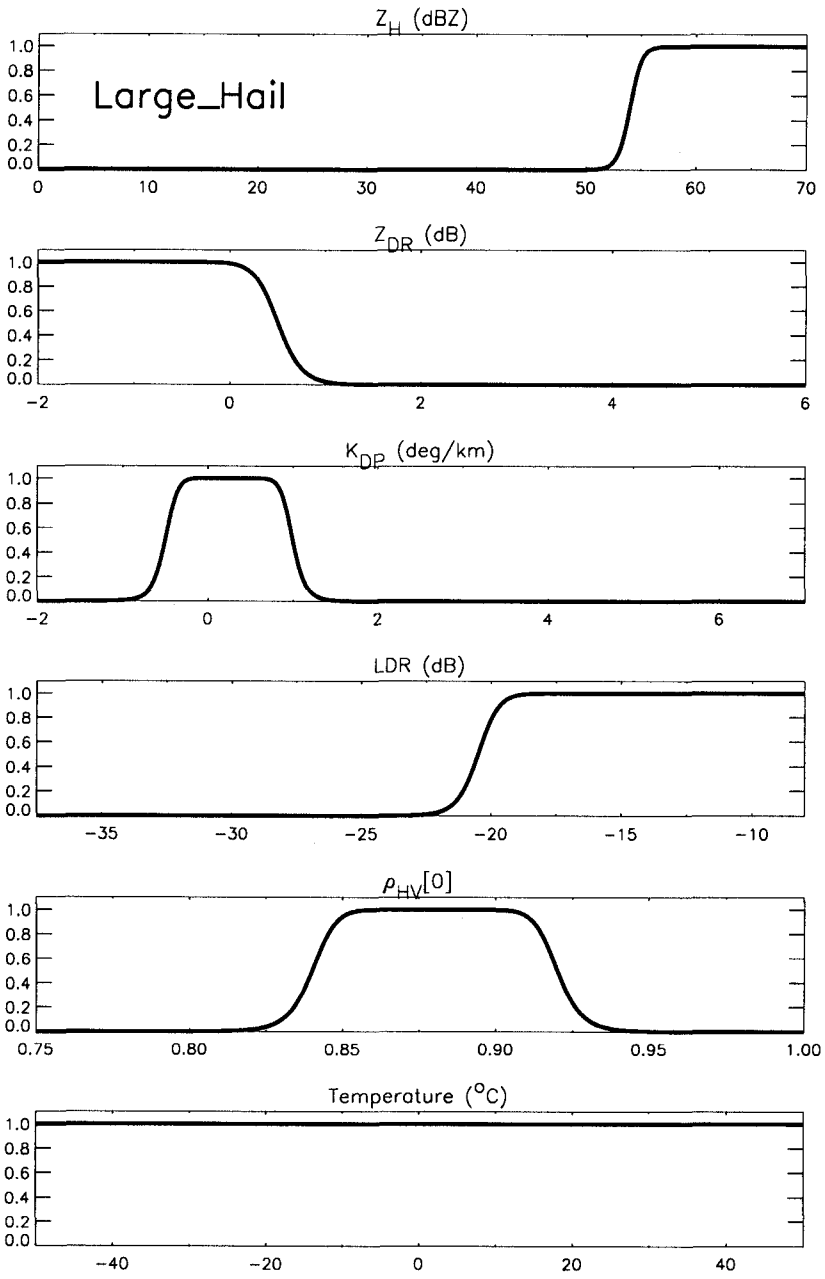

Figure 2.15: MBF for large (d>2 cm) hail.

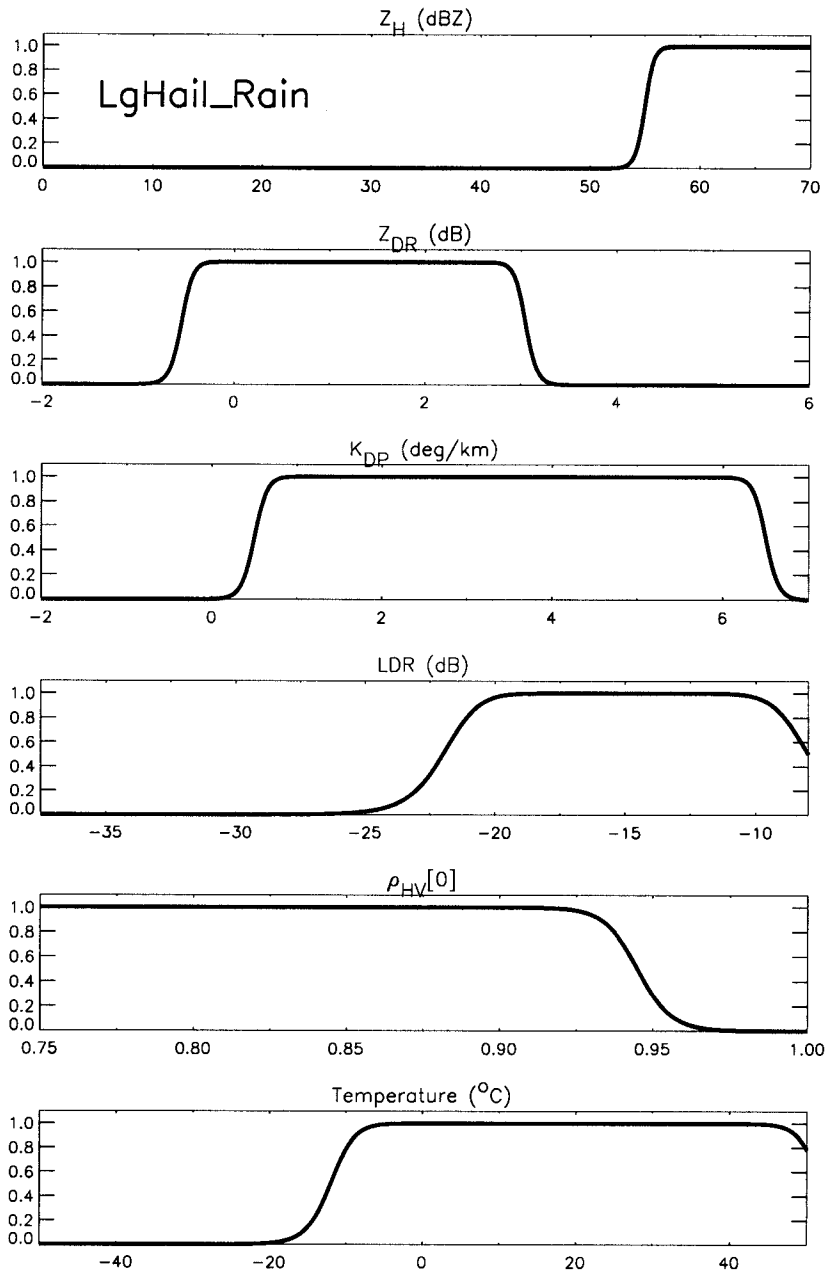

Figure 2.16: MBF for large hail mixed with rain.

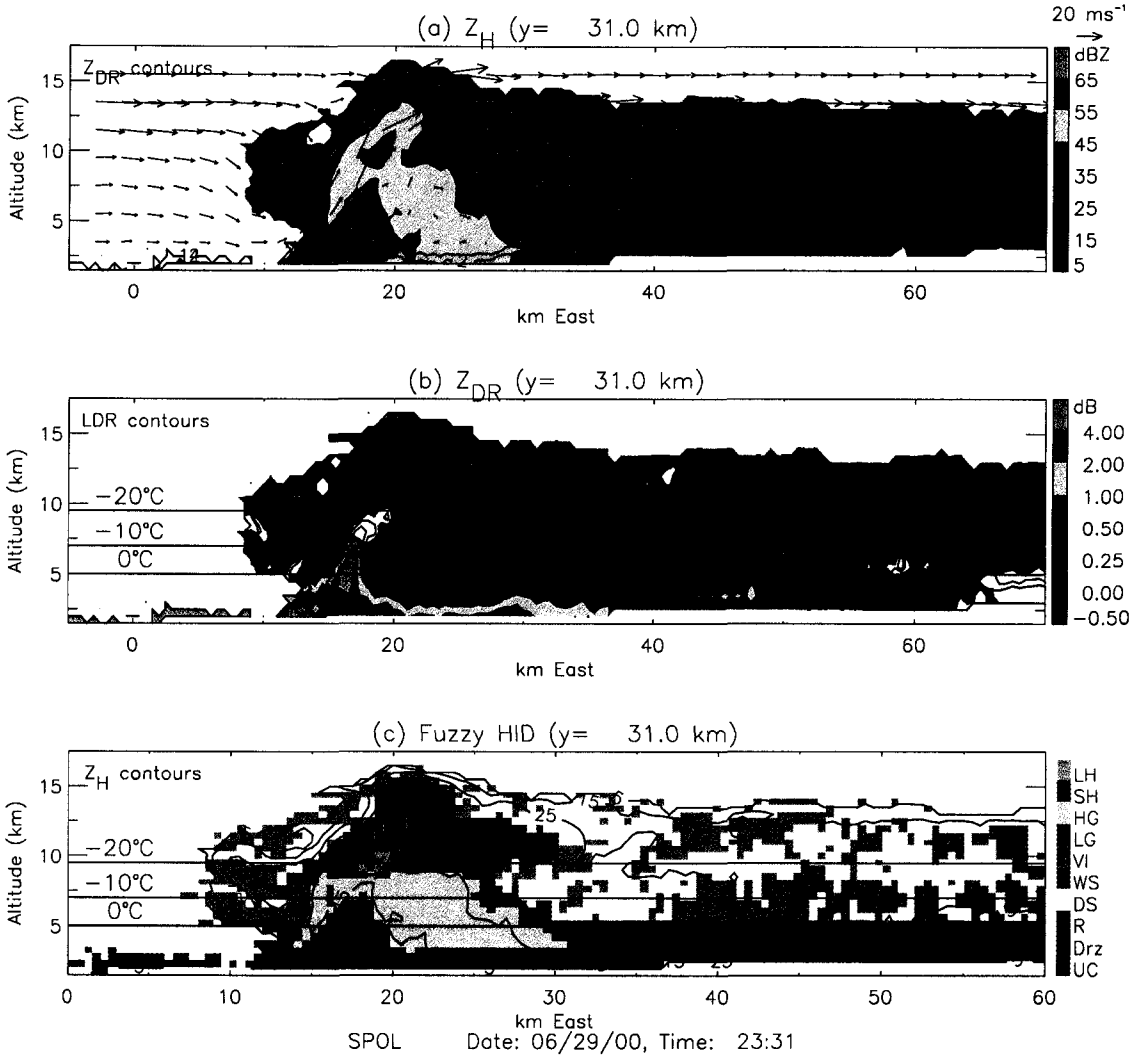

Figure 2.17: Radar vertical cross-sections at 2331 on 29 June 2000 comparing fuzzy logic hydrometeor classification (FHC) results to polarimetric measurements. (a) Color-shaded Z_H with wind flow vectors and additional black contours of Z_{DR} at 1, 2, and 4 dB. (b) Color-shaded Z_{DR} with additional black contours of LDR at −22 and −20 dB. (c) The FHC result (see color bar key on right) with additional black contours of Z_H that repeat the color-shaded contours in (a). Key for FHC categories: LH-large hail, SH-small hail, HG-high density graupel, LG-low density graupel, VI-vertically oriented ice crystals, WS-wet snow, DS-dry snow, R-rain, Drz-drizzle, UC-unclassified.

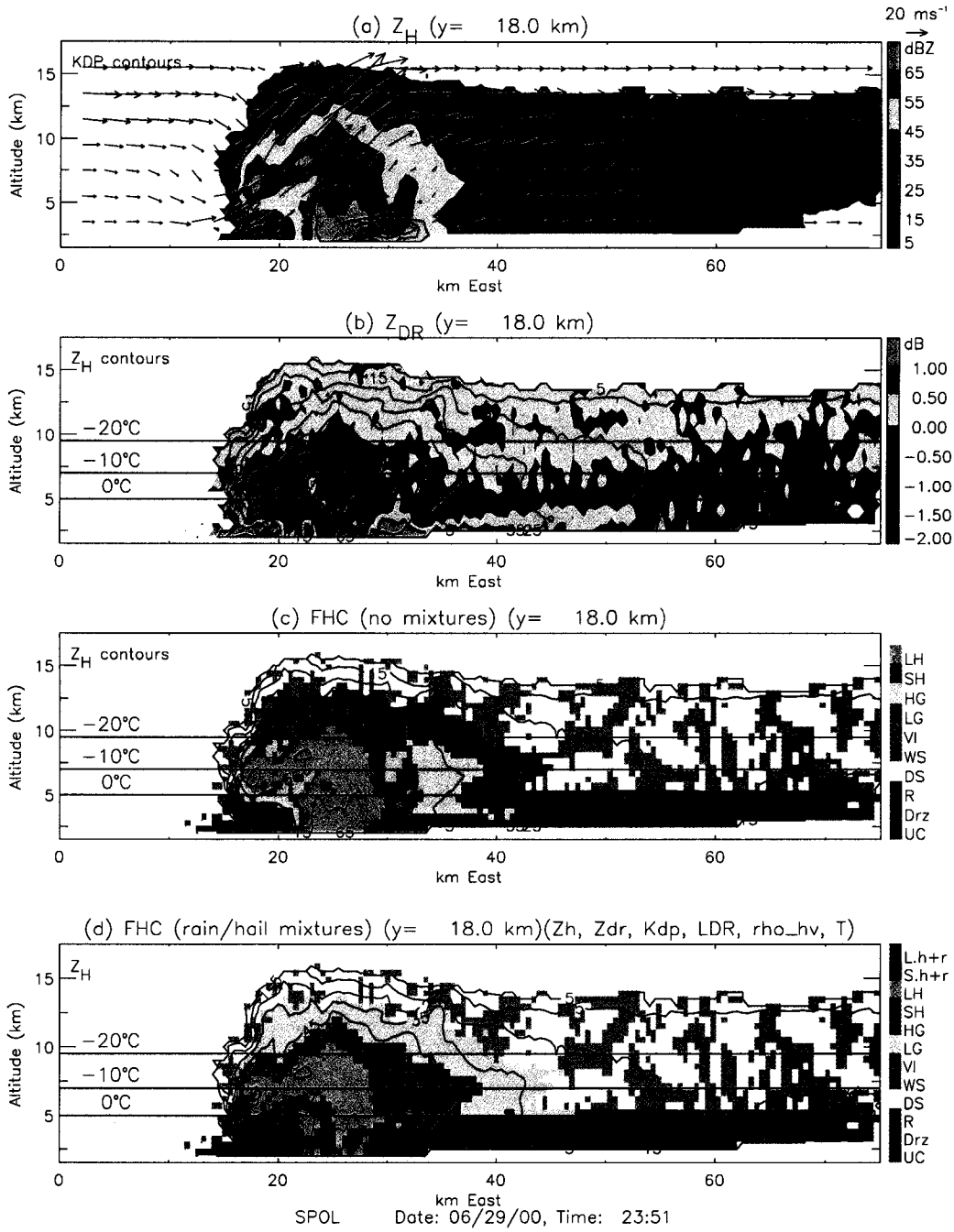

Figure 2.18: Radar vertical cross-sections at 2331 on 29 June 2000 comparing fuzzy logic hydrometeor classification (FHC) results to polarimetric measurements. (a) Color-shaded Z_H with wind flow vectors and additional black contours of K_{DP} at 1, 2, 3, and 4 deg km^{-1}. (b) Color-shaded Z_{DR}. (c-d) The FHC result without and with rain/hail mixtures, respectively. The contours of Z_H from (a) repeated in black on (c-d). Key for FHC categories in (c) is the same as in Fig. 2.17, while (d) has the two additional categories of Lh+r-large hail mixed with rain, Sh+r-small hail mixed with rain. The orientation of these vertical cross-sections are shown in Fig. 2.19.

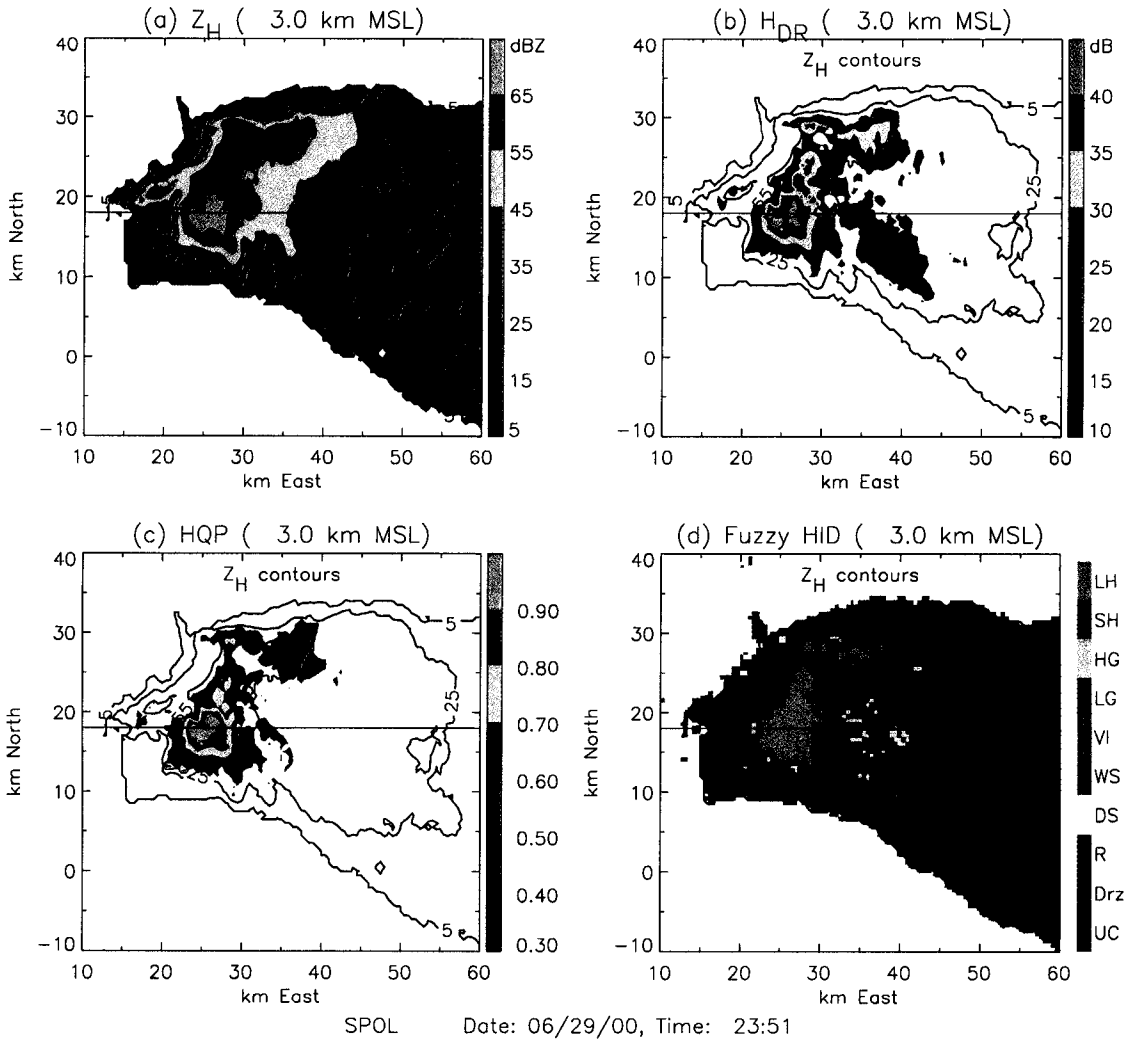

Figure 2.19: Radar horizontal cross-sections at z=3 km at 2331 on 29 June 2000 comparing fuzzy logic hydrometeor classification (FHC) results to other radar-based measures of hail. (a) Color-shaded Z_H. (b) Color-shaded contours of H_{DR}. (c) Color-shaded contours of the hail quadrature parameter (HQP). (d) The fuzzy logic result. Black contours of Z_H are repeated in (b)-(d) at 5, 25, and 55 dBZ. The horizontal lines show the orientation of the vertical cross-sections in Fig. 2.18.

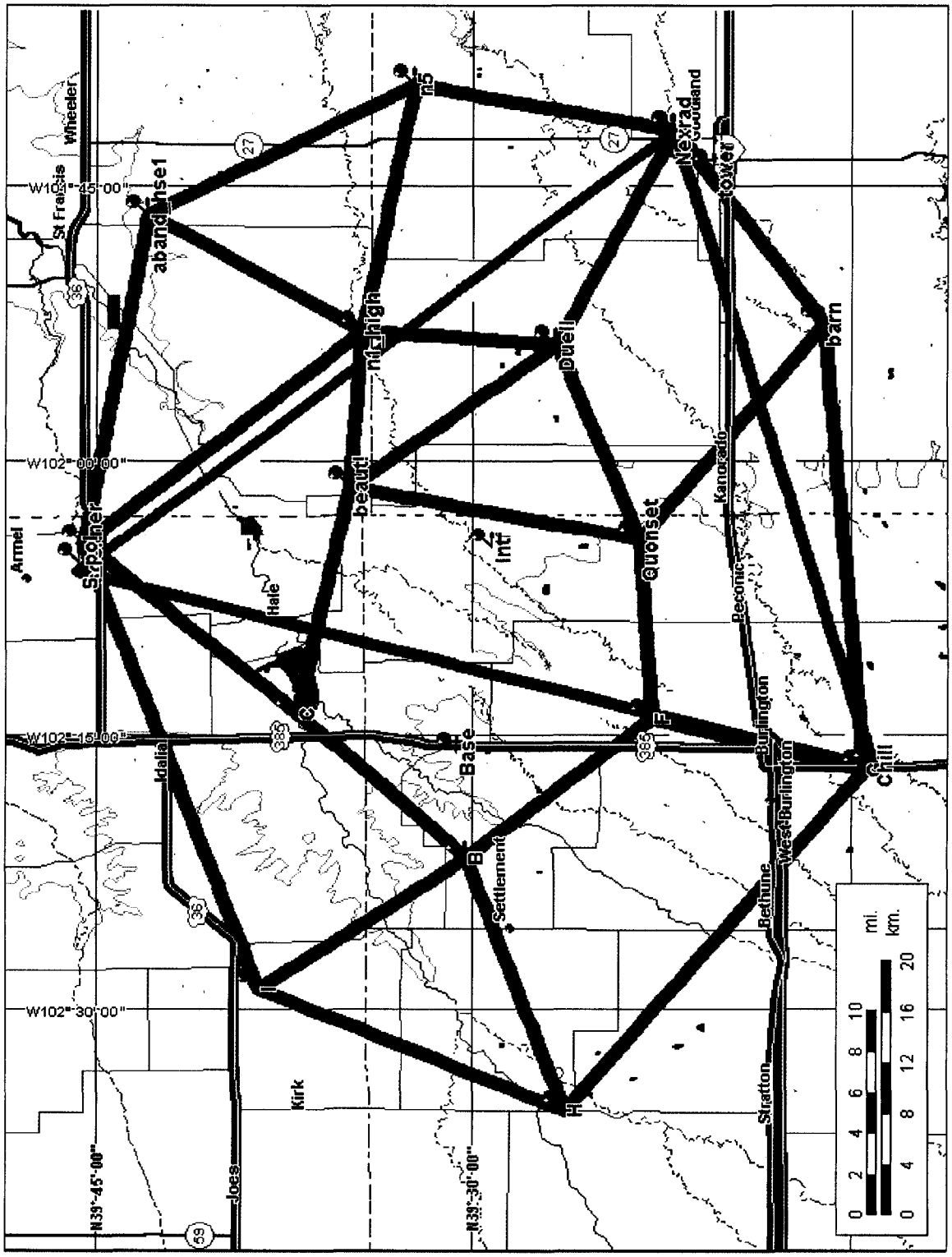

Figure 2.20: Location of STEPS instrumentation. The red lines indicate the layout of the LMA, with a station at each node. The blue-yellow lines show the baselines between the three Doppler radars. The yellow-highlighted dashed line is the Colorado-Kansas border. (From the STEPS web-site at New Mexico Tech: http://lightning.nmt.edu/nmt_lms/steps_2000/steps_config.html).

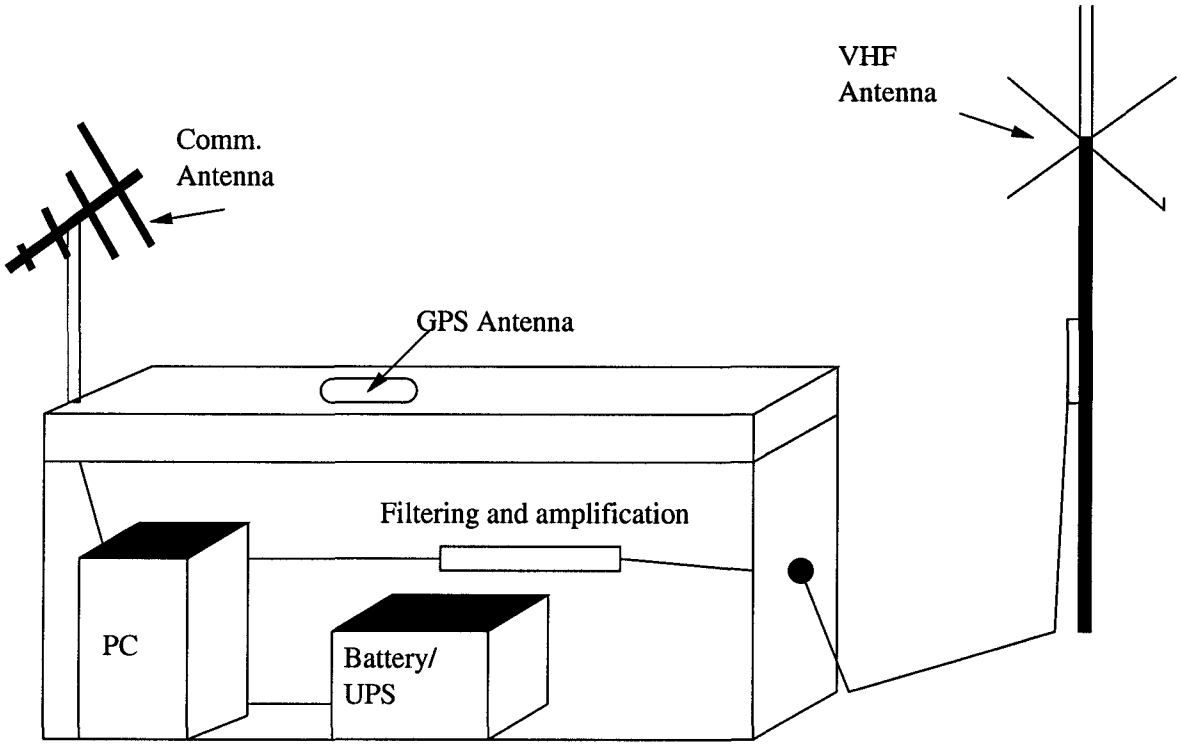

Figure 2.21: Typical setup of an LMA station.

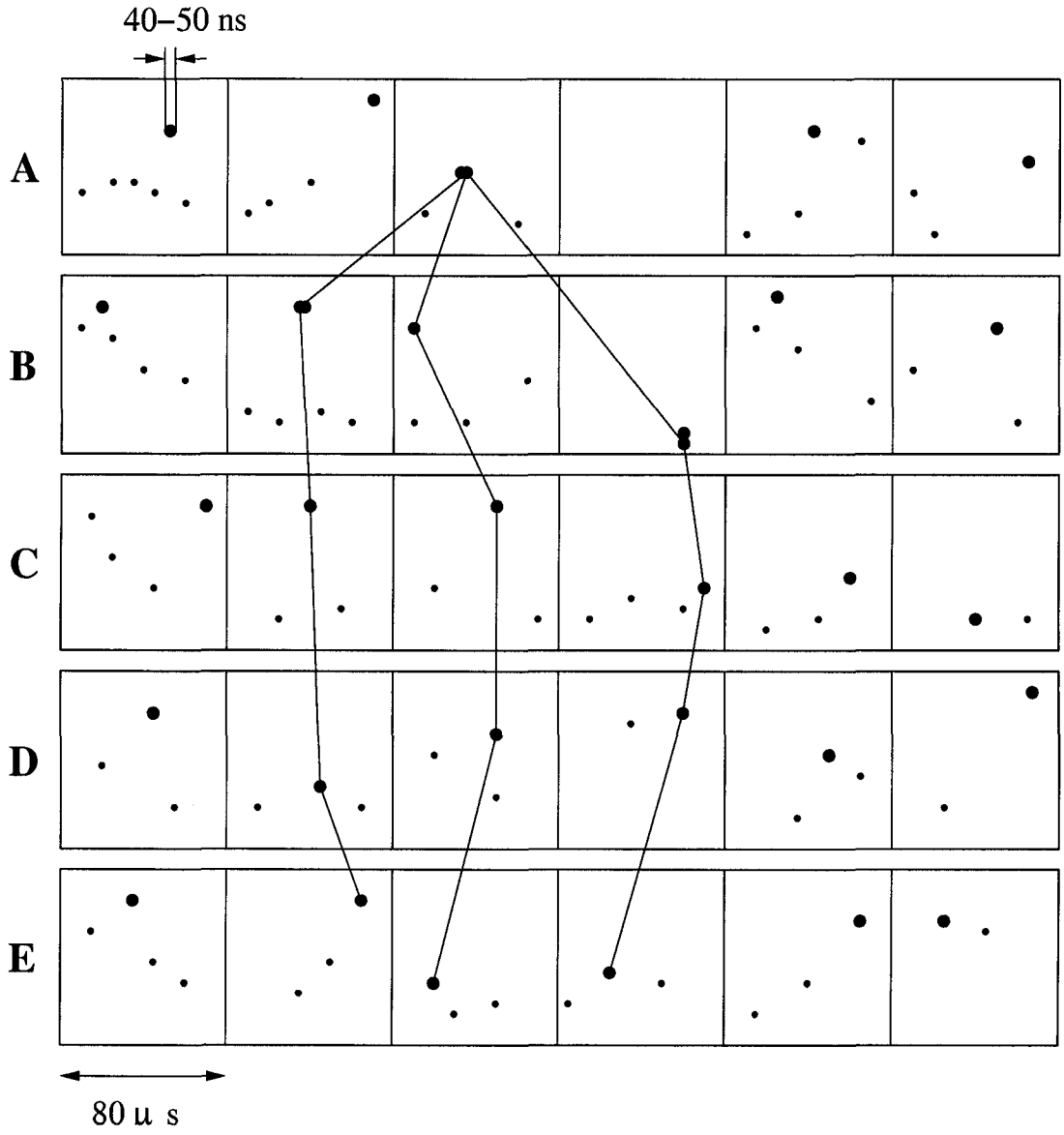

Figure 2.22: Example of LMA data format and processing. The red points indicate times of peak power received at each station (A–E) during each discrete 80 μs window. Smaller black points indicate events with less power that are not recorded by the LMA. The three jointed lines indicate three possible solution combinations using peak power points from other stations within a reasonable time of the event at station A.

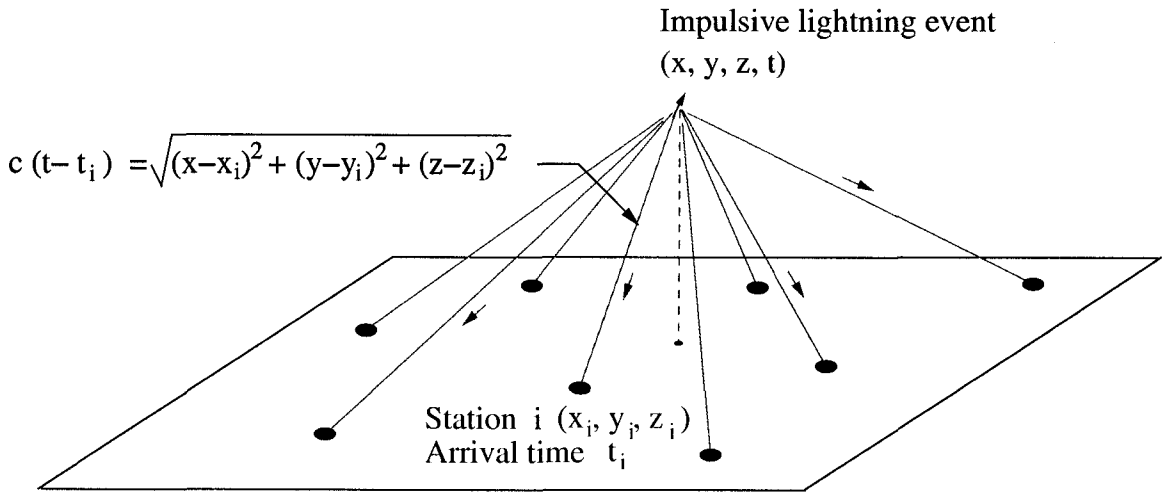

Figure 2.23: Illustration of general LMA station geometry and time of arrival technique. From Hamlin (2004). Used with permission.

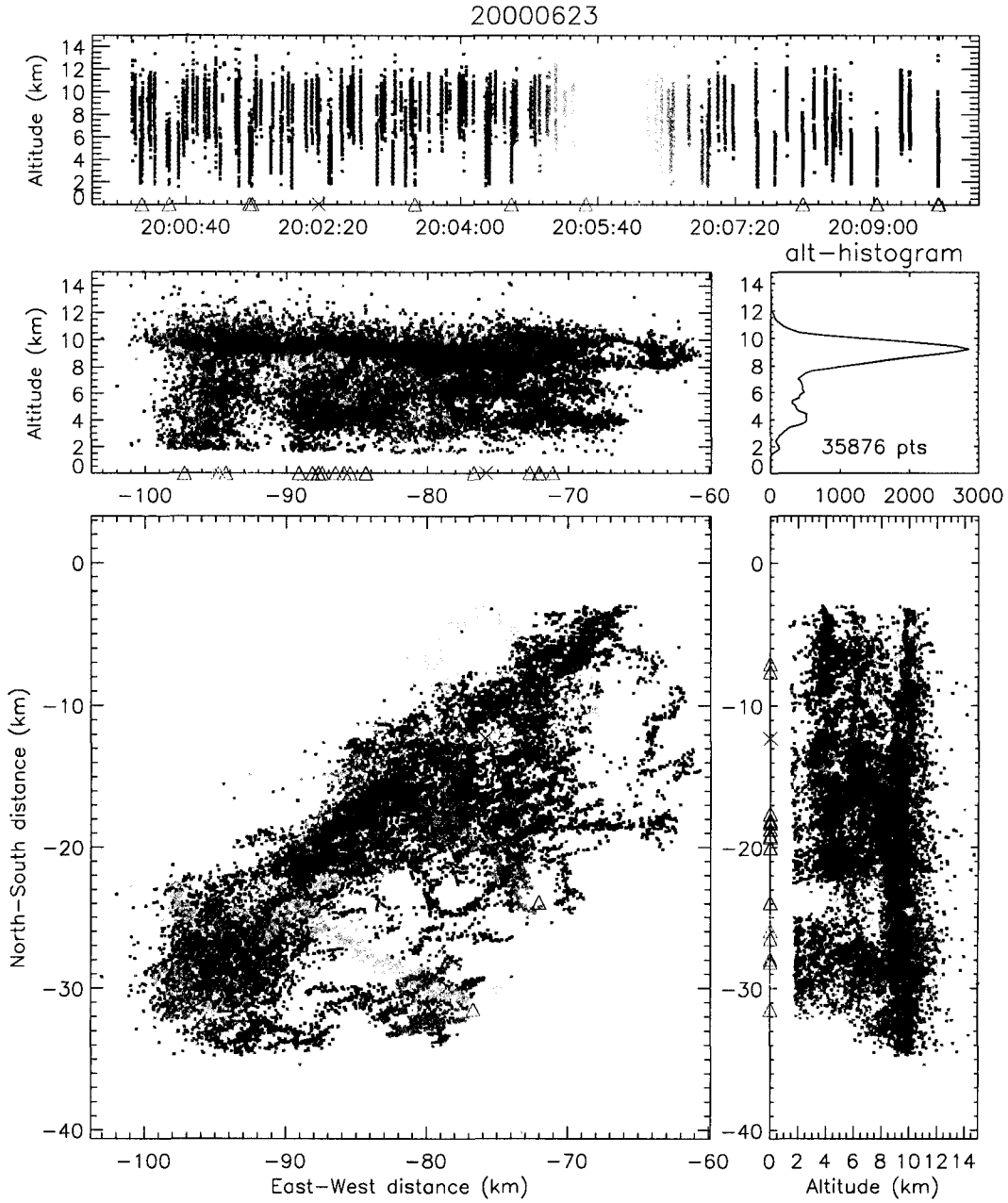

Figure 2.24: Example showing ten minutes (2200–2210) of LMA data from "storm 1" on 23 June 2000. Top panel shows altitude versus time. Lower panels show three different spatial projections along with an altitude histogram of the number of sources. LMA sources are color-coded by time from blue to red. The triangle symbols mark the NLDN-reported location of –CGs. See text for further description.

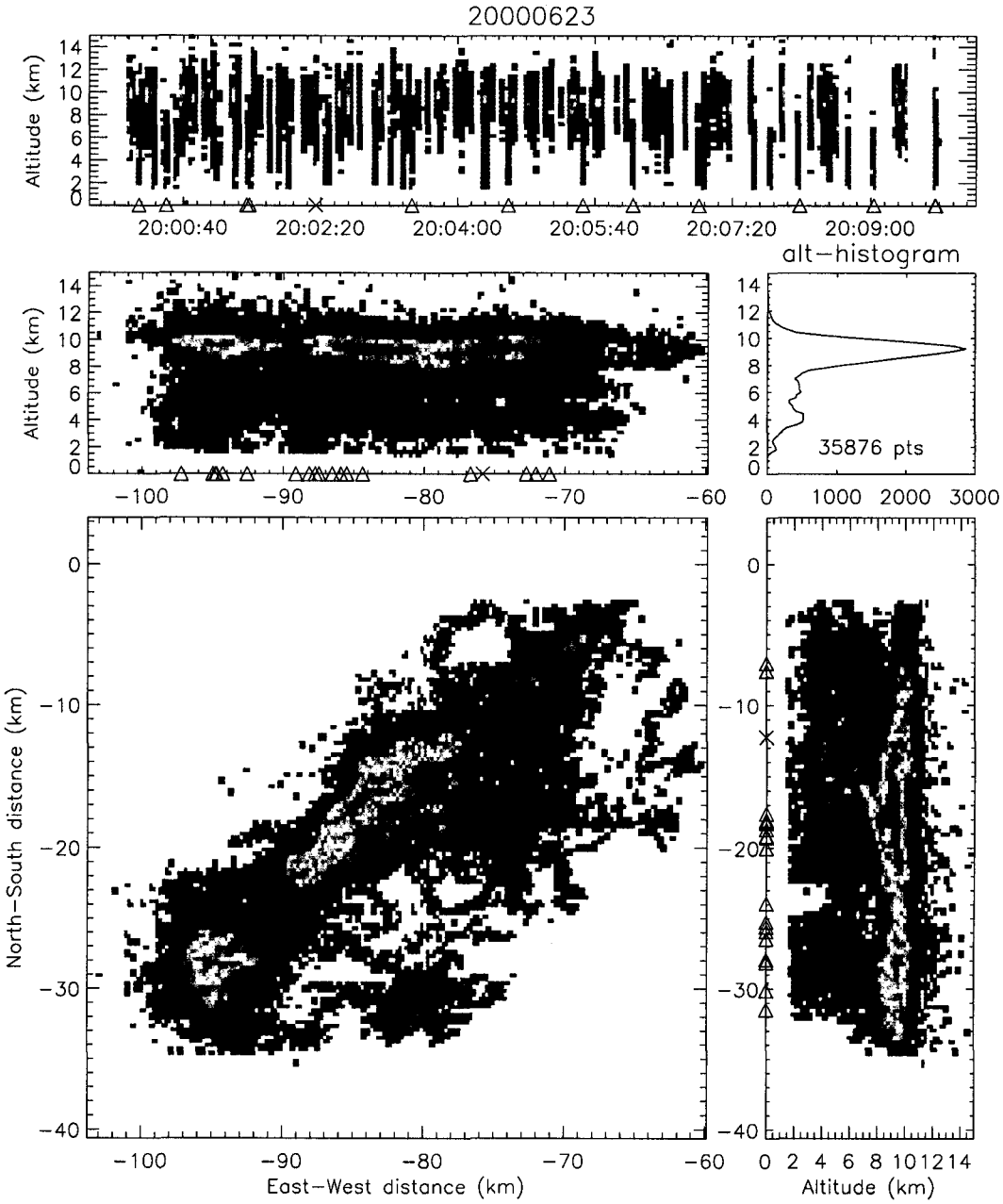

Figure 2.25: As in Fig. 2.24, but sources are color-coded by LMA source density, with warmer colors indicating greater concentration of LMA sources.

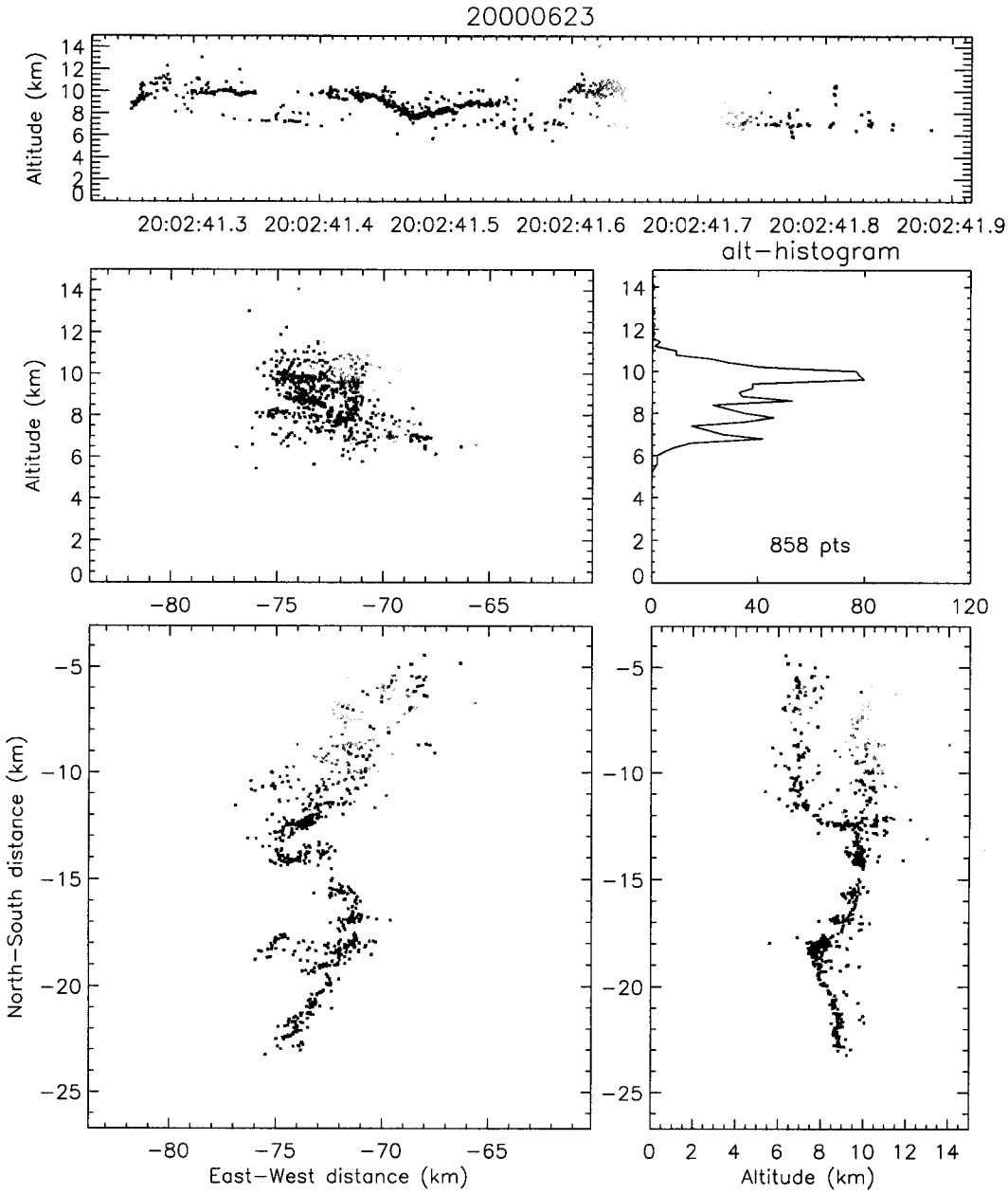

Figure 2.26: As in Fig. 2.24, but for a single flash over a time span of 65 ms. This is a "normal" IC flash that initiated upward from an inferred negative charge region at 6–7 km altitude into an inferred positive charge region at 8–10 km altitude. The stratification of the charge regions is most evident in the N-S vs altitude projection in the bottom-right panel. Sources are color-coded by time in all panels. See section 2.2.3 for more description of charge structure determination.

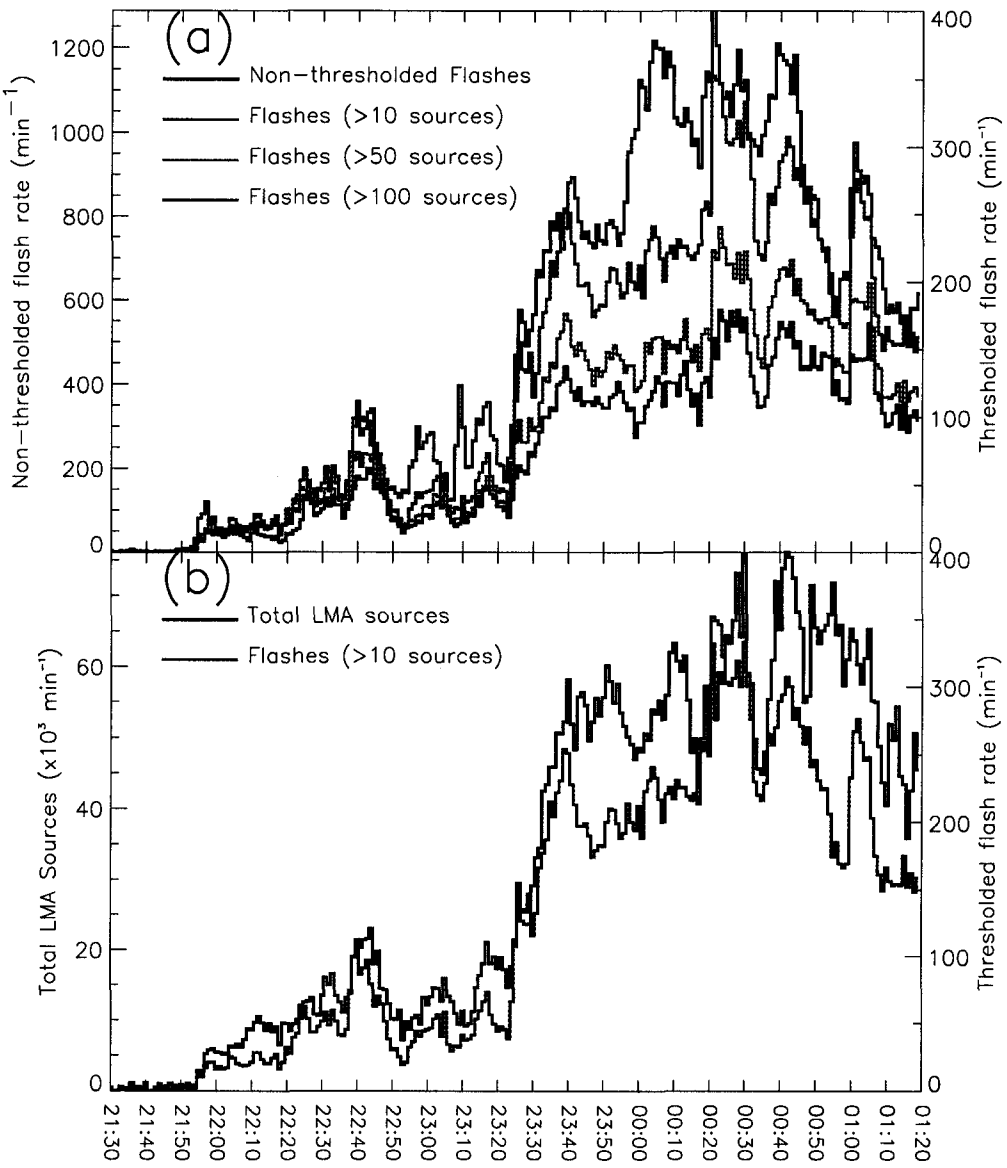

Figure 2.27: Comparison of LMA metrics of lightning intensity for the 29 June 2000 supercell. (a) Total flashes each minute (black) compared with flashes having at least 10 (red), 50 (green), and 100 (blue) sources. (b) Total LMA sources each minute (black) compared with flashes having at least 10 sources (red). Total flashes include all isolated groups of LMA sources (including single sources). Bin size is one minute for all plotted quantities.

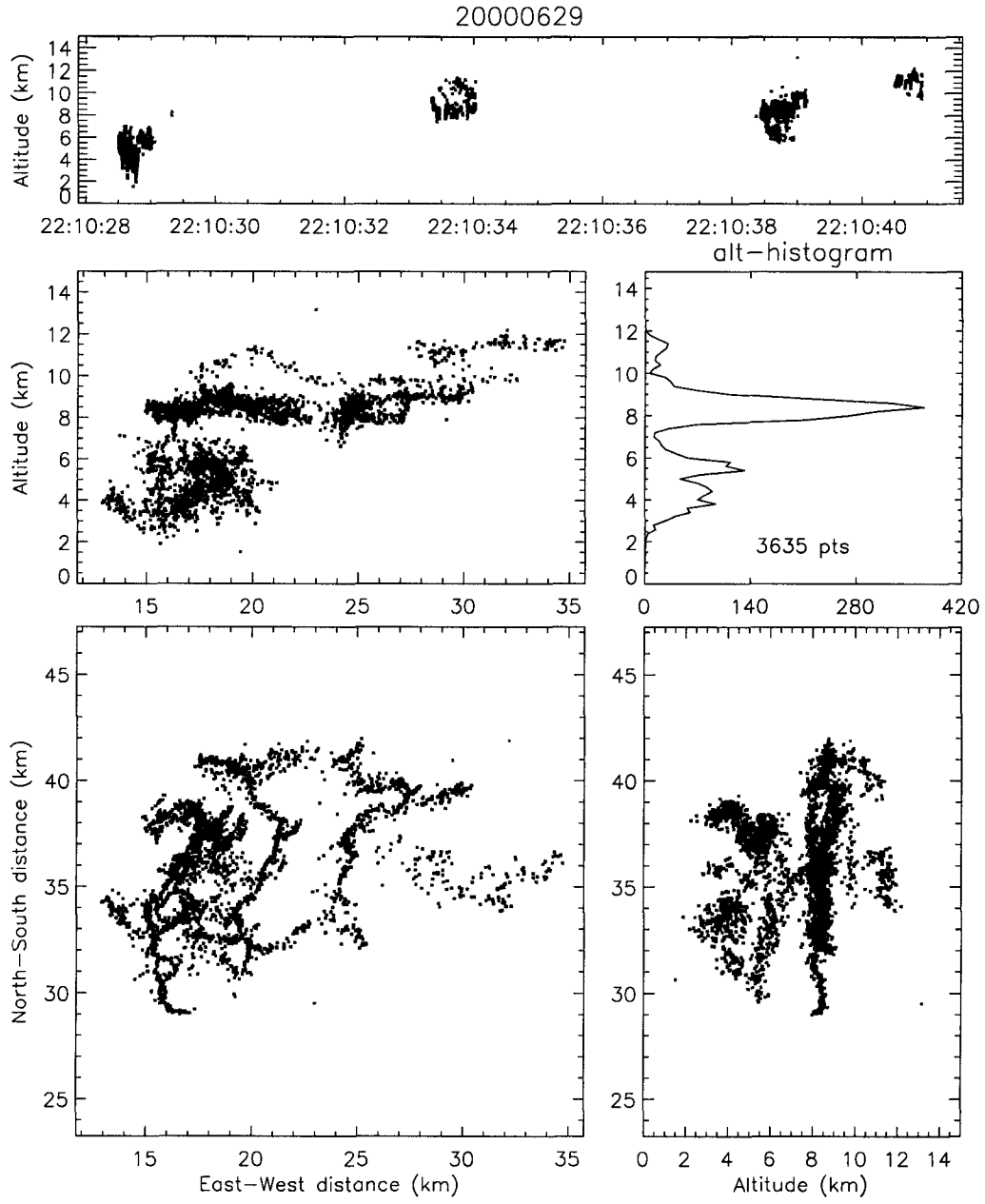

Figure 2.28: Lightning mapping of five flashes (two normal, three inverted) showing 5-layer charge structure at 2210 during the 29 June 2000 storm. Panel layout is the same as in Fig. 2.24, but here the LMA sources are color-coded by inferred charge (red=positive, blue=negative, green=undetermined).

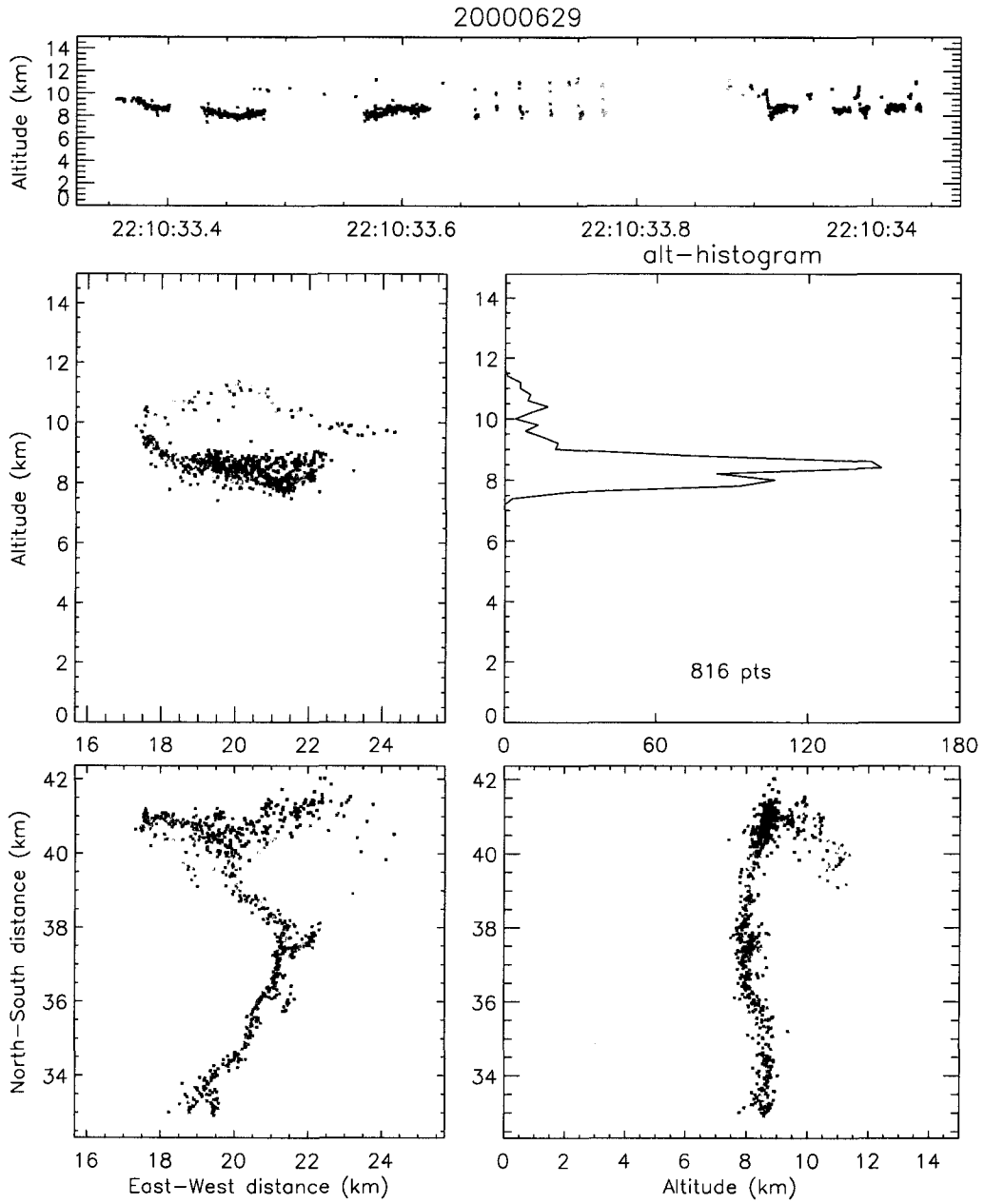

Figure 2.29: The second flash of the 5-flash sequence in Fig. 2.28. This is an "inverted" flash that initiated downward from an inferred negative charge region at 10–11 km into an inferred positive charge region at 8–9.5 km. LMA sources are color-coded by time from blue to red.

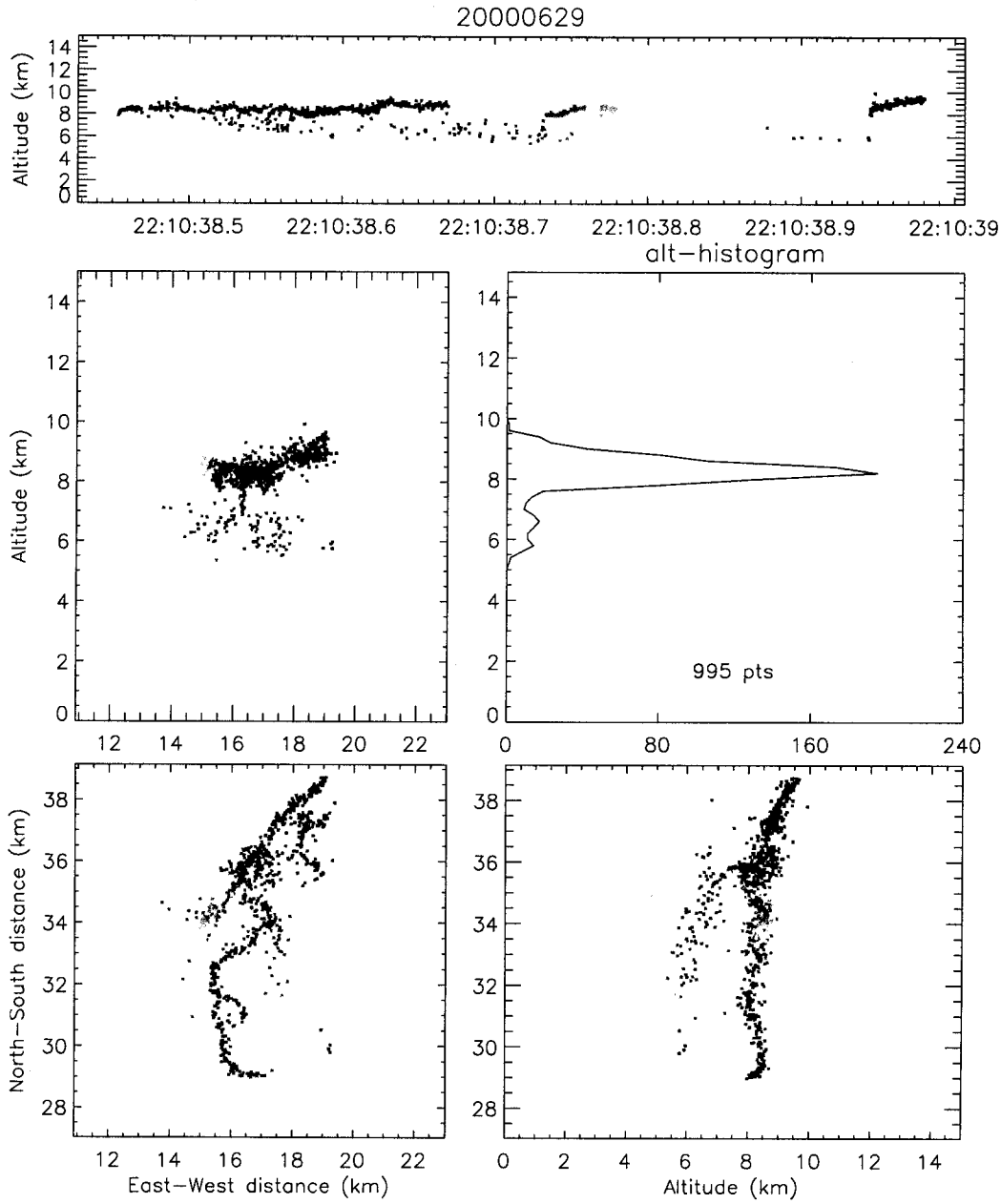

Figure 2.30: The third flash of the 5-flash sequence in Fig. 2.28. This is a "normal" flash that initiated upward from an inferred negative charge region at 6–7 km into an inferred positive charge region at 8–9.5 km. LMA sources are color-coded by time from blue to red.

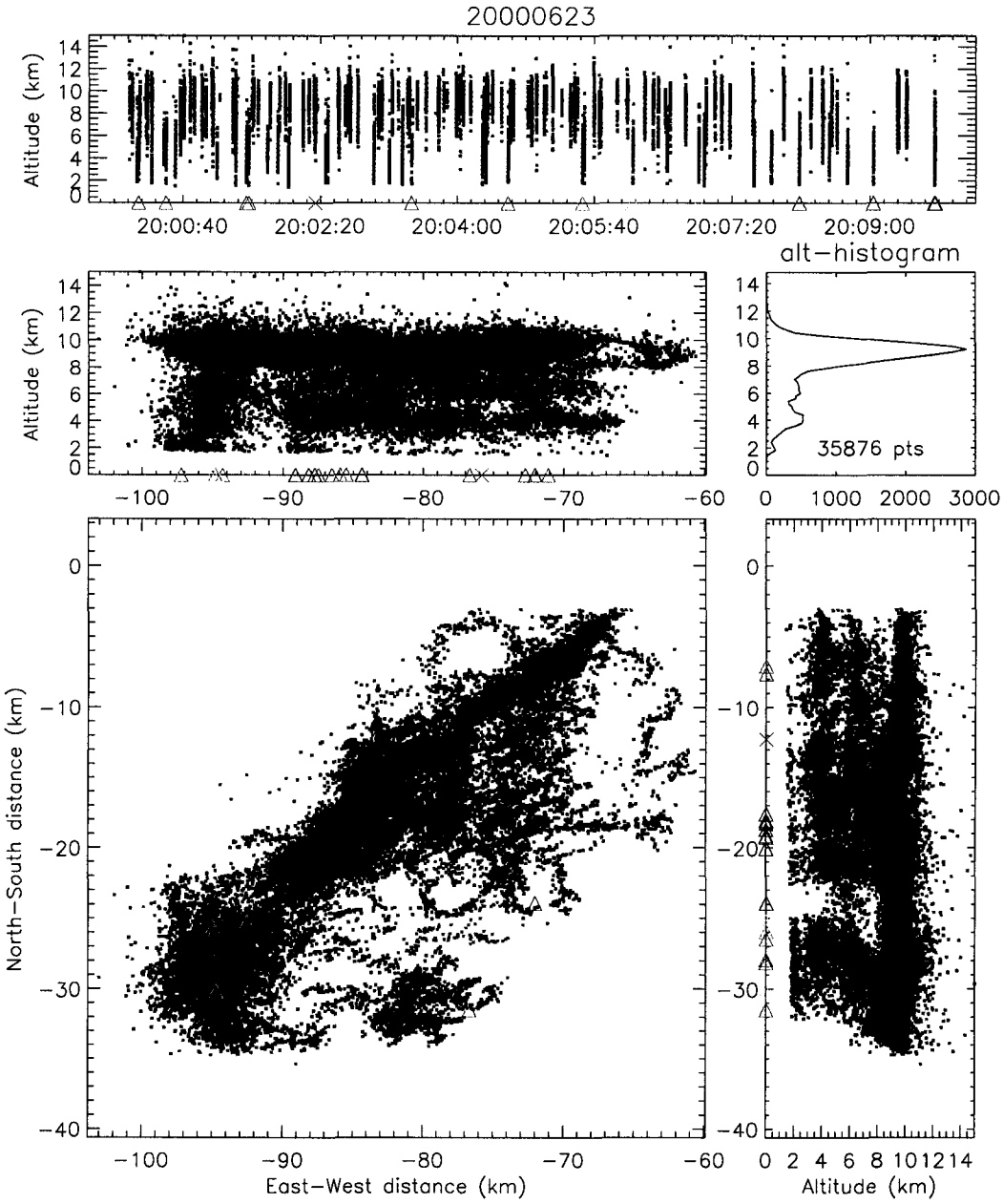

Figure 2.31: As in Fig. 2.24, but sources are color-coded by inferred charge region (red=positive, blue=negative, green=undetermined).

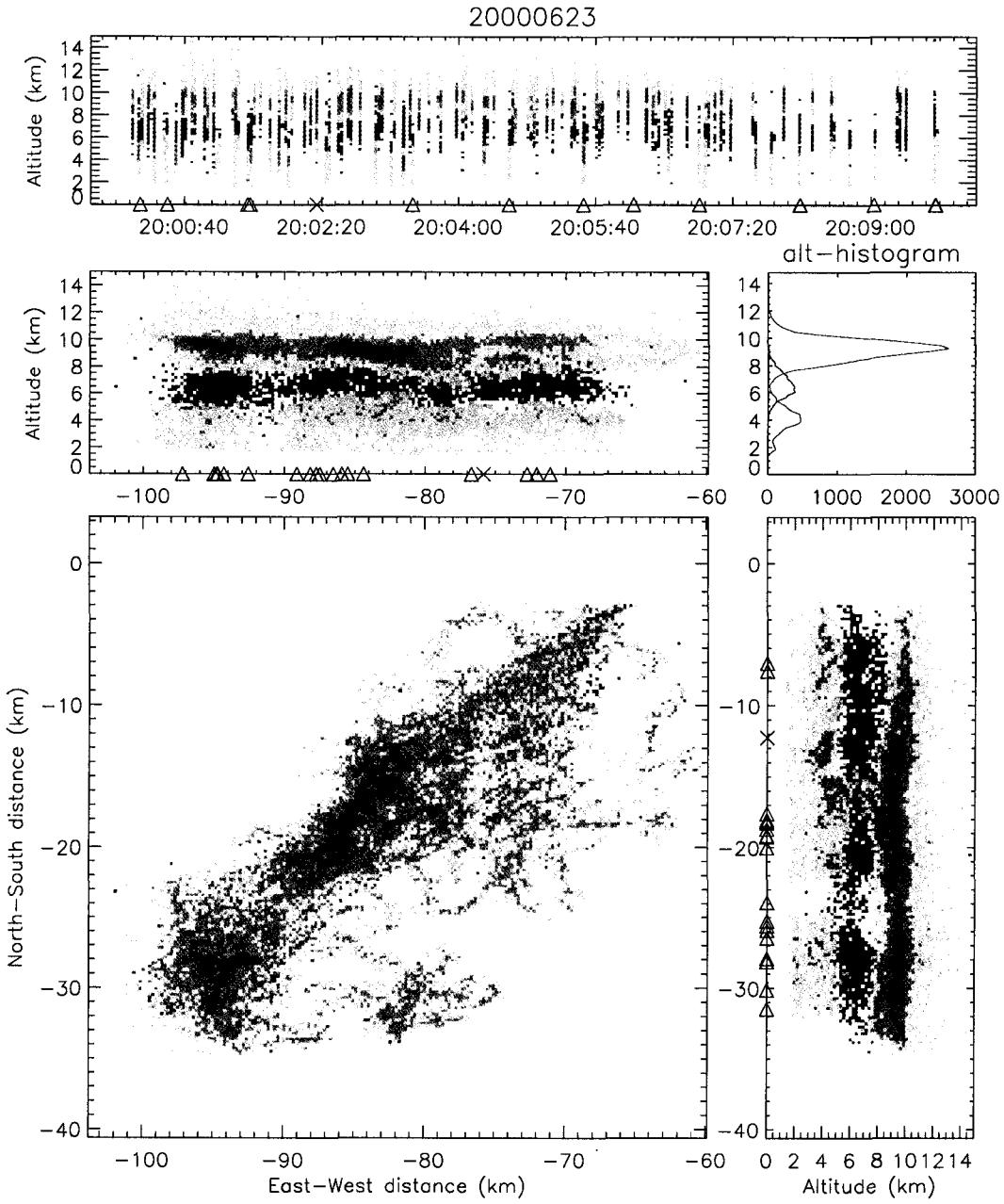

Figure 2.32: As in Fig. 2.24, but sources are color-coded by inferred charge density. Redder (bluer) colors indicate greater number of LMA sources in inferred positive (negative) charge regions. The altitude histogram panel shows separate histograms for LMA sources in inferred positive (red) and negative (blue) charge regions.

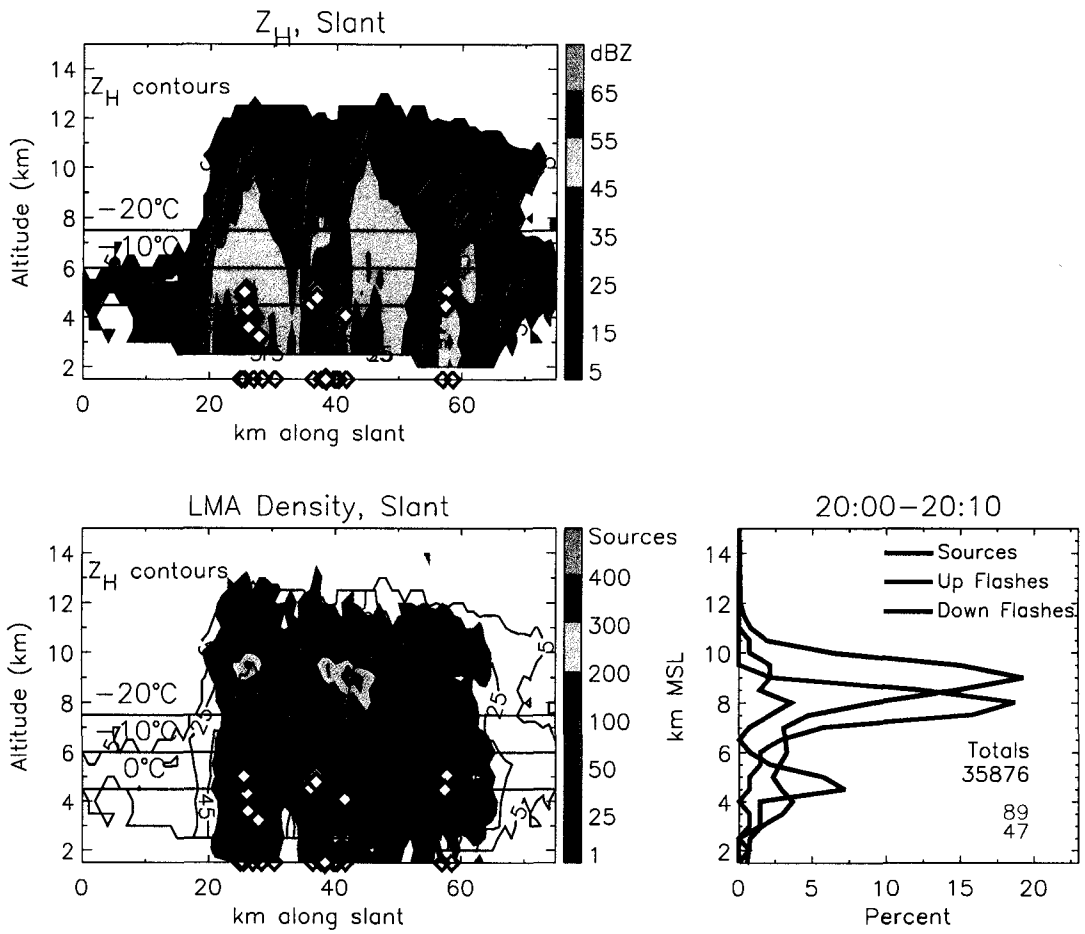

Figure 2.33: Example illustrating comparisons of vertical radar cross-sections of horizontal reflectivity (Z_H, top) to vertical cross-section of LMA source density (bottom-left) and altitude histograms of LMA sources and flash initiation altitudes (bottom-right). Z_H contours are repeated in black on the LMA cross-section at 5, 25, and 45 dBZ. Filled diamond symbols aloft in the vertical cross-sections mark the mean origin heights of –CG flashes, and diamond symbols along the surface mark the NLDN strike points of these –CG flashes. The altitude histograms show total LMA sources (black), initiation of heights upward flashes (red), and initiation heights of downward flashes (blue), all plotted as the percent of the total from 2000–2010, i.e., vertical integration of the black curve gives 100% and vertical integration of the blue plus red curves gives 100%. These data are from "storm 1" on 23 June 2000. The LMA data are the same as what are plotted in Figs. 2.24, 2.25, and 2.31, though in the LMA density cross-section, the LMA sources are restricted to include only those within 5 km of the cross-section plane, See text for more details.

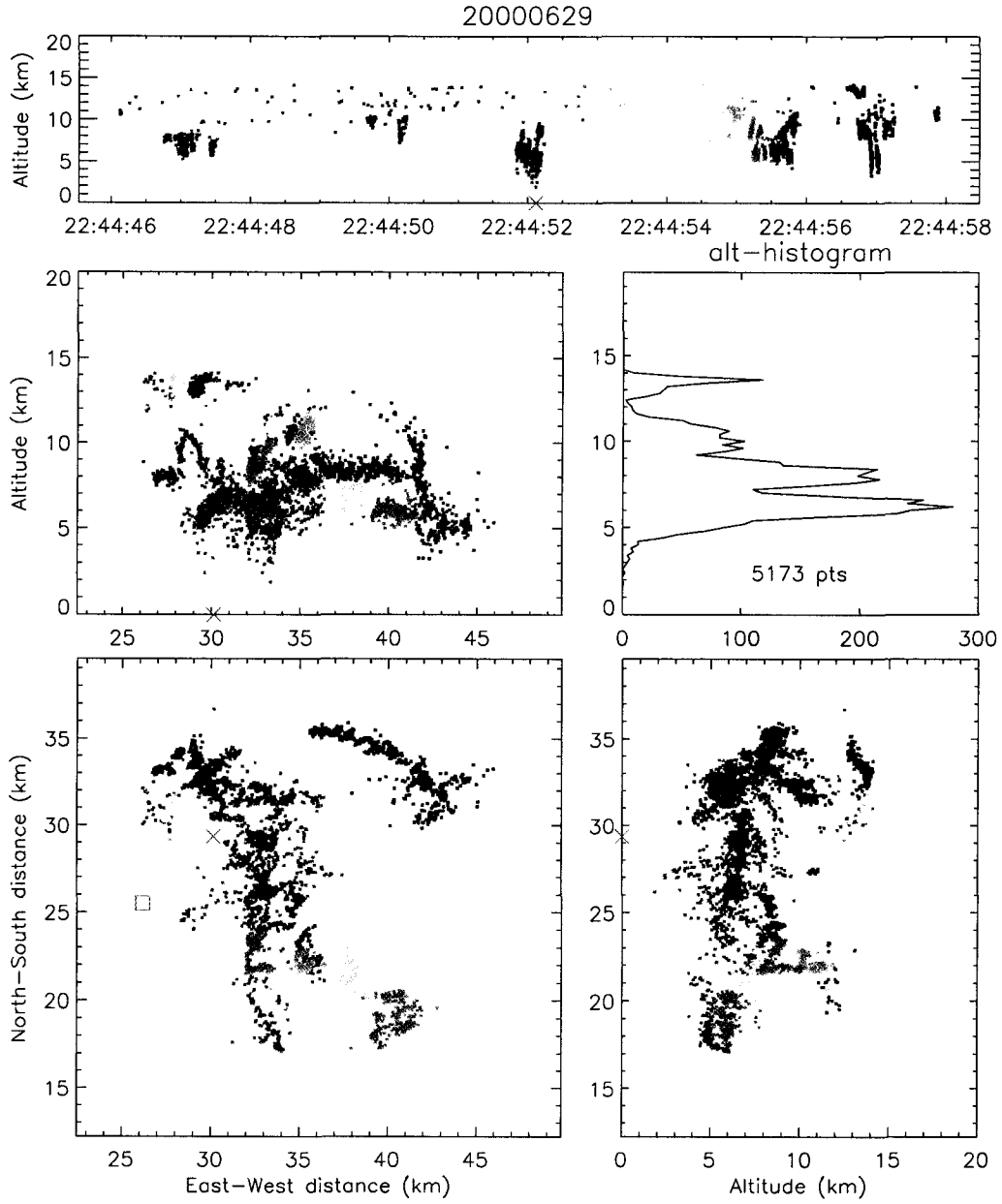

Figure 2.34: Ten seconds of LMA activity centered on a +CG flash at 2244:52 from the 29 June supercell. Sources are color-coded by time from blue to red, and the green X marks the strike point of the +CG flash. Note how the CG's parent flash is distinct (at least temporally) from other lightning.

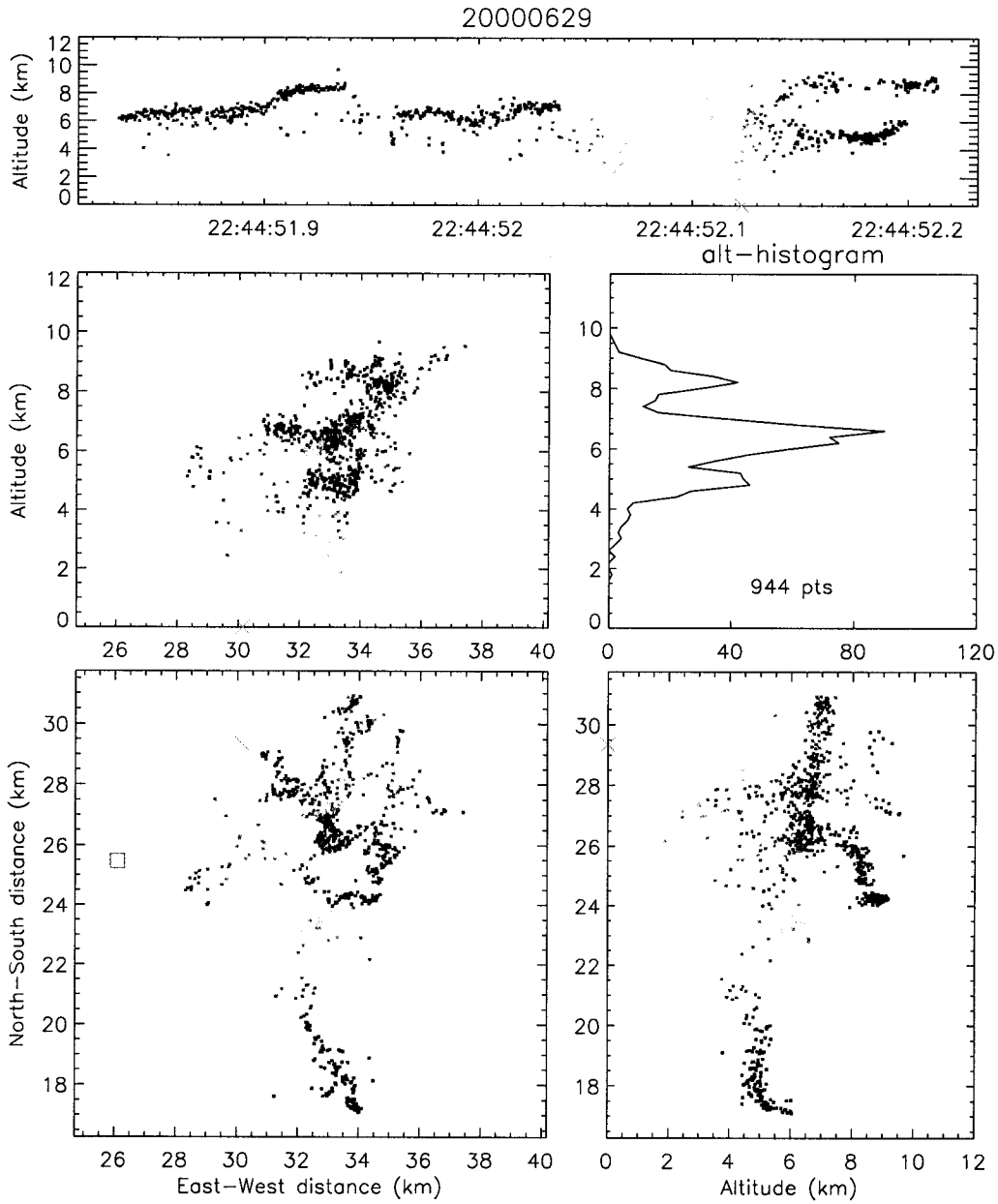

Figure 2.35: As in Fig. 2.34, but "zoomed" in on the +CG flash.

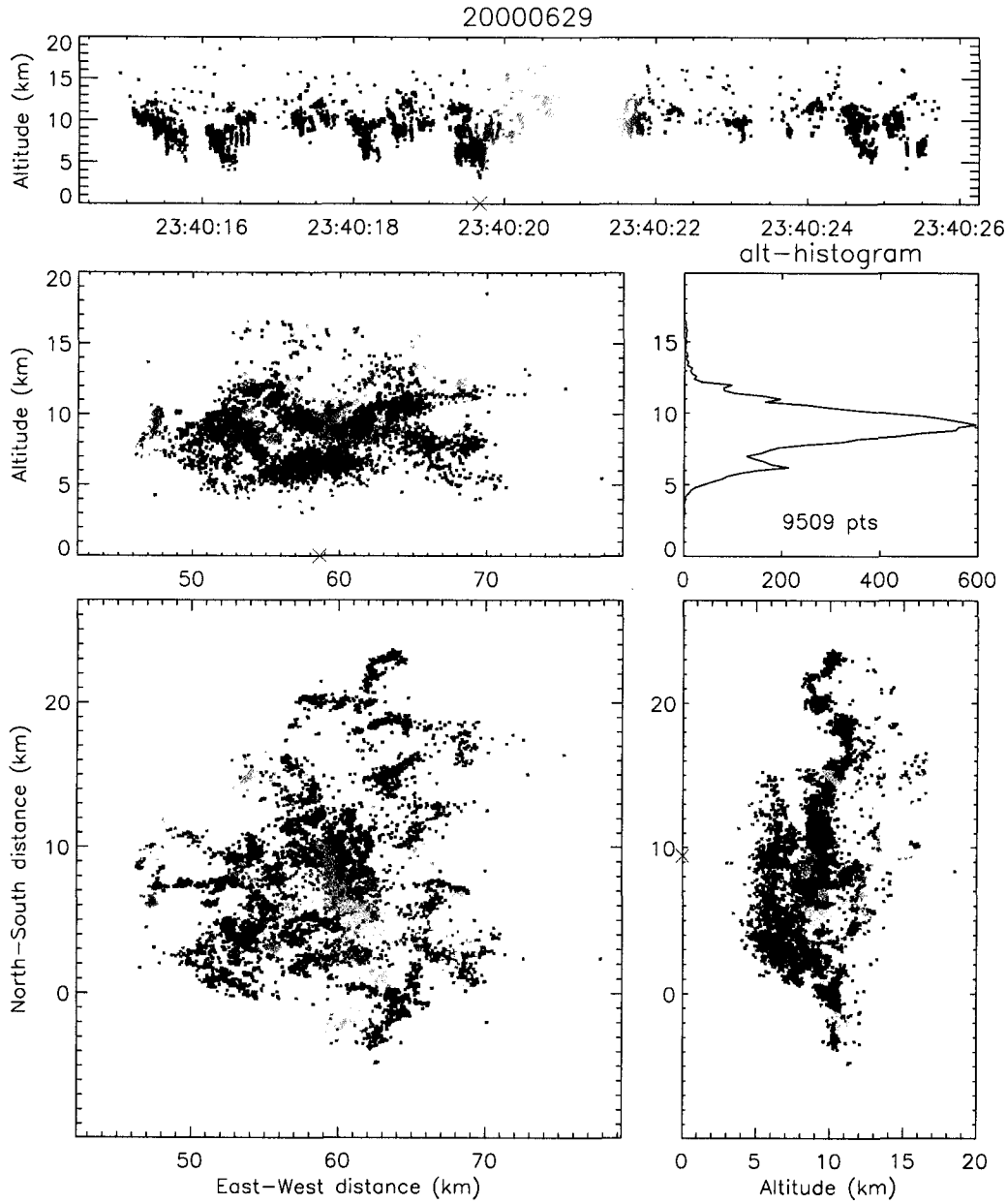

Figure 2.36: As in Fig. 2.34, but centered on a +CG flash at 2340:19. Note how the +CG's parent flash is embedded in other lightning.

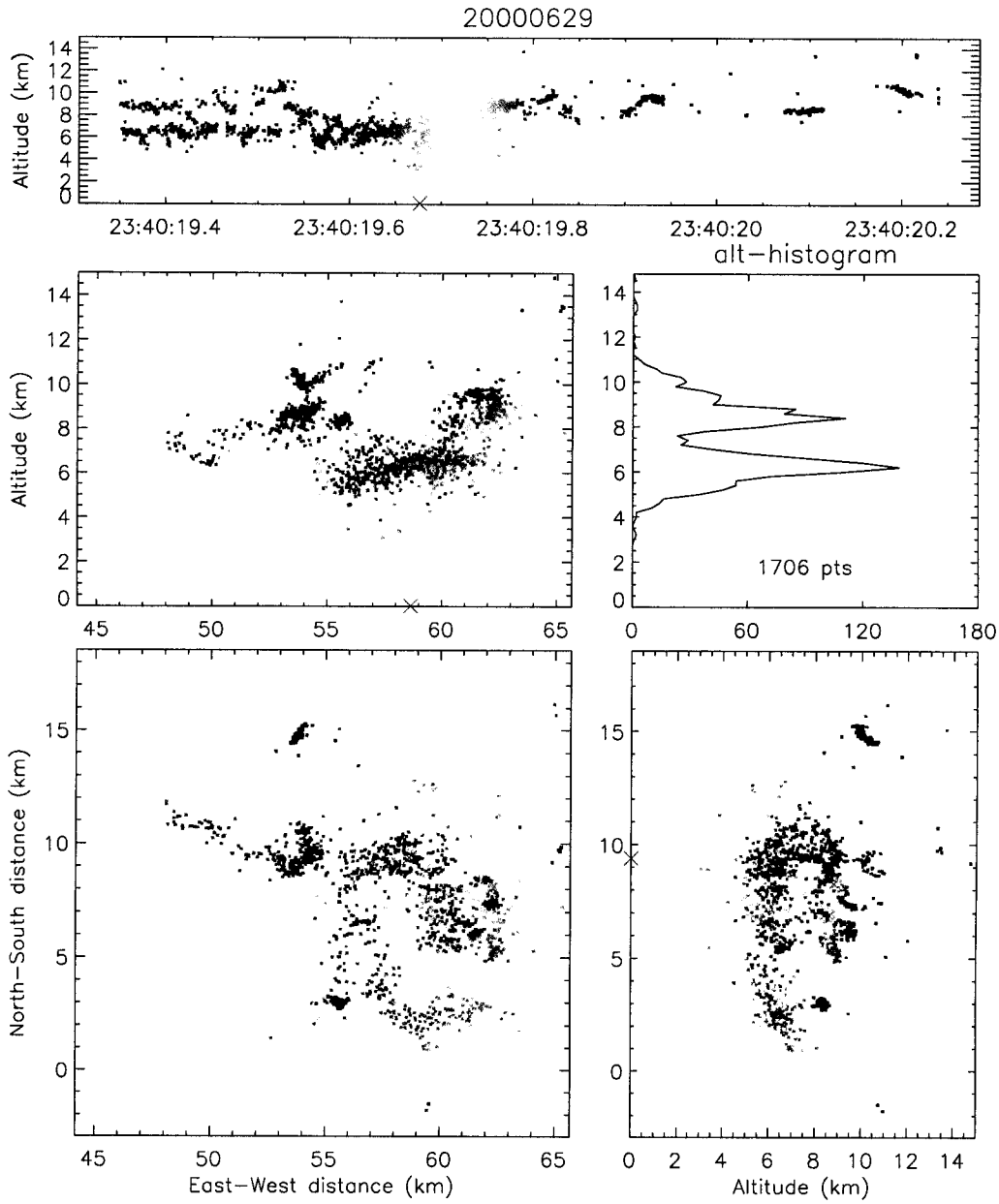

Figure 2.37: As in Fig. 2.36, but 'zoomed' in on the +CG flash.

CHAPTER 3

29 JUNE OBSERVATIONS

3.1 Introduction

Since the completion of field campaign phase of STEPS, the primary focus has been on the +CG-dominated supercell of 29 June. This storm stayed within optimal radar coverage from its very beginning (2130) to near its end, and was penetrated by both the T28 aircraft and EFM balloons. This storm produced only a few CG flashes (all positive) in the initial two hours of lightning activity, and these few initial +CG flashes all occurred during brief surges in updraft and hail production. Copious +CG flashes began nearly coincident with dramatic surges in storm updraft, hail production, total flash rate, the dramatic right turn of the storm, and formation of an F1 tornado (Fig. 3.1). A two-part study of this storm has been submitted to the *Journal of the Atmospheric Sciences* (Tessendorf et al., 2004a– hereafter, Part I; Wiens et al., 2004–hereafter, Part II). Part I provides a detailed analysis of the kinematic and microphysical evolution of this storm. The following observations are essentially the same as those described in Part II, and focus on the storm's lightning activity and diagnosed charge structure.

3.2 Observations

As described in more detail in Tessendorf et al. (2004a), convection on this day developed along a southeastward moving surface boundary. An NCAR Moble GPS/Loran Sounding System (MGLASS) sounding (Fig. 3.2) was taken from the location of the KGLD radar at 2022, about 1.5 hours before the beginning of the

observation period (2130). This sounding shows high ($\approx$ 1200 J kg^{-1}) Convective Available Potential Energy (CAPE) and a veering, strongly sheared (5–10 m s^{-1} per 3.5 km in the low levels) wind profile. Hence, the environment was primed for severe thunderstorm (supercell) development (Moller et al., 1994).

3.2.1 Overall trends and relationships

To provide some context for the detailed observations that follow, Fig. 3.3 provides a time series summary of the storm from 2130 (June 29) to 0115 (June 30). Echo volumes of updraft (w > 10 m s^{-1}; hereafter UV_{10}), graupel, and hail are plotted in Fig. 3.3a along with the total volume of the storm (defined as the total echo volume with radar reflectivity in excess of 0 dBZ). To highlight smaller scale fluctuations, Fig. 3.3b shows echo volumes of UV_{10}, graupel and hail in terms of their percentage of the total storm volume. Total flash rate (IC plus CG; designated as TFR) and CG flash rates are plotted in Fig. 3.3c. Overall, IC flashes dominated the lightning activity, with a *minimum* IC/CG ratio of about 40. Of the 254 CG flashes, 223 of them (88%) were positive[1].

In general, the broad trends in the various echo volume and flash rate time series followed the trend in total storm volume. The dominant feature of these time series is the dramatic increase in updraft, hail, TFR, and +CGs accompanying the right turn of the storm at 2325. However, there were several smaller-scale surges (e.g., at 2144, 2227) that are more apparent in the normalized time series of Fig. 3.3b. For the most part, each of these surges followed the general pattern of a surge in UV_{10}, followed 5–10 minutes later by coincident surges in graupel echo volume and TFR, followed 5–10 minutes later by surges in hail echo volume. Surges in updraft affected the vertical distribution of reflectivity and lightning, as well (Fig. 3.4). Each burst of updraft

[1]As discussed in Part I, a separate smaller cell formed near midnight UTC, just northwest of the supercell of this study. It produced some hail and frequent lightning (though nowhere near the scale of the supercell), and dissipated by 0100. Calculations of flash rates and echo volumes include this separate cell. It produced only six CG flashes (5 –CGs and 1 +CG), all of which occurred as it collapsed during the 0056 volume scan.

generally led to greater vertical extent of both significant reflectivity and lightning. For the first fifteen minutes of the observations period (2130 to 2145), the updraft was weak in terms of both magnitude and volume. Consequently, there was little graupel volume above 8 km (Fig. 3.4a, and the lightning activity was entirely below an altitude of 8 km and highly concentrated near 5 km (Fig. 3.4b). Following the first updraft burst around 2144, the lightning became highly concentrated at higher altitudes in an elevated reflectivity feature (Fig. 3.4), and the flash rate increased substantially (Fig. 3.3c). For the remainder of the observation period (2200 to 0115), the precipitation volumes and lightning pulsed in vertical extent in apparent response to bursts in updraft, though, in general the lightning sources extended further and further upward (Fig. 3.4). Throughout the last three hours of the observation period, there was considerable lightning activity at all altitudes below 15 km. However, *the highest concentration of LMA sources, and thus the highest likely concentration of positive charge, remained at a relatively steady altitude centered near 8 km MSL ($T \approx -12°C$).* There were also surges in the +CG flash rate, and, interestingly, these surges generally occurred during dramatic intensification of the storm's updraft and hail production. For example, the first two +CGs occurred near the time ($\approx$ 2239) of relative maxima in TFR and hail echo volume. There were no +CGs and little hail echo volume from 2252 to 2318. Then, at 2325, as the hail echo volume began to increase dramatically, so did the +CG flash rate. However, near the end of the observation period (0115), the UV_{10}, and hail echo had been declining steadily, while the +CG flash rate reached its *absolute maximum* of the entire observation period.

In an attempt to better quantify the relationships among updraft, precipitation and lightning, we performed residual correlation analyses of their time series. Since the bulk of the variance in all the time series of Fig. 3.3 can be accounted for by the steady quasi-linear increase in total storm volume (Table 3.1), we isolated the correlations from the dominating influence of the total storm volume. In mathematical terms, we first performed separate linear least squares fits of each of the raw time series (e.g., UV_{10}, graupel, TFR) to the total storm volume time series. We then

subtracted these "fitted" time series from the raw series to get the de-trended residual time series which are, by definition, uncorrelated to the total storm volume. We then computed the correlation coefficients between the residual time series as a function of lag[2]. Figures 3.5 and 3.6 show graphical representations of this procedure, and Table 3.1 summarizes the results.

Several studies (e.g., MacGorman et al., 1989; Carey and Rutledge, 1996) have shown that TFR is very well correlated with the volume of 30–40 dBZ radar reflectivity within the mixed-phase region (often called the *Larson Area*; Larson and Stansbury, 1974) where collisional charging is thought to occur. This *Larson Area* essentially describes the same thing as does our graupel echo volume, and we find a similar result for this storm. The TFR shows a robust correlation with graupel echo volume (and with updraft, to a lesser extent) even after the quasi-linear increase of the total storm volume has been removed (Fig. 3.7). Note that the residual correlation between graupel and TFR peaks at zero lag (bottom panel of Fig. 3.5). That is, the best correlation between the residual time series occurs when the time series are contemporaneous. This is true for UV_{10} vs. TFR, as well. However, the correlation vs. lag is not as sharply peaked as is the correlation between graupel and TFR (Fig. 3.6). The UV_{10} vs. TFR correlation decreases more gradually when TFR lags UV_{10} and more sharply when UV_{10} lags TFR. This makes physical sense. Increases in the volume of significant updraft should lead to increases in graupel formation, electrification and flash rate. Hence the overall trends of the storm indicate that increased updraft led to increased precipitation in the mixed-phase region which invigorated the collisional charging, as manifested by the lightning activity.

None of the other time series show such strong contemporaneous residual correlations; however, Table 3.1 shows some interesting results at non-zero lag. The hail volume is best correlated with UV_{10}, graupel and TFR when it lags the UV_{10} by one

[2]MacGorman et al. (1989) performed a similar detrending analysis; however, instead of removing the variance explained by the large-scale trend in overall storm volume, they removed the separate linear trend of each their time series prior to computing the residual correlations.

volume scan interval (5–7 mins) and lags the graupel and TFR by two volume scan intervals (10–15 mins). The +CG flash rate is not well-correlated with any other quantity at zero lag, and the best correlations between +CG flashes and graupel, hail and UV_{10} occur when +CGs lag graupel and UV_{10} but lead hail. One interpretation of these collective results is that the broad, strong updrafts led rapidly to increased graupel and increased charge-separating collisions involving this graupel. With time, the graupel continued to grow within the supercooled liquid water-rich updrafts, forming hail. As discussed in Williams (2001), hail is unlikely to be a major player in charge separation due to its minuscule integrated surface area (compared to an equivalent mass of graupel). The lagged correlation between TFR and hail (and weaker correlation overall) seems to support this idea. Though we hesitate to attach too much significance to these results, the TFR (and to a lesser extent, +CG flash rate) seems to be a good indicator of this storm's intensification and may have some utility as a predictor of severe weather in the form of hail. Williams et al. (1999) found a similar result in their comparison of radar-inferred storm development to TFR derived from the LDAR system at Kennedy Space Center. They found that TFR would often "jump" dramatically during explosive vertical development of the radar echo, and these lightning jumps were typically followed 10s of minutes later by severe weather at the ground in the form of hail and down-bursts.

In order to reveal the relationships among +CG flashes, updraft strength, and hail production, we need to know not just *when* but also *where* in the storm the +CG flashes originated and where they struck ground. To this end, we used the LMA data to extract the origin location of CG flashes (see Section 2.2.4). CG origin heights were determined for 180 of the 254 total CG flashes identified by the NLDN during the observation period of this storm. The disparity between the numbers of CG flashes and CG origin heights occurs for two reasons: (1) An origin location for a CG flash was determined only if its associated LMA sources could be clearly isolated and extracted from the surrounding lightning activity (e.g., Figs. 2.34 and 2.35). (2) As in Lang et al. (2004b), there were several instances in which multiple CG strike points

originated from the same LMA-mapped parent flash (e.g., Fig. 3.19). Each of the strike points is considered a separate CG flash by the NLDN as well as in the CG flash rate time series of this study. However, since these multiple strike points originated from the same flash, they were assumed to share a common origin for the purposes of computing the mean origin height. Figure 3.8a shows an altitude histogram of these CG origin heights, for both positive and negative polarity CG flashes. The CG origin heights are also overlaid onto the time-height contours of Fig. 3.4b. The +CG origin heights were generally constrained between 5 and 9 km MSL with a mean origin altitude of 6.8 km (temperature range of 0° to −20° C, centered near −10° C). This height range was clearly in the low-to-mid-level of the storm, not the anvil region. In contrast, all but one of the −CGs originated from upper-levels of the storm, i.e., above where the +CGs originated. Though there is some scatter, during any given volume scan time interval the mean of the +CG origin heights was between 6 and 7.5 km, which is consistent with the region of dense positive charge implied by the LMA density contours in Fig. 3.4b. Both hail and graupel were highly concentrated in the inferred +CG origin height region, but there were no +CG flashes in the absence of radar-inferred hail.

As shown in Fig. 3.8b, the difference between CG mean origin height and height of the very first source of each CG flash was generally small. This difference histogram also shows the tendency for the height difference to be positive for +CG flashes and negative for −CG flashes (though the sample size of −CG flashes is very small in this case). In other words, the mean origin height of +CG (−CG) flashes tends to be above (below) the height of the very first source of the flash. This is consistent with the assumed configuration of the charge regions involved, the physics of the breakdown process, and, in particular, the way the LMA operates. The first ten sources of a −CG flash typically have a downward trend because the LMA senses the initial negative leader as it initiates downward from negative charge toward positive charge and the ground below. The first ten sources of a +CG flash, on the other hand, typically have an upward trend as the LMA senses the initial negative leader as it initiates upward

from negative into positive charge. Hence, in the mean, the mean origin heights of −CG flashes are generally higher than the "true" origin heights, while the mean origin heights +CG flashes are actually lower than the "true" origin heights.

Finally, for completeness, Fig. 3.8c shows histograms of the peak current of the CG flashes. As suggested by Cummins et al. (1998), these peak currents (I) were computed from the NLDN signal strength (LLP) as

$$I = 0.185LLP \tag{3.1}$$

In their description of the performance of the upgraded NLDN, Cummins et al. (1998) noted a previously undetected population of +CGs with peak currents from 5–15 kA. They stated that "it is likely that not all of these events are CG discharges" and recommend that "the subset of small positive discharges with peak currents less than 10 kA be regarded as cloud discharges unless they are verified to be cloud-to-ground." As shown in Fig. 3.8c, all of the +CG flashes had peak currents in excess of 15 kA. The only +CG flashes in the 29 June 2000 storm with peak currents between 5–15 kA occurred during the volume scan beginning at 2252. The lightning mapping of these two +CG flashes (not shown) suggests that they were, in fact, intra-cloud flashes. They were thus removed from consideration.

3.2.2 Detailed observations of lightning and charge structure

To illustrate the evolution of precipitation and electrical structure in the storm, Figs. 3.9–3.11 show representative horizontal and vertical cross-sections of radar reflectivity and LMA density during selected volume scans, along with a composite schematic of the charge structure inferred from lightning mapping of many individual lightning flashes. The LMA density plots in these figures include only those LMA sources from the start time of the volume scan to five minutes after the start time of the volume scan. These LMA density plots are not exactly cross-sections per se. Rather, the LMA are gridded into the same Cartesian space as the radar data by summing the number of sources within each of the Cartesian grid boxes. Each grid

box has dimensions of $0.5 \times 0.5 \times 0.5$ km. The quantity actually plotted at each grid point in Figs. 3.9–3.11 is the sum of all the LMA sources within a swath centered on the cross-section plane. For example, in the horizontal cross-sections at (z=7 km), the LMA density at each grid point (x,y) is the sum of all the LMA sources from z=4.5 to 9.5 km (i.e., $z = 7 \pm 2.5$ km) at each (x,y). For the vertical cross-sections, the LMA density at each grid point (x,z) is the sum of all the LMA sources within $y = \pm$ 5 km of the vertical cross-section plane at each (x,z). The LMA density plots give an objective depiction of the electrically active regions of the storm, while the charge composites provide a (somewhat more subjective) interpretation of these regions. We must stress that during the later severe phases of this storm, the lightning was very frequent and the LMA-inferred charge structure was not always clear. Thus, the charge composites are likely incomplete and oversimplified, but they do capture the gross charge structure revealed by the majority of the lightning flashes.

Figs. 3.12 and 3.13 illustrate the evolution of the lightning and charge structure of this storm in a somewhat more objective way. Here, altitude histograms of total LMA sources (black) and flash origin heights (red and blue) are plotted for successive 15 minute intervals. As described in Section 2.2.3, the flash origin heights are objectively partitioned, based on their initial velocity, into flashes that initiated upward (red curves in Figs. 3.12 and 3.13) and downward (blue curves). Frequent references to these histograms will be made in the following sections.

EARLY DEVELOPMENT PHASE (2130–2213)

Over the first twenty minutes of the observation period (2130 to 2150), the storm consisted of a disorganized line of convective cells aligned roughly southwest-northeast near the Colorado-Kansas-Nebraska border. New cells developed to the west with precipitation forming and descending to the east of the updraft. The westernmost of these cells developed into the storm of this study. The lightning was relatively infrequent (1–2 flashes min^{-1}), and consisted *entirely* of IC flashes between an inferred negative charge region at an altitude of 7–8 km (−10<T<−15°C) and a lower positive

charge region at 4–5 km (T≈0°C). This arrangement of charge is corroborated by the histograms of LMA sources and flash origin heights in the top-left panel of Fig. 3.12. Here the one maximum in LMA sources (black curve) near 5 km MSL corresponds to the positive charge region, and the flash origin heights (blue curve) show that all of the flashes initiated downward from 6-7 km MSL into the positive charge region below. These IC flashes tended to originate in the elevated precipitation east of the updraft; they then propagated down through the inferred lower positive charge region associated with descending precipitation. The three flashes that occurred from 2140–2144 are representative of this early lightning activity. Their LMA sources are overlaid onto a vertical radar cross-section in Fig. 3.14. This arrangement of charge could be described as an inverted dipole; however, the two charge regions involved in this early lightning activity might correspond to the lowest two charge regions of the tripole model and Stolzenburg et al. (1998a–c) observations. This early charge structure departed from the tripole model in that there was no lightning activity which indicated the presence of a positive charge above the negative charge.

During the radar volume scan beginning at 2144 UTC, the storm developed a strong, broad, rotating updraft on its northwestern edge, with speeds exceeding 20 ms^{-1} at an altitude of 10 km. Prior to this, updrafts did not exceed 6 ms^{-1}. In apparent response to this updraft burst, the storm developed a region of elevated reflectivity aloft and, by 2154, began producing frequent (10s min^{-1}) upper-level inverted IC flashes between a negative charge region at an altitude near 11 km and a positive charge region at 9–10 km. This rapid transition to frequent upper-level flashing is evident in the time series and contours of Figs. 3.3c and 3.4b as well as in comparison of the top-left and top-middle panels of Fig. 3.12. In addition to these upper-level flashes, the storm continued to produce relatively infrequent IC flashes between the mid-level negative and lower positive regions, with the lightning sometimes extending to altitudes as low as 3 km. There were also infrequent compact discharges at even higher altitudes (from 12 km upward to 13 km). These extremely elevated discharges tended to be well downwind of the updraft in the low reflectivity

anvil region of the storm and may have been indicative of a positive screening layer on the upper cloud boundary. Fig. 3.15 shows lightning mapping of five successive flashes (from 2200:46 to 2200:59) that spanned these five inferred charge regions overlaid onto a radar vertical cross-section at 2159. As illustrated by the charge composite and vertical cross-section of LMA source density in Fig. 3.9, the lightning flashes from 2155 to 2210 were all consistent with this basic 5-layer structure. Most of the flashes occurred in the upper inverted dipole, leading to a pronounced peak in LMA source density in the upper positive charge, with a secondary peak corresponding to the positive charge of the lower dipole (see also the top-middle panel of Fig. 3.12). The lightning flashes in the upper inverted dipole remained distinct from those in the lower inverted dipole, with no flashes connecting the two regions, as if the upper-level charge structure developed independently. The most important point to note, however, is that the upper-level lightning activity formed as a result of invigorated updraft and revealed an inverted dipole charge structure. This storm maintained an inverted dipole within the strongest updraft throughout the observation period.

Another feature of the early lightning activity warrants some discussion. The presence of a lower charge region is thought to provide the bias for discharges to propagate to ground as CGs (e.g., Williams et al., 1989b; Williams, 2001; Mansell et al., 2002; Marshall and Stolzenburg, 2002). That is, –CGs (+CGs) are more energetically favorable if there is lower positive (negative) charge which could initiate a downward discharge from a larger negative (positive) charge above it. During the first hour of lightning activity, there were no CG flashes of either polarity even though the LMA data strongly suggest the presence of a lower positive charge. Possible explanations for this lack of CGs include: (1) The magnitudes of the negative and lower positive were significantly different from those of the more commonly observed tripole, such that IC flashes between these regions were more energetically favorable than –CG flashes (e.g., Marshall and Stolzenburg, 2002). That is, the negative (lower positive) charge may have been weaker (stronger) than in the common tripole. (2) There was no apparent negative charge region below the lower positive to provoke a

+CG. There were no in situ electric field measurements taken in the storm during this early lightning period so we cannot determine whether the lower positive charge was larger than usual, nor can we determine if there was negative charge below the positive charge. The LMA did not indicate the presence of any such lower negative charge region.

ORDINARY (NON-SEVERE) MATURE PHASE (2213–2325)

From 2159 to 2213, as the updrafts waned and the lofted precipitation grew and descended, the lightning continued to show 5-layer charge structure (e.g., Fig. 2.28), though more compressed, with the upper-level lightning activity descending along with the precipitation. There were also more "normal" flashes with initial breakdown proceeding upward from the negative charge of the lower inverted dipole into the descending upper positive (e.g., Fig. 2.30). However, inverted flashes in the upper-levels still dominated the lightning activity. By 2220, the lightning activity was much more condensed at mid-levels without as much clear stratification of the charge regions (see bottom right panels of Fig. 3.9). There was still some semblance of a stacked inverted dipole structure, though the lower positive charge was more restricted near the precipitation core, and the next two charge layers above (negative over positive) extended further southeast and sloped downward.

As described in Part I, there were two periods of hail growth and fallout from 2213 to 2325. The first hail growth period followed the updraft surge beginning at 2144 giving a hail maximum at 2220–2227, and the second followed a larger updraft surge that began at 2220 and persisted for 30 minutes (Fig. 3.3). In apparent response to the second of these updraft bursts, graupel echo volumes extended to higher altitudes and resurgence of lightning at upper-levels began around 2227 (Fig. 3.4). By 2239 the TFR reached a peak of nearly 100 min^{-1} (Fig. 3.3c). As described in Part I, a bounded weak echo region (BWER) had developed in association with the strong updraft on the western edge of the storm. The lightning activity mirrored the reflectivity structure of this BWER, with almost no lightning activity within the BWER and

very active lightning in the strong lofted echo above and to the south of the BWER (left column of Fig. 3.10). The lightning was very frequent and somewhat amorphous, making charge structure determination difficult. However, the vast majority of the flashes near and within the echo vault surrounding the BWER were inverted IC flashes, leading to the inference of closely stacked inverted dipoles near and above the main updraft (bottom-left panel of Fig. 3.10). The positive charge regions of these two inferred dipoles correspond to the two prominent peaks of LMA sources in the vertical cross-section in left column of Fig. 3.10. These two maxima of LMA sources also stand out clearly in the altitude histograms of Fig. 3.12 as do the large number of downward flashes initiating from the lower end of the negative charge regions of the two stacked inverted dipoles. As illustrated by the charge composite (lower-left panel of Fig. 3.10), the charge regions of the upper-inverted dipole extended downwind with additional mid-level positive charge east of the precipitation core. Most notably, there were a few normal IC flashes between mid-to-low-level negative charge and positive charge above (e.g., Fig. 3.16). This mid-to-low-level negative charge region extended from the downwind side of the precipitation core to the southeast. The first two +CG flashes of the storm originated from the same region as these normal ICs (though on the northwest edge of this region), and struck ground just southeast of the surface hail swath (Fig. 3.17). Prior to their return strokes, the structure of these two +CG flashes was very similar to the normal IC flashes. That is, the initial breakdown in both the normal ICs and the +CG flashes progressed upward, defining positive charge at mid-to-upper-levels, with later breakdown below the initiation point through presumed negative charge below. In the case of these and other +CG flashes, this lower breakdown (green points in Fig. 3.17) may be more indicative of the leaders to ground and not necessarily of lower negative charge. However, the normal IC flashes in this region suggest that this lower negative charge was present. Additionally, the +CG flashes also appeared to tap some positive charge further west, within the precipitation core and echo vaults surrounding the updraft.

The chain of events leading to the production of these first two +CG flashes was

roughly as follows. An inverted dipole charge structure consistently formed above and within the strong updraft, with low-to-mid-level negative charge further downwind. The positive charge of the inverted dipole was apparently carried by precipitation growing within the updraft. As this precipitation grew further and descended on the downwind side of the updraft, it carried the positive charge with it. The descent of this positive charge is manifested in the time-height contours of LMA sources from 2200 to 2240 in Fig. 3.4b and also in the corresponding sequence of altitude histograms in Fig. 3.12. During this descent, the lower negative charge region persisted further downwind. It's not clear how this lower negative charge formed. The initial breakdown of the first two +CG flashes progressed upward from this lower negative into the descending positive charge region. The ensuing breakdown continued into the descending mass of ice and positive charge, but also tapped positive charge at higher altitudes further downwind (e.g., Fig. 3.17). The positive leaders of these +CG flashes went to ground almost directly beneath the initiation locations. The storm did not produce any more CG flashes of either polarity[3] until the onset of the severe right phase at 2325, though the chain of events leading to the next burst of +CG flashes was very similar.

From 2246 to 2252, hail continued to grow and descend giving a deep hail shaft and relative maximum in hail echo at 2246 (Fig. 3.4a). TFR decreased to 50 min^{-1}. The lightning tended to avoid the >55 dBZ hail shaft almost entirely during this time (Fig. 3.18). By 2259, the hail had almost all fallen out, and the bulk of the lightning activity was again nearer the precipitation core, but was very concentrated above the collapsing hail shaft (middle column of Fig. 3.10). Overall, the LMA indicated an inverted tripole charge structure with frequent IC flashes from both upper and mid-level negative charge into an inferred positive charge region centered at 8–10 km altitude (bottom-middle panel of Fig. 3.10. See also the middle-right and

[3]There were two flashes around 2252 that were identified as +CGs by the NLDN, but, as described earlier, they had very low peak current (<15 kA) and the lightning mapping suggested that they did not contact ground.

bottom-left panels of Fig. 3.12.). Though the lower negative charge was present, this charge structure did not produce +CG flashes. During the brief decline in updraft and hail volumes preceding the onset of the severe right mature phase at 2325, the storm maintained the gross inverted tripole structure shown in the middle column of Fig. 3.10. However, the concentrated region of LMA sources descended and grew deeper with time (Fig. 3.4), with inferred positive charge extending deeper on the upwind (west) side of the precipitation core, and negative charge on the downwind (east) side (see bottom-right panels of Fig. 3.10).

In comparison with the charge structure during +CG flashes (e.g., left and right columns of Fig. 3.10 with the charge structure in the absence of +CG flashes (middle column of Fig. 3.10), the most obvious difference is the height of concentrated LMA sources and inferred positive charge. During the +CG flashes, there was very active lightning in an inferred positive charge region at mid-levels (6-8 km MSL). In the absence of +CG flashes, this mid-level positive was absent or further elevated. Perhaps the elevation of the charge regions allowed for the efficient neutralization of the charge regions via IC flashes thus precluding +CG flashes. Hence, lower negative charge appeared to be a necessary but not sufficient condition for +CG flashes.

SEVERE RIGHT MATURE PHASE (2325–0036)

The storm and charge structure at the beginning of the severe right mature phase (2325) was in many way similar to that at 2239. A strong, broad updraft on the western flank was coincident with an echo vault and mid-level BWER (see top-right panels of Fig. 3.10). As discussed in Part I, the flow diverged around the updraft, particularly to the south, leading to a reflectivity maximum southeast of the main updraft. Again, the lightning density mirrored the reflectivity structure in the mid-to-upper-levels, with a pronounced lightning hole coincident with the BWER, and active lightning above and downwind (especially southeast) of the BWER. As with 2239, the TFR increased dramatically (to nearly 150 min^{-1}), and the storm began producing frequent +CG flashes.

Though much of the lightning within the echo vault above the updraft consisted of compact flashes lacking clear vertical charge structure, there were still many flashes indicating an inverted dipole structure here and in the upper-levels further downwind (see bottom-right panel of Fig. 3.10). In addition, relatively infrequent "normal" IC flashes continued to indicate the presence of lower negative charge just downwind of the precipitation core. The seven +CG flashes during the 2325 volume scan struck ground in two clusters. Each cluster appeared to be associated with the separate diverging flows around the updraft, with one cluster of three +CG flashes along the northeast path, and the other cluster of four +CG flashes along the more dominant southeast path. The initial breakdown of all seven +CG flashes proceeded upward from 6–7 km into a distinct mid-level maximum of LMA density just downwind of the hail shaft (see second from bottom panel in the right column of Fig. 3.10). Following their return strokes, most of them tapped additional mid-level positive charge extending south and east, but rarely extended back westward into the more intense precipitation. Leading up to the peaks in hail echo volume and +CG flash rate at 2343–2351, the majority of +CG flashes continued to cluster (in both origin and strike location) on the downwind side of the hail shaft along these divergent flow paths. Figs. 3.19 and 3.20 show one particularly clear example of these +CG flashes.

By 2351, the BWER had filled in with large hydrometeors, and the lightning activity had wrapped around it, leading to a pronounced peak in LMA density on the southwestern side of the updraft (see left column of Fig. 3.11). Flashes in this western portion of the hail shaft generally indicated an inverted dipole with a deep positive charge region. The two +CG flashes that struck south of the updraft tapped this positive charge region. The remainder of the +CG flashes also showed limited propagation into inferred positive charge in the lower portion of the hail shaft, but the majority of the breakdown continued to be through mid-level positive charge from the downwind edge of the hail and extending eastward.

From 0000 to 0030 UTC, the storm continued to produce frequent inverted flashes in the upper-levels. The lightning was essentially continuous during this time, with

no apparent break cessation between one flash and the next. Hence, we did not attempt to diagnose the detailed charge structure from the lightning mapping. However, Lang et al. (2004a) and MacGorman et al. (2004) report on the charge structure inferred from an instrumented balloon flown through the storm during this time. Within the updraft, they found positive charge from 8–10 km, with alternating negative/positive/negative above, with the uppermost negative charge at 12–13 km MSL. Along the descent, they again found positive charge from 9.5–12 km with four additional regions of charge below, alternating in polarity with positive charge at 5.8–8 km and below 4 km. They posited that +CG flashes could involve any of the positive charge regions found in the downward sounding. From the lightning mapping, we found that the majority of the +CG flashes continued to cluster near and downwind of the core, with initial breakdown progressing upward from inferred negative charge at 5–7 km into positive charge at 7–9 km, which *roughly* corresponds to the mid-level charge structure inferred from the downward balloon sounding. However, a half dozen or so +CG flashes initiated to the south-southeast of the hail, with little discernible structure other than extensive low-level breakdown back westward into the hail core (e.g., Fig. 3.21). This extreme lower-level charge may correspond with the lowest positive charge region of the balloon sounding. Comparison with the balloon sounding is difficult, however, because the charge structure varies greatly in the horizontal while the balloon measures only along its flight path.

During the radar volume scan at 0030, the +CG flash rate reached a relative maximum and the +CG strikes clustered along a roughly north-south line 5–15 km east of the elongated hail shaft (middle column of Fig. 3.11). Exterior to the updraft and hail core, the lightning-mapped structure of the flashes was relatively consistent and revealed a basic inverted tripole charge structure. Keeping with the recurring theme of this storm, the lightning mapping of most of the +CG flashes showed the initial inferred negative breakdown progressing upward into the eastern, downward-sloping positive charge of this inverted tripole. However, unlike during previous peaks in +CG flash rate, both the strike points and continued propagation of the +CGs

during 0030 were markedly further downwind of the descending ice mass in the hail core. The one –CG flash during this time, however, initiated near the top of the hail core and descended through it (and presumably through positive charge). Figure 3.22 shows the lightning mapping of this –CG flash along with a representative +CG flash further downwind. There were a few other instances like this of –CG flashes initiating near the top of the hail shaft and propagating through it, while the +CG flashes clustered further downwind. Perhaps the hail core contained relatively low concentration of positive charge during these times, such that the breakdown from negative charge above was able to propagate through it and, instead of halting within the lower positive to make an IC flash, continued on to ground.

DECLINING PHASE (0036–0115)

As the updraft, graupel, and hail echo volumes steadily declined during this declining phase (Fig. 3.3), the bulk of the lightning activity and initiation height of +CG flashes slowly descended (Fig. 3.4b). During the last volume scan of the observation period (0115), the +CG flash rate reached its absolute maximum, and all but four of the 23 +CG flashes from 0115–0120 struck ground in a very tight cluster nearly coincident with the hail swath, beneath a very dense concentration of LMA sources (right column of Fig. 3.11). The +CG flashes points were so clustered that it is difficult to resolve the individual strike points or to discern the underlying storm structure. In contrast to earlier times, almost all of these +CG flashes tapped the inferred positive charge low down in the hail shaft (e.g., Fig. 3.23), though some also continued to tap into mid-level positive charge further east. Of the two –CGs during this time, one struck in the hail shaft and one northeast of it. The former's strike point is buried within the clustered +CG strike points in the right column of Fig. 3.11). Both –CG flashes initiated near 9 km MSL, atop the LMA density maximum (see vertical cross-sections in right column of Fig. 3.11).

3.3 Summary and Discussion

The following points summarize the key observations from the 29 June supercell storm:

1. The LMA-inferred total flash rate (TFR) reached 200–300 min^{-1} during the severe phase, with an IC/CG ratio of at least 40 during the entire storm. Nearly 90% of the CG flashes delivered positive charge to ground, with a peak +CG flash rate of nearly 5 min^{-1}.

2. The TFR was well-correlated temporally with volumes of updraft (w>10 m s^{-1}) and inferred graupel echo. This latter correlation highlights the importance of charge-separating collisions within the mixed-phase region thought to be crucial in thunderstorm electrification. TFR was decidedly less correlated with hail echo volume, and the lightning sometimes avoided the >55dBZ hail shaft, suggesting that hail plays less of a role in charge separation.

3. As shown in the schematic of Fig. 3.24, the LMA-inferred charge structure of this storm varied greatly in the horizontal and with time. The first 20 minutes of lightning activity in this storm indicated a charge structure consisting solely of a mid-level negative charge region and lower positive charge region, with no indication of an upper-positive charge, which we termed an inverted dipole. Then, shortly after a strong surge in updraft, the storm rapidly developed upper-level charge regions which dominated the ensuing lightning activity. For a brief period of time (10–20 minutes) after this surge in updraft and lightning, the storm exhibited a distinct horizontally stratified, vertically layered charge structure which consisted of five charge regions, alternating in polarity, with positive nearest the ground. Over the remainder of the observation period, the lightning was very intense and the charge structure was less obvious. However, the storm consistently produced a dominant upper-level inverted dipole structure with each updraft surge, and "inverted" flashes between these two (negative

over positive) charge regions dominated the lightning activity throughout the storm (see, e.g., Fig. 3.13). This basic inverted dipole structure also extended downwind, but sloped downward along the direction of Doppler-inferred wind flow. Additional low-to-mid-level negative charge formed on the downwind side, beneath the sloping inverted dipole. The term "inverted tripole" is thus a reasonably accurate description of the later charge structure, but a simple *vertical* description would be a gross oversimplification of this storm.

4. The +CG flashes of this storm all originated at 5–9 km altitude and generally clustered on the downwind side of the main precipitation/hail core. For the vast majority of the +CG flashes, the initial lightning-mapped breakdown proceeded upward from lower negative charge (revealed by surrounding normal IC flashes) into positive charge within the hail shaft. Continued breakdown frequently tapped into the mid-level positive charge extending further downwind.

5. Four of the maxima in +CG flash rates (at 2239, 2325, 2343, and 0015) each seemed to follow this chain of events: Surges of strong, broad updraft led to inverted dipole charge structure aloft, with positive charging of graupel and/or hail within lofted echo. The downward descent of this ice mass carried the positive charge with it. The +CG flashes initiated between lower negative charge (described above) and the positive charge of the descending ice mass. Sustained +CG flashing throughout the severe right phase and the other +CG maximum at 0030 do not fit as simply into this chain of events, but updraft and hail production were strong throughout the severe right phase, which continued to produce an apparently vast reservoir of positive charge from 7–9 km altitude extending further downwind (as suggested by the contours of LMA density in Fig. 3.4). This chain of events is somewhat similar to that described in Williams et al., 1989b. However, Williams et al. describe these events within the context of normal tripole thunderstorms in which the descent of the ice mass leads to formation of the lower positive charge and onset of –CG flashes.

6. Finally, lightning "holes" were often coincident with bounded weak echo regions (BWERs), with active lightning in the lofted echo above the BWER. In their LMA observations of tornadic storms in Oklahoma, Krehbiel et al. (2000a) noted similar lightning "holes" in otherwise volume-filling lightning activity. Hence, there is little doubt that, like BWERs, such lightning holes are indicators of strong, broad updrafts and hence should have value as an indicator of severe weather.

Why was this storm inverted and how did it form such a deep, persistent region of positive charge? As suggested by Williams (2001) in his discussion of +CG-dominated storms, one possible explanation is that the strong, broad updraft suffered less entrainment which allowed supercooled liquid water (SLW) contents to reach near adiabatic values in the mixed-phase region, resulting in the transfer of positive charge to graupel and hail via the non-inductive ice-ice collision (NIC) mechanism (e.g., Takahashi, 1978; Saunders and Peck, 1998). The coincident hail and +CG production of this storm were both the products of strong broad updraft in a SLW-rich environment. Carey et al. (2003b) proposed a similar explanation for the +CG-dominance of the 1998 tornadic storm in Spencer, SD (though there was less evidence of associated hail formation in their study). The results of Lang and Rutledge (2002) offer further support. Their study included 11 storms which spanned a wide range of severity. In general, they found that –CG production decreased with increased updraft and hail production. The two storms of their study (one of which was the 29 June, 2000 storm) which had the strongest, broadest updrafts and greatest hail production, also produced predominantly +CG flashes.

Much as a lower positive charge appears to be a requirement for –CG flashes in "normal" tripole thunderstorms, the presence of a lower *negative* charge region appeared to be a requirement for the +CG flashes of this storm. Assuming the NIC mechanism was primarily responsible for the formation of the charge structure, how did this lower negative charge form, and how was it maintained? Our

observations cannot answer this question. However, simulations of this storm using a high-resolution model that includes explicit kinematics, microphysics, charging, and lightning, were able to reproduce many of the observed features described here (Kuhlman et al., 2003; Kuhlman, 2004). In these simulations, the lower negative charge formed due to collisional charging of graupel on the periphery of the updraft and was then reinforced by inductive processes.

Severe hailstorms are not always dominated by +CG flashes, so there is still something unique about the STEPS region that our observations have yet to reveal. Williams et al. (2004) suggest that large convective available potential energy combined with the elevated cloud base height (CBH) of storms in the STEPS region may be the answer. Such conditions would tend to inhibit warm rain processes, allowing for "superlative" (i.e, near-adiabatic) SLW in the resulting broad, strong updrafts. This could lead to rapid hail growth (if the conditions outlined in Part I are also met), and would also have implications for the lightning. The higher CBH (and attendant strong updraft) would elevate the charge-bearing hydrometeors, accelerate the electrification, and increase the TFR and IC/CG ratio. With little liquid water lost to coalescence below elevated CBH, the SLW may reach near-adiabatic values in the broad updrafts, resulting in a deeper region of positive charging of graupel and hail via the NIC mechanism.

Lightning mapping combined with multiple-Doppler polarimetric radar allowed for detailed observations of this +CG-dominated supercell storm. Though this study has answered some questions about the production of hail and +CG flashes, the results are based on only one storm. In subsequent chapters, the analysis techniques of this study are applied to other STEPS cases to gain more understanding of the electrification of the storms in this region.

	Total Storm Volume	Updraft Volume (> 10 ms^{-1})	Graupel Echo Volume	Hail Echo Volume	Total Flash Rate
Updraft	0.95				
Graupel	0.99	0.95 (0.23)			
Hail	0.84	0.89 (0.53) (0.57@–1)	0.85 (0.24) (0.73@–2)		
Total Flash Rate	0.90	0.95 (0.68)	0.95 (0.84)	0.90 (0.58) (0.75@+2)	
+CG Flash Rate	0.81	0.76 (–0.02) (0.31@–1)	0.81 (0.08) (0.58@–1)	0.72 (0.10) (0.67@+2)	0.74 (0.04) (0.52@–1)

Table 3.1: Correlation coefficients between radar and lightning time series for 29 June. Values outside of parentheses give correlations between zero-lag time series, prior to any trend removal. Values in parentheses give correlations between detrended time series at zero lag. Additional correlation coefficients and lag values are given if the best detrended correlation occurred at non-zero lag. Each lag increment corresponds to one 5–7 minute radar volume scan interval. For example, the best detrended correlations for the +CG flash rate time series occurred when the +CG flash rate lagged the updraft, graupel, and TFR time series by one scan interval, but led the hail time series by two scan intervals.

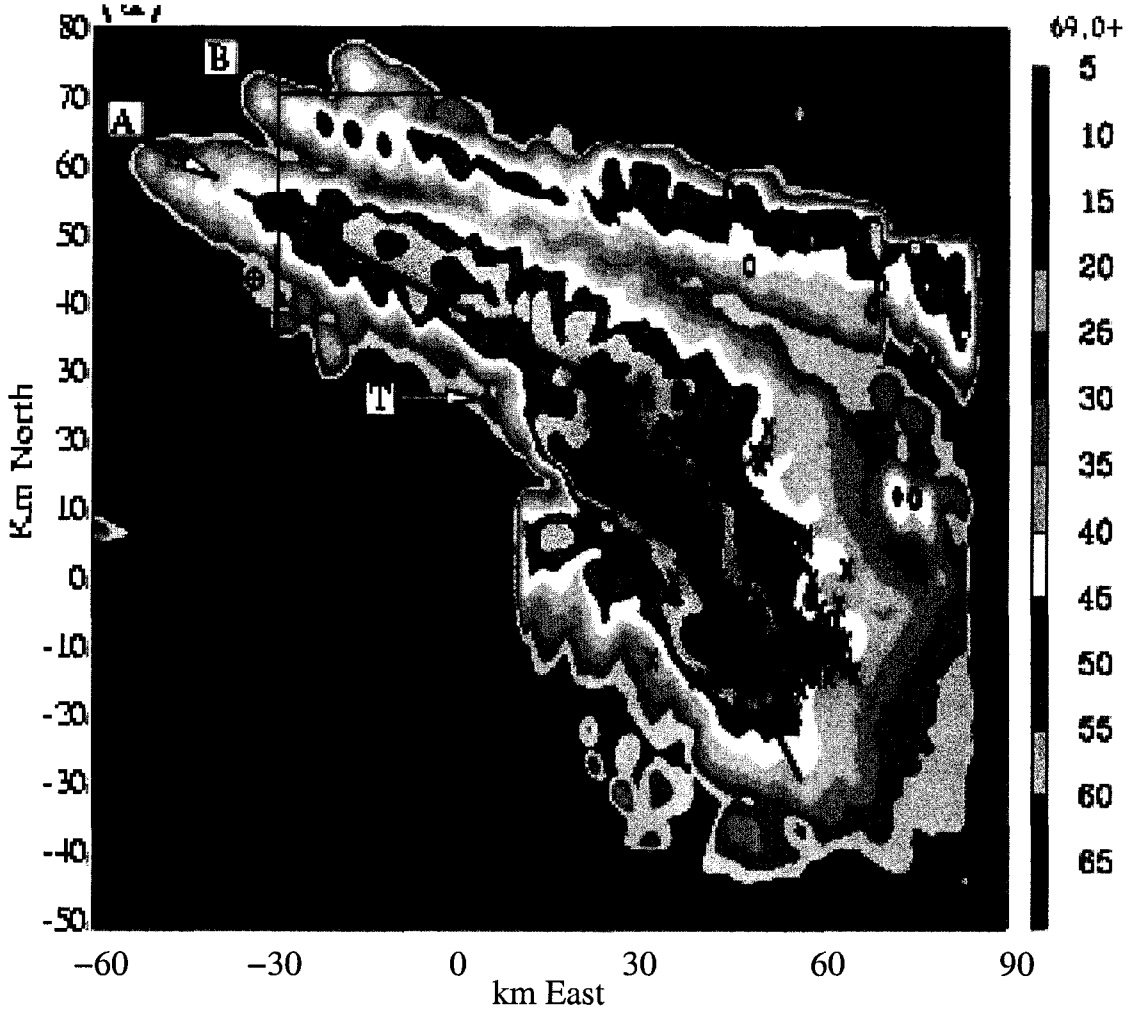

Figure 3.1: Swath of KGLD maximum reflectivity in each vertical column, from 2130 on 29 June to 0115 on 30 June. Axes are centered on the KGLD radar. Cell 'A' is the supercell. The thick black lines indicate the path of mean storm motion before and after the supercell made the right turn at 2325. The 'T' marks the time and location of the tornado, and 'X' and '0' symbols mark the NLDN locations of +CG and −CG flashes, respectively. The ⊕ symbols mark the locations of the three radars. Adapted from Tessendorf et al. (2004a).

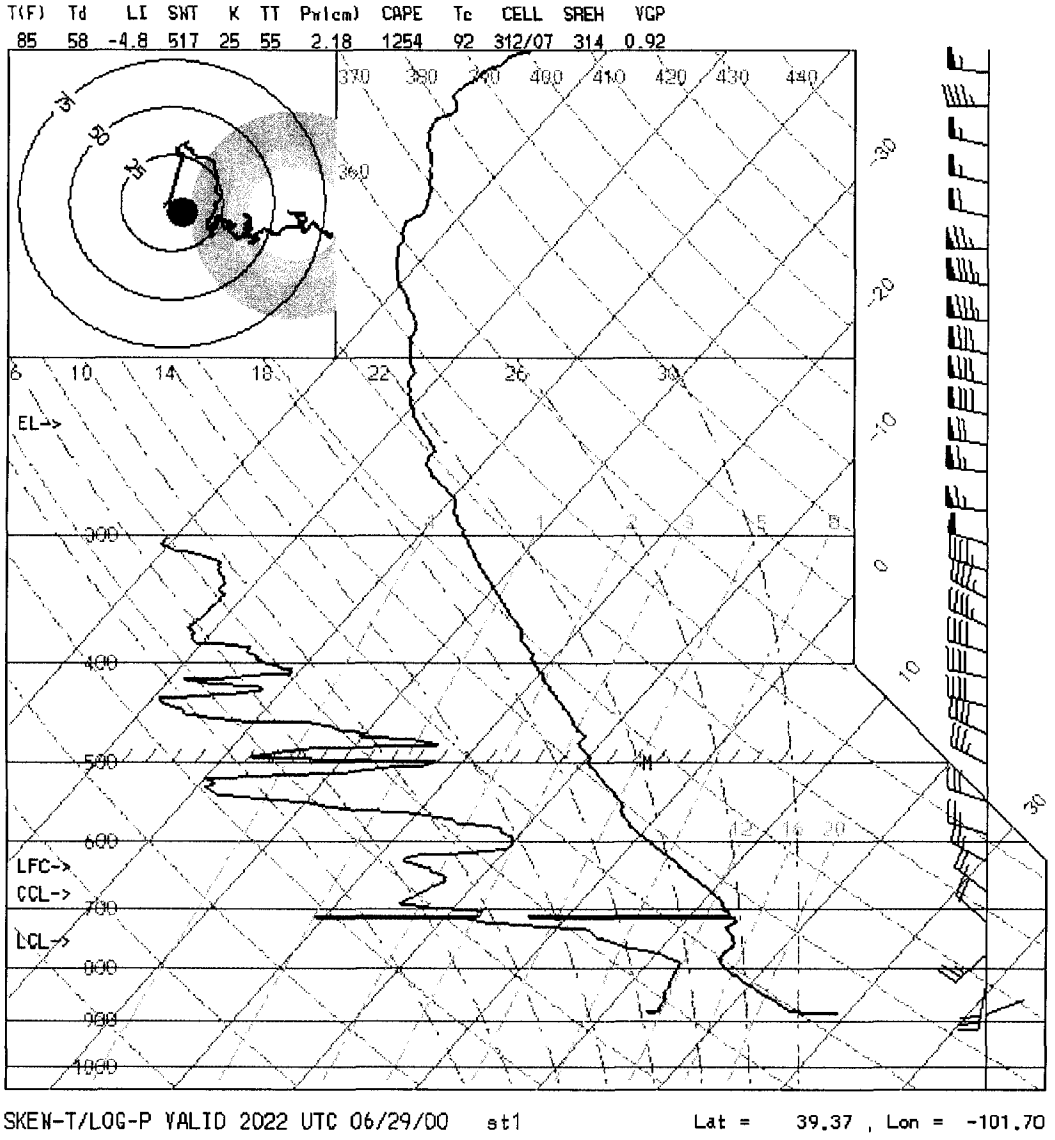

Figure 3.2: MGLASS sounding from 2022 UTC on 29 June. This sounding was launched from the KGLD radar which is the origin of the coordinates (0,0) in all the radar cross-section plots.

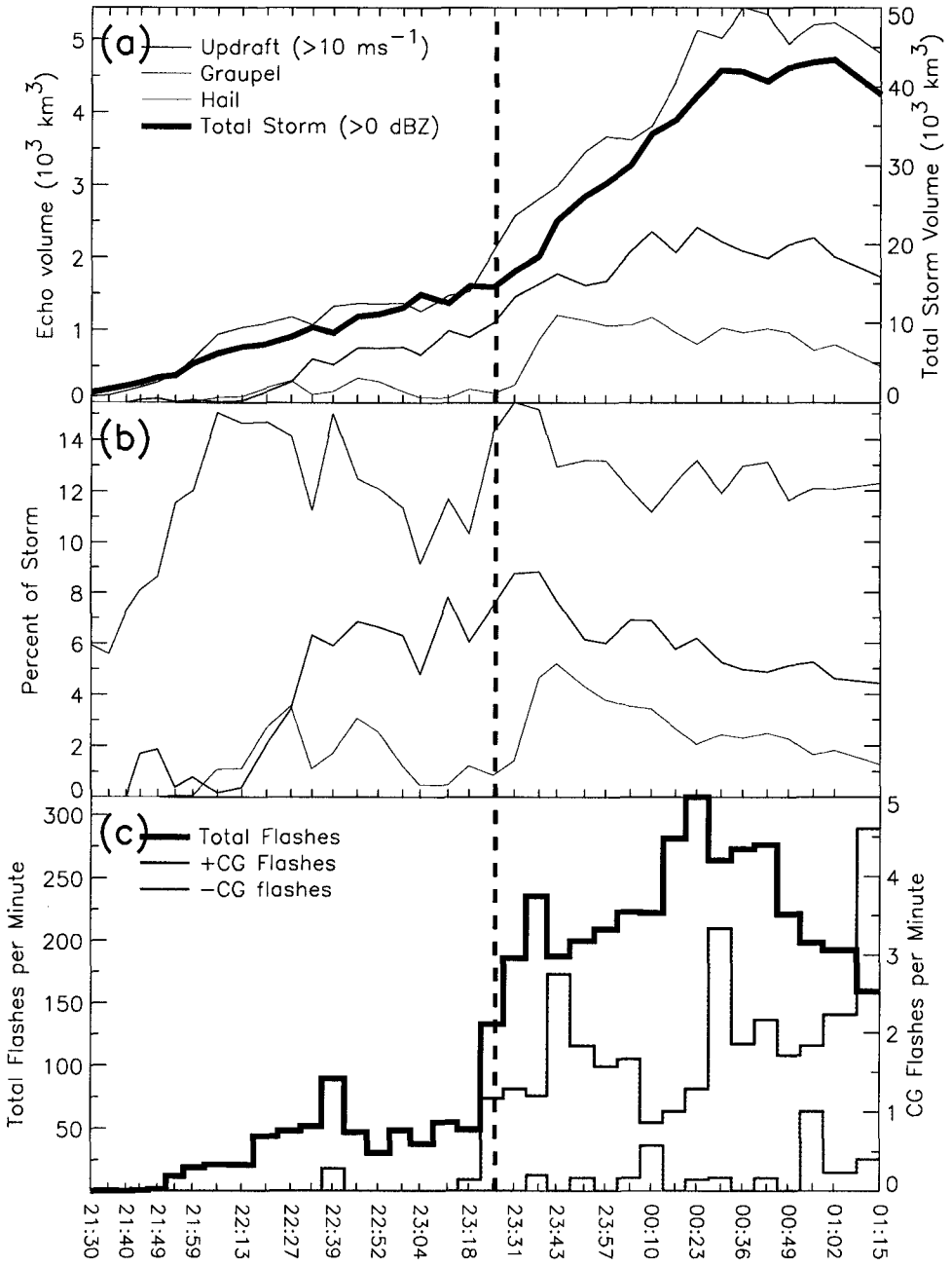

Figure 3.3: Time series summary of the 29 June 2000 supercell. (a) Radar-inferred echo volumes of storm updraft (w > 10 m s^{-1}), graupel and hail. Thick black line shows total storm volume (defined as volume of storm with radar reflectivity exceeding 0 dBZ). (b) As in (a), but with echo volumes plotted as percent of total storm volume. (c) Total and cloud-to-ground flash rates averaged over each radar volume scan time interval. Each tick mark on the time axis indicates the start time of a radar volume scan. Vertical dashed line indicates the time (2325) when the storm made a right turn.

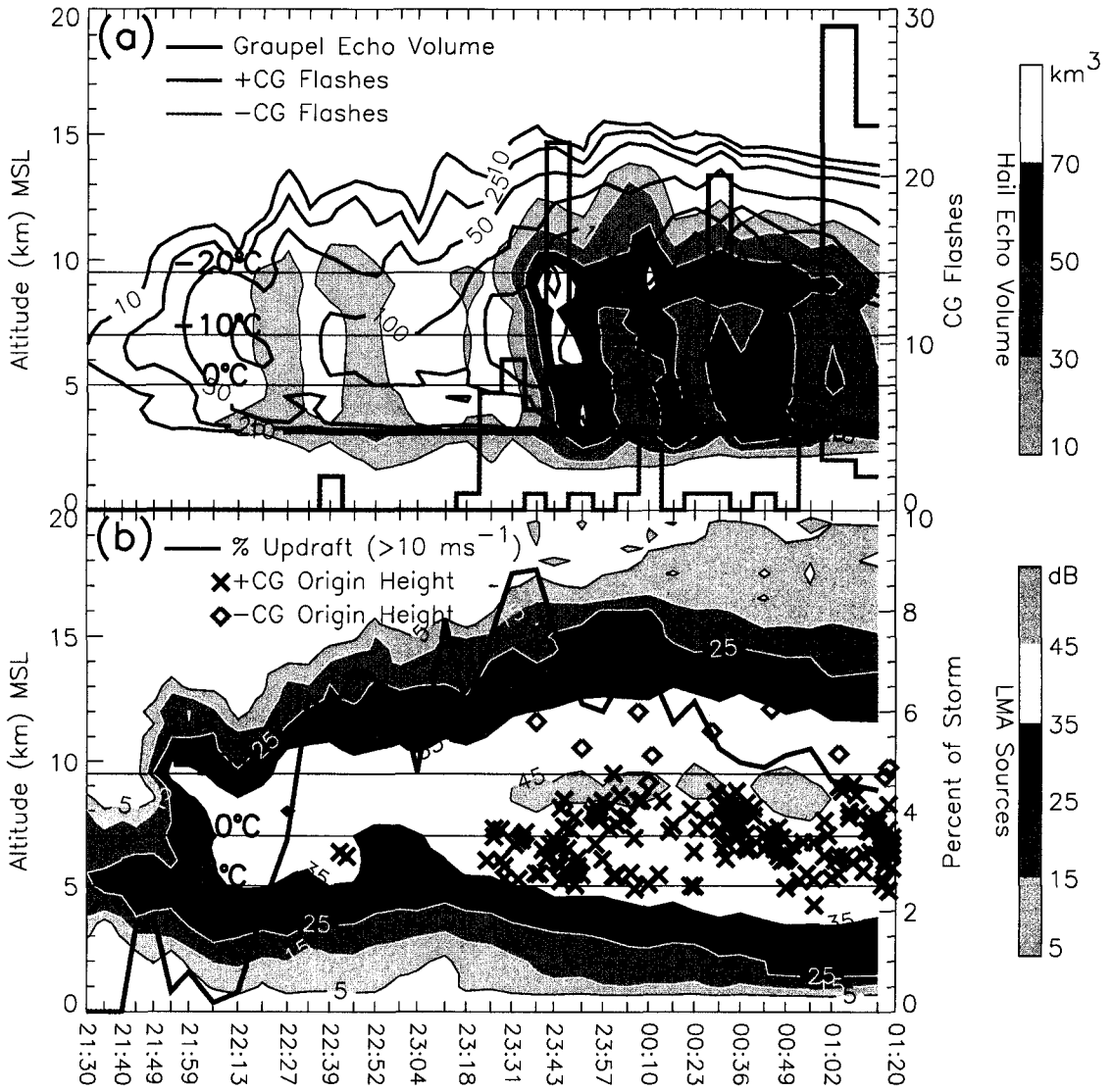

Figure 3.4: 29 June 2000 supercell. (a) Time height contours of hail (in gray scale) and graupel echo volumes (blue), in units of $km^3/0.5$ km, along with the total number of +CG (red) and −CG (green) flashes during each volume scan, i.e., the CG flashes are summed (not averaged) over the duration of each volume scan. (b) Time height contours of total LMA sources (in gray scale) normalized to a five-minute time interval. Contour values for the LMA sources are in decibel units (i.e., $10log_{10}$(# sources) per 0.5 km) due to huge variation in magnitude. The percent volume of updraft exceeding 10 m s^{-1} is overlaid onto (b) as a thick blue line. Origin altitudes of +CG and −CG flashes are overlaid onto (b) as red X's and green diamonds, respectively.

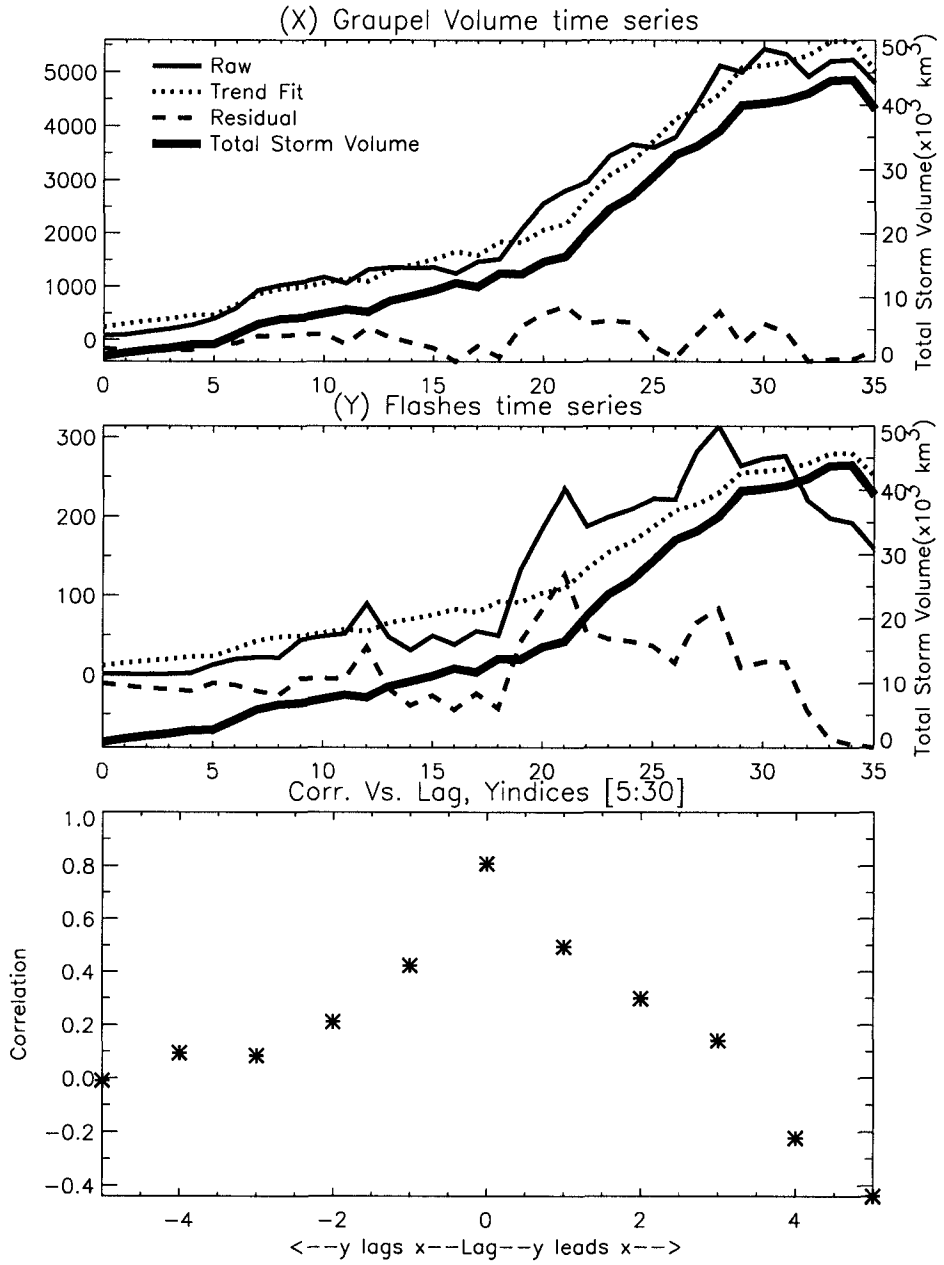

Figure 3.5: Graphical example of residual correlation analysis procedure. The upper two panels show the raw time series (in this case graupel echo volume and total flash rate (TFR)) along with their linear least-squares fits to the total storm volume and their resulting residual time series. Bottom panel shows the correlation coefficient between the two residual time series as a function of lag. Each lag increment corresponds to the time interval (5–7 minutes) between successive radar volume scans. See text for details.

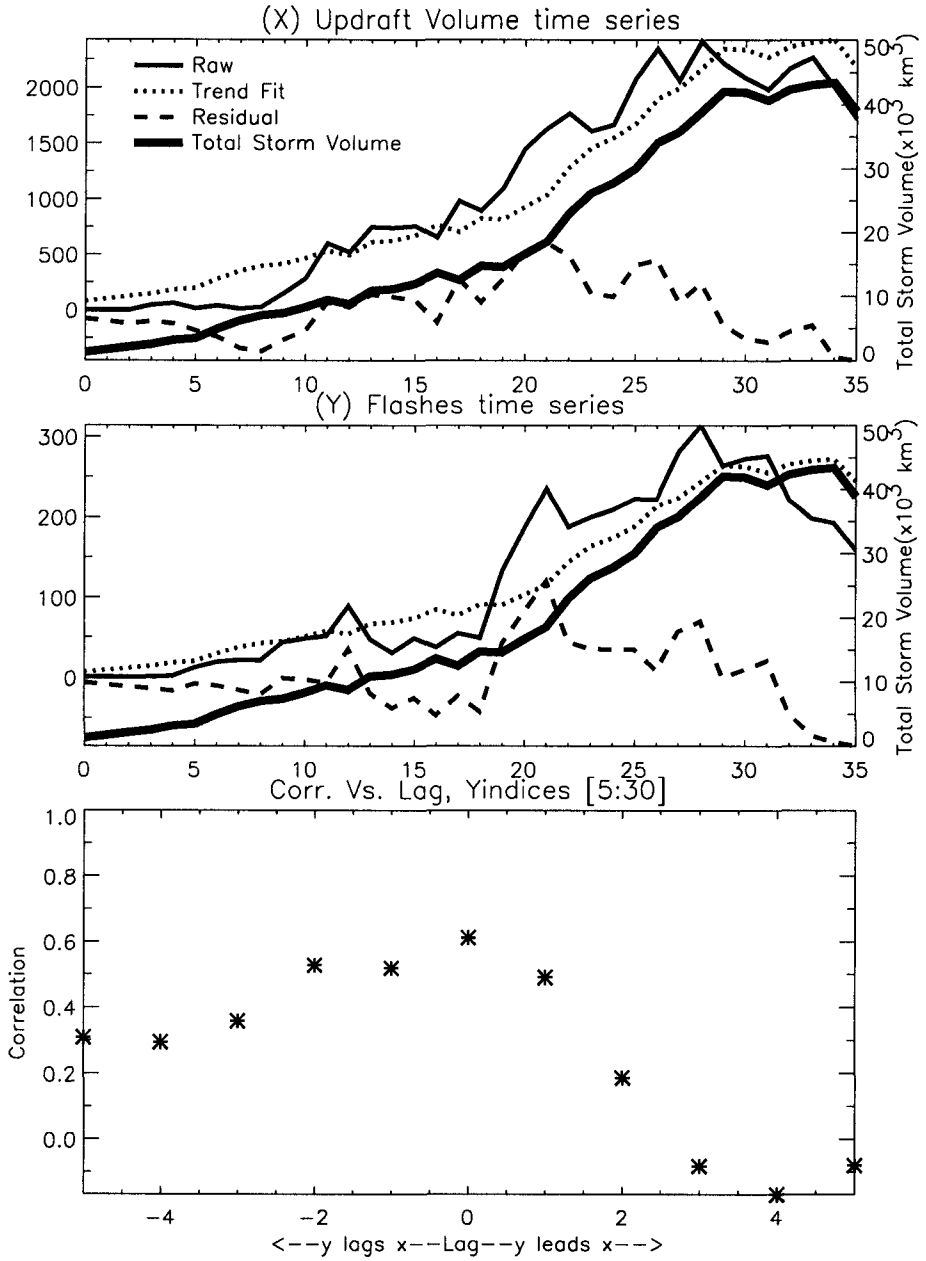

Figure 3.6: As in Fig. 3.5, but for UV_{10} and TFR.

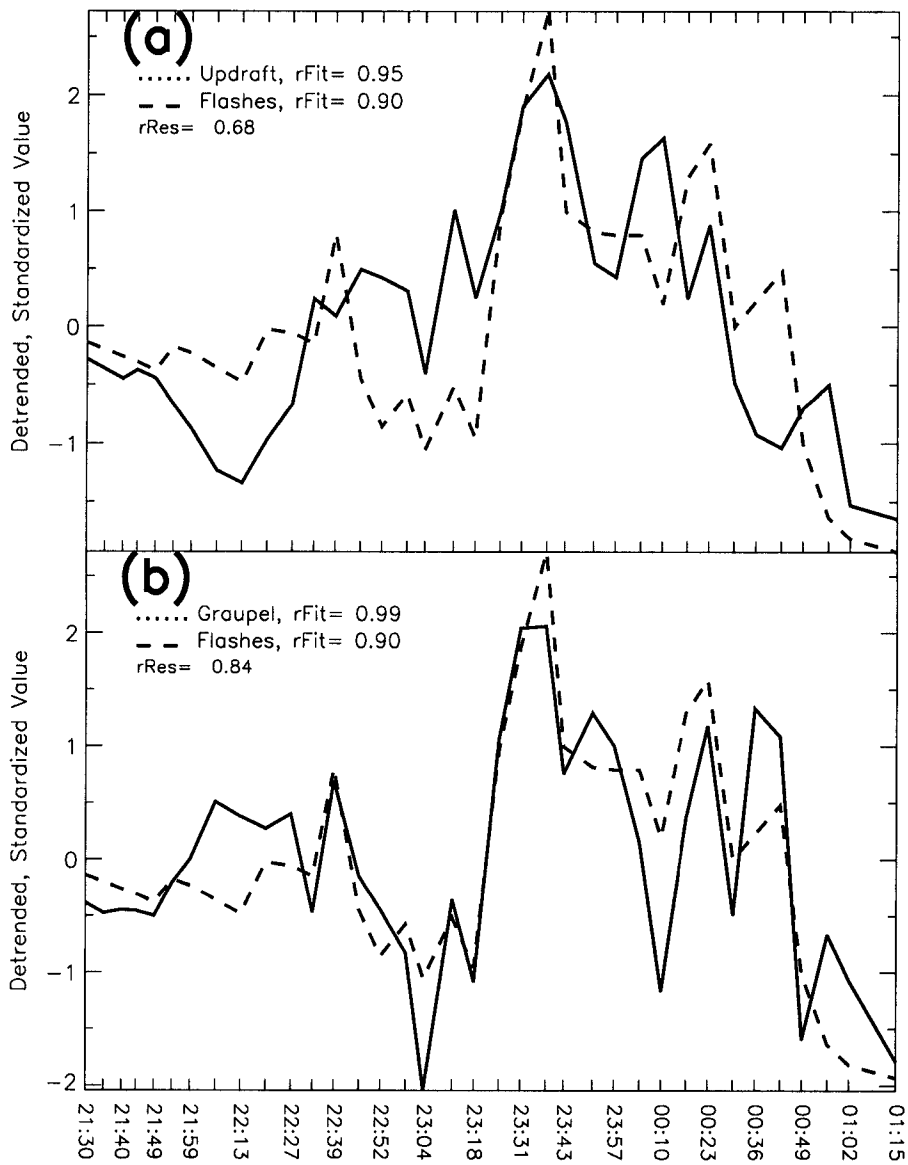

Figure 3.7: Residual time series of (a) storm updraft volume (w > 10 m s^{-1}) and TFR and (b) graupel echo volume aloft and TFR. The 'rFit' numbers give the correlation coefficient between the raw time series and the time series of total storm volume, while the 'rRes' numbers give the correlation coefficient between the two plotted residual time series. See text for details.

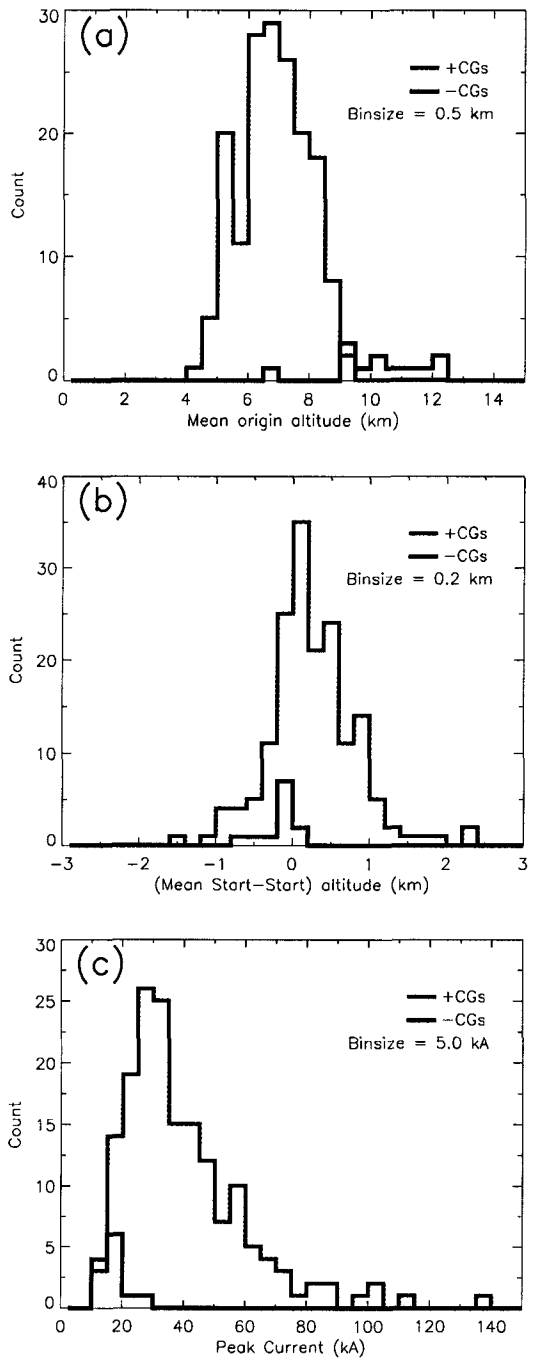

Figure 3.8: CG flash histograms for the 29 June 2000 supercell. (a) Mean LMA-inferred origin height, i.e., mean height of first ten LMA sources of each CG flash. (b) Difference between height of first LMA source and mean origin height. Positive values mean the first source was lower than the mean origin height. (c) Peak current computed from $I = 0.185LLP$, where LLP is the NLDN signal strength.

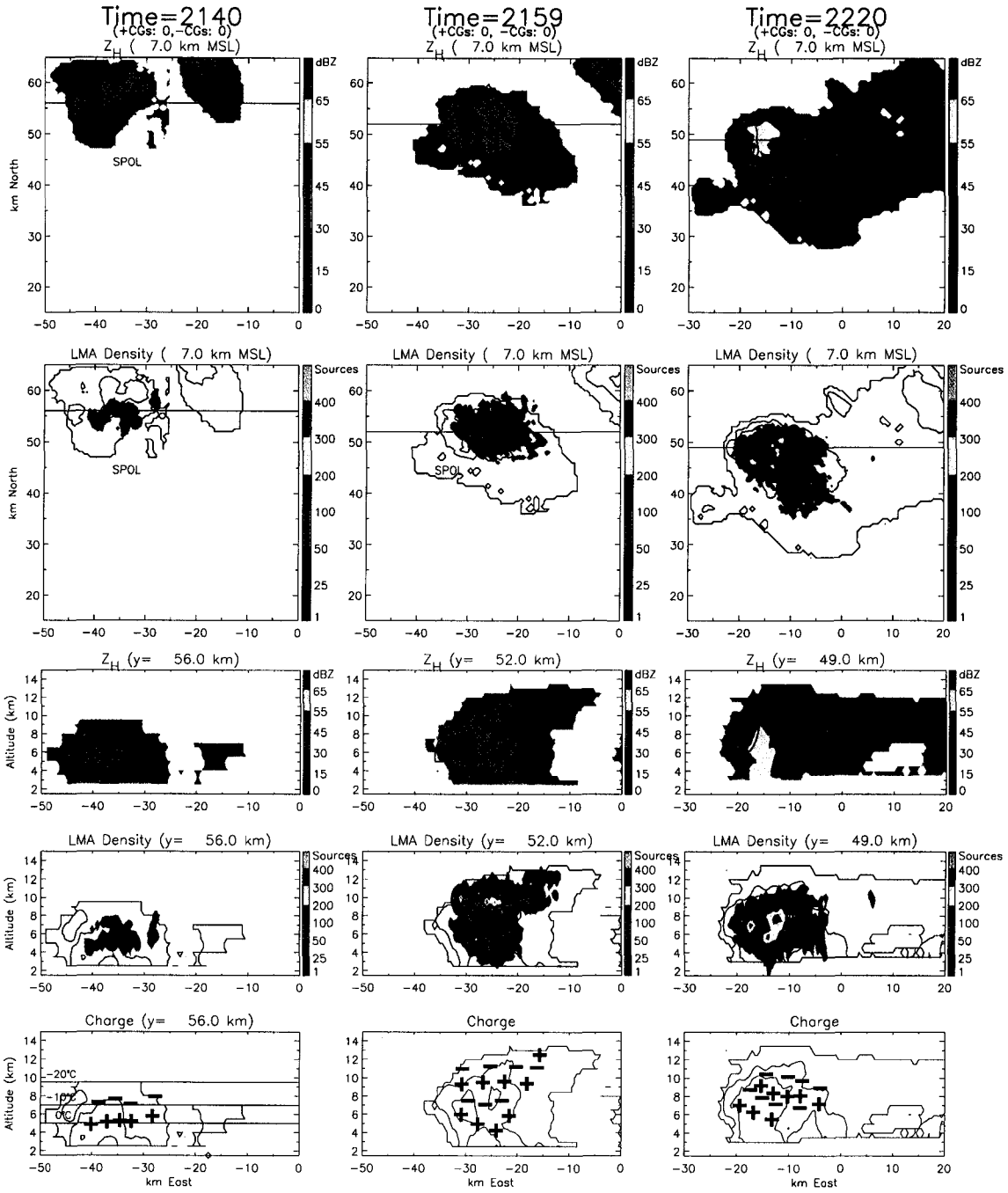

Figure 3.9: Representative cross-sections of the 29 June 2000 supercell, for volume scans beginning at 2140, 2159, and 2220. Each column corresponds to the same time. Top two panels show horizontal cross-sections of radar reflectivity (Z_H) and LMA source density at 7 km altitude. Next two panels show east-west vertical cross-sections of the same quantities along the lines indicated in the top two panels. LMA source density plots include only those sources within 2.5 (5.0) km of the horizontal (vertical) cross-section and include only those sources from the start time of the corresponding volume scan to five minutes after the start time. Bottom panels show composite schematics of the LMA-inferred charge structure at each time. Z_H panels have black updraft contours at 10, 20, 30 ms^{-1}, and the Z_H contours are repeated on the LMA and charge structure plots, with intervals of 0, 30, and 45 dBZ.

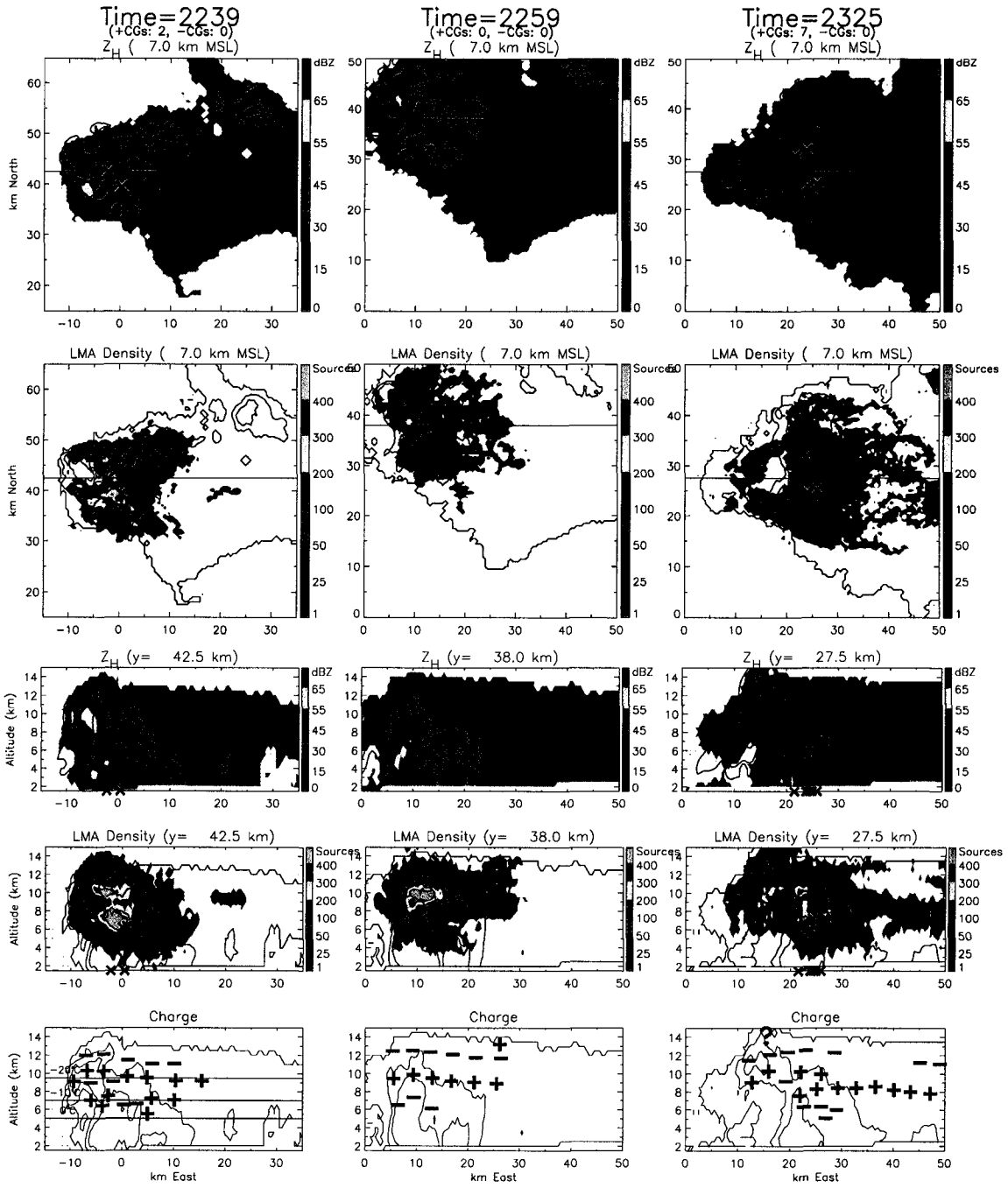

Figure 3.10: As in Fig. 3.9 but for volume scans beginning at 2239, 2259, and 2325. In addition, the X symbols on the horizontal cross-sections and along the bottom of the vertical cross-sections indicate the NLDN strike locations of +CG flashes. The X symbols at higher altitudes on the vertical cross-sections indicate the LMA-inferred origin locations of +CG flashes. Only those CGs that struck within 5 km of the cross-section plane are shown on the vertical cross-sections.

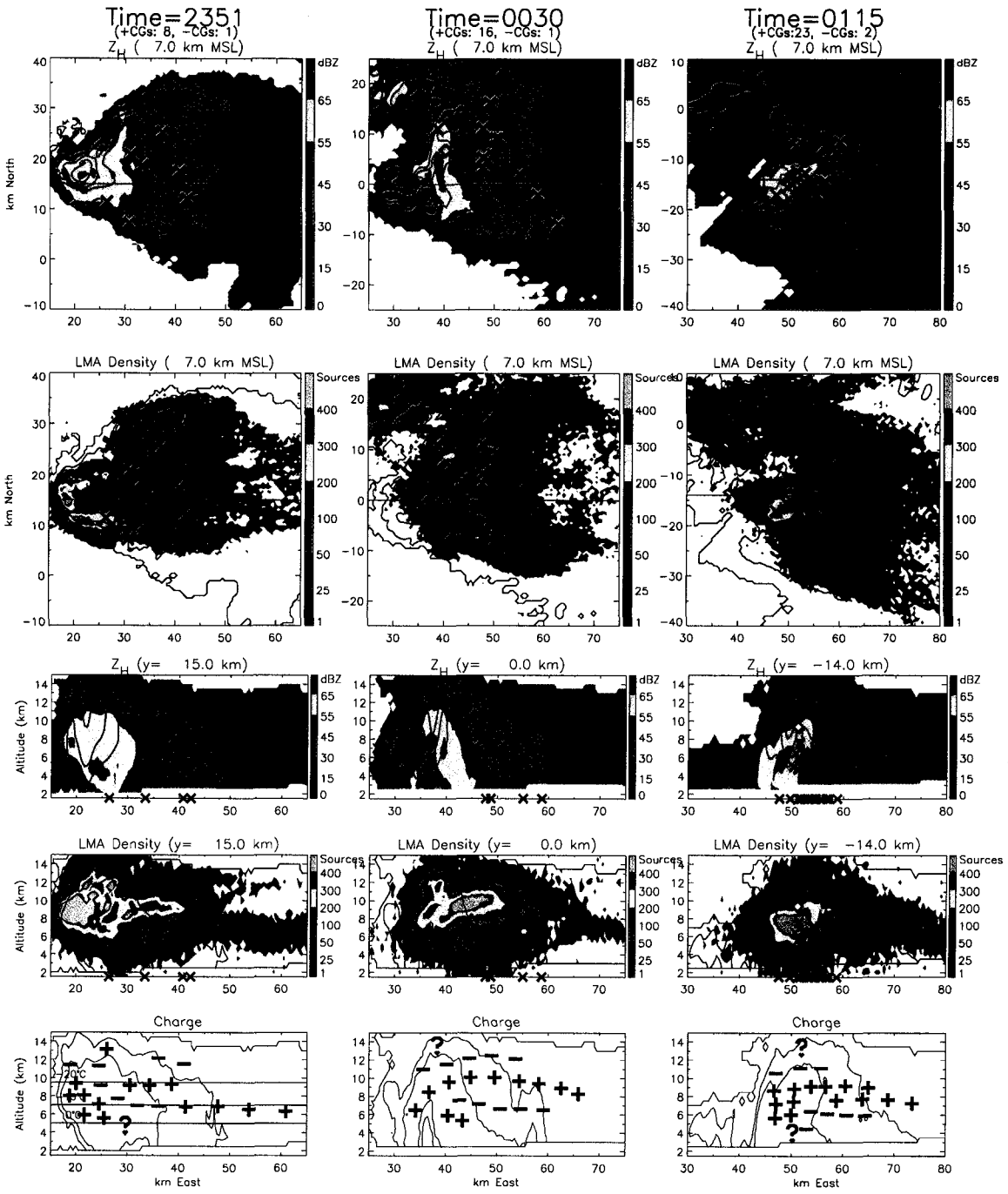

Figure 3.11: As in Fig. 3.9 but for volume scans beginning at 2351, 0030, and 0115. Origin and strike locations of CG flashes are indicated as in Fig. 3.10, with −CG flashes indicated by diamond symbols.

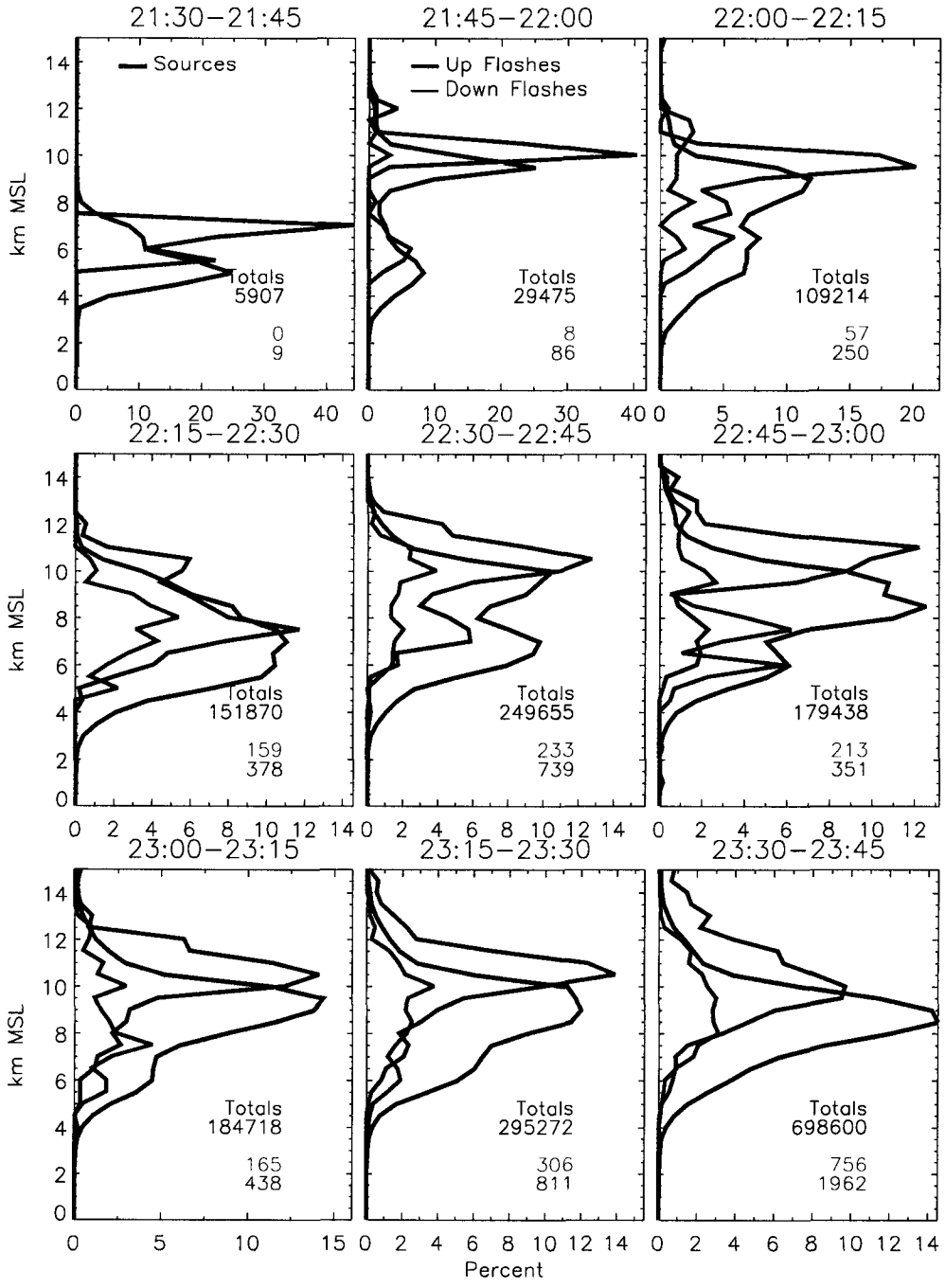

Figure 3.12: Altitude histograms of LMA sources (black) and flash origins (red and blue) from 2130 to 2345 on 29 June 2000. The red and blue curves show origin heights of those flashes that initially went up and down, respectively. Each panel shows 15 minutes of data, plotted as the percentage of the total for each 15 minutes. The up/down flashes are both plotted as a percentage of the total number (up + down) of flashes in each time interval. Numbers in the bottom-right of each panel give the total number of sources and flashes for each 15-minute interval. Binsize is 500 meters.

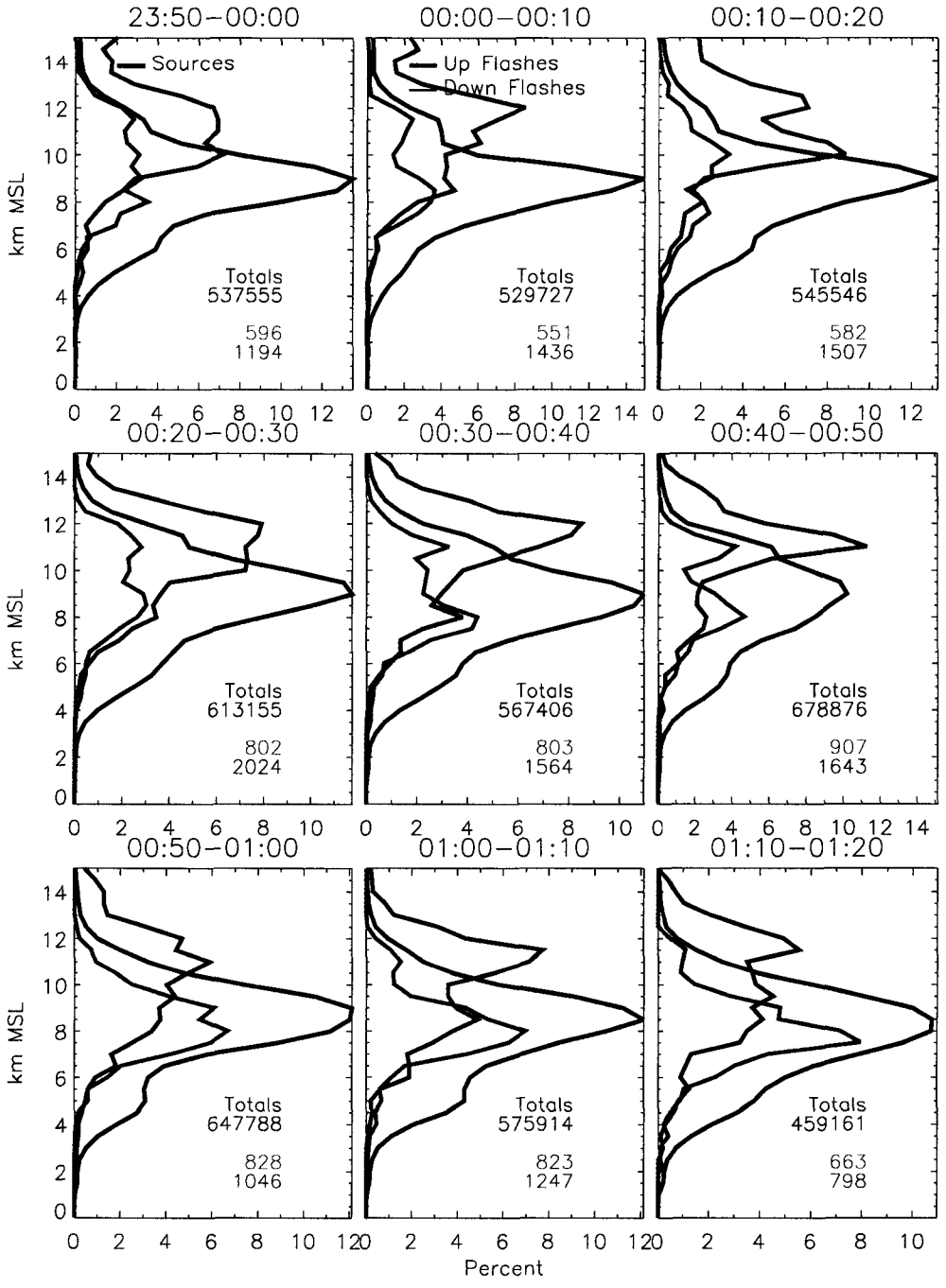

Figure 3.13: As in Fig. 3.12, but for 2350 to 0120. Time increment is ten minutes.

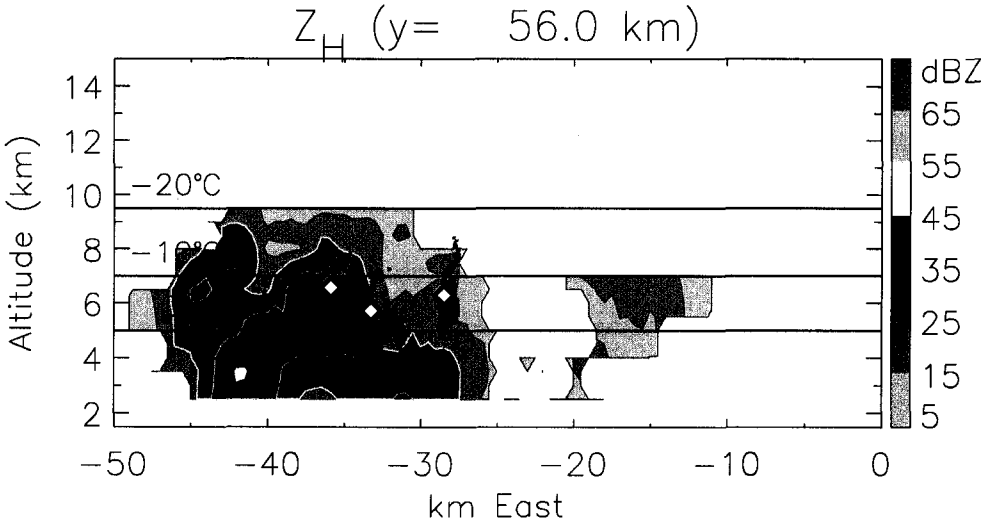

Figure 3.14: Vertical radar cross-section of horizontal reflectivity (Z_H) at 2140 in the 29 June storm (same vertical cross-section as in left column of Fig. 3.9). LMA sources from three flashes are overlaid and color-coded by inferred ambient charge region (red for positive, green for negative). The filled diamond symbols mark the first LMA source of each flash. All three flashes were "inverted", i.e., the initial breakdown proceeded downward and the flash revealed a negative over positive charge structure.

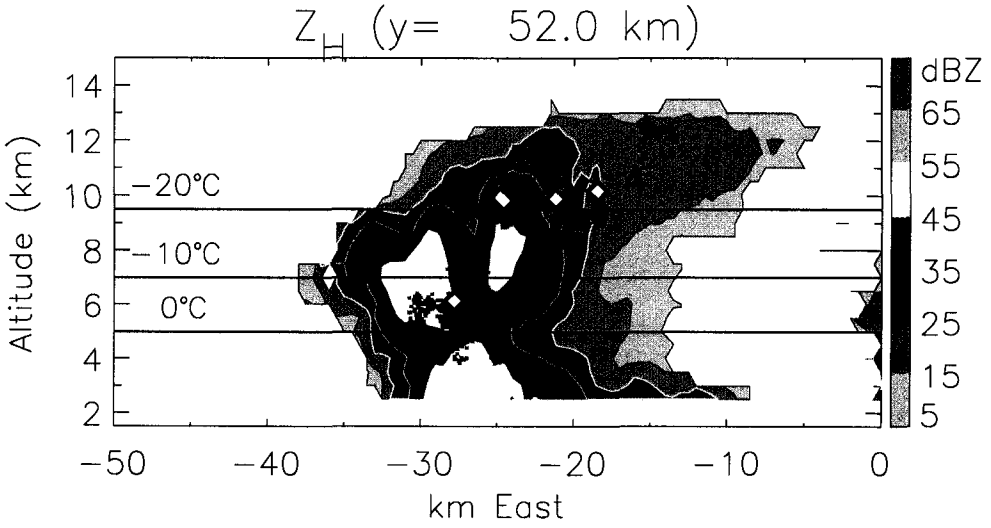

Figure 3.15: As in Fig. 3.14, but for volume scan beginning at 2159 (same vertical cross-section as in middle column of Fig. 3.9). LMA sources from five successive flashes from 2200:46 to 2200:59 are overlaid and color-coded according to inferred ambient charge region as in Fig. 3.14. Magenta triangle (filled diamond) symbols indicate the first sources of flashes whose initial breakdown proceeded upward (downward). There are four downward flashes and one upward flash.

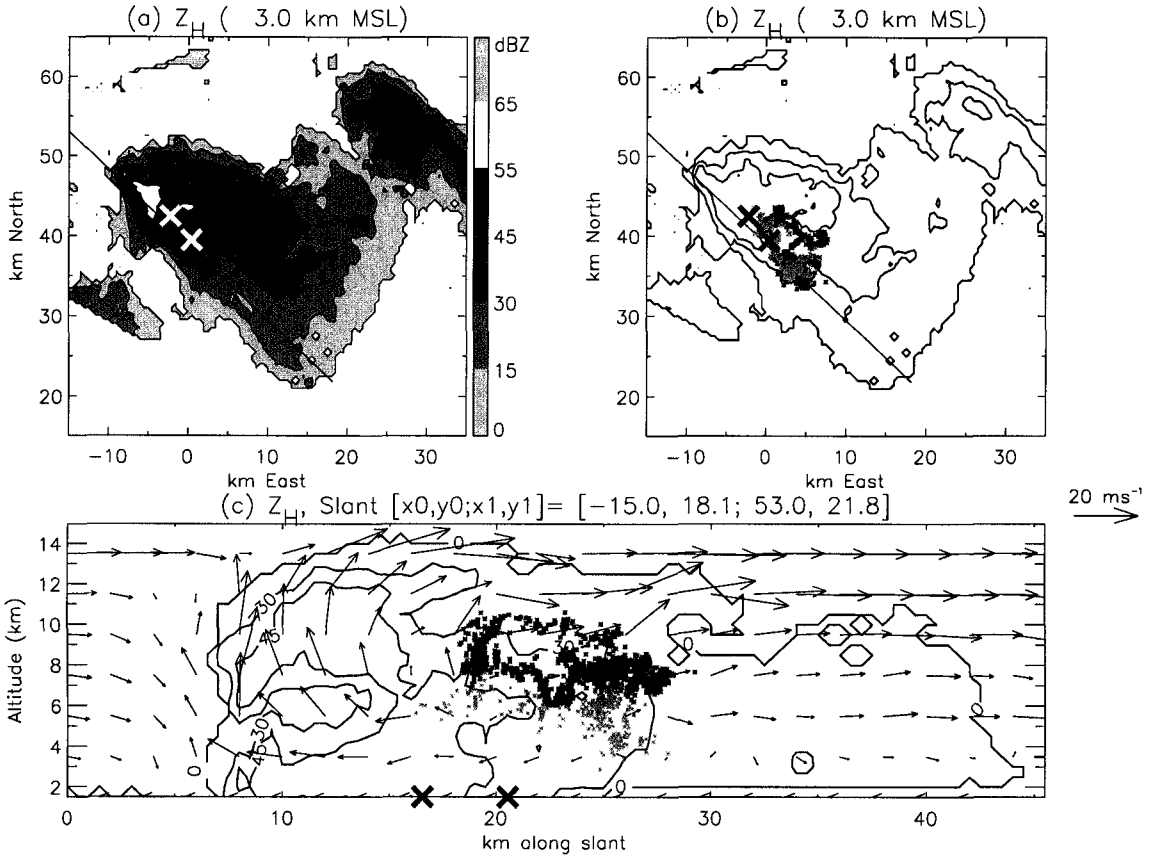

Figure 3.16: Radar cross-sections of radar reflectivity (Z_H) for volume scan beginning at 2239. LMA sources from five "normal" IC flashes are overlaid onto (b) and (c) and color-coded by inferred ambient charge region (black for positive, gray for negative). For reference, NLDN strike points corresponding to the two +CG flashes shown in Fig. 3.17 are indicated by X's. (The lightning mapped flashes shown here are not the flashes that produced the +CG strikes.) Z_H is gray-shaded in (a), and contoured in (b) and (c) with intervals of 0, 30, 45 dBZ. Doppler-derived flow field is also shown in (c).

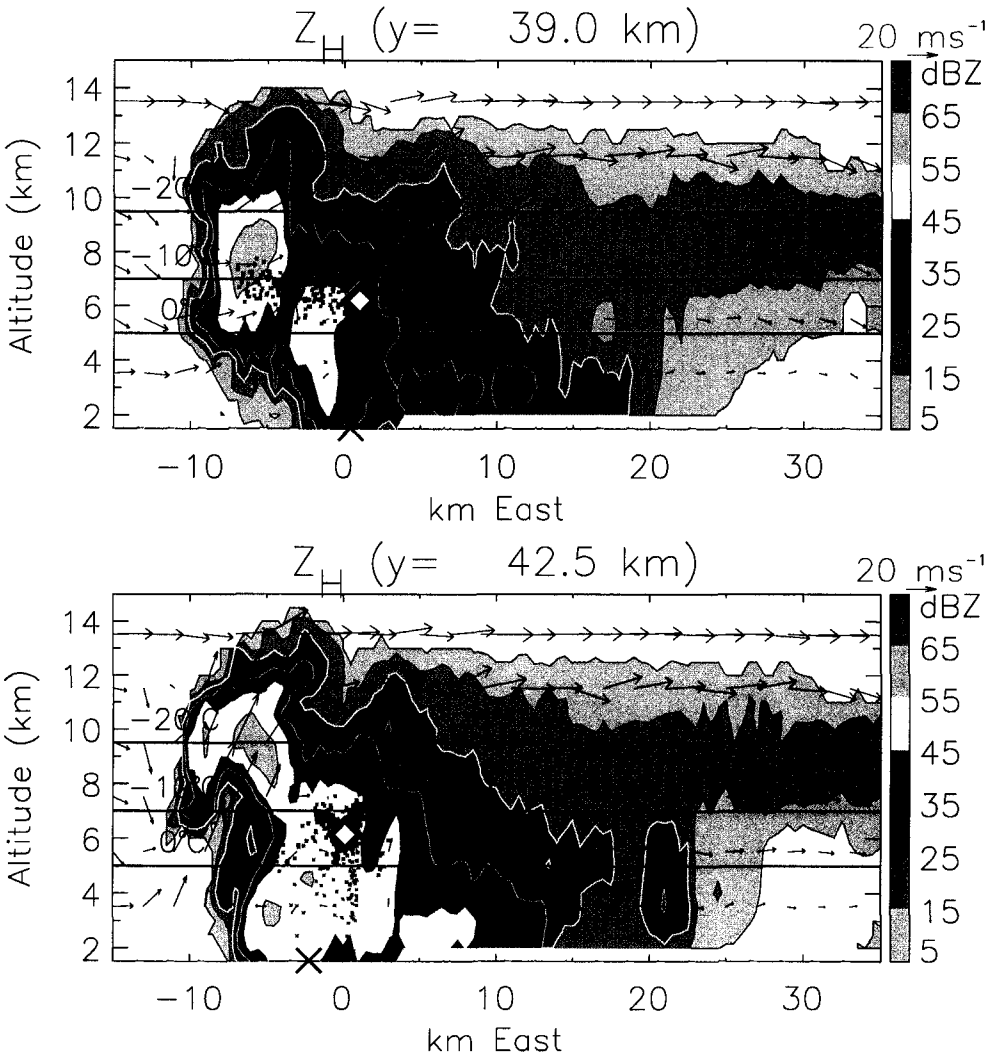

Figure 3.17: Vertical cross-sections of radar reflectivity (Z_H) and Doppler-inferred wind flow for volume scan beginning at 2239. LMA sources from the first two +CGs at 2242:07 and 2244:51 are overlaid on the top and bottom panels respectively, and color-coded by inferred ambient charge region as in Fig. 3.15. The magenta X symbols indicate the NLDN strike points of these two flashes, and filled diamond symbols mark the first source of each flash. The conventional LMA plot of the second +CG flash is shown in Fig. 2.35.

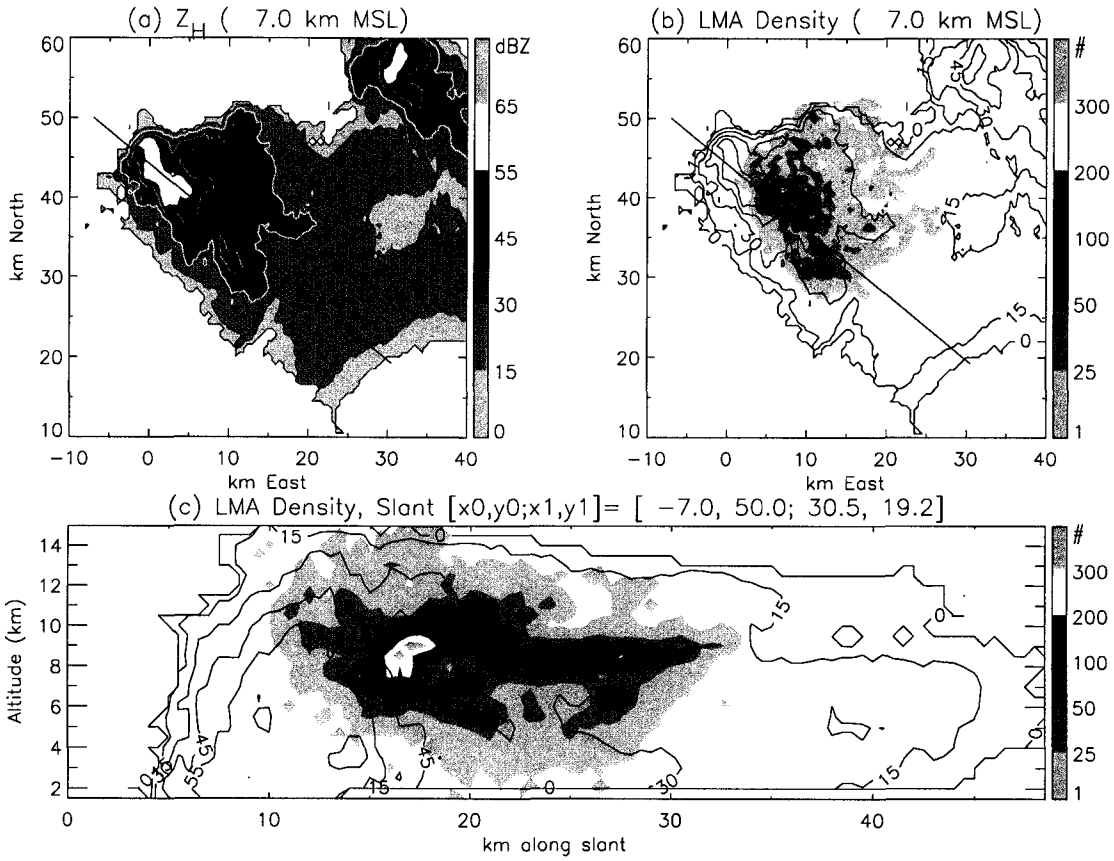

Figure 3.18: Cross-sections of (a) radar reflectivity (Z_H) for volume scan beginning at 2252 and (b,c) LMA density during the first four minutes of this volume scan. LMA density includes all sources within 5 km of each cross-section. Contours of Z_H are gray-shaded in (a) and repeated in (b) and (c) with intervals of 0, 15, 30, 45, 55, and 65 dBZ.

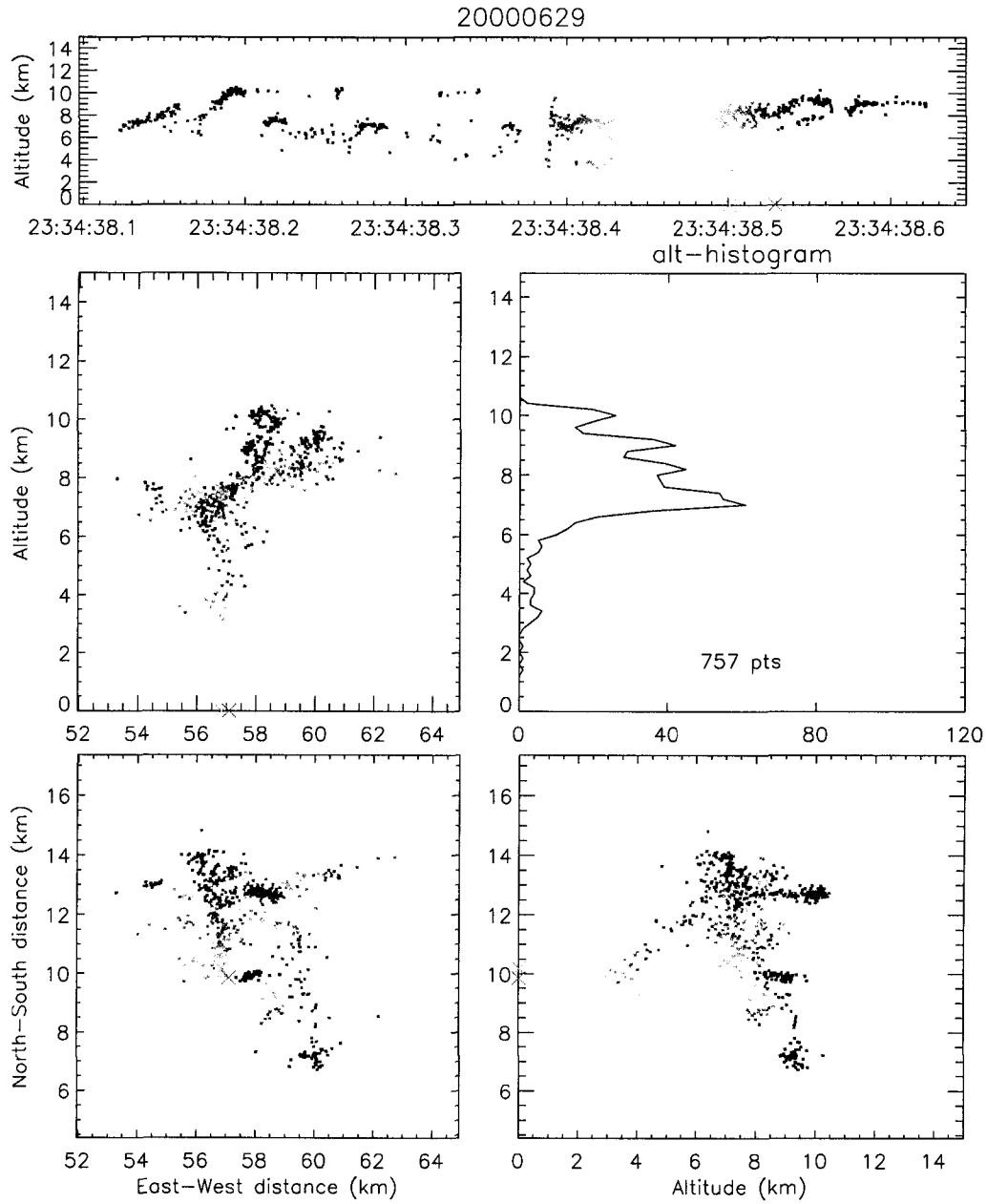

Figure 3.19: Lightning mapping of a +CG flash at 2334:38. Sources are color-coded by time from blue to red. Note the multiple NLDN strike points.

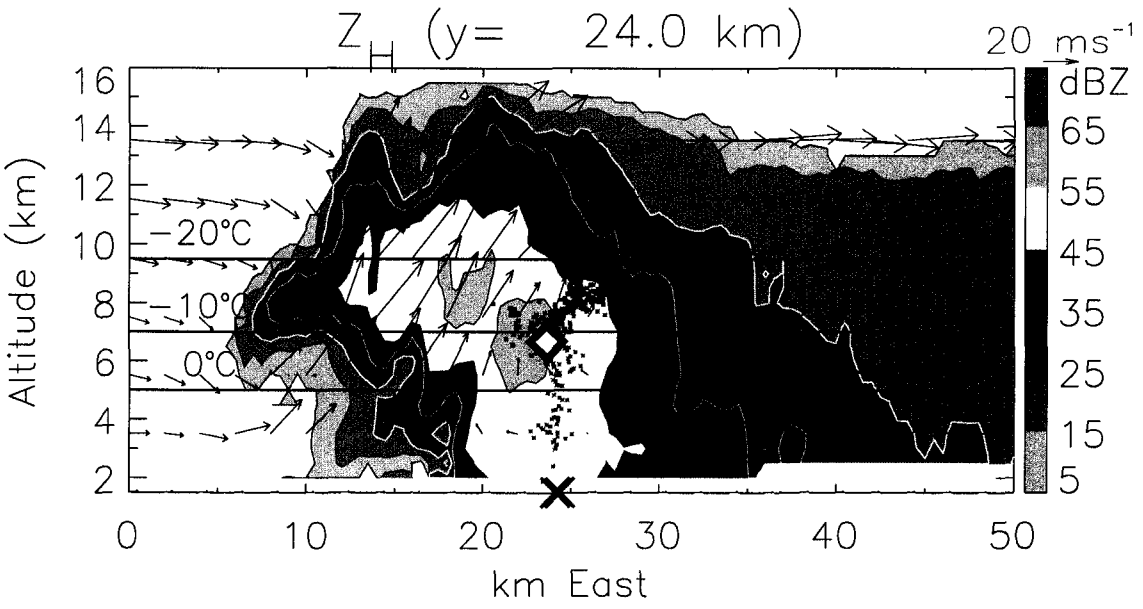

Figure 3.20: As in Fig. 3.17, but for volume scan beginning at 2331 with LMA sources from the +CG flash in Fig. 3.19. Note the very clear leader to ground.

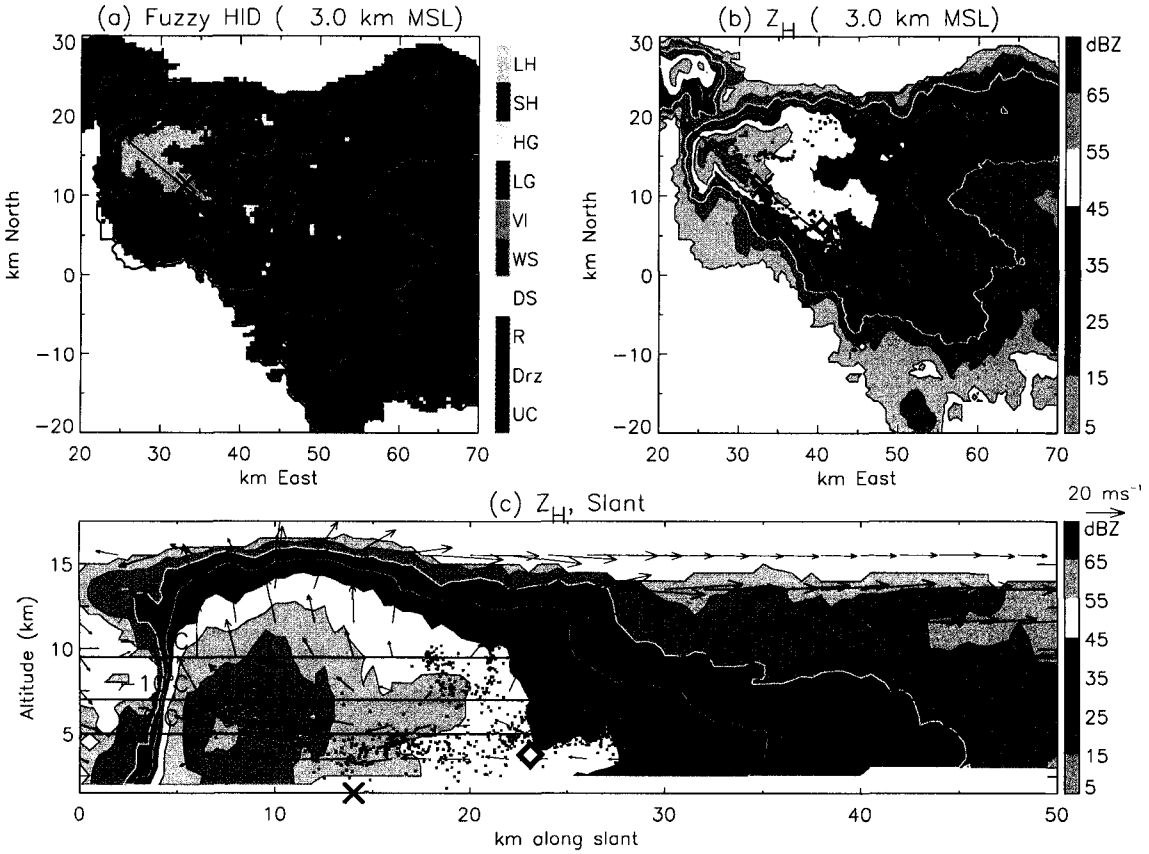

Figure 3.21: Radar cross-sections from volume scan at 0010. (a) Fuzzy logic hydrometeor identification (FHC) at 3 km MSL. (b) Horizontal reflectivity (Z_H) at 3 km MSL. (c) Slant vertical cross-section of Z_H and Doppler-inferred wind flow. LMA sources from a +CG flash at 0013:15 are overlaid onto (b and c) with no charge color-coding. Diamond symbol indicates the first source of the flash and X symbol indicates the NLDN strike point. For reference, contours of Z_H are repeated on (a) at 5, 25, and 45 dBZ.

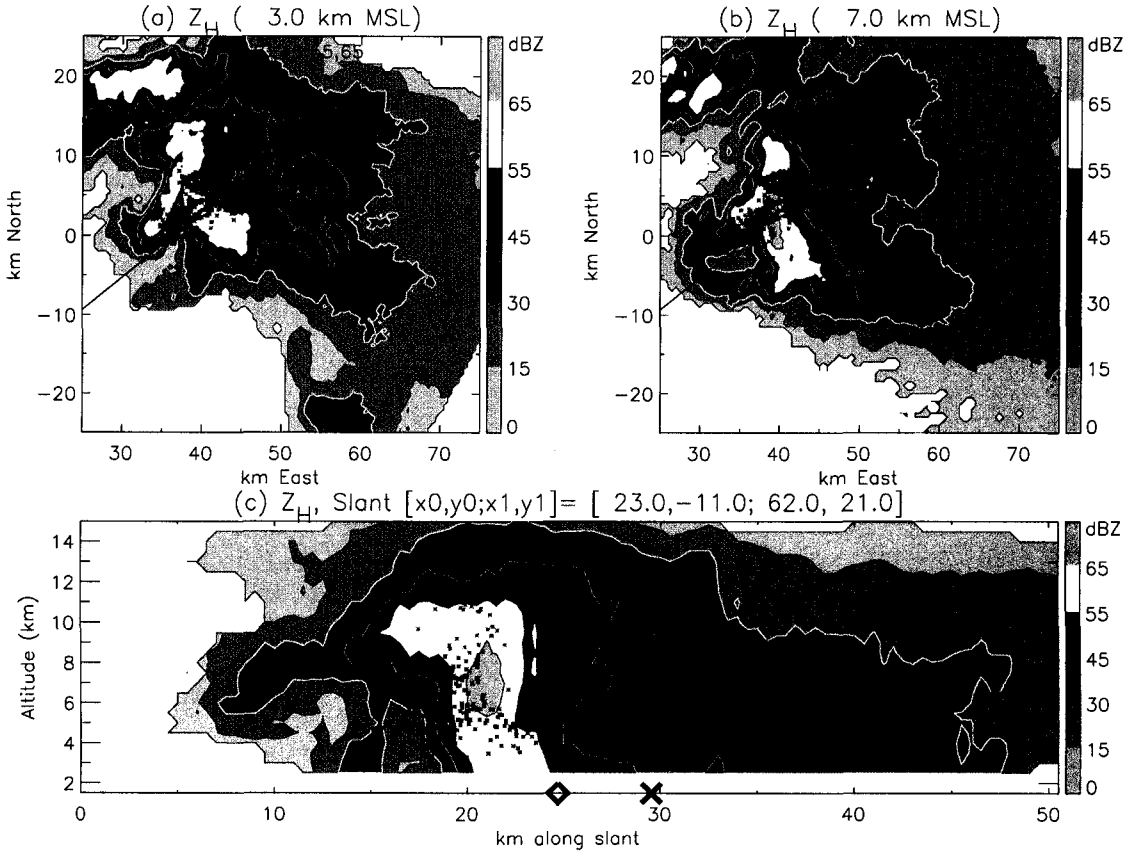

Figure 3.22: Radar cross-sections for volume scan beginning at 0030. LMA sources from a −CG flash and a +CG flash are overlaid and color-coded by inferred ambient charge region, with red for positive and green for negative. In the horizontal cross-sections, the X's and diamonds indicate the +CG and −CG strike points, respectively. In the vertical cross-section, the X and diamond aloft indicate mean initiation height of the CG flashes.

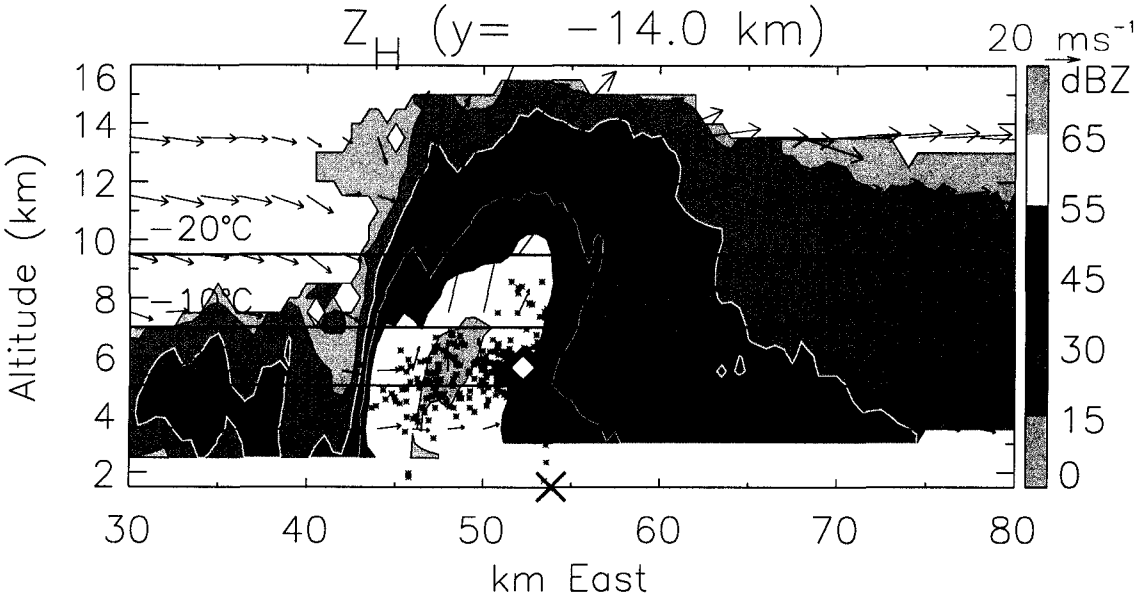

Figure 3.23: As in Fig. 3.20, but for volume scan beginning at 0015 and with +CG flash at 0117:21.

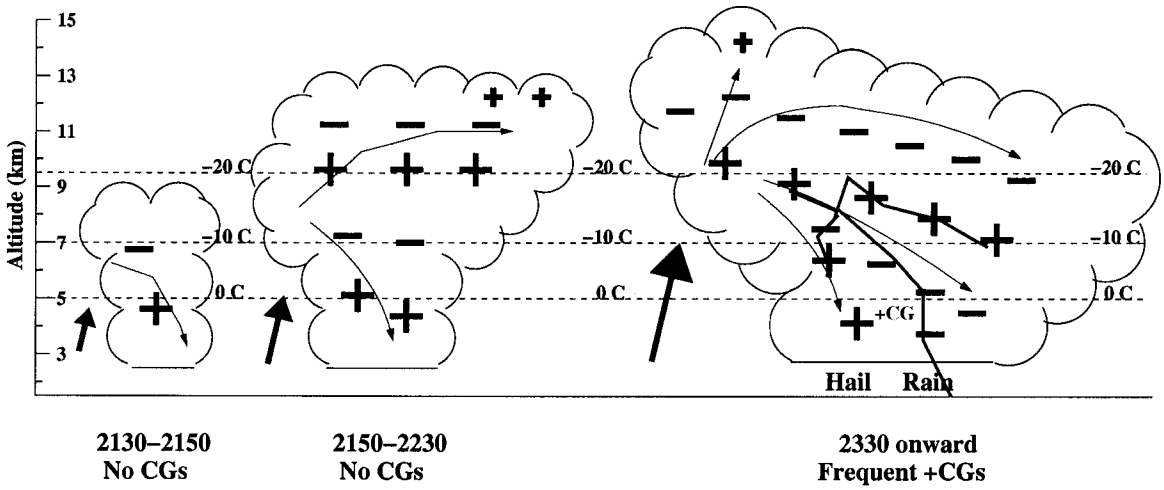

Figure 3.24: Schematic of the evolution of the 29 June supercell. Thick blue arrows show main updraft, and thin blue arrows show air flow. The red disjointed lines indicate a +CG discharge.

CHAPTER 4

3 JUNE OBSERVATIONS

4.1 Introduction

The 3 June 2000 storm provided an excellent case study for several reasons. It was isolated, so there was no ambiguity in the echo volume and flash rate calculations due to contamination of other surrounding cells. It was observed by at least one of the research radars continuously for almost 3.5 hours (2210–0120), from its very early stages to its complete dissipation. The radar coverage began 30 minutes prior to the first lightning at 2240 and continued for 40 minutes after the last lightning at 0045, so the relationships between lightning and the convective state of the storm could be further explored (i.e., comparison of storm structure in both the absence and presence of lightning). *Finally, this storm produced no CG flashes of either polarity despite relatively active intra-cloud lightning.*

The only real downside of this case was the Doppler coverage. The storm was already well-developed by the time it entered the multiple-Doppler coverage area at 2300, so the wind flow in its earliest stages could not be characterized. The Doppler coverage lasted for over two hours (2300 to 0120), but there was a 30 minute gap in the middle of the multi-Doppler coverage (from 0000 to 0026) when the S-Pol radar went down. Unfortunately, the storm was at its peak intensity during this gap. When the multi-Doppler coverage resumed, the updraft had weakened considerably, associated with the collapse of the storm.

4.2 Overview

As described in Tessendorf et al. (2004b), a southwest-to-northeast-oriented surface boundary was moving southeastward through the STEPS domain on this day. An MGLASS sounding launched at 0012 on 4 June ahead of the boundary (and ahead of the storm under study) indicated southwesterly surface winds and strong westerly winds aloft (Fig. 4.1 and top-middle panel of Fig. 4.11). Ahead of the boundary (i.e., south of it), the temperature was near 90° F and the dew point was in the mid-50s°F. Convective Available Potential Energy (CAPE) was marginal (700 J kg^{-1}), and the atmosphere was notably drier above 500 mb. Conditions were drier behind the boundary, with similar temperature but dew points in the mid-30s°F. C

Around 2210 a pair of cells initiated in southwestern Nebraska on the northern end of the surface boundary. The cells tracked southeastward (Fig. 4.2), and the southern cell (cell 'A' in Fig. 4.2) developed into the storm under study. By the time dual-Doppler coverage began (around 2250), the targeted cell already had peak updrafts near 20 ms^{-1} (Fig. 4.3a), and peak updrafts of this magnitude were sustained up until the S-Pol radar went down at midnight UTC. By 2330, the northern cell (cell 'B' in Fig. 4.2) had almost completely dissipated and merged into cell 'A'. Visually, the targeted storm appeared to split around 2356, with the left-moving cell rapidly diminishing and the right-moving cell continuing on. Fig. 4.3b shows that the echo volume of updraft exceeding 10 ms^{-1} (hereafter, UV_{10}) was pretty small, but grew rapidly during the merger of cell 'B' and the ensuing storm split. By the time S-Pol came back up and multi-Doppler was possible again (0030), updrafts were weak and narrow. The storm completely dissipated by 0120.

As in the 29 June supercell case, there was a close correspondence between total flash rate (hereafter, TFR) and development of significant echo aloft (i.e., graupel). Since the radar coverage began well before the first lightning flash in this storm, it's even more apparent that active riming growth aloft was crucial to the electrification. As clearly illustrated in Fig. 4.4, there was no lightning until there was a significant

volume of reflectivity above 30 dBZ. Throughout the storm, the flash rate time series tracked the graupel echo time series, though there was some indication that the lightning led the graupel. Figure 4.5 shows this graupel-lightning relationship in a time-height sense. The peaks in LMA sources tend to coincide with those of graupel echo, in both time and height. Both graupel echo and flash rates peaked near 2315 and 0000, following increases in the updraft volume at approximately 2315 and 2330. During the gap in the multi-Doppler coverage (0000 to 0030), the graupel echo volume and flash rate steadily decreased, so presumably the updraft was weak and UV_{10} was steadily declining during this period. By the time the Doppler-synthesis started again (0030), peak updrafts were only $\sim$5 ms^{-1}, and UV_{10} was very small. Correspondingly, the graupel echo volume and TFR were much decreased. The last lightning flash was at 0045. There was some graupel (a very little) remaining in the storm after this last lightning flash, but there was little significant updraft and hence no continued driving force for charge-separating collisions involving graupel growing in an environment of supercooled water and ice crystals.

Compared with the 29 June supercell, this storm produced very little radar-inferred hail (Fig. 4.6), and what little hail it did produce was identified by the FHC as mostly small hail (<0.75 in). Much of the hail echo identified by the FHC resided only near the surface, which is somewhat suspicious because one would expect to see a hail signal aloft prior to seeing one near the surface. It's possible that the hail signal early in the storm (2300–0000) was the result of a misclassification by the FHC. For example, the hail signal may be indicative of the melting of graupel or small hail as it descends past the freezing level. This melting would increase Z_H and LDR, resulting in a transition from a "graupel" category to a "small hail" category in the FHC. In any case, there was a robust signal of hail growth aloft during only one period of time (0000–0020), and the FHC identified large hail (>0.75 in) in just one (0.5×0.5 km) grid point during the 0013 volume scan. The timing of this hail growth aloft makes physical sense with respect to the trends in the updraft strength, i.e, the robust signal of hail growth aloft occurred just after the most intense observed

updraft growth starting at 2330 (Fig. 4.3). Incidentally, this hail growth period was coincident with maxima in graupel echo volume and lightning flash rate. According to NCDC Storm Data, there was only one report of large (>0.75 in) hail associated with this storm. The report was at 0015 (1815 CST) in agreement with the FHC results.

4.2.1 Correlation Analysis

Before discussing more quantitative relationships between radar-derived echo volumes and flash rates, it should be noted that the radars employed differing scanning strategies at various time periods during this storm. Figure 4.7 shows the computed time series of total storm volume (defined as total echo with $Z_H > 0$ dBZ). Note the dramatic increase from 2320 to 2325. It's likely that this sharp increase was due not only to the growth of the storm, but also to the change in the scanning strategy. From 2210 to 2233 and from 2320 onward, the radars were executing planned position indicator (PPI) volume scans which encompassed the entire > 0 dBZ echo of the storm. However, from 2233 to 2320, the radars were executing Range Height Indicator (RHI) volume scans which encompassed the vertical extent of the echo but not the full horizontal extent. Hence, some of the weaker echo in the anvil region and periphery of the storm was not sampled during these RHI volume scans (see, for example, the clear cut-off in the vertical cross-sections of Figs. 4.12 and 4.14). These differing scanning strategies likely affected the time series computations of echo volumes and especially the correlation analysis. Since the RHI volume scans did not always encompass the full horizontal extent of the echo, the total storm volume time series during these RHIs was reduced from the actual total storm volume, i.e., reduced from what it would have been in PPI volume scans. When this total storm volume was used to remove the large scale trends from other time series (e.g., graupel, hail, TFR), the resulting detrended correlations were likely affected by such transitions in the scanning strategy.

Despite these issues with the radar scanning strategies, detrended correlation

analyses for graupel and hail echo volumes and TFR were performed following the same procedure used for the 29 June supercell (see Section 3.2.1). The results are shown in Table 4.1. Recall in the 29 June case (see Table 3.1) that the echo volume and flash rate time series were very strongly correlated with the total storm volume, having correlation coefficients ≥ 0.9. For the 3 June case, the correlations with total storm volume are much lower, ranging from 0.47 for TFR to 0.69 for graupel echo volume. One obvious reason for the reduced correlations with total storm volume is that there was variance in the total storm volume during the first 40 minutes of the observation period, but there was no graupel, hail, or lightning (and thus no variance in their respective time series) during the first 40 minutes. This is a weakness of this sort of correlation analysis. However, correlations between TFR and hail/graupel echo volumes were higher than with total storm volume (> 0.8 vs. 0.47). Like the 29 June storm, the TFR was best correlated with hail echo volume ($r = 0.79$) when TFR led hail echo volume by 2 scan intervals ($\approx$ 10 minutes). Unlike the 29 June storm, the best correlation between TFR and graupel echo volume ($r = 0.89$) occurred when TFR led the graupel echo volume by two scan intervals. This latter lagged correlation is evident in the non-detrended time series of Fig. 4.4b. The coarse temporal sampling of the radar echo volumes (relative to the finer temporal sampling of the flash rate) may be partially to blame for this lag. However, there are many other sources of uncertainty in these computations. For example: (1) Identification of graupel (or hail) by the FHC gives only a qualitative description of the radar resolution volume, (2) Quantification of the amount of graupel (or hail) in terms of echo volume may not be representative of the *mass* of the graupel (or hail) in that volume, (3) The LMA-derived flash rate is not a perfect metric of the electrification process.

Hence, in the precise mathematical terms of these correlation computations, the relationship between graupel echo volume and TFR is not as robust as in the 29 June case, but the physical interpretation is the same. Increased graupel led to increased lightning, and as graupel volume decreased (more specifically, riming growth and collision rate decreased), lightning flash rate declined rapidly.

4.2.2 Charge Structure

To give a general large-scale picture of the charge structure of this storm, Fig. 4.5c shows time-height contours of the flash initiation heights (i.e., the first source of each flash, which can be roughly interpreted as the height of the maximum electric field between vertically adjacent oppositely charged regions, e.g., Coleman et al., 2003) in comparison with the time-height contours of total LMA sources in Fig. 4.5b. Nearly all the flashes initiated from 9–11 km altitude, above the –20° C isotherm. The LMA sources were generally broadly distributed around the maximum at 7–8 km, i.e, the bulk of the LMA sources was below the flash initiation heights. In a gross sense, this indicates that the main positive charge region (bulk of LMA sources) was below where most of the flashes initiated and the negative charge was above where most of the flashes initiated. All in all, this indicates an inverted dipole charge structure with deep (or multi-layered) lower positive charge extending downward from 9 km altitude and negative charge above the positive. This inverted dipole structure is perhaps better illustrated in Fig. 4.8, which shows the same information as Fig. 4.5b,c. Instead of time-height contours, though, the LMA sources and flash origin heights are plotted here as altitude histograms for several 15-minute intervals. Each histogram is plotted as the percent of the height-integrated total for each time interval, so the black and red curves in Fig. 4.8 should each sum to 100%. For most of the storm, the LMA sources had just one broad maximum (corresponding to the deep positive charge) centered at 6–8 km. The flash origin heights generally also had just one maximum that lay consistently above the LMA source maximum. In other words, nearly all of the flashes initiated downward from upper negative charge into the deep positive charge below.

In an attempt to further objectively diagnose the gross charge structure, the flash origin heights were partitioned into flashes that initiated upward and flashes that initiated downward (blue and green curves in Fig. 4.8). As discussed in Section 2.2.3, this sort of objective calculation of the initial flash direction is not always correct. That is, the objective result doesn't always give the same "sense" of the flash (i.e.,

upward or downward initiating, normal or inverted) that a detailed manual inspection does. However, the cumulative results of such objective calculations do add some additional qualitative information about the large scale charge structure that nicely summarizes and corroborates the labor-intensive flash-by-flash analysis. In the case of this storm, a large majority of the flash start heights were associated with downward flashes (green curves in Fig. 4.8) that initiated above the main peak of LMA sources. This is consistent with the assumed dominant inverted dipole charge structure since the initial sources of a flash are generally due to negative breakdown toward the positive charge region, i.e., in the direction opposite to the electric field. However, there were also significant numbers of upward flashes (blue curves in Fig. 4.8). Most of these upward flashes initiated at the same altitude as the majority of the downward flashes. This is physically reasonable, but suspicious. For example, if the charge structure were a tripole, the downward flashes would presumably initiate in the strong electric field between upper negative and lower positive, while the upward flashes would initiate between the upper negative and extreme upper positive. However, it is suspected that many of the upward flashes were simply incorrectly identified by the objective upward/downward calculation. This is for two reasons: (1) If the upward and downward flashes were indeed describing the tripole structure, one would expect that the heights of the peaks of the upward and downward flash histograms would be more indicative of the upper extent of the lower positive and the lower extent of the upper positive, respectively. Or, stated another way, upward flashes should initiate in the strong negative E-field on the upper side of the negative charge and downward flashes in the strong positive E-field on the lower side. (2) In the detailed flash-by-flash analysis, there simply weren't that many upward initiating flashes in this storm, especially in its later stages. That being said, there were many upward flashes in the first 30 minutes (e.g., top three panels in Fig. 4.8) that do form distinct distributions above the downward flashes. As described in detail in the next section, the manual flash-by-flash analysis confirmed that this storm did have an extreme upper positive charge from 11–12 km during the first 30 minutes. The distribution of upward flashes

(especially from 2255–2310) indicate this upper positive pretty clearly.

One final important thing to note about the altitude distributions in Fig. 4.8 is that there are essentially no flashes (up or down) that originate below the LMA source maximum. In other words, there is no indication of a lower charge region (specifically no lower *negative* charge region) from which flashes would initiate upward into the broad mid-level maximum of LMA sources. This seems to be the most likely reason why this storm produced no CG flashes, specifically no *positive* CG flashes. *It had an inverted charge structure, but no additional lower negative charge to initiate positive flashes to ground.*

The very gross microphysical/electrical interpretation of these first few large-scale time series figures is this: charging processes began when there was graupel present, and the intensity of the charging process (as manifested by lightning flash rate and location of concentrated LMA sources) mirrored the trends in graupel volume in both time and height. The graupel echo and LMA source maxima were nearly co-located in the vertical, while the bulk of the flash initiations was systematically above these maxima. Hence, the majority of the graupel appeared to gain positive charge and hence defined the deep lower positive. Presumably, ice crystals carried the upper negative charge. The fleeting extreme upper positive may have been a screening layer, but as described below, was more likely the result of a separate embedded convective element in which rebounding collisions granted positive charge to smaller ice crystals and negative charge to the graupel.

4.3 Detailed analysis

As in the 29 June case, it is difficult to convey and fully appreciate the time-evolving structure of this storm without analyzing and scrutinizing many, many radar cross-sections and lightning flashes. Verbal descriptions just don't suffice, nor do static images of radar cross-sections and lightning flashes. However, Figs. 4.9–4.11 provide a reasonably good and representative sense of the storm's structural evolution. The goal with these figures is to bring the radar and LMA measurements together in

order to give as complete a picture as is possible of the microphysical, kinematic, and electrical structure of the storm at each time. View each row in these figures from left to right to get a sense of the evolution. While reading the following narrative, refer to a specific column in these figures to get a sense of the state of the storm at each sampled time.

4.3.1 2200–2300: Initiation and early electrification

Radar scan coverage began around 2210. These initial scans were coarse PPIs, and the data from these scans have no echo below 4.5 km. The radars were scanning lower than 4.5 km, but the echo was not that close to the ground yet. By 2240 the storm started to develop >30 dBZ echo aloft, and lightning flashes soon followed. During the 2247 volume scan (left column of Fig. 4.9), the storm had strong (>35 dBZ) lofted echo to the northwest, with precipitation descending to the southeast. Fig. 4.12 shows a couple representative flashes in this developing echo. There are three flashes overlaid here, all of which were inverted IC flashes that initiated near 10 km altitude. Two of them stayed compact in the extreme NW echo, while the other extended further SE and downward. The inferred positive charge followed the stronger echo in both the compact flashes and in flashes that extended deeper through the descending precipitation. The inferred negative charge region was more horizontally stratified in the weaker echo from 10–11 km MSL.

Over the next few minutes, the stronger echo deepened and descended toward the surface. The lightning continued to be much the same: all inverted IC flashes, with the negative breakdown through the positive charge sometimes staying in the NW lofted echo, sometimes extending further SE and downward, but always hugging the $\geq$ 35 dBZ contour. Looking at several flashes in sequence gives the impression that the positive charge region was continuous, sloping downward from the NW to the SE within the descending precipitation.

In addition to these numerous inverted IC flashes, at 2253 the storm started to produce normal IC flashes above the preceding inverted IC flashes. That is, these

flashes initiated from negative charge that resided near the same altitude as the negative charge revealed by downward flashes in the main inverted dipole, but they initiated upward into positive charge above. Flashes involving this extreme upper positive were decidedly downwind of the core of the storm and bulk of the lightning activity (e.g., Figs. 4.13–4.15) . These upper-level normal IC flashes moved farther and farther downwind as time progressed, and they ceased altogether by 2330. As described in more detail in Section 4.4, these upward flashes were somewhat of an anomaly compared with the vast majority of the lightning activity.

4.3.2 2300–2330: Intensification and updraft split

Multi-Doppler coverage began with the volume scan at 2301, and the first detection of reflectivity exceeding 45 dBZ also occurred at this time. As suggested by the storm structure in the preceding volume scans, the Doppler synthesis showed the main updraft co-located with the echo vault on the northwest part of the storm (see middle column of Fig. 4.9). At 2301, the peak updraft speed was near 20 ms^{-1} in this main updraft. There was also a secondary, weaker (10 ms^{-1}) updraft further downwind.

From 2301–2330, the storm experienced two cycles of growth and decay, with maxima in UV_{10} around 2300 and 2315 and minima in UV_{10} around 2305 and 2325 (Fig. 4.3). The influence of each of these updraft surges is apparent in the time series of reflectivity and lightning (Figs. 4.4 and 4.5). The 35 and 45 dBZ echo heights reached maxima during the UV_{10} maxima, then descended during the UV_{10} minima. Graupel echo volume steadily increased during these two updraft surges, reaching a pronounced maximum at 2320, then tapering off a bit. The lightning response was similar to that of the graupel echo, though the lightning led the graupel somewhat.

During these two growth cycles, the main updraft appeared to split into a northern and southern component. Perhaps "split" is not the best terminology. In any case, a new updraft formed to the north of the pre-existing updraft. The northern updraft tracked eastward relative to the southern updraft and dissipated. The southern

updraft "split" again around 2331 (see the top panels in Figs. 4.9–4.11). In general, the southern updraft was the more dominant of the pair after each split and persisted through the duration of the storm. The northern updraft dissipated more rapidly. As shown in Fig. 4.16, both the northern and southern updrafts had associated vaulted echo structures, reflecting their separate precipitation growth paths and resulting in a "split" in the 45 dBZ echo aloft. The lightning was highly concentrated in both echo vaults and continued to reveal an inverted dipole structure, with a thin region of upper negative charge at 10–12 km altitude and deep and/or multi-layered lower positive charge. The lower positive charge continued to be co-located with the strongest echo, both within the lofted echo vaults and within the descending precipitation. This basic echo structure and inverted dipole charge structure persisted throughout the storm. Flashes from the upper negative into the extreme upper positive charge also continued during this time period, but these flashes remained well downwind in the eastern anvil region (e.g., bottom-right panel of Fig. 4.9 and Figs. 4.13–4.15).

4.3.3 2330–0000: Peak intensity

From 2325 to 0000 UTC, the updraft speed and updraft volume underwent their strongest periods of growth (Fig. 4.3). The echo top heights, graupel echo volume, and flash rates again followed suit (Figs. 4.4 and 4.5). Graupel echo volume nearly doubled. Total flash rates more than tripled, reaching a midnight UTC peak of nearly 35 flashes min^{-1}. The flashes into the extreme upper positive charge had completely ceased, and structurally, the storm continued to exhibit vaulted echo structure and only a persistent inverted dipole charge structure everywhere. So, overall, the storm was much the same as it had been, only stronger. However, there were some interesting variations that are worth discussing. Refer to Figs. 4.10–4.11 for the context of the following narrative.

At 2331, the northern updraft had a larger volume of 45 dBZ echo associated with it and more lightning than did the southern updraft. The stronger southern updraft was redeveloping its vaulted echo which included an appendage forming out

west of the core. A weak BWER and lightning hole was also co-located with the southern updraft at this time. From 2331 to 2344, the northern updraft weakened while the southern updraft split again. Meanwhile, the western echo vault appendage had grown and deepened, filling with lightning and leading to a more pronounced lightning hole. From 2350 to 2356, the northern updraft died away while the southern updraft intensified further. The UV_{10}, graupel and hail volumes and flash rates increased markedly during this time and peaked about 10 minutes later. Nearing UTC midnight, the echo vault near the main updraft filled in further, also extending south of the updraft. The only robust hail signal of the entire storm formed within this southern echo. The bulk of the lightning activity shifted south, following this new precipitation growth. Overall, the invigoration of the southern updraft and associated precipitation growth aloft was largely responsible for the dramatic jump in the lightning flash rates from 2345 to 0000.

4.3.4 0000–0130: Dissipation

From 0000 to about 0030, S-Pol went down so multi-Doppler synthesis (and calculations of updraft speeds and UV_{10}) was not possible during this time. Data from the CHILL radar and LMA were still available though, and these data indicate that the storm reached its peak intensity right at the time the S-Pol radar went down. The storm steadily dissipated thereafter. The echo top heights, graupel echo volume and TFR all dropped off rapidly after midnight (Figs. 4.4 and 4.5). Graupel echo volume decreased by almost an order of magnitude and flash rates dropped from 35 flashes min^{-1} to only a few flashes min^{-1} in a span of about 30 minutes.

The northern updraft (and its associated precipitation dissipated first) leaving only a small remnant of >45 dBZ echo aloft by 0016 (Fig. 4.11). The southern updraft appeared to remain fairly strong up to 0016, as evidenced by the continued presence of lofted 45 dBZ echo. The lightning continued to concentrate in the echo to the southeast of the southern updraft and continued to show a simple inverted dipole charge structure. The lower positive continued to be deep and generally constrained

in the strongest precipitation. By the time multi-Doppler resumed (0030), there was only a weak ($\sim$5ms^{-1}) and narrow updraft on the extreme southwest edge of the storm. Up to the very end of the lightning activity, the flashes were clear inverted ICs between the upper negative and deep lower positive charge regions.

4.4 Discussion and Conclusions

Though this storm was fairly intense in terms of updraft strength (>20 ms^{-1}) and total lightning flash rate (tens of flashes min^{-1}), it produced no CG flashes of either polarity. The charge structure inferred from the lightning mapping of the flashes consistently revealed an inverted dipole. A thin region of negative charge resided in weak echo at 10–12 km altitude, with deep or multi-layered positive charge in the stronger echo below. The lightning mapping gave no indication of a lower negative charge region below the main positive. As discussed in Section 1.1.3, modeling studies such as Mansell et al. (2002) and Marshall and Stolzenburg (2002) suggest that a lower charge center is required to initiate flashes to ground. The lack of a lower negative charge is likely the reason why this storm produced no +CG flashes, despite its inverted charge structure.

The information provided by the Doppler winds greatly aided the interpretation and understanding of the echo and lightning structure. Referring to the situation at 2301 (middle column of Fig. 4.9): Note how the LMA sources are all downwind of the main updraft and how the charge regions all slope downward to the southeast, with the lower positive charge following the descending precipitation. The interpretation is that most of the charge-separating collisions were occurring in the main updraft. The charge-bearing particles then drifted downwind and separated according to size [i.e., larger positively charged hydrometeors (graupel) fell faster than small negatively charged ones (ice crystals)]. This resulted in vertical separation of the net oppositely charged regions, build up of the electric field, and lightning. By 2316 (right column in Fig. 4.9), the secondary updraft had tapered off, while a >45 dBZ echo vault had formed near the main updraft. The lightning and inferred positive charge was

highly concentrated in this lofted echo, with negative charge above in weaker echo. This inverted structure was maintained further downwind and, with the highest concentration of lightning and inferred positive charge constrained within the strongest echo.

Similar structure persisted throughout the storm, though there was some variability due to surges of updraft and cycles of precipitation growth and descent, Hence, the electrification process near the main updraft appeared to consistently grant positive charge to the larger particles, resulting in an inverted dipole charge structure. The persistence of the vaulted echo and high cloud base near the main updraft and charging region may explain why the rimer was consistently charging positively. Following the arguments of Williams et al. (2004), higher cloud base would reduce the warm-rain collision/coalescence growth, allowing for near adiabatic supercooled liquid water contents and elevated riming rates in the charging/collision region. According to laboratory studies of the collisional-charging mechanism, such conditions would promote positive charging of the rimer (e.g., Takahashi, 1978; Saunders and Peck, 1998).

In addition to the persistent inverted dipole near the core of the storm, from 2253 to 2330 there were many flashes indicating an additional upper positive charge. That is, the flashes initiated upward from negative charge into positive charge above the main inverted dipole structure. In general, this extreme upper positive lay downwind (i.e., east and southeast) within the leading anvil echo. Given that the electrification process in the main updraft consistently formed an inverted dipole, how did this upper positive charge form? Here are two explanations: (1) The upper positive charge was a screening layer. This is reasonable given that the upper positive often appeared to lie along the upper echo boundary. (2) The upper positive charge resulted from a different charging regime associated with either the periphery of the main updraft or, more likely, the weaker secondary updraft further downwind. That is, the collisions in weaker updraft granted negative charge to the rimer. This latter explanation is more consistent with the observations. Referring again to the middle column of Fig. 4.9:

Note how the secondary updraft is within much deeper echo, i.e., there is no associated echo vault and cloud base is much lower. Hence, the liquid water contents (or, riming rate) may have been reduced in the collision zone of the secondary updraft because (a) the updraft was weaker and narrower and suffered more entrainment and (b) more of the liquid water may have been lost to collision/coalescence. From 2255 to 2310, there were at least as many normal IC flashes involving the extreme upper positive as there were inverted IC flashes near the core of the storm (e.g., Fig. 4.8), which suggests there was a robust charging process responsible for the upper positive charge region. Furthermore, the flashes involving the extreme upper positive charge were all downwind of the secondary updraft and proceeded to be even further downwind as time went on and the secondary updraft dissipated (i.e, compare the middle and right columns of Fig. 4.9.). For further clarification, Figs. 4.13 and 4.14 show two representative flashes during the 2301 and 2316 volume scans, respectively. In each figure, one of the flashes was a deep inverted IC flash near the main updraft; the other was a normal IC flash involving the extreme upper positive. Finally, Fig. 4.15 shows another similar pair of flashes, this time during the 2325 volume scan. By this time, the upper positive had moved much further downwind, and the normal IC flash shown was the last such flash involving the extreme upper positive. Note that the positive LMA sources are decidedly within significant echo in this last normal IC flash. This is more evidence that the extreme upper positive was not a screening layer.

Finally, NSSL launched an EFM balloon through this storm at 0013 on 4 June. Fig. 4.17 shows the trajectory of this balloon relative to the echo and lightning structure. Fig. 4.18 shows the electric field measured along the balloons path. The balloon managed to penetrate the updraft and lofted echo region of the storm, traveling through the region of highest lightning concentration. However, the balloon missed the lower extent of the precipitation and lower positive charge. As described in Rust and MacGorman (2002), the charge structure inferred from the vertical electric field (E_z) profile generally agrees with the LMA charge structure: positive charge from $\approx$7–10.5 km, a very strong but vertically thin negative charge region from 11–12 km,

and a poorly resolved positive charge at the top. The strongest E_z in the sounding is between 10–12 km, which is consistent with the location of the vast majority of flash initiation altitudes in Figs. 4.5c and 4.8. Though there are fluctuations in the sign of the gradient of E_z from 7–10.5 km, Rust and MacGorman (2002) identified this region as only positive charge, with no intervening negative charge. This agrees with the lightning mapping. However, Rust and MacGorman identified the negative gradient of E_z from 4–6 km as a negative charge region, though there was never any lightning mapping indication of this lower negative charge. It is possible that the balloon may not have been passing through a net negative charged region (as a Gauss' Law interpretation would indicate), but instead the electric field was simply pointing away from the positive charge above it. For example, according to the lightning mapping in Fig. 4.17d, the balloon encountered the lower positive charge near 6 km MSL, which is in very good agreement with the point on the balloon sounding where the E-field gradient becomes positive. Hence, the negative gradient of E_z in this lowest balloon-inferred "negative" charge region may have been due to the balloon nearing the positive charge above it rather than an actual negative charge region.

	Total Storm Volume	Graupel Echo Volume	Hail Echo Volume
Graupel	0.69		
Hail	0.59	0.84 (0.75)	
Total Flash Rate	0.47	0.81 (0.76) (0.89@+2)	0.69 (0.58) (0.79@+2)

Table 4.1: Correlation coefficients between radar and lightning time series for 3 June. Values outside of parentheses give correlations between zero-lag time series, prior to any trend removal. Values in parentheses give correlations between detrended time series at zero lag. Additional correlation coefficients and lag values are given if the best detrended correlation occurred at non-zero lag. Each lag increment corresponds to one 5–7 minute radar volume scan interval. For example, the best detrended correlation between hail and graupel was at zero lag, while TFR was better correlated with graupel and hail when the TFR led graupel and hail by two scan intervals.

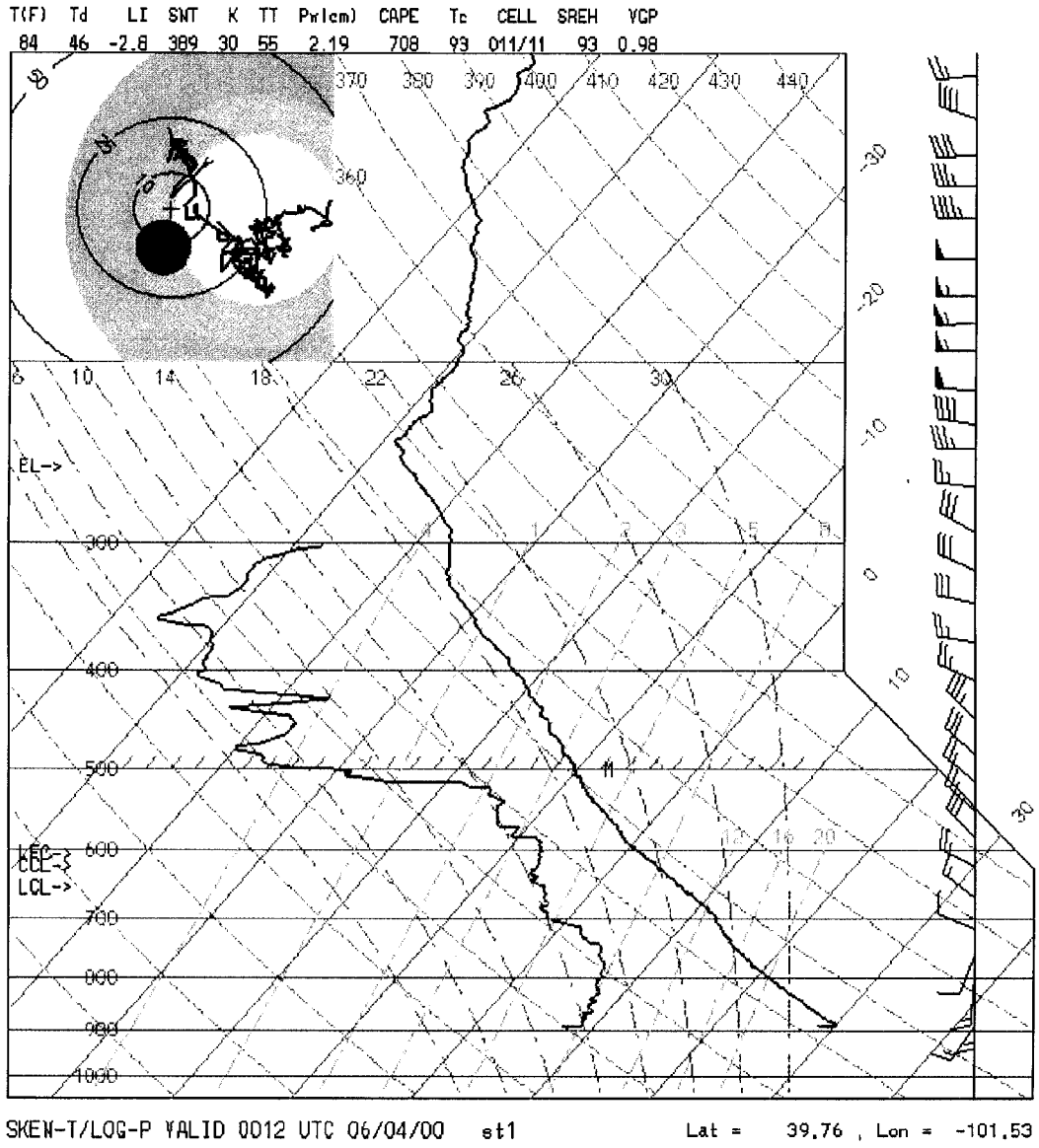

Figure 4.1: MGLASS sounding from 0012 UTC on 4 June. The location and flight path of this sounding is shown in the top-middle panel of Fig. 4.11.

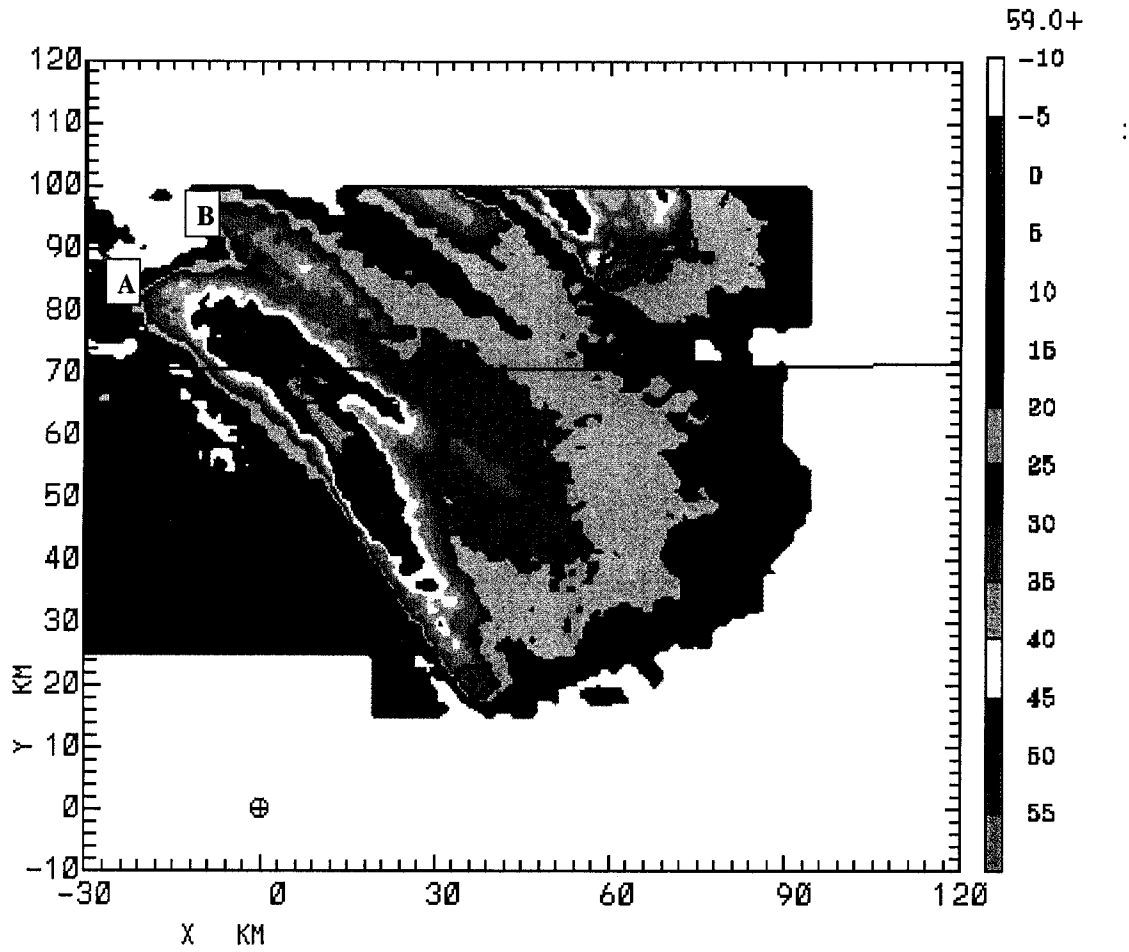

Figure 4.2: Swath of KGLD maximum reflectivity in each vertical column, from 2236–0021 UTC, color shaded according to the color bar on the right. Origin of the coordinates is the KGLD radar. (Courtesy of S. Tessendorf)

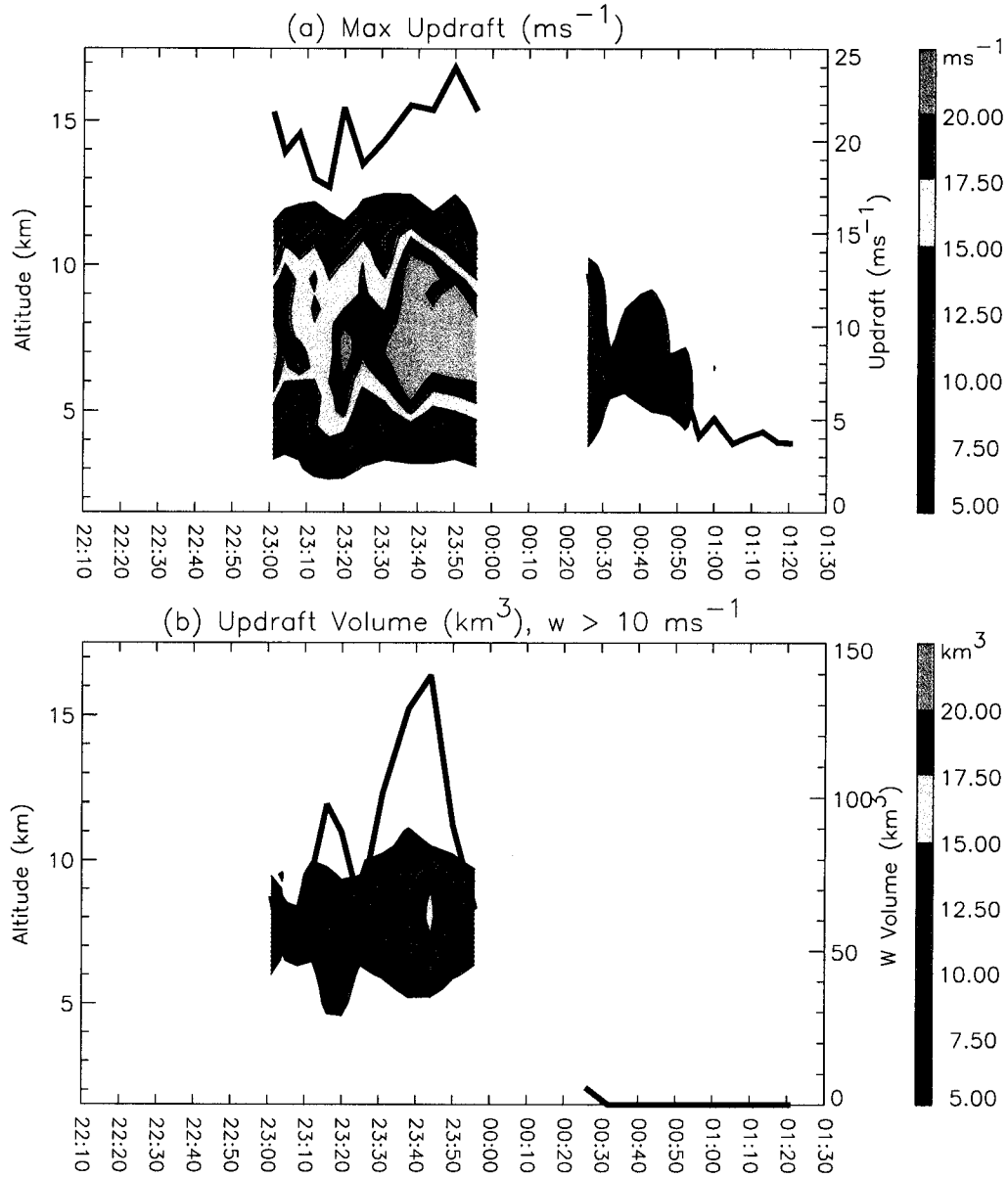

Figure 4.3: (a) Color contours of multi-Doppler-inferred max updraft at each height and time, with overall max value for each time overplotted as thick black line. (b) Color contours of updraft volume exceeding 10 ms^{-1} (UV_{10}) at each height, with height-integrated volume overplotted as thick black line.

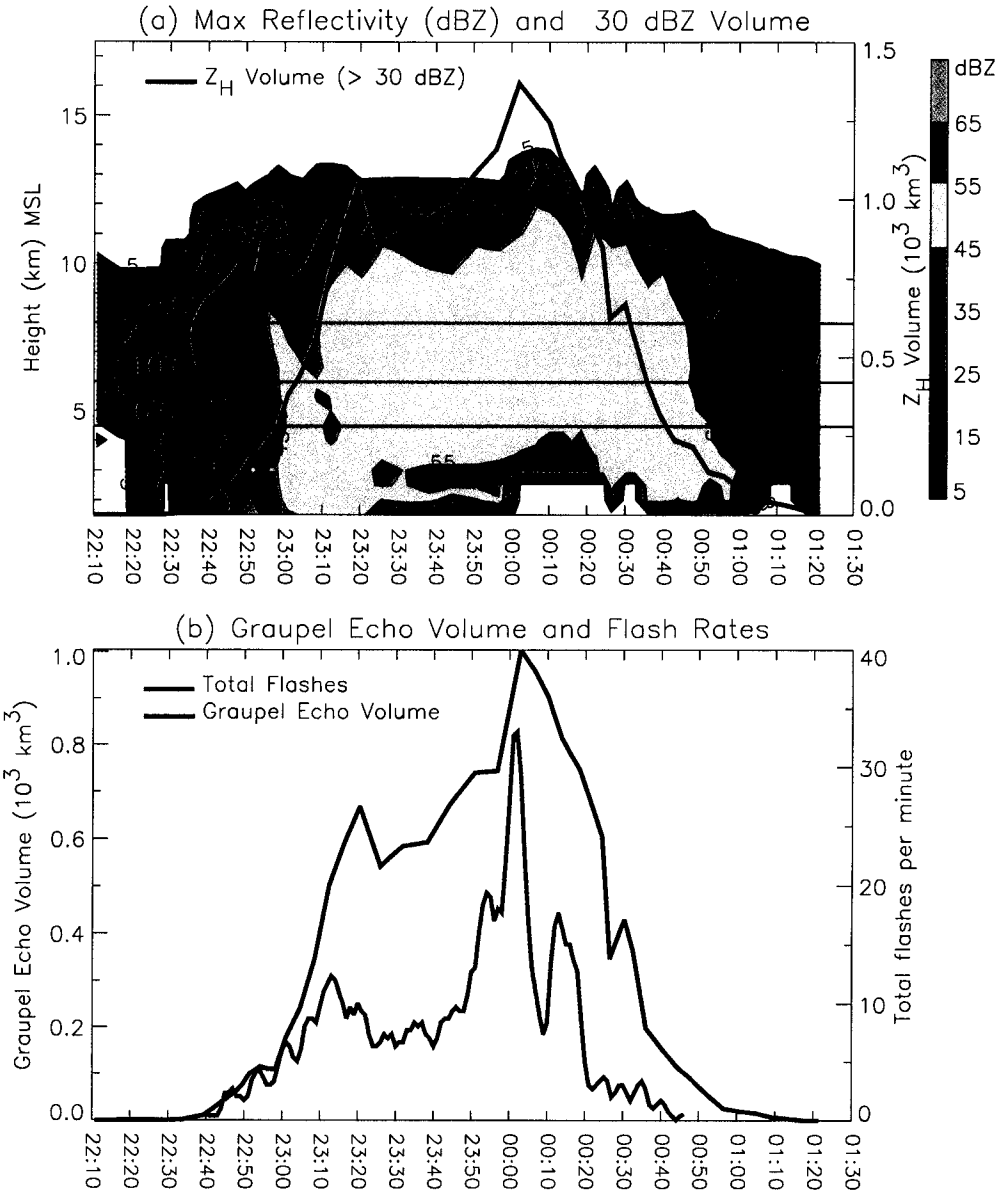

Figure 4.4: (a) Time-height contours of max reflectivity with total volume of storm ($Z_H \geq 30$ dBZ) overlaid as thick black line. (b) Graupel echo volume and total flash rate. Radar quantities are from the CHIL or S-pol radars and are plotted at the beginning of each volume scan time. Flash rates are plotted at each minute and have been smoothed by a 3-pt running mean filter.

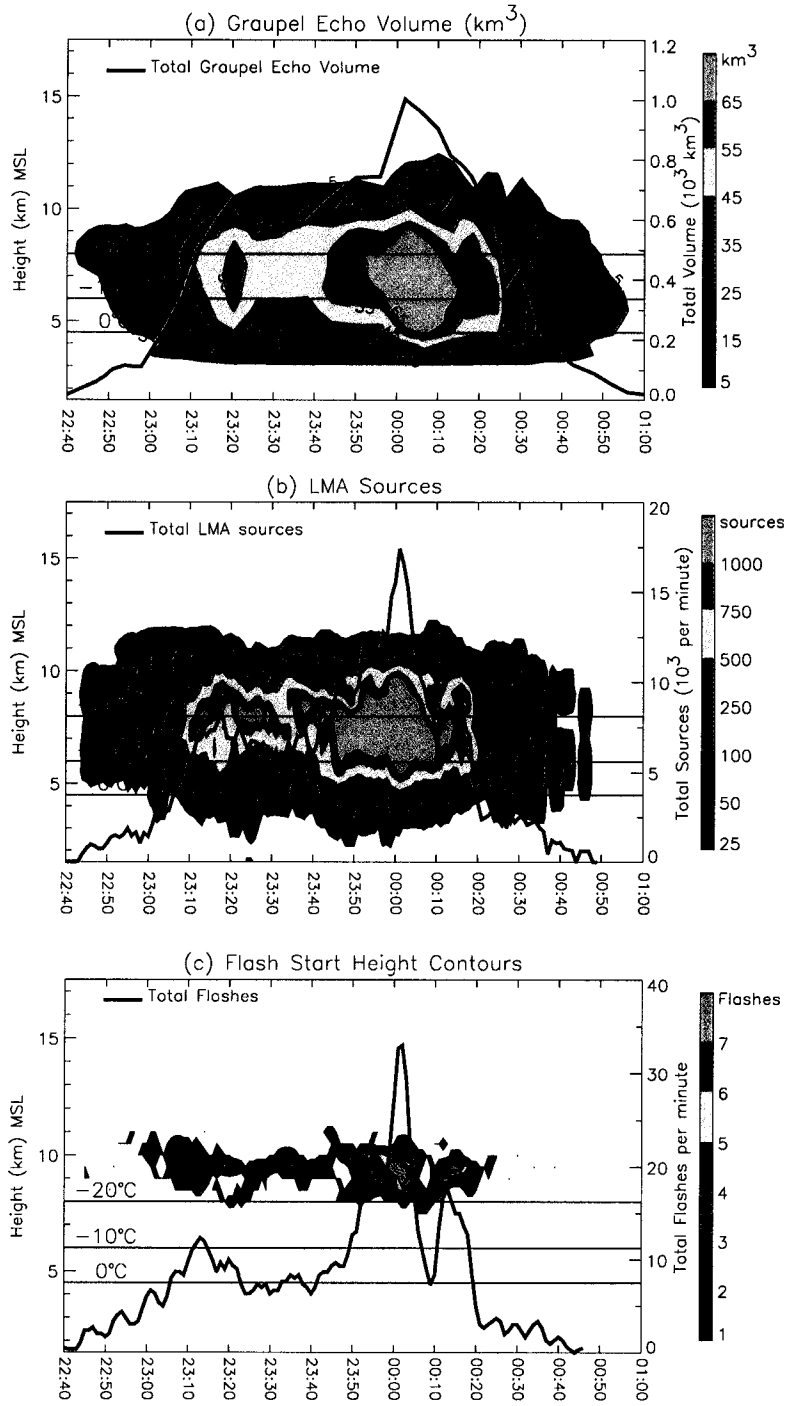

Figure 4.5: (a) Time-height contours of graupel echo volume with height-integrated graupel echo volume overplotted as thick black line. (b) Time-height contours of total LMA sources, with total (height-integrated) LMA sources overlaid as thick black line. (c) Time-height contours of flash start heights with total flash rate overlaid as thick-black line. All lightning quantities are plotted at each minute and smoothed by a 3-pt running mean filter.

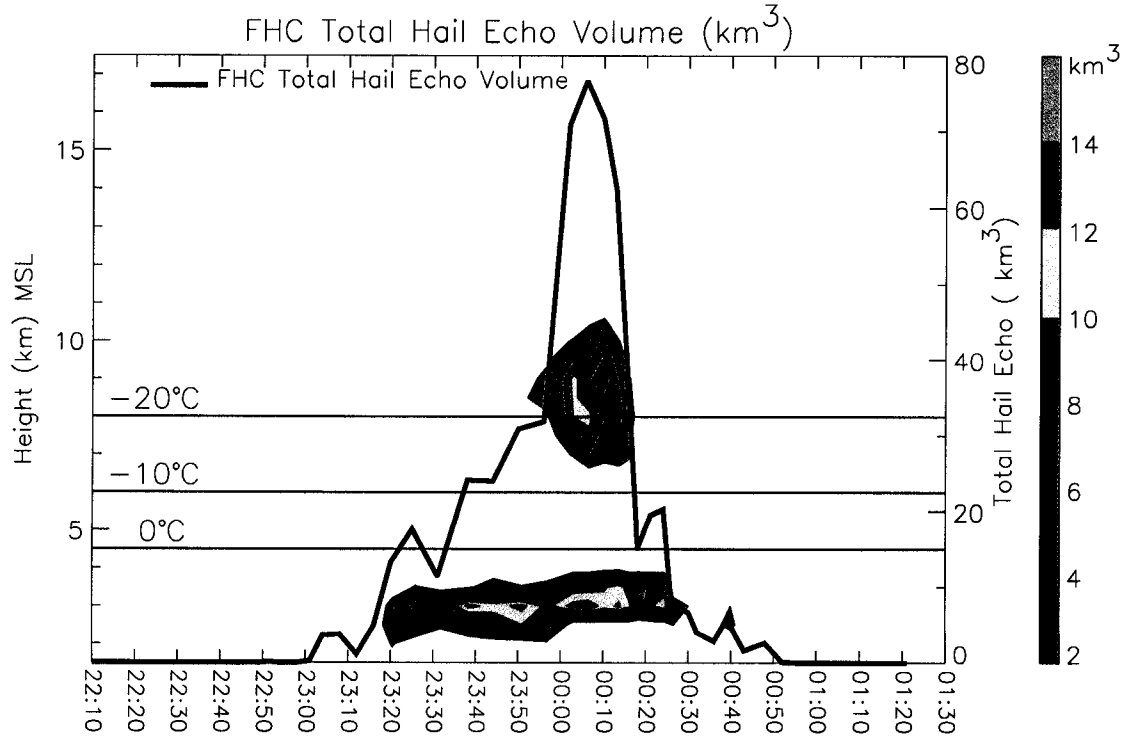

Figure 4.6: Color contours of FHC hail echo volume, with total (height-integrated) hail echo volume overplotted as black line. The "hail" here is composed entirely of small (<2cm) hail. The only large hail signal was at 0013.

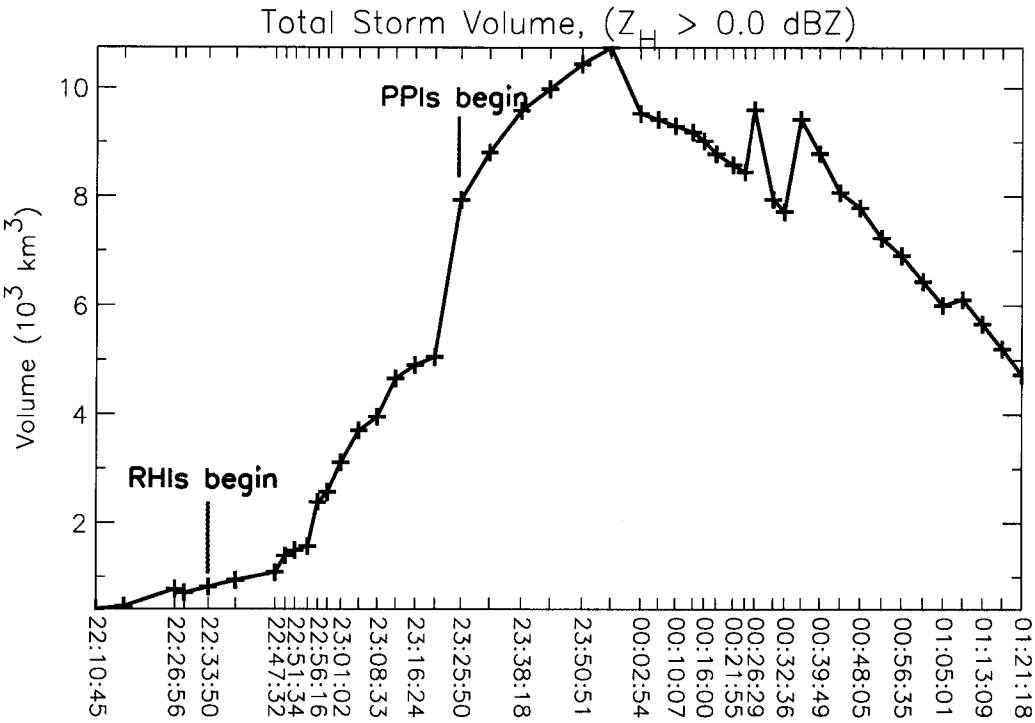

Figure 4.7: Time series of total storm echo volume ($Z_H > 0$ dBZ) for 3 June 2000. Each tick mark on the time axis corresponds to the beginning of a volume scan (some of the time axis labels have been omitted for clarity). The blue and red text indicates times when the scanning strategy transitioned from RHIs to PPIs. RHI scans were conducted from 2233 to 2320, and PPI scans were conducted at all other times.

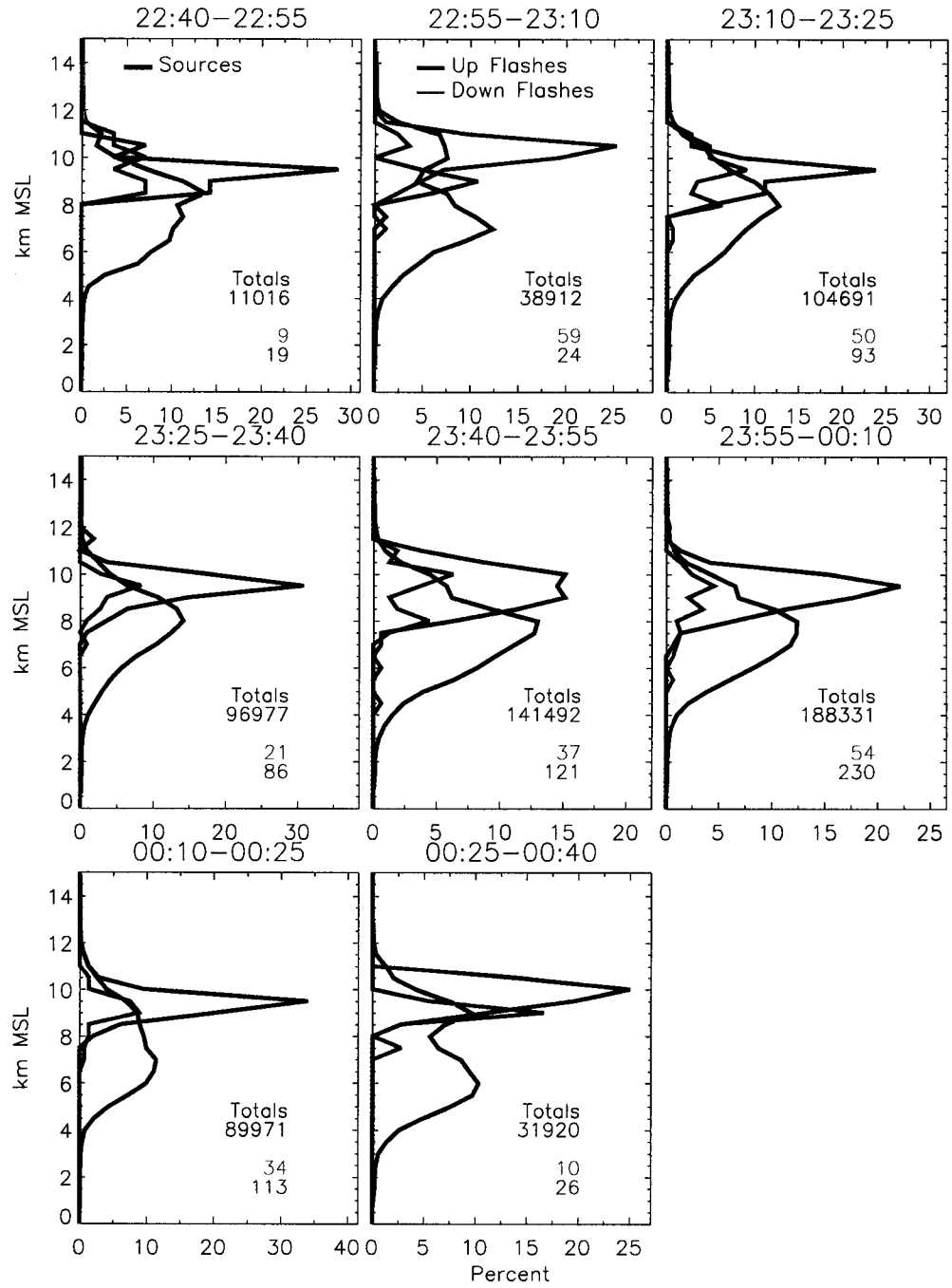

Figure 4.8: As in Fig. 3.12, but for the 3 June storm.

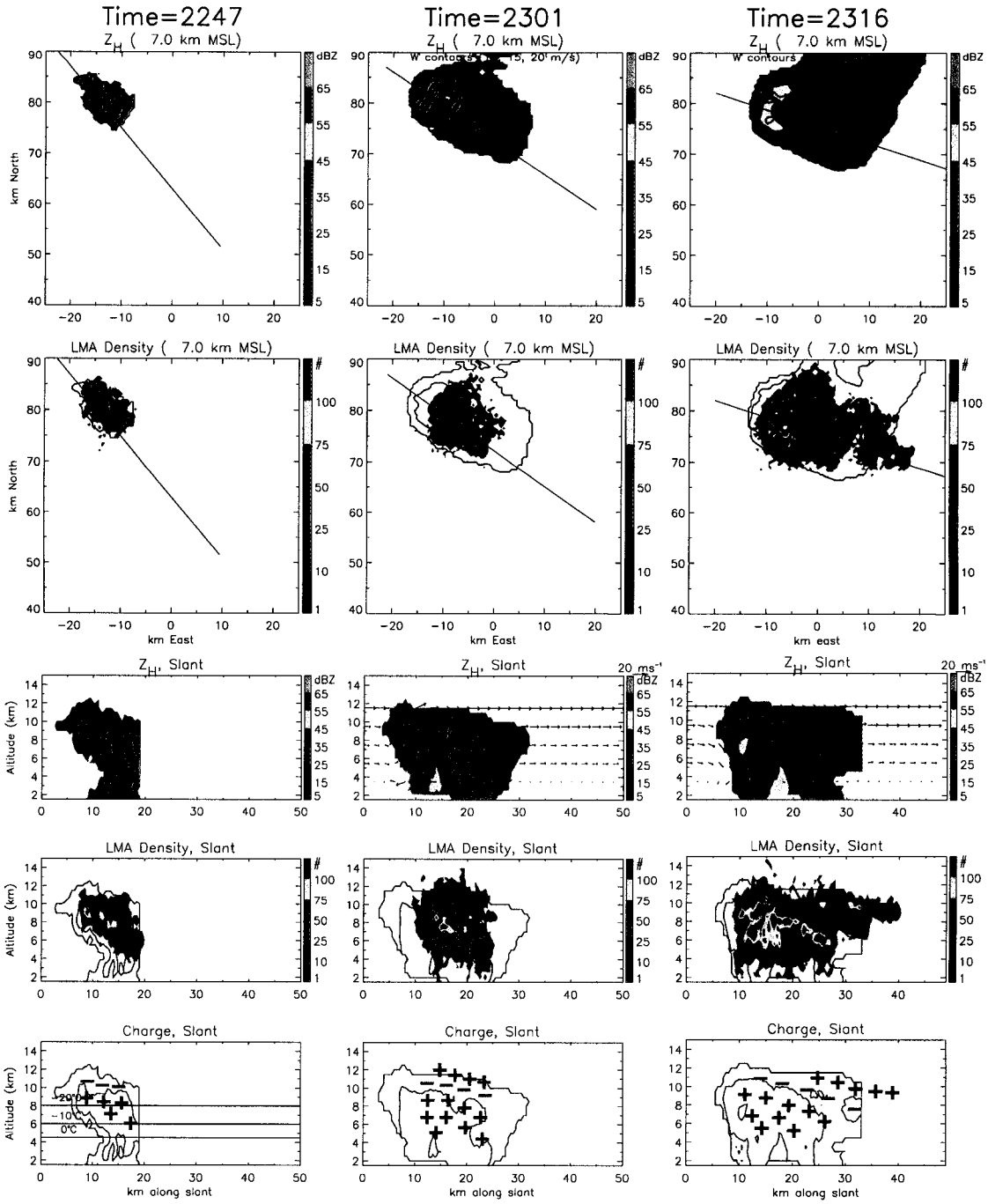

Figure 4.9: Representative cross-sections at 2247, 2301 and 2316. Each column corresponds to the same time. From top to bottom: Horizontal cross-sections at 7 km altitude of radar reflectivity (Z_H) and LMA density. Vertical cross-sections of Z_H (with wind vectors), LMA density and composite charge structure along the line indicated in the horizontal cross-sections. Top panels also have additional black contours of updraft in 5 ms^{-1} intervals starting at 10 ms^{-1}. Contours of Z_H (5,25,45 dBZ) are repeated on the LMA density and charge composites. LMA densities are cumulative over five-minute intervals starting at the volume scan time and are restricted to within 5 km of the cross-sections. There was no multi-Doppler coverage during the 2247 volume scan.

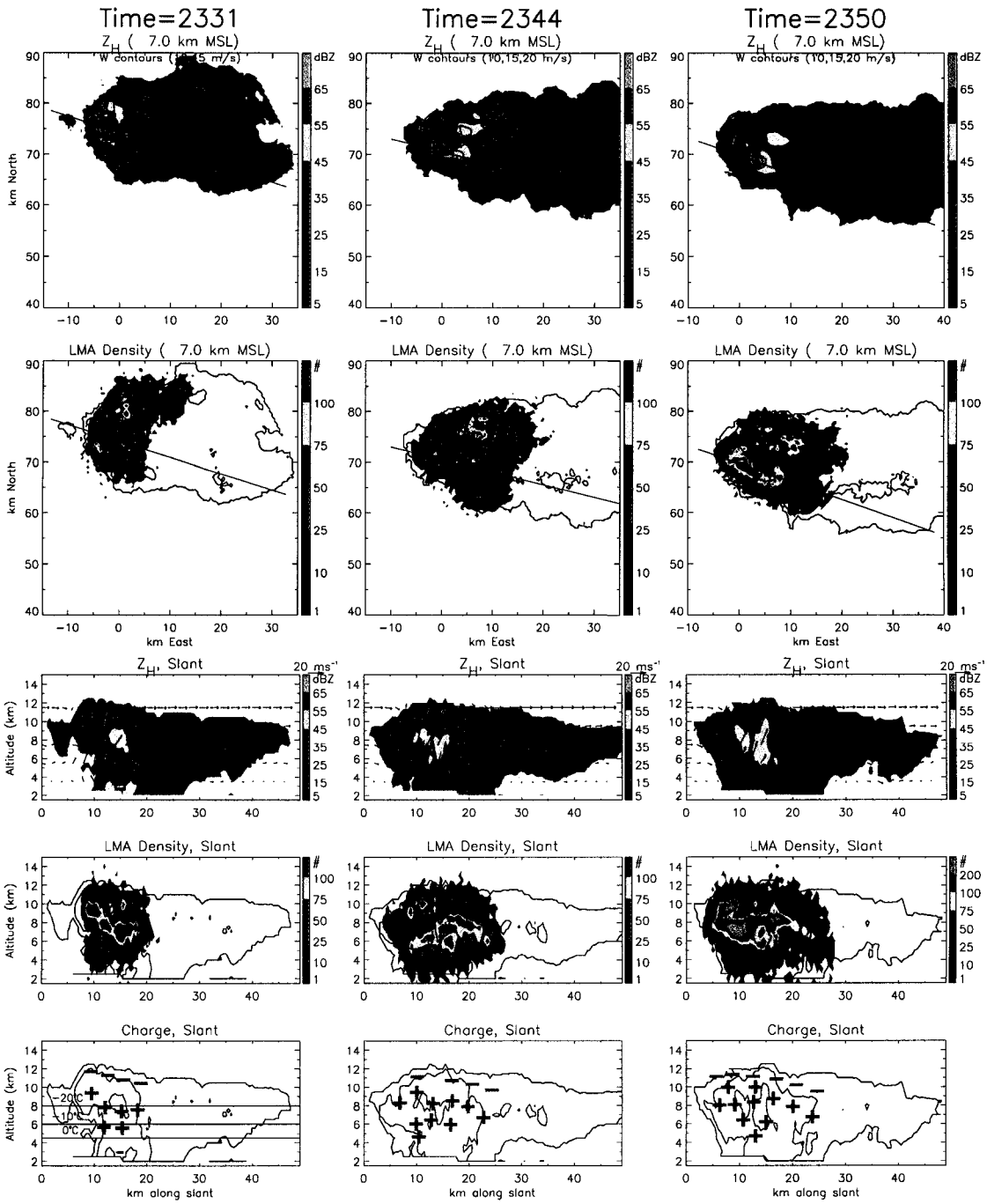

Figure 4.10: As in Fig. 4.9, but for volume scans beginning at 2331, 2334, and 2350.

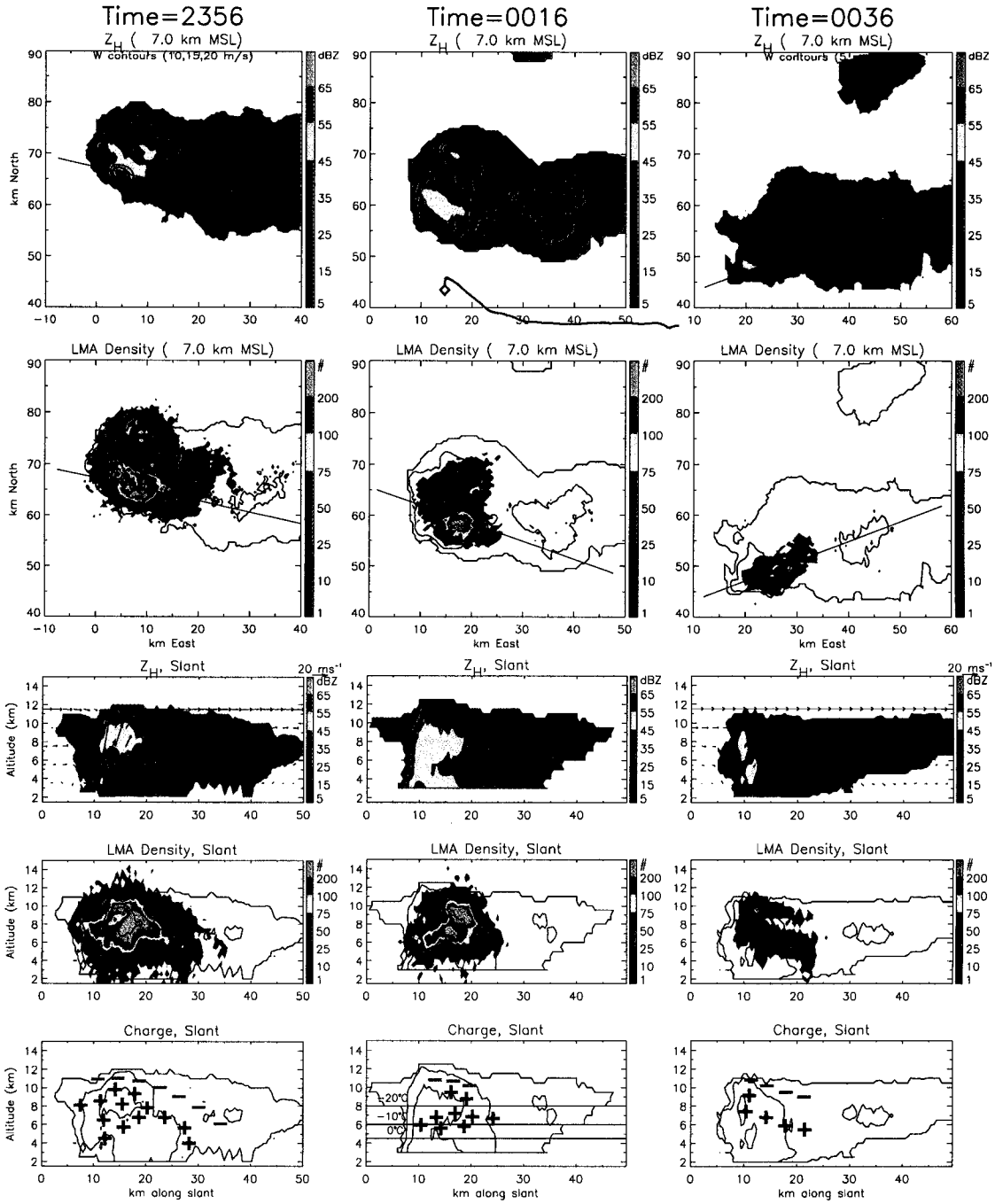

Figure 4.11: As in Fig. 4.9, but for volume scans beginning at 2356, 0016, and 0036. There was no multi-Doppler coverage during the 0016 volume scan. The magenta line in the top panel at 0016 shows the trajectory of the MGLASS sounding in Fig. 4.1, and the filled diamond symbol marks the launch site of the sounding. The updraft contour in the top panel at 0036 is 5 ms^{-1}.

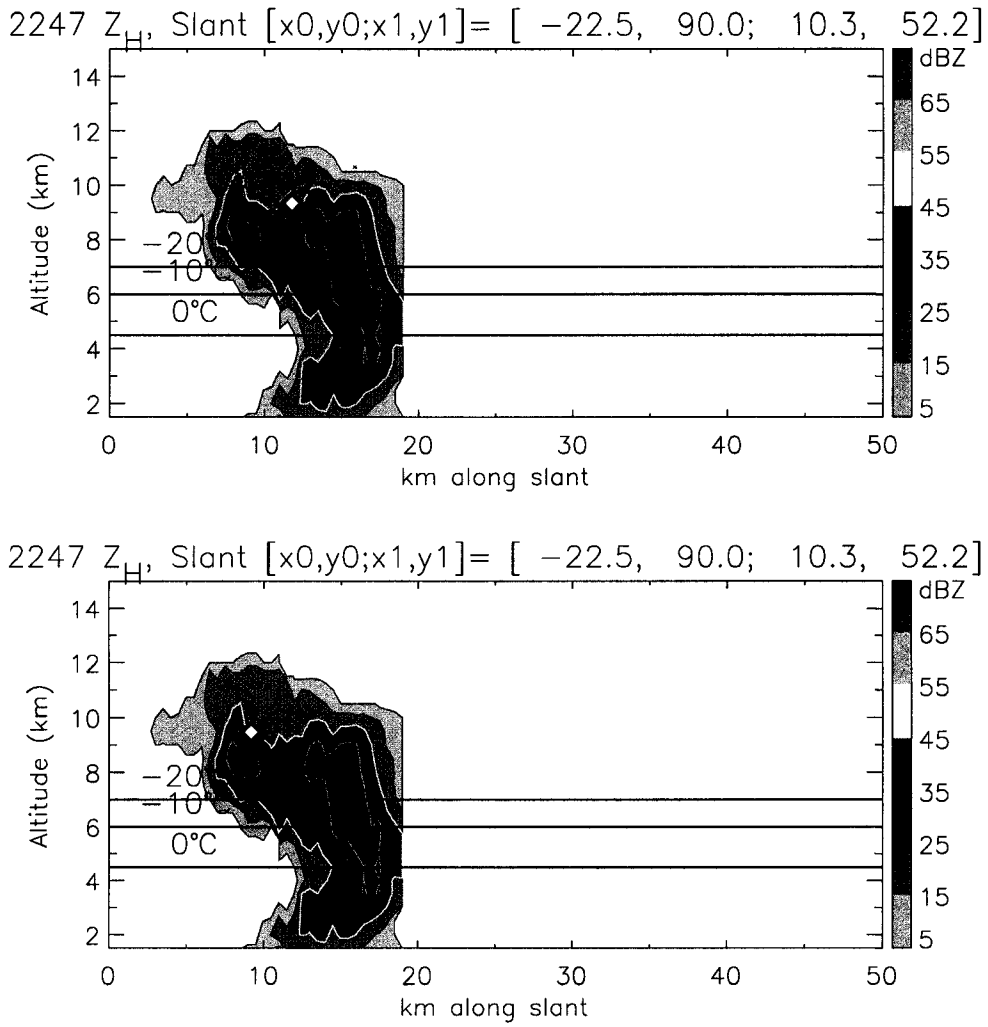

Figure 4.12: Vertical cross-section at 2247, with charge-coded LMA flashes at (top) 2247:35 and (bottom) 2249:51. There are actually two flashes in the top panel, one more compact on the left side, the other deeper on the right. The black and white filled diamond symbols mark the first source of each flash. These vertical cross-sections are along essentially the same slant path as in the left column of Fig. 4.9.

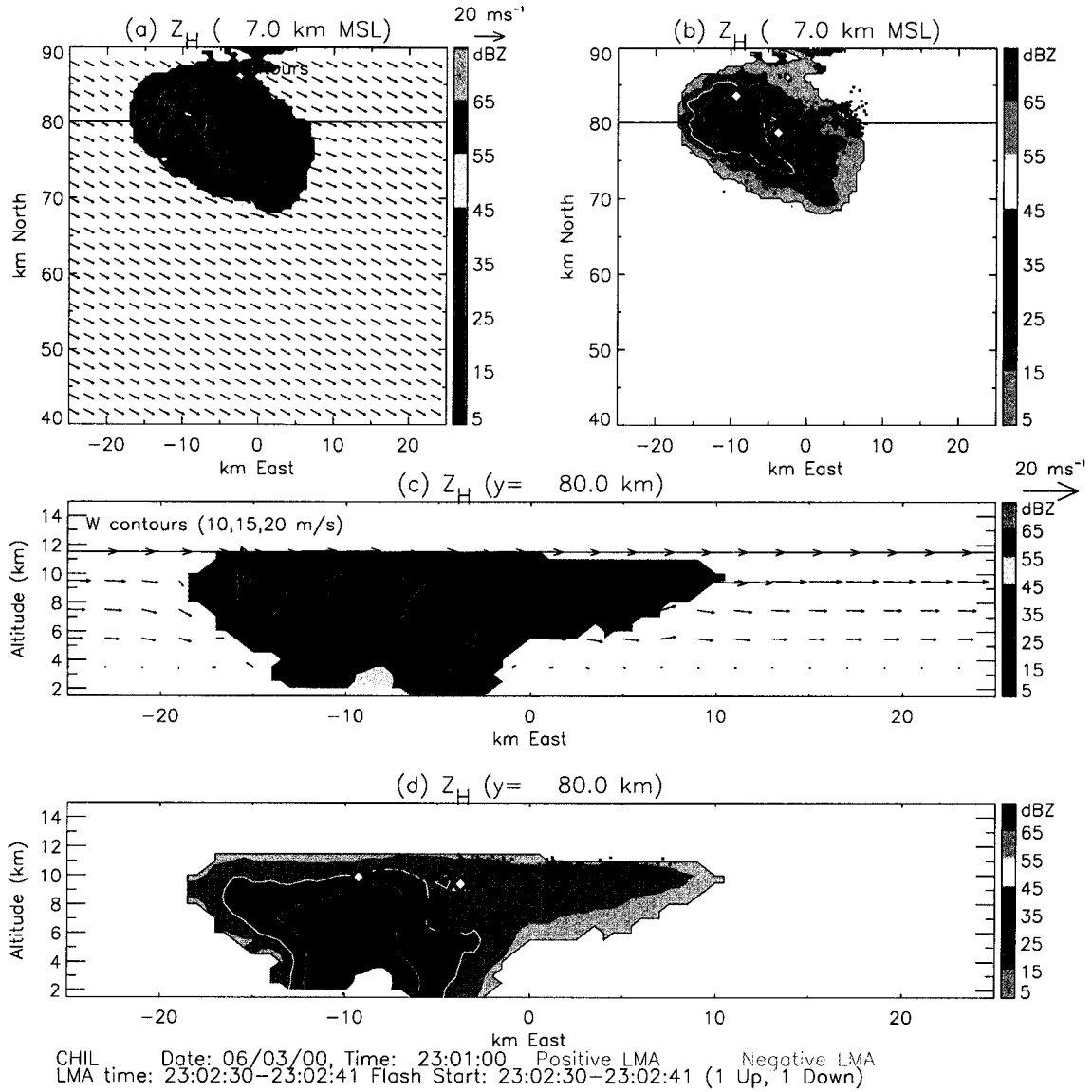

Figure 4.13: Radar cross-sections at 2301. (a) and (c) have horizontal and vertical cross-sections of Z_H (color-shaded) with wind vectors and additional black contours of updraft (10, 15, 20 ms^{-1}. (b) and (d) are the same cross-sections as (a) and (c) but have instead the lightning mapping of two flashes at 2302:30–41 overlaid and color-coded by inferred charge. Only those LMA sources within 5 km of the vertical cross-section are plotted in (d). The black and white filled diamond symbols mark the first source of each flash.

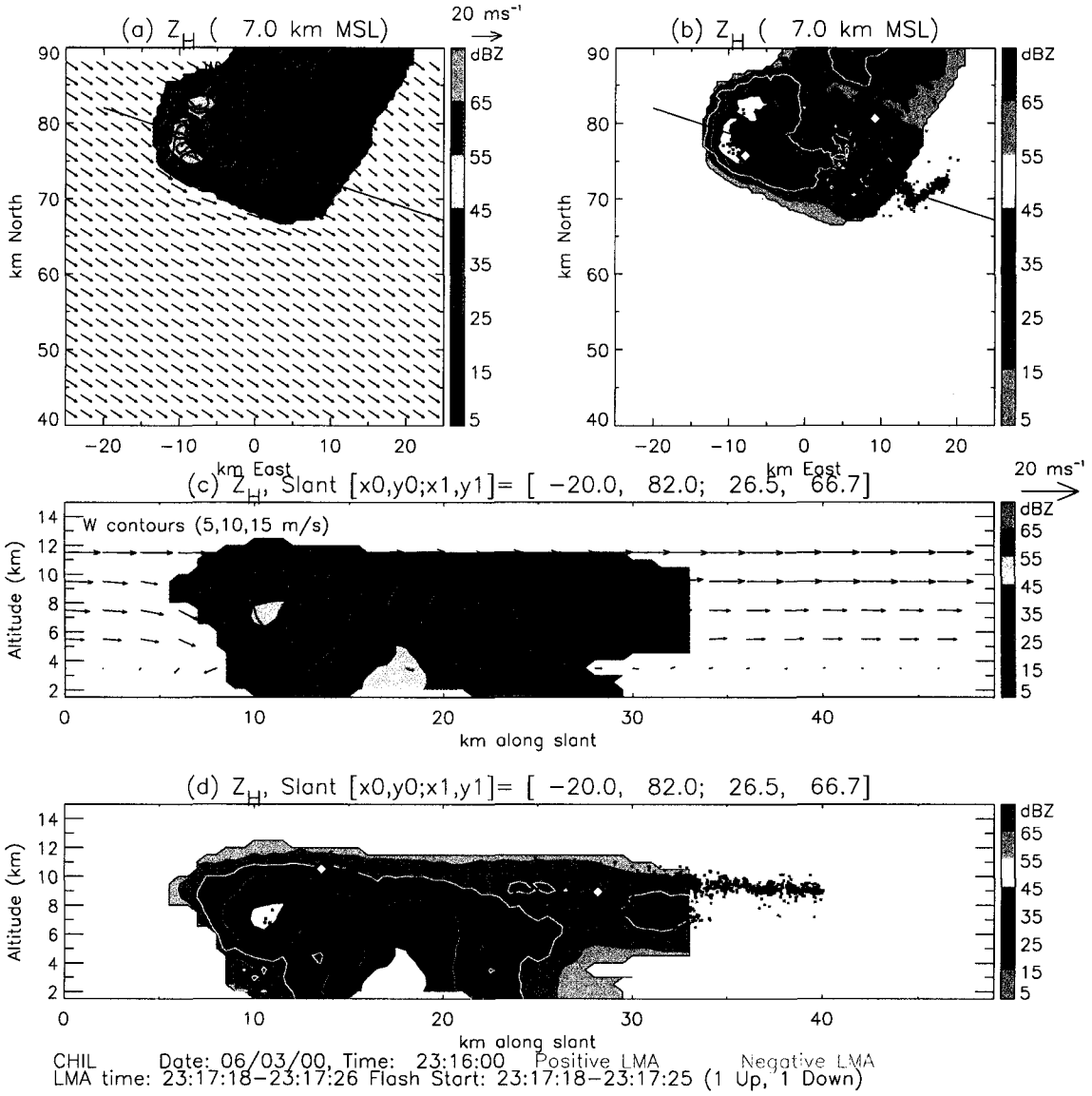

Figure 4.14: As in Fig. 4.13, but for the volume scan at 2316. Updraft contours are 5,10,15 ms^{-1}. Overlaid LMA sources are from two lightning flashes at 2317:18–26.

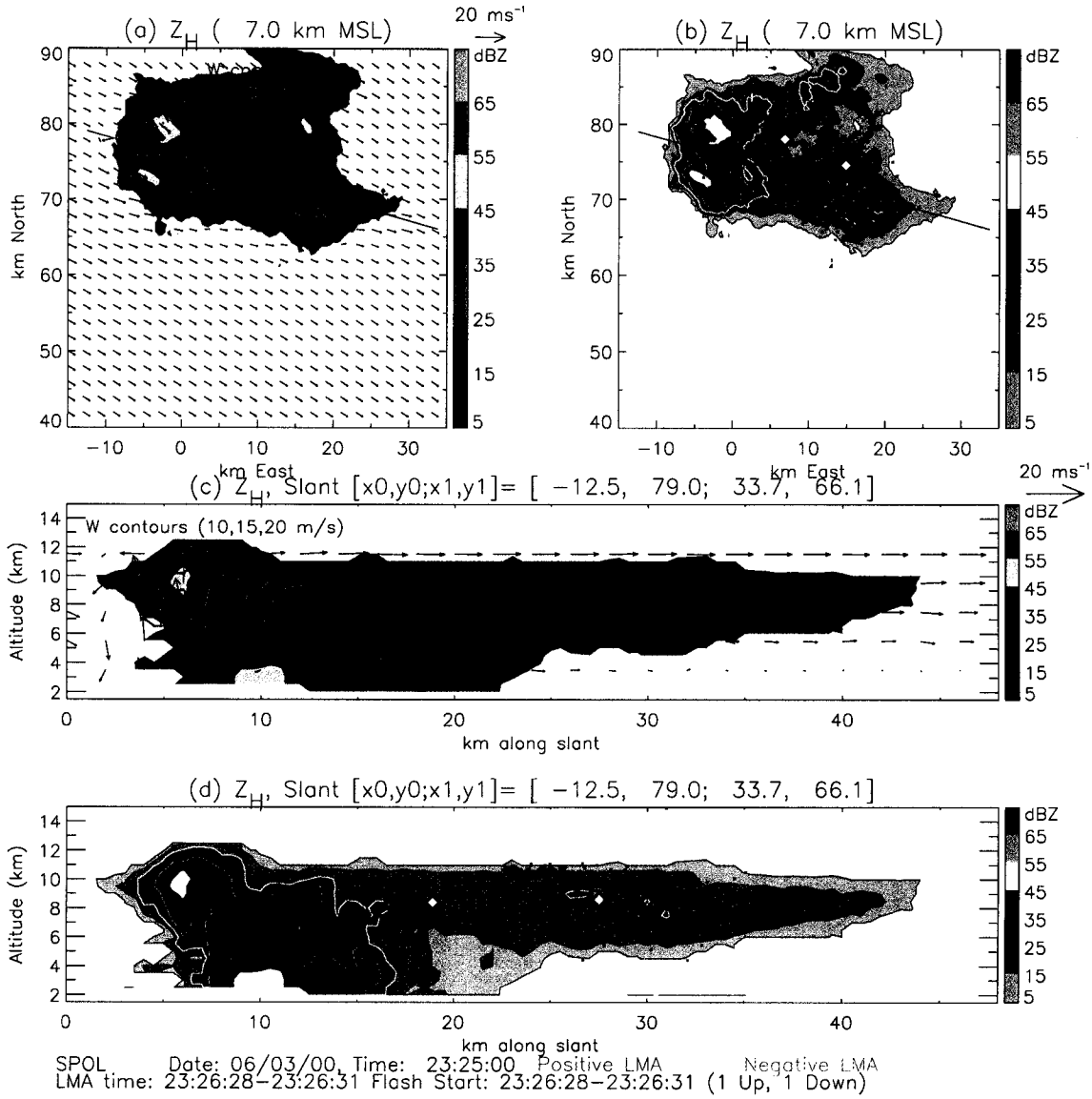

Figure 4.15: As in Fig. 4.13, but for the volume scan at 2325. Updraft contours are 10,15,20 ms^{-1}. Overlaid LMA sources are from two lightning flashes at 2326:38–41.

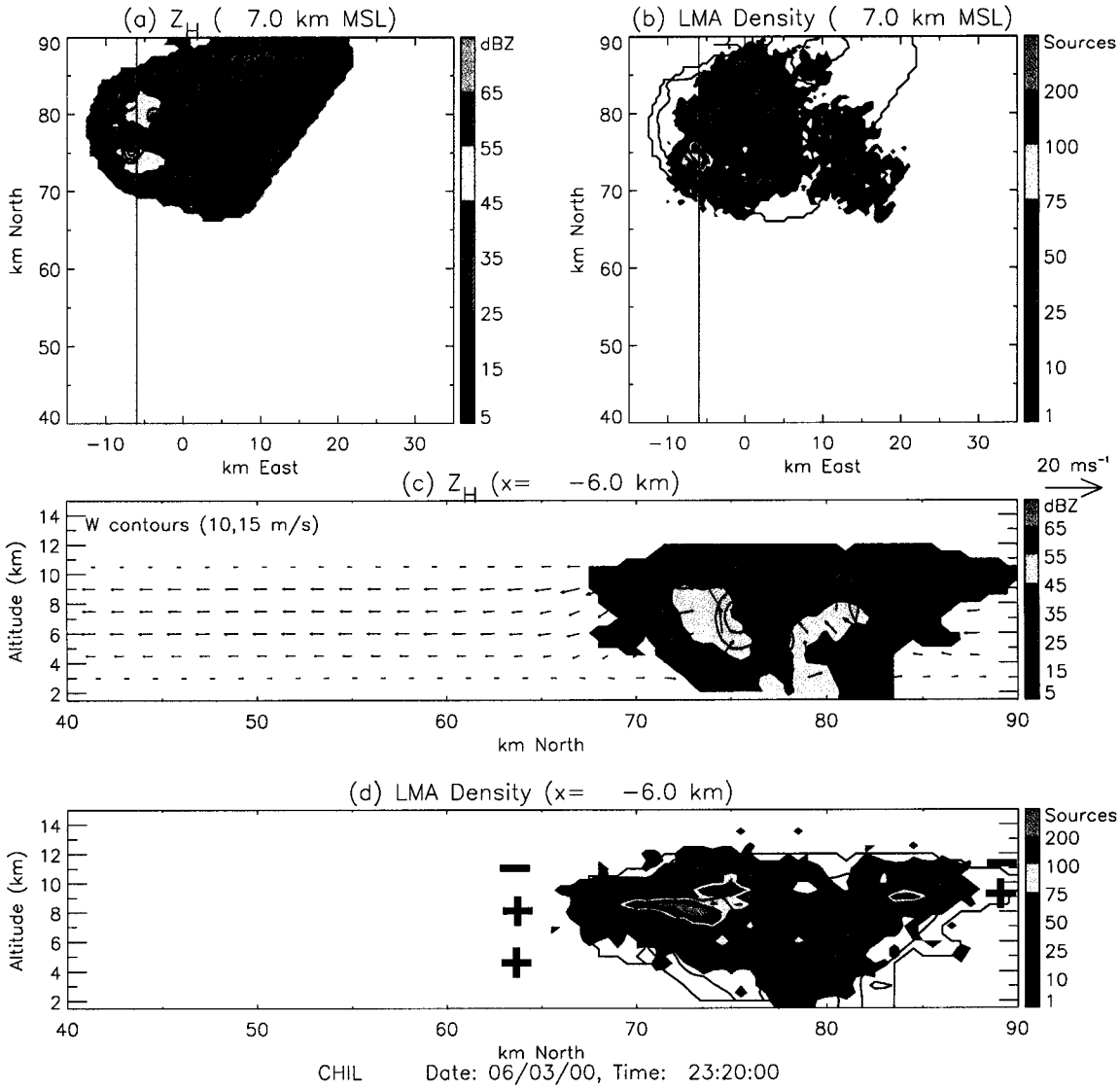

Figure 4.16: Radar and LMA density cross-sections during 2320 volume scan. LMA sources are from 2320–2325 and restricted to within 5 km of the cross-section. Plus and minus symbols in (d) indicate the gross vertical charge structure.

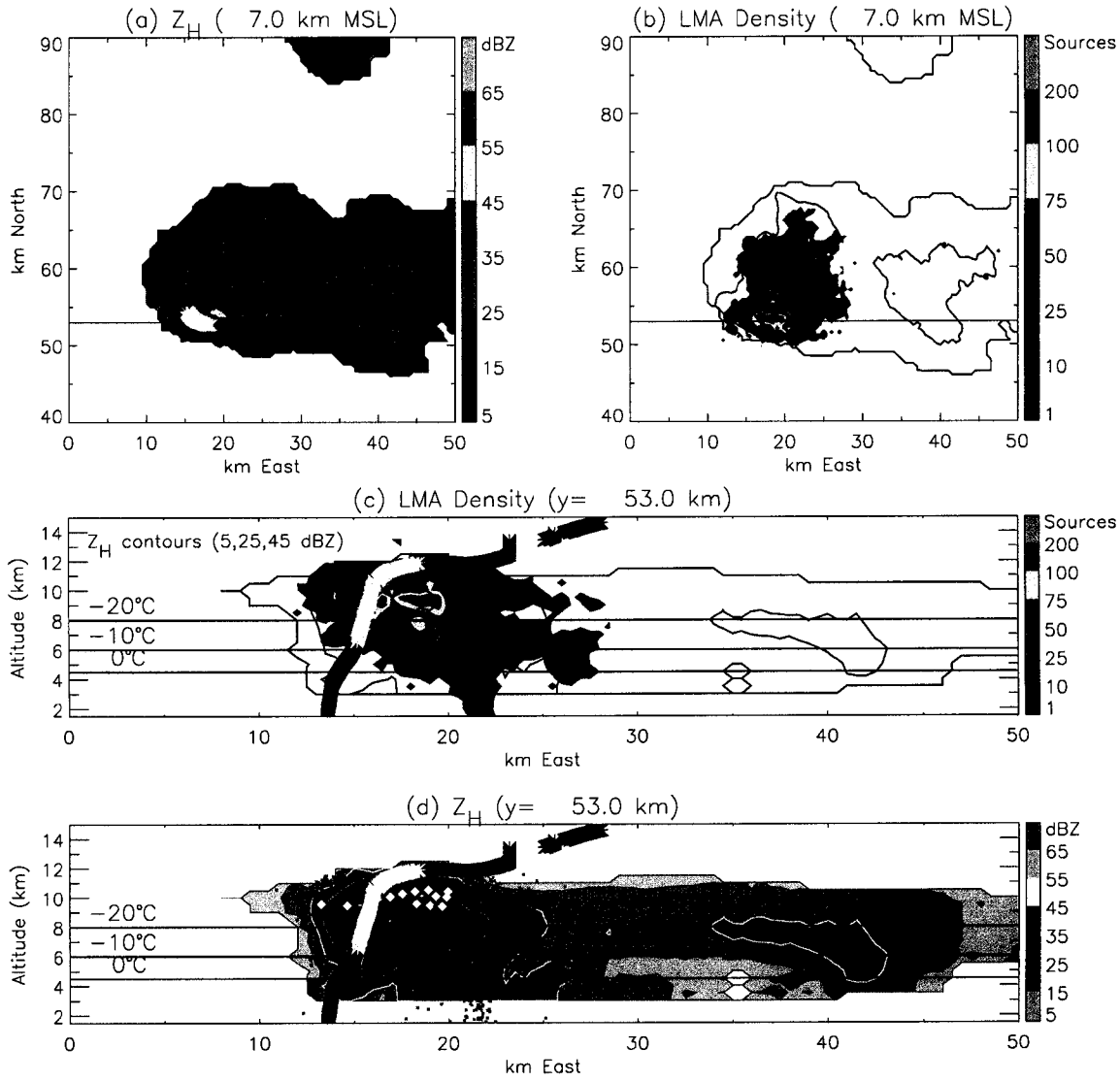

Figure 4.17: Radar and LMA cross-sections from volume scan at 0024, with EFM balloon sounding trajectory overlaid onto (a), (c) and (d). LMA sources are from 0023–0028 and plotted in terms of density in (b) and (c) and overlaid and color-coded by inferred charge in (d). The black and white filled diamond symbols in (d) mark the first source of each flash. The balloon was launched at 0013:51 and traveled eastward. The thick black line shows the complete trajectory, with the thick orange line indicating the part of the trajectory from 0023–0028.

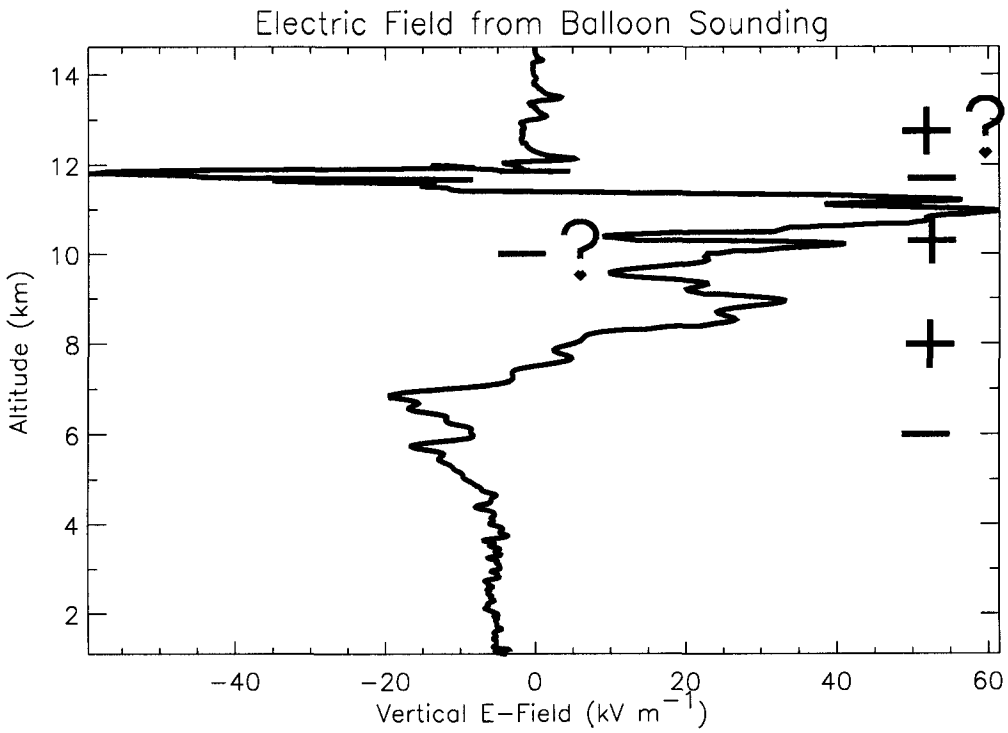

Figure 4.18: Vertical electric field profile measured by the balloon sounding shown in Fig. 4.17. Plus and minus symbols indicate the charge regions inferred from a 1-D interpretation of Gauss' Law. (See also Rust and MacGorman, 2002).

CHAPTER 5

23 JUNE OBSERVATIONS

5.1 Overview

There was a variety of storm activity on this day, most of it of a multi-cellular character. Fig. 5.1 shows the maximum reflectivity in each vertical column every 30 minutes over a 300x300 km domain centered on KGLD. Locations of +CG and –CG flashes are indicated by the green diamonds and red X's, respectively, and the total CG flash counts are listed beneath each panel. Isolated cells were rare and hence it was very difficult to follow and isolate a given cell from beginning to end. However, a few cells and distinct collections of cells were isolated enough to at least investigate their initial evolution and electrification prior to their merger with neighboring convection. This day was chosen for study because of the interesting pattern in ground flash activity. For the first hour of the observation period (1930 to 2100), negative CG flashes dominated. Though the –CG flash rate varied from cell to cell, there were up to ten –CG flashes min^{-1} during the first hour and a half, with only two +CG flashes in the entire domain. The ground flash activity then made a dramatic switch to positive polarity around 2100, with +CG flashes constituting 50–100% of the ground flashes in any given cell for the next hour and a half (2100 to 2230).

The blue numbers in Fig. 5.1 indicate the "storms" chosen for in-depth analysis. The first group of cells developed into a southwest-northeast oriented convective line about 125 km west of KGLD. Additional cells popped up to the north and south of the main convective line. This entire convective group tracked eastward at roughly 5 ms^{-1}. Hereafter this first group of cells will be referred to collectively as "storm

1". A weak, short-lived cell ("storm 2" in Fig. 5.1) formed just north of KGLD at 1930, produced a few –CG flashes and little lightning overall before dissipating by 2030. More vigorous, longer-lived, and +CG-dominated cells ("storm 3" and "storm 4") developed around 2040 near the remnants of "storm 2". Storm 3 remained relatively stationary and merged into storm 1 around 2200. Storm 4 tracked slowly northeastward and was the most intense storm of the four. Of the four storms, only storm 3 was scanned by one of the polarimetric radars for most of its lifetime and was also the only storm for which high-quality multi-Doppler synthesis was possible. The following sections discuss Storms 1 and 3 in more detail. Unfortunately, there was not enough time to analyze storm 4.

5.2 Storm 1

Radar coverage of storm 1 was less than optimal. Polarimetric radar coverage (CHILL or S-Pol) extended only from 1945 to 2054, and multi-Doppler coverage only from 2022 to 2041. The KGLD radar scanned this storm continuously from 1930 to 2200, but KGLD had problems with attenuation from heavy precipitation nearby and went down at 2200 due to a lightning strike. Despite these issues with the radars, storm 1 was chosen as a case study because of its interesting ground flash production. Of the 324 CG flashes from 1930 to 2115, only two of them were +CG flashes. Frequent (1–2 min^{-1}) +CG flashes began at 2117, and –CG flashes ceased altogether by 2130. Of the 27 CG flashes from 2120 to 2200, 20 of them were +CG flashes. Hence, this case provides the opportunity to contrast the radar echo and charge structure during both –CG-dominance and +CG-dominance. This case also serves as a nice comparison to the +CG-dominated 29 June supercell and the no-CG storm on 3 June.

An MGLASS sounding (Fig. 5.3) was launched 20 km west of the CHILL radar site at 1728, about an hour and a half before the development of storm 1. The location of this sounding is indicated by the magenta line in the top-left panel of Fig. 5.1. This sounding was to characterize the pre-storm environment for storm 1, and its

temperature profile was used in the FHC computations. According to this sounding, surface winds were generally southerly and weak, and upper-level winds were westerly and strong. The environment was dry and hot, with a surface temperature near 90°F and dew point of 45°F. Convective Available Potential Energy (CAPE) was around 300 J kg^{-1}, substantially less than the CAPE in the 29 June and 3 June storms. The sounding-inferred cloud base was near 600 mb.

5.2.1 Storm 1 Overview

The evolution of this storm is best summarized by the series of representative radar cross-sections in Figs. 5.4 and 5.5. The format of these summary cross-section figures is essentially the same as in Chapters 3 and 4. The convection on this day was disorganized, with few cases of isolated cells. The complex of cells that comprised storm 1 was no exception. The first cell of this storm initiated around 1900 at the southern end of what would become a southwest-northeast oriented line of cells. The first lightning flash was at 1925, and by 1941 (left column in Fig. 5.4), this first cell had already developed a strong (>55 dBZ), deep precipitation shaft. As the storm 1 complex evolved, new cells developed further north along the main convective line, with additional development to the north and south of the line. The whole storm 1 complex tracked eastward at roughly 5 m s^{-1}. As is evident in the horizontal cross-sections of Figs. 5.4 and 5.5, the lightning activity (in terms of LMA source density) generally mapped out the convective cores of each cell in this storm complex. Where you see strong (>35 dBZ) reflectivity at 7 km MSL, you also see lightning, and the stronger, deeper convective cells generally have much more lightning. One could almost use the cross-sections of LMA source density as proxy for the radar cross-sections. This reinforces the idea that robust riming growth and the resultant precipitation-sized ice is crucially important to thunderstorm electrification (assuming, of course, that smaller ice crystals are also present and involved in the collisions with the rimers).

The time series of radar echo volumes and flash rates in Fig. 5.6 serve as a com-

panion to the cross-sections in Figs. 5.4 and 5.5. For comparison, these time series are shown for both the KGLD and polarimetric (CHILL and S-Pol) radars. Note the discontinuity in the KGLD echo volumes of Fig. 5.6, especially apparent at 2045. KGLD had apparent attenuation problems from 2045 onward. There was a separate, strong storm just west of the KGLD radar at this time[1], and the heavy precipitation from this separate storm system may have been the cause of KGLD's attenuation. As a result, much of the mid-level echo of the storm 1 complex was lost and/or not corrected for attenuation. Because of the issues with the radar coverage and because of the multicellular nature of the convection, no effort was made to compute time series of echo volumes and lightning flash rates for a specific isolated cell. Hence, the time-series plots of reflectivity echo volumes and flash rates in Fig. 5.6 include all the cells of the domain shown in Figs. 5.4 and 5.5. Despite the issues of radar data quality and disorganization of the convection, these time series plots still show some interesting features. There were three or four distinct periods of growth, each of which was generally associated with development of new convective cells:

1. The initial formation and intensification of the cells along the main southwest-northeast line from 1930 to 1950.

2. Onset and intensification of convection to the north and south of the main line from 2020–2040.

3. Development of a very strong cell on the southeast edge of the storm complex from 2100 to 2130 combined with continued intensification of cells to the east-southeast.

The lightning flash rate was not as well-correlated with the various radar echo volumes as it was in the 3 and 29 June cases. This is likely due to the relatively poorer quality and coverage of the radar data as well as to the overall disorganization of

[1]This separate storm was storm 3 which also produced the +CG strike that knocked out the KGLD radar from 2200–2300. See, for example, the bottom-right panel Fig. 5.1.

the convection on 23 June. However, the total flash rate clearly increased during each growth period. This is most evident when comparing the total flash rate and contours of total LMA source density to the echo top heights and volumes of reflectivity exceeding 40 and 50 dBZ (i.e., Figs. 5.6 and 5.7). Total flash rates were 10s min^{-1} until the rapid increase at 2040 which took the flash rate to near 100 min^{-1}. Additional lightning "jumps" occurred thereafter, with the flash rate fluctuating by 100% between 100 to 200 min^{-1}.

This storm complex was utterly –CG-dominant for its first two hours (Fig. 5.7), and there is some indication that –CG flash rates followed the trends in the total flash rates (and, by association, the trends in storm growth). However, during the storm's most intense later stages (e.g, after 2100), the total flash rate increased substantially while the –CG flash rate steadily declined. Around 2115, the polarity of the CGs switched to all positive, and ground flashes ceased altogether during the absolute peak in total flash rates from 2150–2200. Though the time series plots don't extend past 2200[2], Fig. 5.1 shows that this storm produced another flurry of +CG flashes before merging with other convection and dissipating.

5.2.2 Initial Growth and Electrification

During the first hour and a half (1930 to 2100) of lightning activity, all of the lightning within each cell of the storm 1 complex indicated a consistent normal tripole charge structure (see e.g., Figs. 5.4 and 5.5). The main negative charge region resided at an altitude of 6–8 km ($-10 > T > -20°$ C), with positive charge above, and a lower positive charge region extending downward from 5 km MSL (T$\approx$ 0°C). Essentially all of the lightning flashes were either normal ICs (between the mid-level negative and upper positive charge) or inverted lower ICs (between the mid-level negative and

[2]The time series and general observation period of storm 1 end at 2200 for several reasons. Again "storm 3" was mostly to blame. Storm 1 had been slowly merging into the stationary storm 3 to the east. Around 2200 the storms had merged to such an extent that it was nearly impossible to tell which lightning was caused by which storm. Meanwhile, the CHILL and S-Pol radars were scanning only storm 3 and ignoring storm 1.

the lower positive charge). Many, but not all, of these lower flashes continued on to ground as –CG flashes. As is evident in the vertical cross-sections of LMA density in Fig. 5.4 the normal IC flashes in the upper levels were the most frequent type of flash. Note that for each cell, the highest concentration of LMA sources in each cell was at 8–10 km altitude, corresponding to the inferred location of the upper positive charge. The secondary maximum in the LMA concentration near 5 km altitude corresponds to the inferred location of the lower positive charge.

To further illustrate this charge structure, Fig. 5.8–5.10 provide some representative examples. Fig. 5.8 shows 20 seconds of lightning mapping data around 1954 comprised of nine normal IC flashes and four low inverted flashes along the line of cells. Fig. 5.9 shows these flashes overlaid onto radar cross-sections. Note the consistent location of the mid-level negative charge in both the upper normal and lower inverted flashes. Also note that only three of the four lower flashes were associated with –CGs. Fig. 5.10 shows the the charge structure revealed by lightning mapping for the surrounding ten minutes. Here the LMA sources are plotted in terms of "charge density" which highlights the strikingly consistent structure along the line of cells. In particular, note the altitude histogram in the top-right of Fig. 5.10. Here the red (blue) curve includes only those LMA sources in inferred positive (negative) charge regions. The two positive charge regions stand out quite clearly, with the upper positive being the more active of the two. According to Cummins et al. (1998), the –CG detection efficiency of the NLDN is 80–90% in the STEPS region. Note, however, that not all (indeed, less than half) of the low inverted flashes in Fig. 5.10 were identified as –CGs by the NLDN. Hence, the lower positive charge of the tripole was revealed by low inverted flashes regardless of whether these flashes continued on to ground as –CGs.

Figure 5.11 shows altitude histograms of the LMA sources and flash start heights for nine 15-minute blocks from 1945 to 2145. These histograms provide another very illuminating and more objective way to illustrate (or at least corroborate) the gross vertical charge structure inferred from the tedious flash-by-flash analysis. Note that

from 1945 to 2030, most of these LMA source histograms (black curves in Fig. 5.11) have a prominent maximum at 8–10 km, with a secondary maximum at 4–6 km. Recall that the LMA is most sensitive to negative breakdown through positive charge. Hence, these two maxima correspond to the upper and lower positive charge regions of the tripole charge structure consistently observed in the detailed flash-by-flash analysis. During this same time period, the flash initiation distributions (red curves) show about the same shape as the LMA source distributions, but the altitudes of the flash start maxima are systematically offset from the maxima of the LMA sources in a way that is consistent with a tripole charge structure. In each of these histograms, the main flash start height maxima that systematically lie *below* the main LMA source maxima correspond to normal IC flashes that initiate between the upper positive and mid-level negative charge regions and proceed upward into the upper positive charge region. The secondary flash start height maxima that systematically lie *above* the secondary LMA source maxima correspond to low inverted flashes that initiate between the mid-level negative and lower positive charge regions and proceed downward through the lower positive charge region, sometimes continuing on to ground as –CGs. All in all, the upper and lower maxima in the flash start distributions may be interpreted as the approximate upper and lower bounds of the main mid-level negative charge region. Or, in other terms, these two flash start maxima correspond to the altitudes of maximum vertical electric field between regions of net positive and net negative charge (Coleman et al., 2003). Fig. 5.12 offers further clarification of this interpretation. Here, the flash start heights are objectively partitioned, based on their initial velocity, into flashes that initiated upward and downward. As expected, the main upper flash start height maxima are composed mostly of flashes that initiated upward, and the secondary lower flash start height maxima are composed of flashes that initiated downward.

This persistent and pervasive tripolar charge structure is consistent with the overwhelming dominance of –CG flashes during the first hour and a half of ground flashes, with lower positive charge providing the necessary downward bias for these –CG

flashes. As shown in Fig. 5.13, the bulk of the –CG mean origin heights lie between the altitudes of the two LMA source maxima in Fig. 5.11. That is, the –CG flashes are obviously originating from the negative charge region. Hence, the origin heights of the –CG flashes are also consistent with this tripole structure. To place these –CG origin locations within the context of the storm, they are plotted as green diamond symbols in Fig. 5.7b and on the vertical cross-sections of LMA density in Figs. 5.4 and 5.5. Though there is some scatter, the majority of the –CG flashes originated on the upper side of the inferred lower positive charge region. The majority of the –CGs tended to cluster near the strongest precipitation, and low inverted flashes without attendant –CGs did the same. This suggests that the lower positive charge involved in these flashes was carried by the largest precipitation particles, which is in accordance with the tripole model, the NIC mechanism, and the concept of a charge reversal level.

More information about the charge structure and CG flashes can be gleaned from further examination of the altitude distributions in Fig. 5.13a which show the *mean* origin heights (i.e., the mean altitude of the first 10 sources of each CG flash). The mean of the first 10 sources is used instead of the very first source in order to reduce the effect of location errors and noise sources. As shown in Fig. 5.13b, there's generally little difference between the mean origin height and height of the very first source. However, this height difference tends to be systematically of one sign for –CG flashes and the other sign for +CG flashes. This difference is consistent with the assumed configuration of the charge regions involved, the physics of the breakdown process, and, in particular, the way the LMA operates. The first ten sources of a –CG flash typically have a downward trend because the LMA senses the initial negative leader as it initiates from negative charge toward positive charge and the ground below. The first ten sources of a +CG flash, on the other hand, typically have an upward trend as the LMA senses the initial negative leader as it initiates upward from negative into positive charge. Hence, in the mean, the mean origin heights of –CG flashes are generally slightly higher than the true origin heights, while the mean origin heights

+CG flashes are actually slightly lower than the true origin heights. Incidentally, this may partially explain the extremely low mean origin heights of some of the –CGs, because sometimes the initial negative leaders of –CGs propagate rapidly downward, resulting in a downward bias of their mean origin heights.

5.2.3 Dipoles, Tripoles, and –CGs

In the archetype tripolar airmass thunderstorm, IC lightning typically precedes –CG lightning by several minutes (e.g., Williams et al., 1989b). The initial IC flashes describe an upper dipole (positive over negative) charge structure, with the main negative charge consistently located within a specific temperature regime (roughly near 6 km MSL). The onset of –CG flashes is generally coincident with the descent of the ice mass in the convective core. Once the lofted ice particles grow large enough to achieve a terminal velocity that exceeds the updraft velocity (or updrafts weaken), the ice mass descends. Laboratory measurements (e.g., Takahashi, 1978; Saunders and Peck, 1998), observations (e.g., Krehbiel 1986; Williams, 1989; Williams et al., 1989b), and modeling studies (e.g., Mansell 2000; Mansell et al., 2002) consistently indicate that this descending ice starts to acquire positive charge in collisions after descending through the height (or temperature range) of the main negative charge region, thus forming the lower positive charge. This lower positive charge provides the impetus for –CG flashes from the main negative charge region (e.g., Jacobson and Krider, 1976; Williams et al., 1989b; Mansell et al., 2002; Marshall and Stolzenburg, 2002). Though further observations of such relationships between lightning type and convective state wouldn't bring anything new to the field of thunderstorm electrification, they are worth at least a brief discussion due to the additional insight provided by the LMA measurements.

Nearly every cell in the storm 1 complex exhibited the pattern of storm growth and lightning activity described in the previous paragraph. There were certainly variations, but in general, each cell typically followed this sequence of events:

1. During initial growth, all flashes were normal IC flashes indicating a simple dipole, with the negative charge in the stronger lofted echo (graupel), and upper positive charge in weaker echo above (presumably consisting of smaller ice crystals).

2. During the mature stage, after the lofted precipitation grew and descended to the ground, inverted flashes began between the pre-existing main negative charge in strong echo aloft and lower positive charge in the strongest echo nearest the surface. Negative CG flashes commenced only after this precipitation descent and attendant formation of the lower positive charge region. Inverted IC flashes through the lower positive charge typically revealed this lower positive charge prior to the onset of –CG flashes; however, the –CG flashes consistently initiated at the same location as lower inverted IC flashes. During this mature stage, the majority of flashes continued to be normal ICs between the upper two charge regions of the tripole.

3. During the dissipating stage, the entire tripole structure descended, and flash rates tapered off. Remnants of the upper positive charge sometimes remained and were tapped by flashes initiating within neighboring cells.

For example, Fig. 5.14 shows five minutes of lightning mapping during the first ten minutes of lightning activity in the initial cell of the storm 1 complex. Fig. 5.15 shows this lightning in the context of radar data. This cell was in a developing stage at this time, with its strongest echo residing aloft and no >35 dBZ echo yet reaching the surface. Accordingly, until the low inverted flash at 1932:10, all the lightning flashes were normal IC flashes between the mid-level negative and upper positive charge regions. The inferred negative charge was apparently carried by the largest ice particles in the strong lofted echo while the upper positive charge was in the weaker echo aloft. The low flash at 1932:10 was the first such flash to indicate the lower positive charge. Over the next ten minutes (e.g., left column of Fig. 5.4), the lofted precipitation grew and descended, the lower positive charge became more actively

involved in the lightning production, and –CG flashes ensued. There were a total of three low flashes through the lower positive charge prior to any –CGs through the same lower positive. (As a counter-example, there was also a very weak and short-lived cell just northeast of the main cell in Figs. 5.14 and 5.15. This cell produced only two flashes, both of them –CGs.)

These relationships between lightning type and convective state of the storm are also evident when viewing multiple cells side-by-side, with each cell in a different stage of its life cycle. Due to the multicellular convection, this day provided many opportunities for such side-by-side comparison. For example, the first column of Fig. 5.4 shows a new convective cell growing to the northeast of the main cell. This developing cell has its strongest echo aloft with little or no significant precipitation reaching the surface. Consequently, all of its initial lightning was composed of normal IC flashes describing only a normal dipole charge structure. Meanwhile, the more mature cell to the southwest had its strongest echo reaching the surface, a fully formed tripole charge structure, and numerous –CG flashes. Figs. 5.16 and 5.17 show a representative example of one of these –CGs which traveled directly through the strongest precipitation on its way to ground. The heights of the upper positive and main negative charge regions were roughly the same in both cells, though somewhat more elevated in the newer cell. By 1953 (middle column of Fig. 5.4), the newer northeastern cell had reached the mature stage with strong precipitation reaching the surface, a fully formed tripole charge structure and numerous –CGs discharging through the lower positive charge region.

5.2.4 Transition to Inverted Tripole and +CG Dominance

After 2045 or so, the morphology of the cells in storm 1 took a turn toward greater complexity as the total flash rates surged and –CG flash rates plummeted. Frequent clustered +CG flashes began soon after. The goal of this section is to answer the following question: How did the storm complex transition from –CG dominance to +CG dominance, and more specifically, was the charge structure that produced the

clustered +CG flashes significantly different from a normal tripole? The answer is that the +CG flashes did, in fact, result from a different parent charge structure, and this charge structure is best described as an *inverted* tripole. The source region of the clustered +CGs was a very active mid-level (5–8 km MSL) positive charge bracketed by negative charge regions on either side. As shown in the right column of Fig. 5.5, this inverted tripole structure formed in a collapsed cell in the middle of the storm 1 complex. The following describes how this process occurred.

Let's first examine this transition in the broad context provided by the LMA and flash start distributions of Figs. 5.7b, 5.11, and 5.12. As discussed above, prior to 2045 there were two distinct, vertically separated populations of LMA sources corresponding to the upper and lower positive charge regions of a normal tripole. From 2045 onward, these distributions flattened, with many more LMA sources in the lower population and a significant amount of LMA sources across a broad range of altitude (Fig. 5.11). By the time of the onset of +CG flashes at 2115, there were as many LMA sources in the lower population as in the upper one. Furthermore, the lower population had shifted upward to peak at near 6 km, suggesting that the lower positive charge was deeper or just further elevated from ground. The flash start height distributions also changed significantly. From 2045 to 2100, these flash heights continued to indicate a normal tripole charge structure, but with some perturbations. For example, there were more frequent downward flashes initiating from 5–8 km (Fig. 5.12), which is consistent with the increase in the growth of the lower population of LMA sources. There was also a new population of downward flashes near 11 km MSL (i.e, above the inferred location of the upper positive charge) suggesting an extreme upper negative charge. From 2100 to 2115, the distribution of flash initiation heights broadened out, forming a single broad maximum at 8 km that was bracketed by maxima of LMA sources above and below (Fig. 5.12). This single flash initiation maximum was composed of roughly the same number of upward and downward flashes. From 2115 to 2130, the upward and downward flash start distributions were again distinct, with most of the upward flashes indicating discharges into an active upper positive charge

region and most of the downward flashes indicating discharges into an equally active lower positive charge region (Fig. 5.12). The broad interpretation of these altitude histograms is that the increase of lightning in the lower population was the result of a stronger, or at least more active (in terms of LMA sources), lower positive charge. The decreased number of –CG flashes during this time may have been due to the increase in height of the lower positive along with the increase in strength or extent of the lower positive. That is, the lower positive may have effectively shielded the negative charge region from ground, making IC flashes involving the lower positive charge more energetically favorable than –CG flashes. Recall that a similar explanation was proposed to explain the lack of –CG flashes in the early stages of the 29 June supercell. Finally, note the small but distinct population of upward flashes in the lower panels of Fig. 5.12 that lie below the inferred location of the strong lower positive. This indicates a negative charge region below the lower positive. Hence, the onset and dominance of +CG flashes were likely due to the combined effects of (1) a large mid-to-low-level positive charge region and (2) a negative charge region below the positive that served to initiate positive flashes to ground.

Though the altitude distributions described in the previous paragraph give a broad summary of the charge structure evolution, these distributions contain lightning from more than just the collapsing cell that formed the inverted tripole and +CGs. In other words, they are somewhat ambiguous and overly coarse representations. To clarify and justify the interpretation of these altitude distributions, Figs. 5.18–5.28 show a series of radar and LMA cross-sections that the illustrate the transition to +CG flashing more explicitly.

At 2035, all cells still showed simple tripolar structure (Fig. 5.18). The central cell (hereafter called cell 'a') was well-developed but dissipating, with a lower positive charge actively involved in the lightning activity and frequent –CG flashes clustered in the precipitation core. The newer cells further south (hereafter called cells 'b' and 'c') were in earlier stages of development, with the majority of the lightning activity (i.e., LMA sources) in the upper positive charge, little lightning in the lower positive,

and comparatively few –CG flashes. Note also that the Doppler-inferred wind flow in Fig. 5.18c suggests that some of the hydrometeors from cells 'b' and 'c' were advected northwestward toward the collapsing cell 'a'. Presumably these hydrometeors carried charge, which may have had some influence on the charge structure transition that followed.

By 2048 (Fig. 5.19), cell 'a' had collapsed, with lower-level flashes becoming more frequent and upper-level flashes becoming less frequent. Comparison the structure of cell 'a' in Figs. 5.18d and 5.19d, suggests that this cell just collapsed, with the two lower charge regions of the tripole descending, leaving a remnant of the upper positive charge aloft. Lightning flashes within the negative and the upper positive charge region extended further downwind (northwest) and sloped downward. Unfortunately, Doppler-synthesis was not possible during this time, but presumably the flow structure was not much changed from that shown in Fig. 5.18. The northwestward extension and downward sloping of the mid-level negative and upper positive charge regions of cell 'a' generally follow the streamlines of this flow. Meanwhile, to the near south, cell 'b' continued to intensify with very active lightning in both the upper and lower positive of its tripole structure (but no -CG flashes) as well as an additional population of flashes between the upper positive and an extreme upper negative charge (Fig. 5.19). Recall that the altitude histograms in Fig. 5.12 also show this population of downward flashes in the upper levels.

The situation became much more complicated over the next 20 minutes (2055–2115) as the transition to an inverted tripole structure neared completion. In an attempt to illustrate this as clearly as possible, Figs. 5.20 and 5.21 show a series of vertical cross-sections of Z_H and LMA source density from 2054 to 2111. The locations of these slant cross-sections are essentially the same as in Fig. 5.19. Over this time period, cell 'a' collapsed further. It's lower positive charge appeared to simply "fall out", leaving remnants of its negative and upper positive charge, and these charge remnants apparently descended with time. Cell 'b' then also collapsed, and during its collapse, the LMA sources were concentrated in one mid-level peak. The

charge structure within this merged blob of lightning was difficult to determine (as indicated by the lack of charge notation in the middle panels of Fig. 5.21). Scanning the LMA density cross-sections in Fig. 5.21 from top-to-bottom gives the impression that the entire charge structure of cell 'b' experienced a downward shift, with the lower positive raining out or dissipating and the remaining upper three charge regions shifting downward, resulting in an inverted tripole structure. During the collapse of cells 'a' and 'b', cell 'c' to the south invigorated, with growth of precipitation aloft that subsequently grew and descended to form a deep 45–55 dBZ shaft by 2111. Though the lightning during the invigoration of cell 'c' indicated a roughly normal tripolar structure, the tripole was relatively elevated (e.g., compare cell 'c' to the tripole structure in the cells in the far north of Fig. 5.21 at 2111. This elevated structure may explain why cell 'c' produced only two –CG flashes during this time and stopped producing –CG flashes altogether by 2111.

By 2116, the lightning mapping within the collapsed remnants of cells 'a' and 'b' became clearer and consistently described an inverted tripole charge structure (Fig. 5.22). Inferred positive charge sloped downward from 8 km altitude on the north end to near the surface on the south end. The majority of the flashes in this inverted tripole were inverted ICs from the similarly sloping negative charge above. Only a few flashes initiated upward from inferred negative charge below and on the north side of the dominant middle positive charge. As shown in Fig. 5.23, the first "real" +CG of the storm was one of these upward initiating flashes[3].

The cross-sections in Figs. 5.24-5.28 indicate that over the next 30–40 minutes the convection associated with this inverted tripole structure experienced a brief resurgence that apparently served to maintain this charge structure and intensify the lightning production within it. Flashes between the lower negative and mid-level positive charge of the inverted tripole became more frequent during this time. The flash

[3]The qualifier "real" is used here because, as described in the next section, the two +CG flashes earlier in the storm were probably misidentified by the NLDN.

start histograms at 2115 and 2130 in Fig. 5.12 show both the upward and downward flashes in the inverted tripole quite clearly. For example, there were almost as many downward flashes (blue curves) above the lower maximum in LMA sources (lower positive charge) as there were upward flashes (red curves) below the upper maximum in LMA sources (upper positive charge). Some of these downward flashes occurred between the lower two charge regions of the normal tripolar cell 'c', though most of them occurred between the upper negative and low-to-mid-level positive charge of the inverted tripole downwind. Essentially all of the upward flashes from 8-10 km MSL were between the mid-level negative and upper positive charge of the normal tripolar cell 'c'. Finally, there was also a small but distinct population of upward flashes below the lower peak of LMA sources that correspond to flashes between the mid-level positive and lower negative of the inverted tripole, and the clustered +CG flashes are a subset of these. Nearly all of the +CG flashes originated near the inverted tripole and tended to cluster beneath it (see, for example, the dense clusters of +CG flashes in Fig. 5.27 and in the right column of Fig. 5.5). The origin heights of the +CGs clustered near 4–6 km (Figs. 5.7b and 5.13). With little exception, these +CG flashes initiated upward between the lower negative and mid-level positive of the inverted tripole. Some of these +CGs remained compact and tapped only the positive charge within the inverted tripole (e.g., Fig. 5.26a) while others tapped additional positive charge within the more collapsed, stratiform echo further north (e.g., Fig. 5.26b). The +CG flashes ended by 2150 as the supporting convection finally dissipated (Fig. 5.28).

5.2.5 Other Non-clustered +CGs

In their description of the performance of the upgraded NLDN, Cummins et al. (1998) noted a previously undetected population of +CGs with peak currents from 5–15 kA. They stated that "it is likely that not all of these events are CG discharges" and recommend that "the subset of small positive discharges with peak currents less than 10 kA be regarded as cloud discharges unless they are verified to be cloud-to-

ground." As shown in Fig. 5.13c, there were only two +CGs near the suggested 10 kA threshold, one with a peak current of 10.7 kA, the other with a peak current of 10.9 kA. These are the two +CG flashes that occurred early in the storm during a period of utter –CG-dominance (see, e.g., Fig. 5.7).

Though it is not within the scope of this study to use the LMA in an attempt to verify the NLDN's detection of every ground flash, the lightning mapping of these first two anomalous +CGs suggests that they were actually cloud discharges. In general, these first two +CGs were quite different structurally than those later in the storm (e.g., those in Figs. 5.23 and 5.26). Fig. 5.29 shows the lighting mapping of the first of these suspicious +CGs (blue sources) along with a normal IC flash (red sources) that occurred at about the same time and location. These two flashes are overlaid onto radar cross-sections in Fig. 5.30. The spatial and temporal development of both of these flashes was very similar, suggesting that they were both normal IC flashes between mid-level negative and upper positive charge. There was no clear positive leader to ground associated with the suspicious +CG. However, it's important to recall that the LMA is relatively insensitive to the breakdown associated with positive leaders, so, to paraphrase Carl Sagan, absence of evidence does not imply evidence of absence. Figs. 5.31 and 5.32 show the second suspicious +CG flash. In this case, the discharge was more complex. There are probably two separate "flashes", one right after the other, in Fig. 5.31. Though complex, this flash (or pair of flashes) also indicated upper-positive over mid-level negative structure, much like the two flashes in Fig. 5.29.

Apart from the first two suspicious +CGs, there was only one other +CG in storm 1 exterior to the main +CG cluster. This other +CG occurred at 2123:44 in the collapsing cell far north of the main cluster (see, e.g., Fig. 5.24). Of the 10 flashes produced by this northern cell in its last 10 minutes of lightning, almost all of them were *very* clear normal IC flashes describing broad stratified positive charge over negative charge. Figs. 5.33–5.35 show examples of two of these flashes, one of which, according to the NLDN, produced a +CG. The +CG looks almost identical

to the IC flashes that surrounded it, which raises some suspicion about whether it was really a +CG. However, the peak current was 21.2 kA which is well above the recommended threshold. As described above, many of the +CGs in the main cluster extended north to tap the same positive charge region that the northern normal ICs and +CG did (e.g., Figs. 5.23 and 5.26b).

5.2.6 Discussion and Tentative Conclusions from Storm 1

Despite the disorganization of the convection and less-than-optimal radar coverage, this case provided significant insight into the electrification of both +CG-dominated and –CG-dominated storms. In general, the initial convection and electrification closely followed the "normal" airmass thunderstorm paradigm. Essentially all of the cells in storm 1 initially developed a normal dipole (positive over negative) charge structure within lofted echo, followed by formation of a lower positive charge as the lofted echo grew and descended. All of the cells also initially produced only –CG flashes, and the source regions of these –CG flashes were remarkably consistent with the overall tripolar charge structure (see, for example, any of the bottom two panels of Fig. 5.4).

The parent charge structure responsible for the clustered +CG flashes later in the storm was quite different from a normal tripole. The most fitting description is an inverted tripole (see, for example, Figs. 5.22, 5.24, and 5.25). This inverted structure and attendant clustered +CGs apparently resulted from convective collapse. Hence, the precipitation unshielding mechanism proposed by Carey and Rutledge (1998) seems like an apt fit to the observations. Unlike the sustained inverted charge structures in the 29 June and 3 June cases, the inverted tripole in this case was much more compact and closer to the ground. That is, the upper negative charge region of the inverted tripole in this case was still in the general altitude range (6–8 km) of the normal tripole cells earlier in the storm. However, the positive charge region was deeper and more lightning-active than in the normal tripole cells. Again, this seems more in line with the precipitation unshielding hypothesis.

The large scale descent of the charge layers and transition from a normal to inverted tripole structure is also very reminiscent of the so-called *end-of-storm-oscillation* (EOSO: Moore and Vonnegut, 1977; Marshall and Lin, 1992; Williams et al., 1994; see also Section 7.2.1 of MacGorman and Rust, 1998). In an EOSO, the electric field measured at the ground (E_{gnd}) undergoes a slowly decaying oscillation between a foul weather field (E_{gnd} pointing up) to fair weather field (E_{gnd} pointing down) as the storm dissipates. This effect is thought to be due to the lower charge regions sequentially dissipating and/or raining out. As the precipitation from each charge region nears ground, it exerts a greater influence on E_{gnd}, thus switching the polarity. Alternatively, the complete rain-out of the lowest charge region would expose the next higher charge region to ground, which would also switch the polarity of E_{gnd}. Positive CG flashes are often observed during EOSOs and are typically the final lightning flashes of the storm. The precipitation unshielding hypothesis and EOSO seem to be similar descriptions of the same thing, i.e., a transition and/or descent of the vertically charge structure during convective collapse. It's important to point out though that the terminology "precipitation unshielding" implies that the negative charge rains out, leaving the positive charge exposed to ground. This is not quite what happened in storm 1. The precipitation did appear to carry the negative charge toward ground, but instead of "unshielding" the positive charge above and allowing +CG flashes to occur from the unshielded positive charge, the descending negative charge served to *provoke* the +CG flashes. Indeed, a very similar process occurs for normal tripole storms that produce –CG flashes: the lower positive charge carried by precipitation doesn't unshield the main negative charge; it serves to provoke –CG flashes from the negative charge. Perhaps Carey and Rutledge's +CG hypothesis should be renamed to "precipitation provoking" to avoid misconceptions.

There are still some lingering inconsistencies between the observations of +CG flashes in this case and the mechanism of precipitation unshielding and EOSO. There were numerous episodes of cell growth and collapse. Why then didn't any of the other collapsing cells form similar inverted tripoles or produce clustered +CG flashes?

There was the one other +CG flash from the collapsing cell further north, but the parent charge structure was quite different from the inverted tripole near the main +CG cluster. In fact, in some ways the demise of northern cell seems more in line with the precipitation unshielding hypothesis and EOSO explanation. As this northern cell collapsed, the upper two charge regions of its normal tripole structure gradually descended, presumably as the lower positive and then mid-level negative sequentially "rained out". The one +CG flash occurred near the end of this rain out. Whereas, in the clustered +CG region, the inverted tripole structure was sustained for an hour or so, with very frequent flashes between the mid-level positive charge and negative charge above it. As described above, there is evidence (e.g., reappearance of strong lofted echo) that the convection associated with this inverted tripole experienced a brief resurgence after the inverted tripole had formed. This resurgence appeared to reinforce the pre-existing charge structure and intensify the lightning production within it. Perhaps this re-invigoration allowed for increased charge-separating collisions at warm enough temperatures to sustain the mid-level positive charge and upper-level negative charge in a manner analogous to the formation of the lower two charge regions of a normal tripole. This would not, however, explain the persistent *lower* negative charge. Another explanation is that inductive processes served to reinforce the inverted tripole. Yet another explanation is that the inverted tripole was influenced and/or sustained by charge advected northward from the more vigorous cell adjacent to and south of the +CG source region. Unfortunately, none of these explanations is entirely satisfying or testable with the available observations.

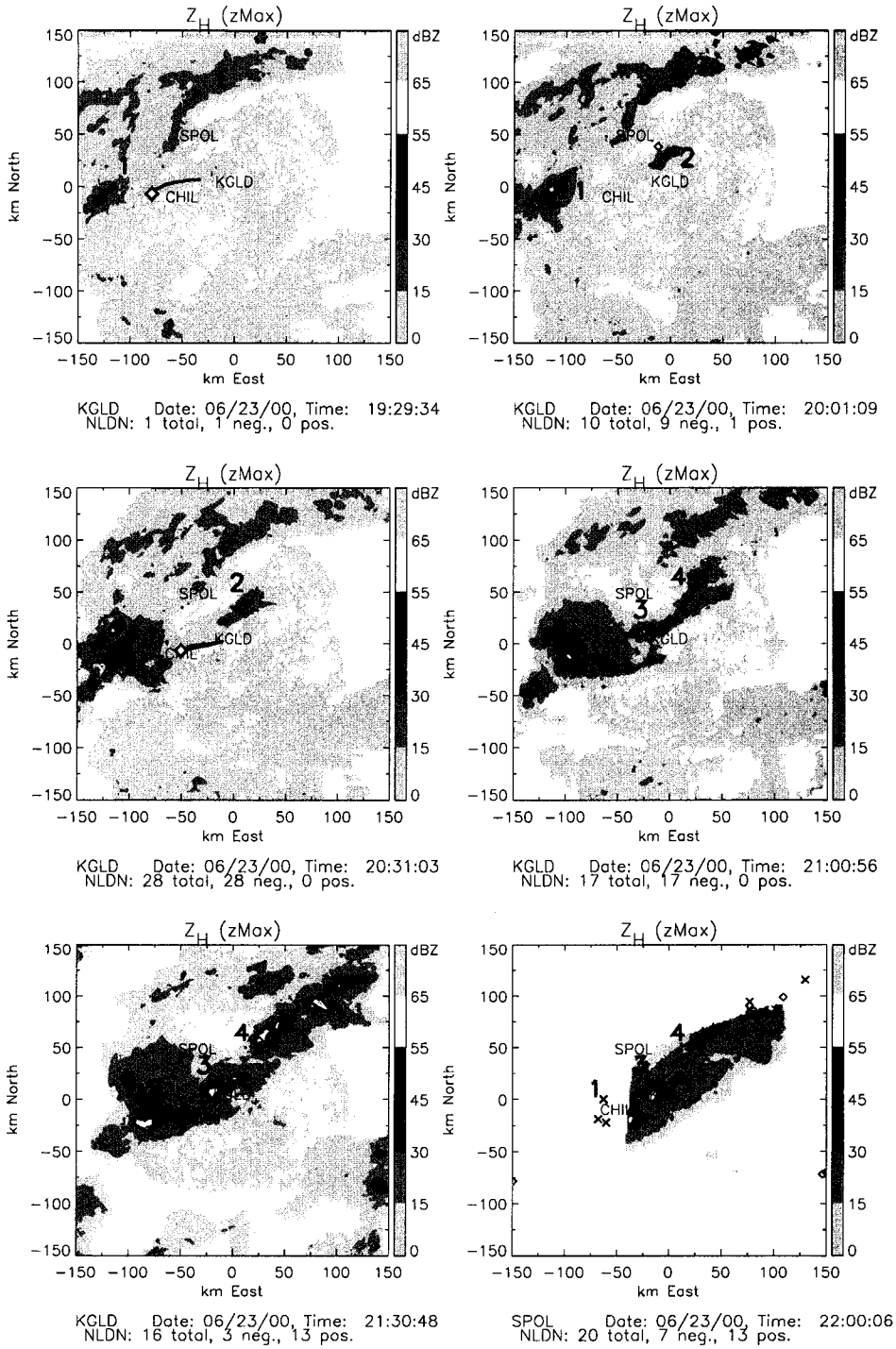

Figure 5.1: Radar summary of storms on 23 June 2000. Each panel shows vertical column max reflectivity from the KGLD radar, along with NLDN CG strike locations (−CGs in green, +CGs in red) within 5 minutes of the beginning of each volume scan. The radar scan time and number of CGs are listed beneath each panel. The blue numbers indicate the separate "storms" discussed in the text. The magenta lines are the trajectories of MGLASS soundings, with the filled diamond symbols marking their launch sites.

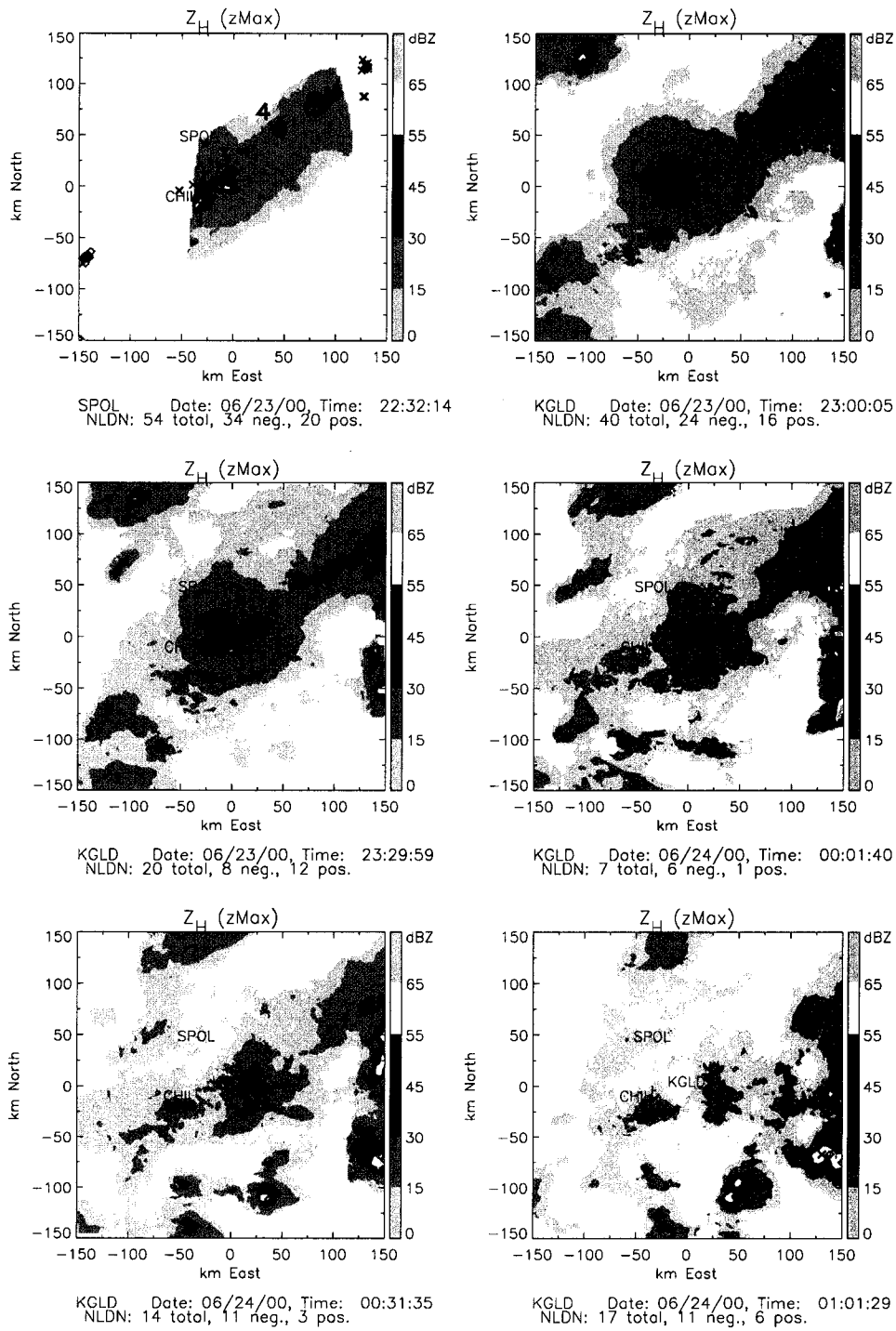

Figure 5.2: Fig. 5.1 continued.

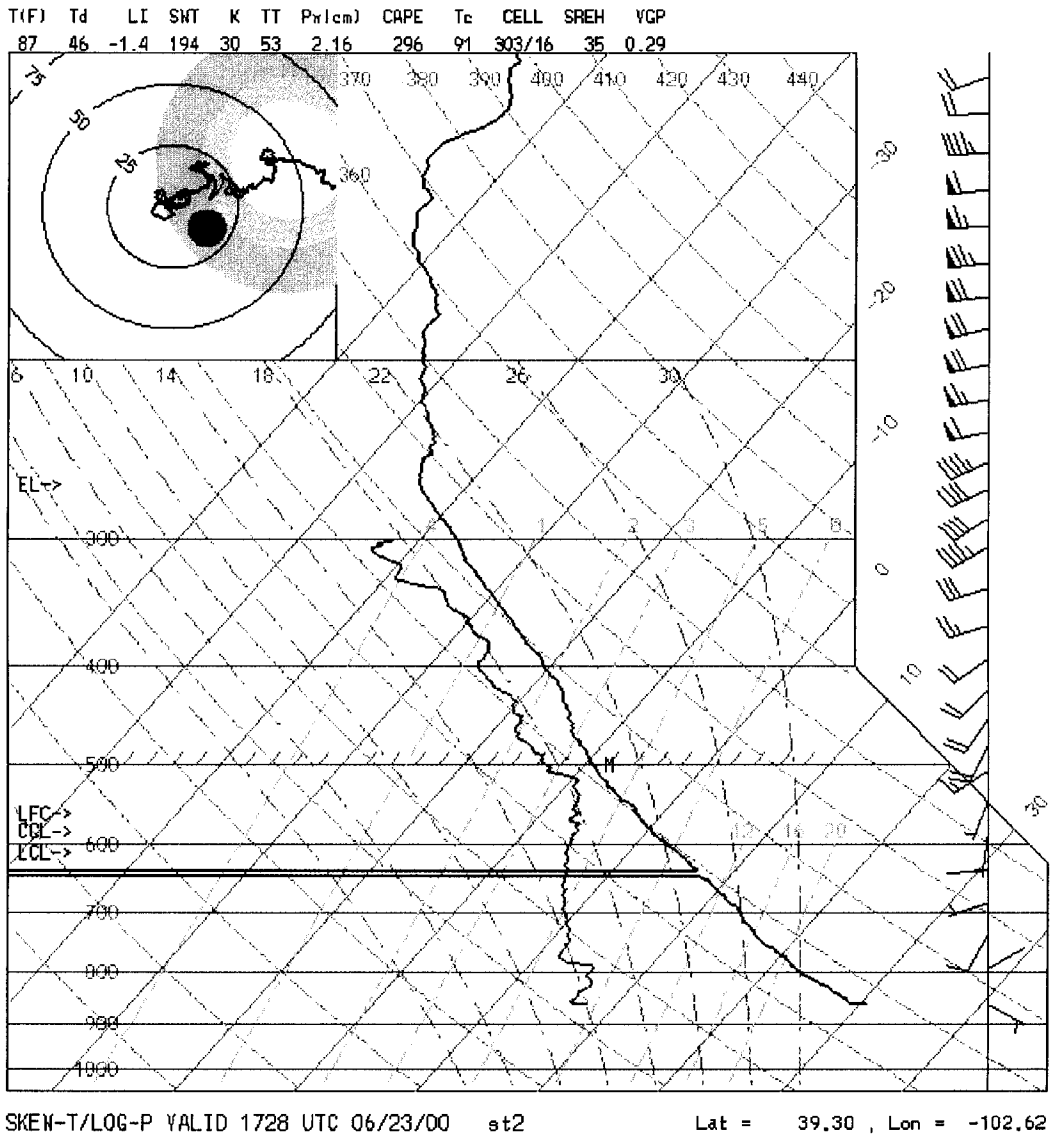

Figure 5.3: MGLASS sounding used for 23 June, storm 1. This sounding was launched 20 km west of the CHILL radar site at 1728 UTC. Its trajectory is indicated in the first panel of Fig. 5.1.

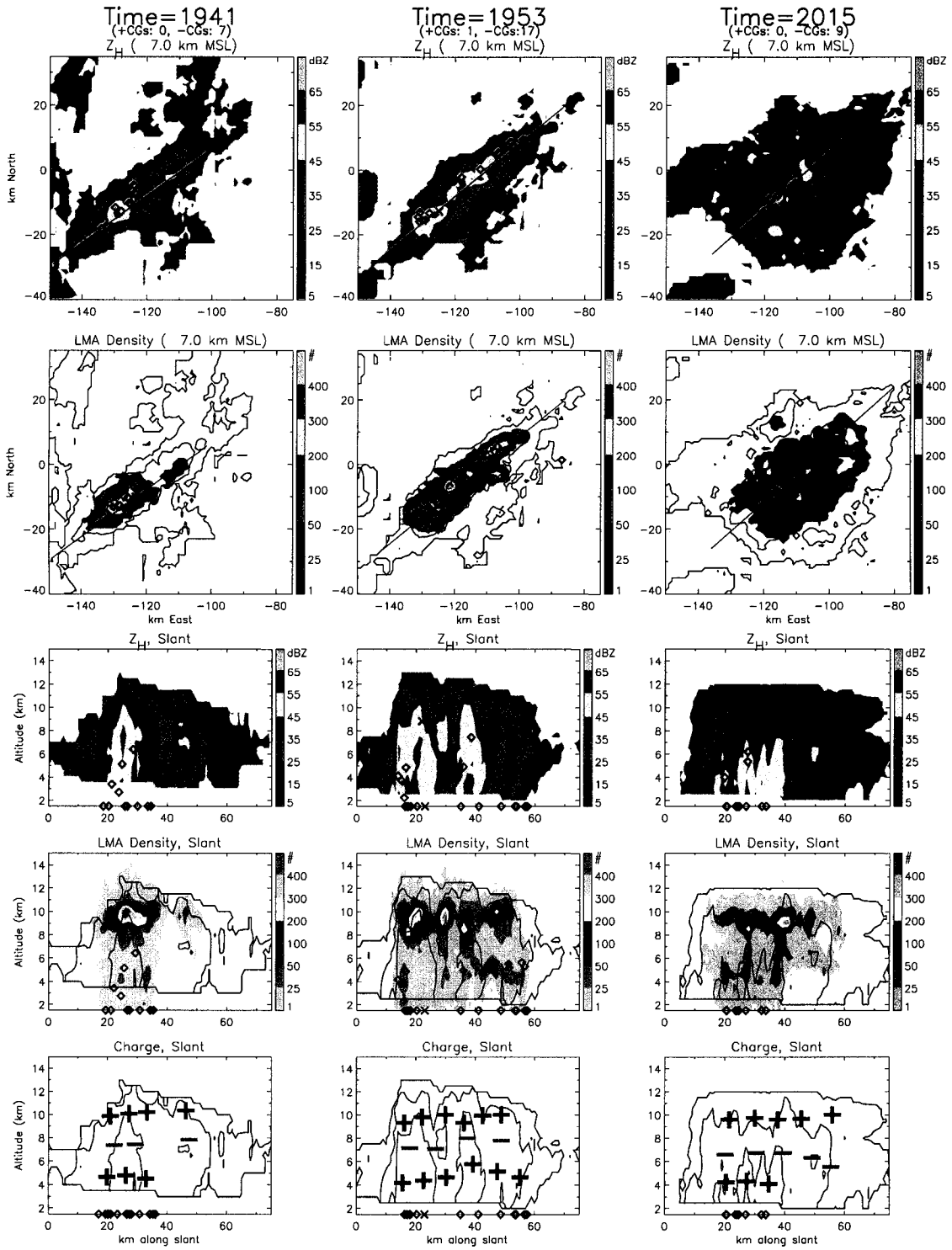

Figure 5.4: Representative cross-sections of storm 1 on 23 June at 1941, 1953 and 2015. Each column corresponds to the same time. From top to bottom: Horizontal cross-sections at 7 km altitude of radar reflectivity (Z_H) and LMA density (5 minute cumulative) followed by vertical cross-sections of Z_H, LMA density and composite charge structure along the line indicated in the horizontal cross-sections. Contours of Z_H at 5, 25, and 45 dBZ are repeated on the LMA density and charge composites. Black and green diamonds (black and red X's) are NLDN strike locations and origin locations of –CG (+CG) strikes, respectively.

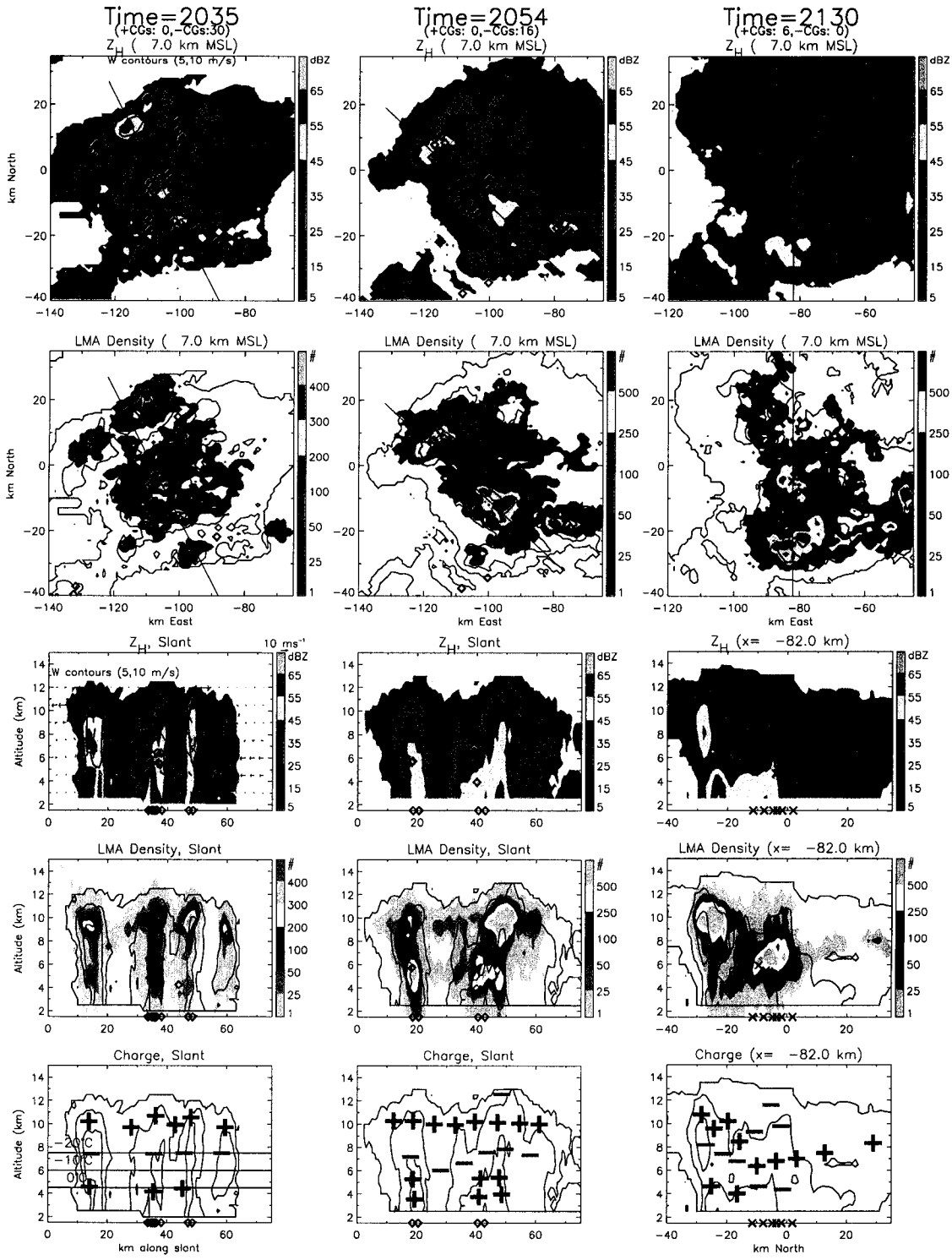

Figure 5.5: As in Fig. 5.4, but for volume scans beginning at 2035, 2054, and 2130. Additional contours of updraft at 5 and 10 m s^{-1} and storm-relative wind vectors are also included during the brief multi-Doppler coverage at 2035.

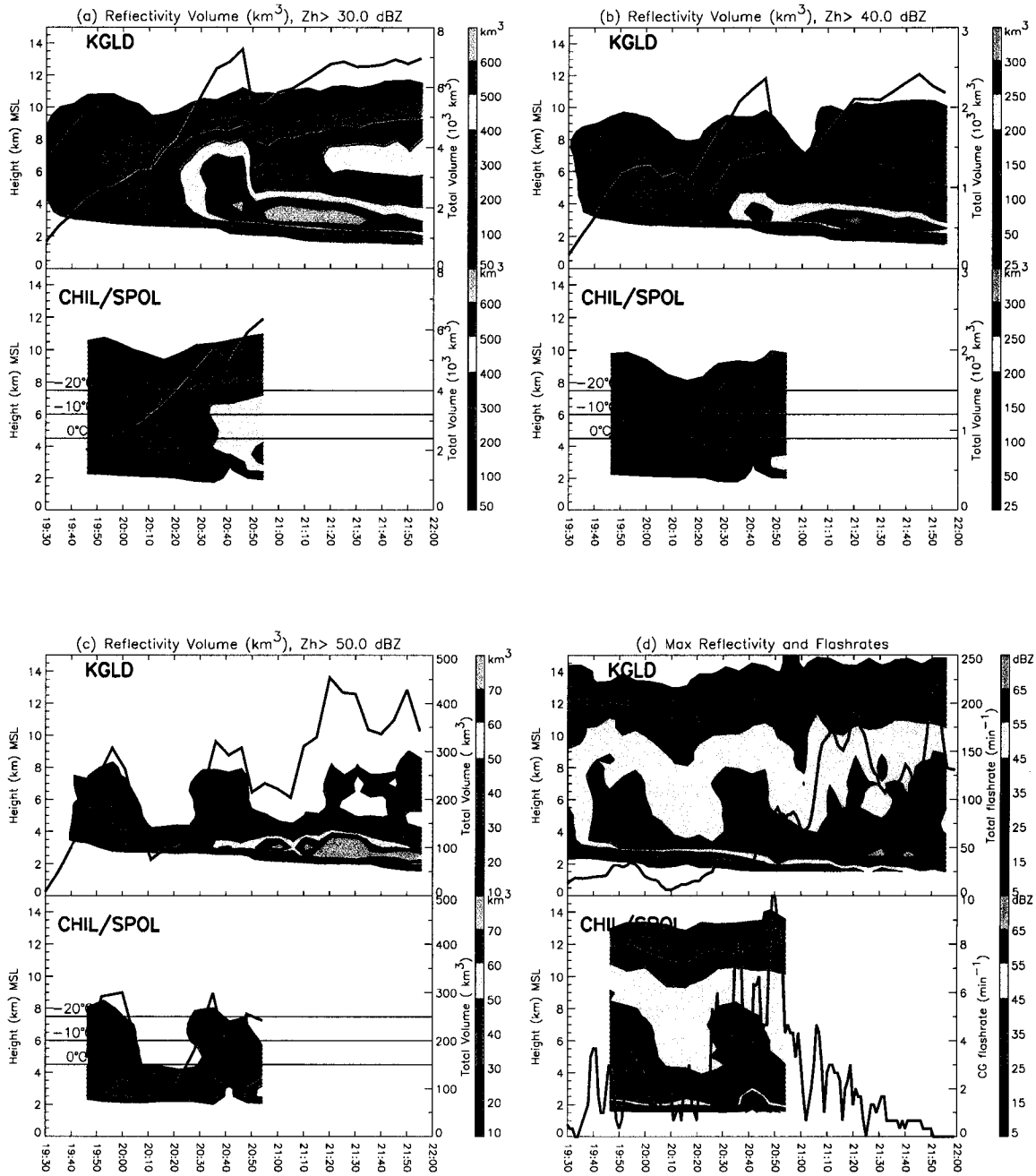

Figure 5.6: Time-height contours of KGLD and CHIL/SPOL radar echo volumes exceeding (a) 30, (b) 40, and (c) 50 dBZ with the total (height-integrated) echo volume of plotted as the thick black line in each case. Time-height contours of maximum reflectivity are plotted in (d) with total and CG flash rates plotted as the thick black lines.

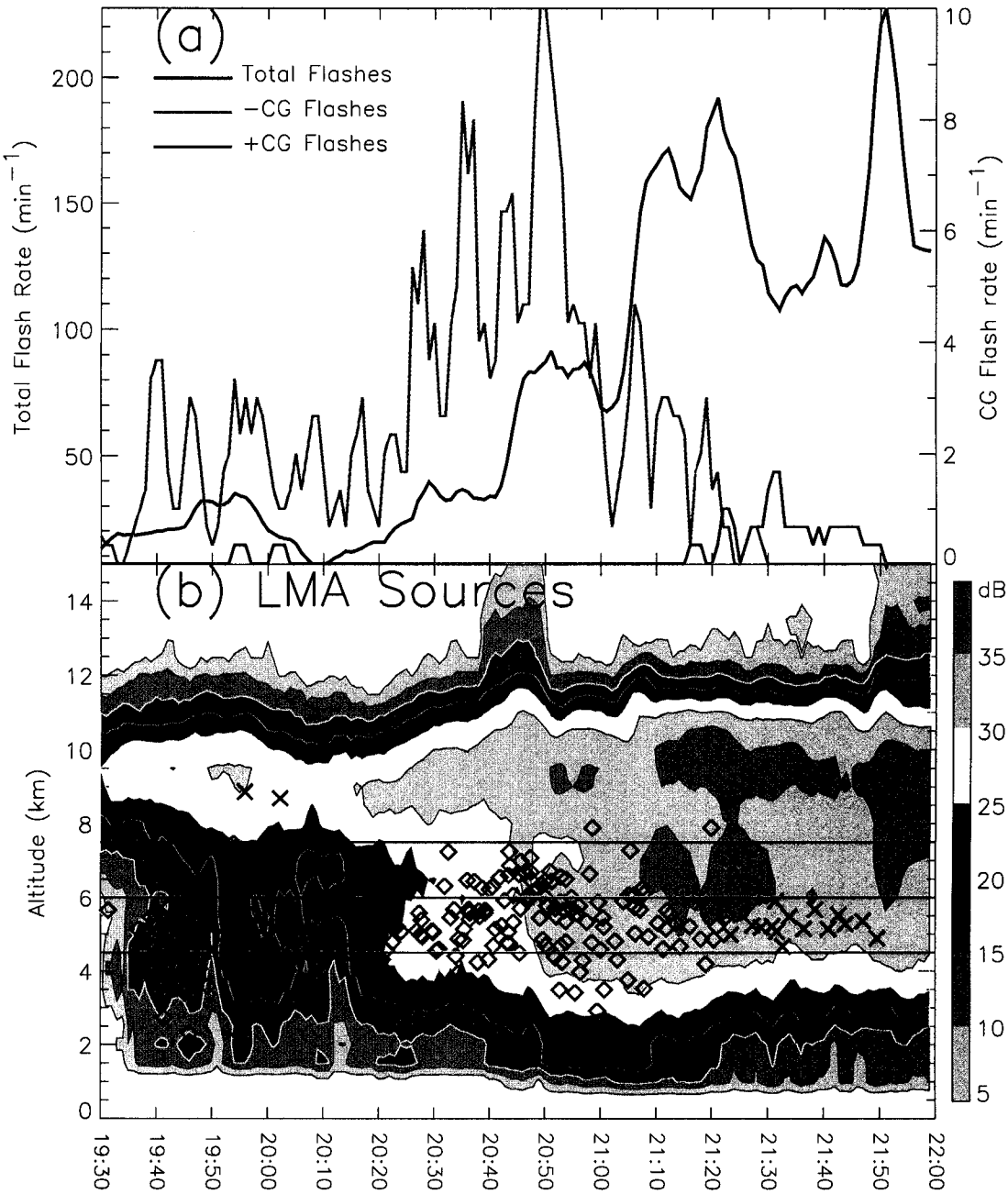

Figure 5.7: Lightning time series for storm 1 on 23 June 2000. (a) Total, −CG, and +CG flash rates. (b) Time-height contours of total LMA sources in logarithmic units as shown by the color bar. Mean origin heights (i.e., mean of first 10 sources in each flash) of −CGs and +CGs are overplotted as green diamonds and red X's, respectively. The three horizontal black lines indicate the height of the 0, −10, and −20°C isotherms.

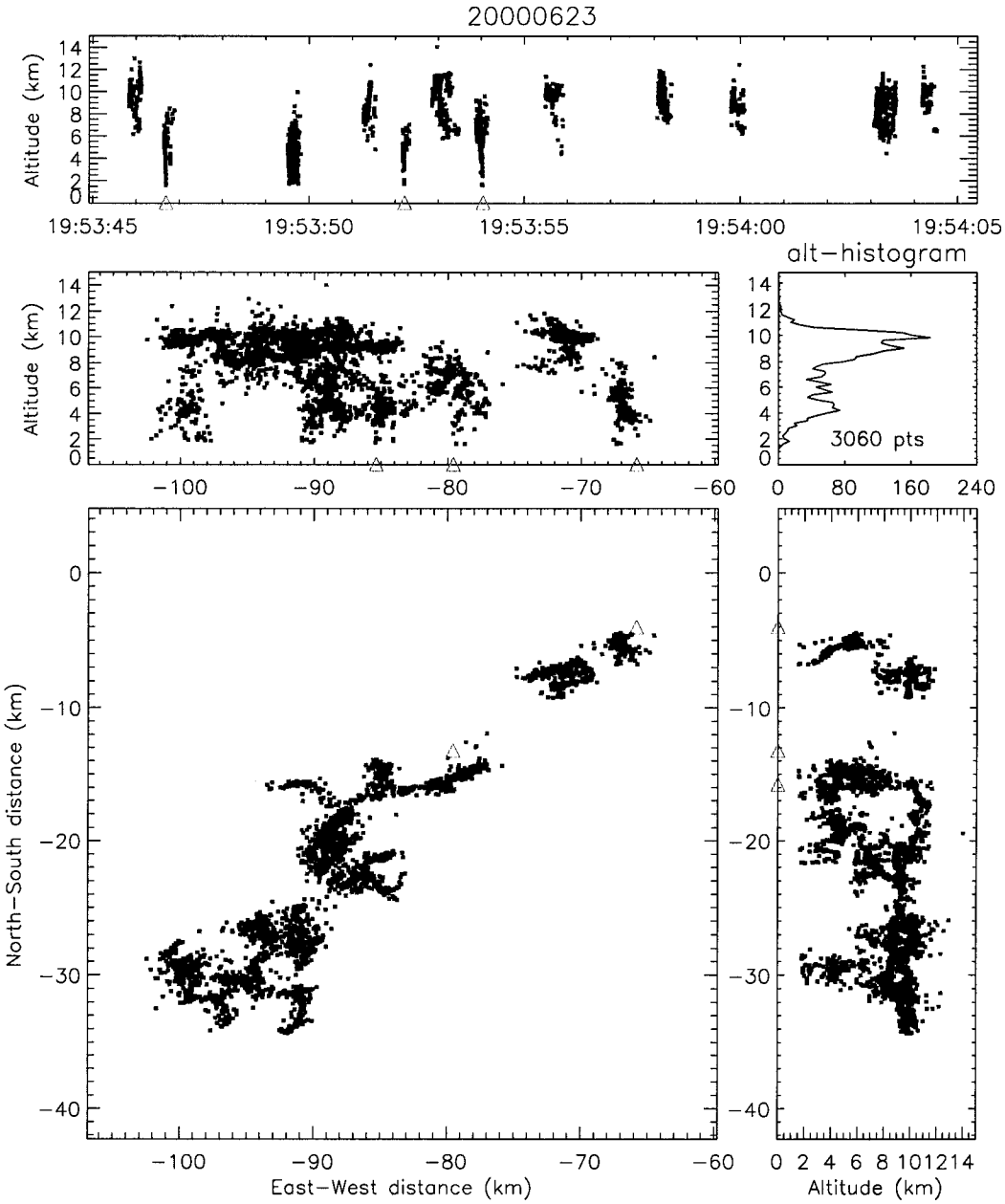

Figure 5.8: Lightning mapping of 13 flashes from 1953:45 to 1954:05. LMA sources are color-coded by inferred charge: red for positive, blue for negative, green for undetermined. There are nine normal flashes between mid-level negative and upper positive and four low inverted flashes between mid-level negative and lower positive. The NLDN identified three of the lower flashes as –CGs (as indicated by the triangle symbols).

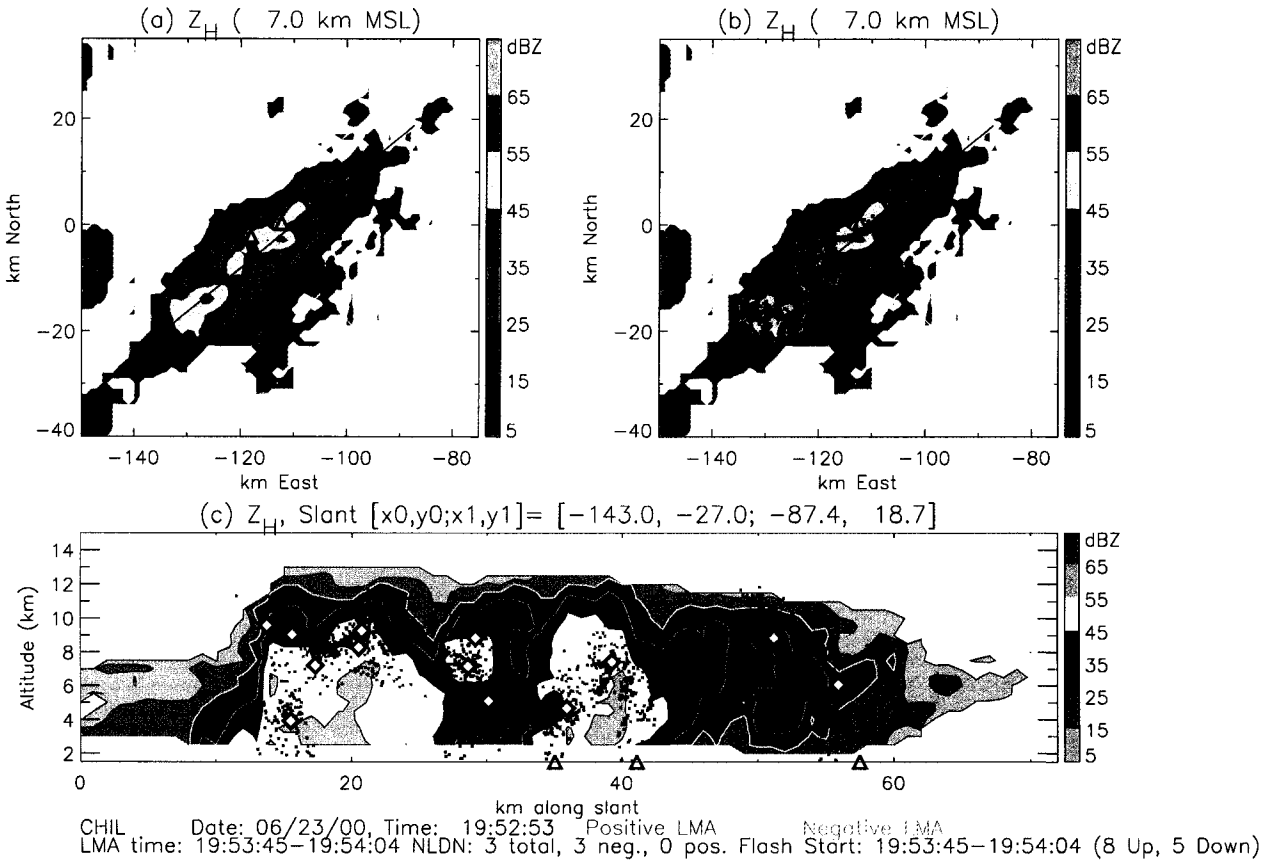

Figure 5.9: Radar cross-sections at 1953 with the LMA sources of the flashes in Fig. 5.8 overlaid onto (b) and (c) and color-coded by inferred charge region: red for positive, green for negative. The triangle symbols in (a,b) and along the surface in (c) are the NLDN strike locations of the three –CGs. The filled diamond symbols aloft in (c) indicate the first source of each of the flashes. The vertical cross-section is along the same slant path as in Fig. 5.4.

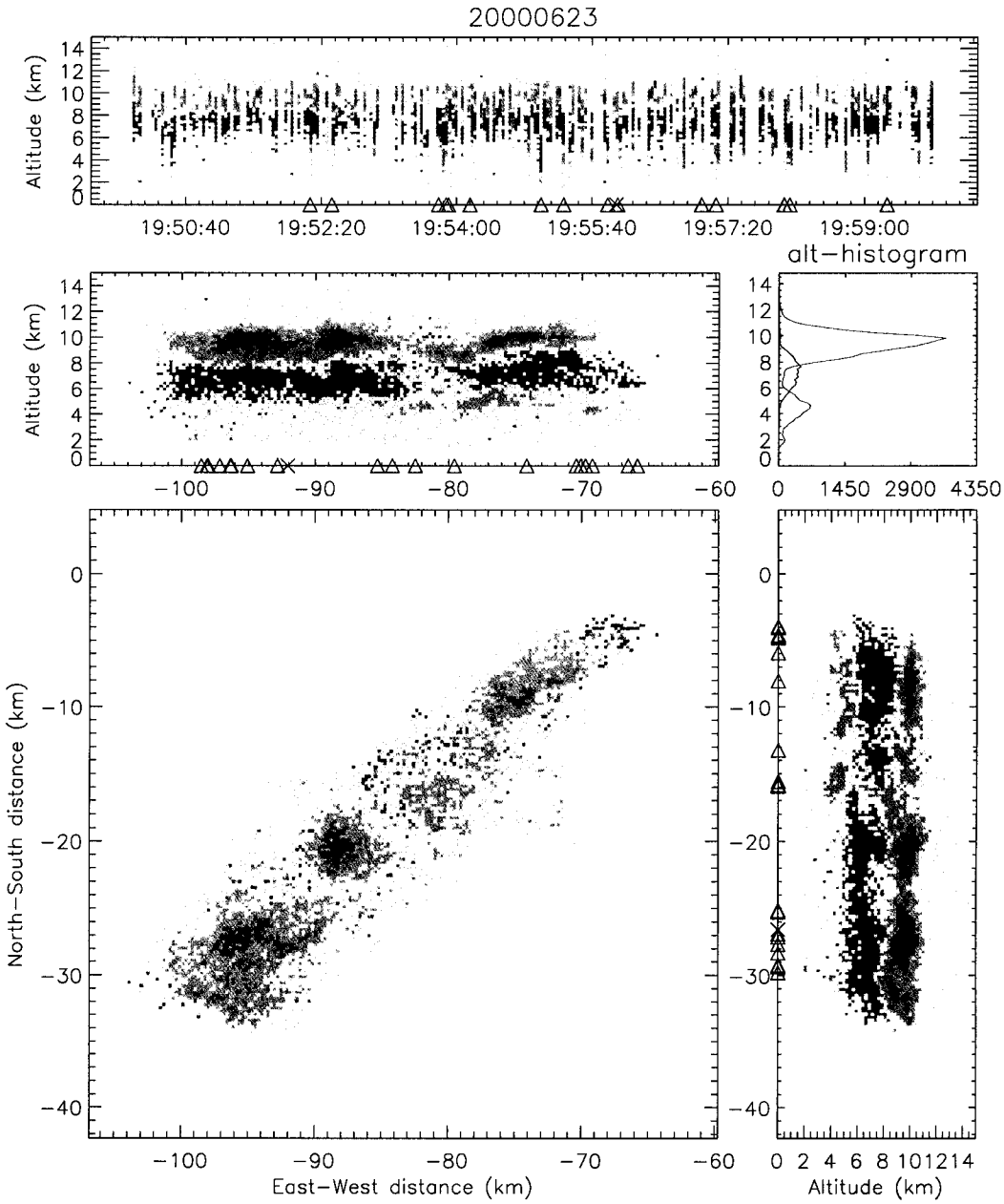

Figure 5.10: Lightning mapping data from 1950 to 2000. Here the sources are plotted in terms of "charge density", with redder (bluer) colors indicating greater concentration of sources within inferred positive (negative) charge regions.

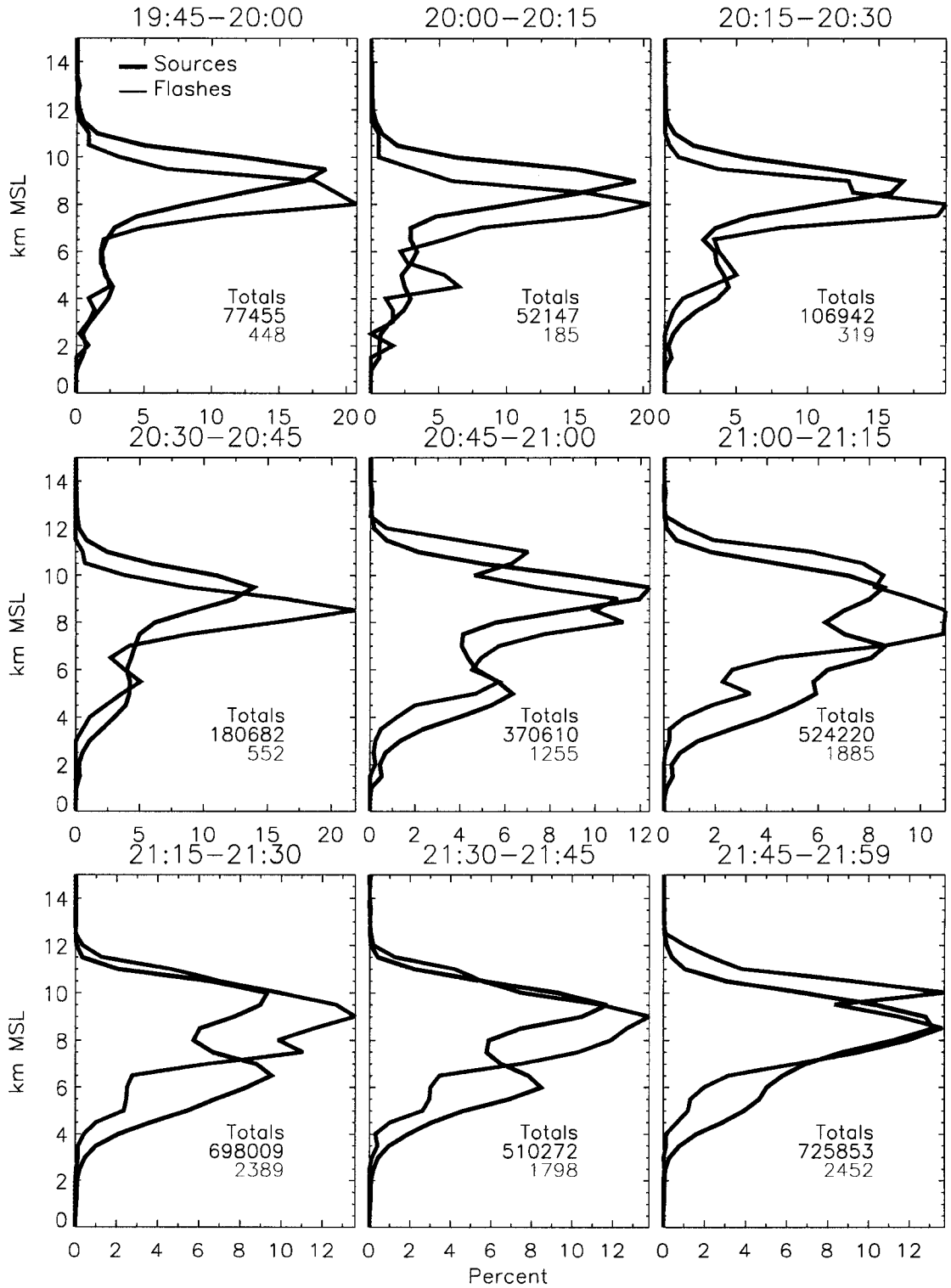

Figure 5.11: Altitude histograms of LMA sources (black) and flash origins (red) for storm 1 on 23 June. Each panel shows 15 minutes of data, plotted as percentage of the total for that 15 minutes. Numbers in bottom-right of each panel give the total number of sources and flashes during each 15 minute interval.

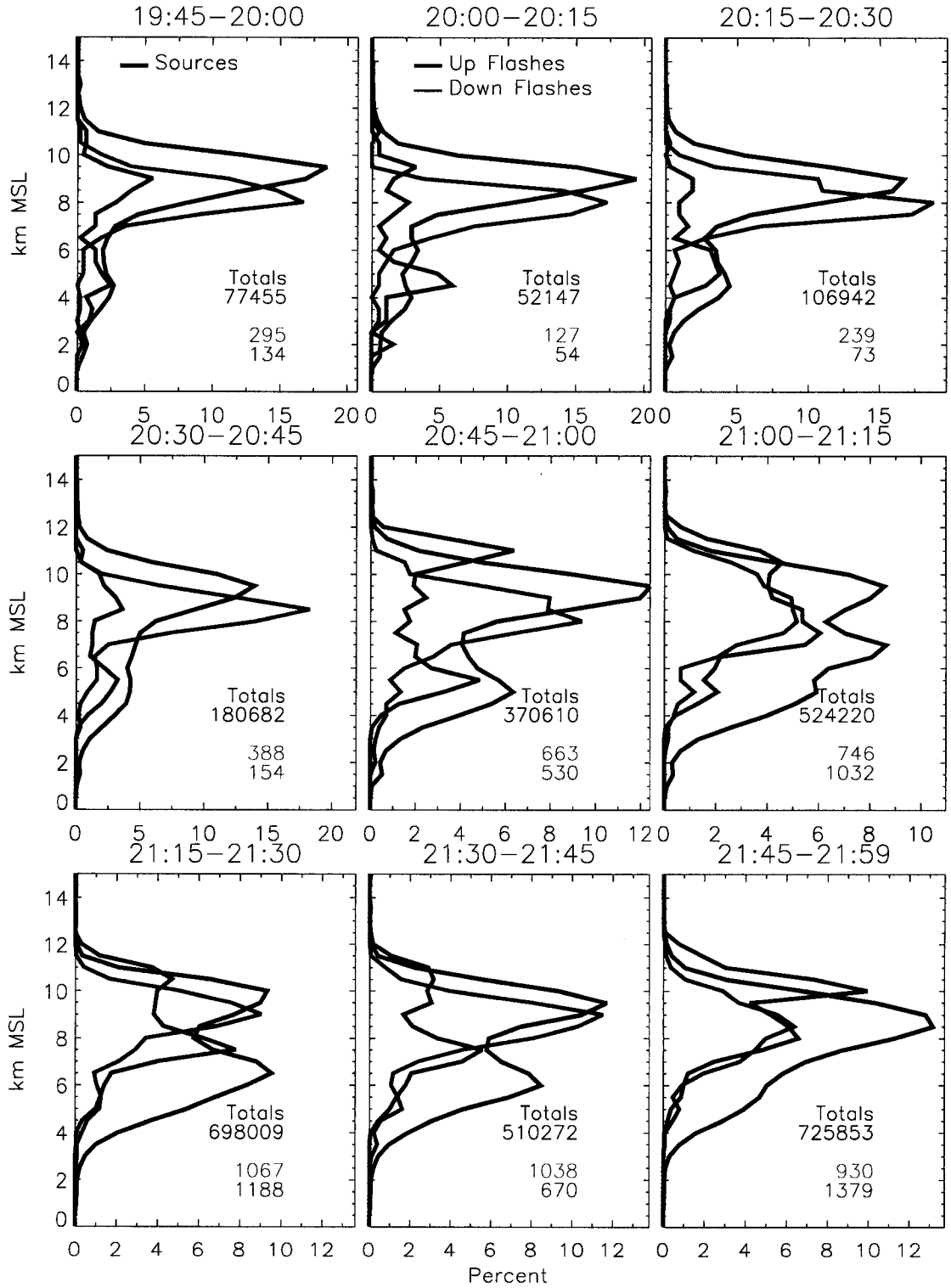

Figure 5.12: As in Fig. 5.11, but with additional partitioning of flash origins into those that initiated upward (red) and downward (blue). The up/down flashes are both plotted as a percentage of the total flashes, so the red curve of Fig. 5.11 is roughly the sum of the red and blue curves shown here. There are some flashes whose initial velocities were not determined, leading to the slight disparity between the total flashes and the sum of the up/down.

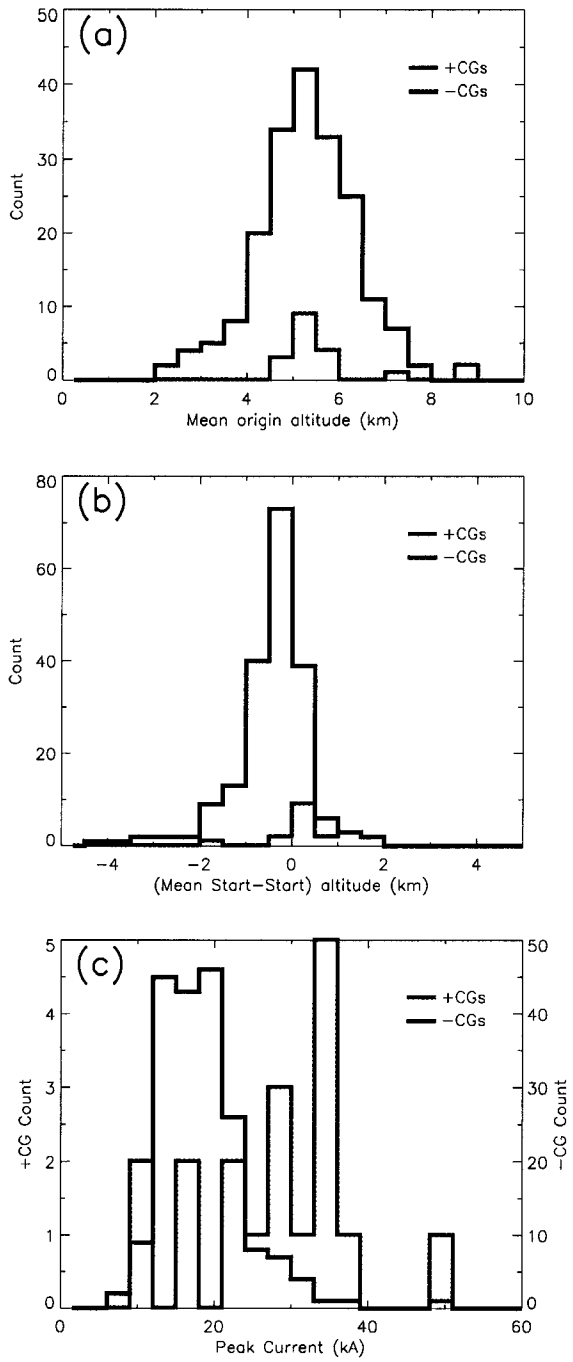

Figure 5.13: CG histograms for 23 June, storm 1. (a) Mean origin height. (b) Difference between height of first source and height of the mean of the first 10 sources, i.e., if positive, then first source was lower than the mean of the first 10 sources. (c) Peak current. Note that +CGs and −CGs use different ordinates in (c). Only those CGs that occurred from 1930 to 2200 UTC are included. There was also a +CG with peak current of 71 kA that's off the scale in (c).

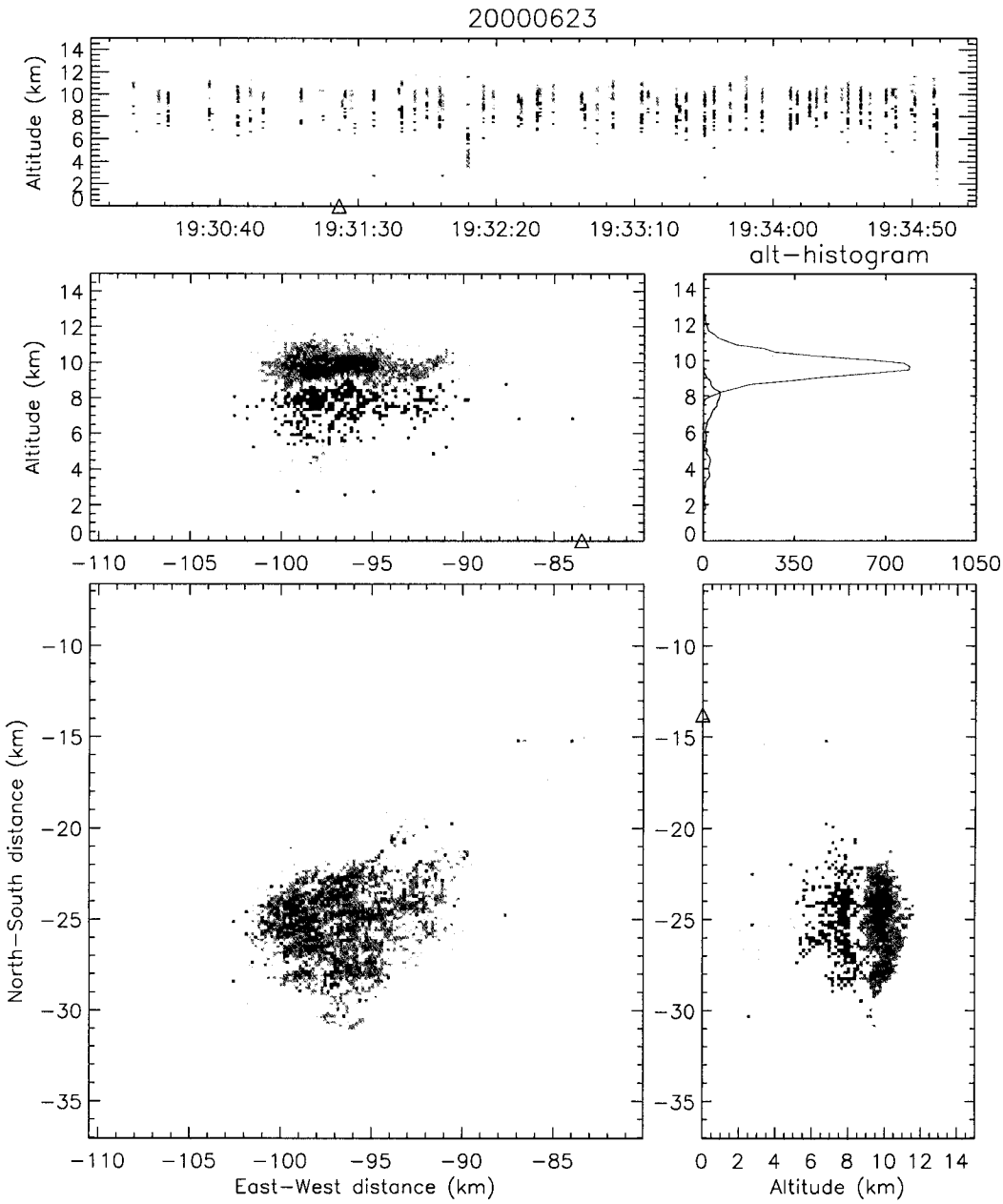

Figure 5.14: Lightning mapping of storm 1 from 1930 to 1935. Sources are color-coded by "charge density" as in Fig. 5.10.

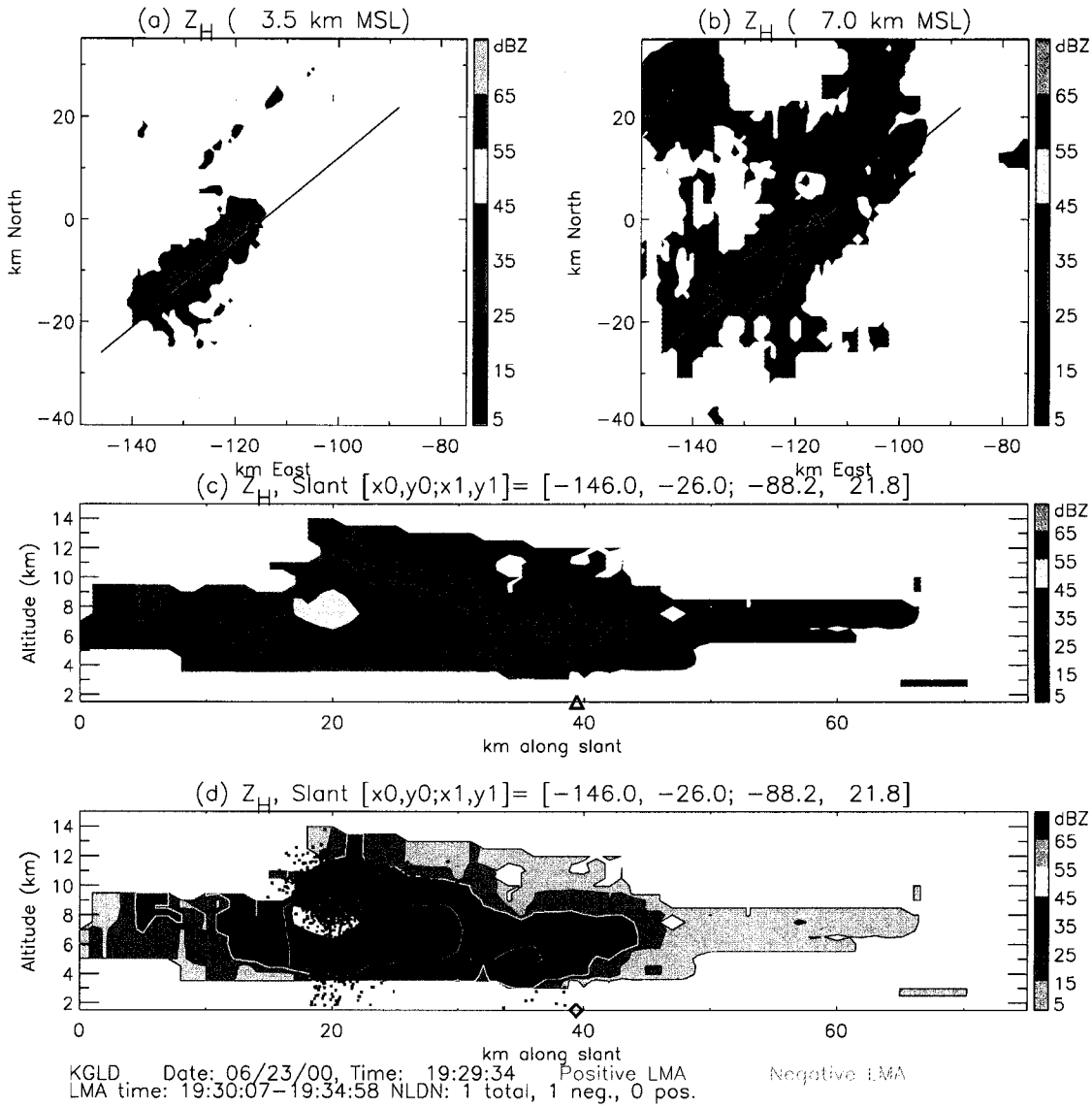

Figure 5.15: KGLD radar cross-sections at 1930 with the LMA sources from Fig. 5.14 overlaid and color-coded by charge.

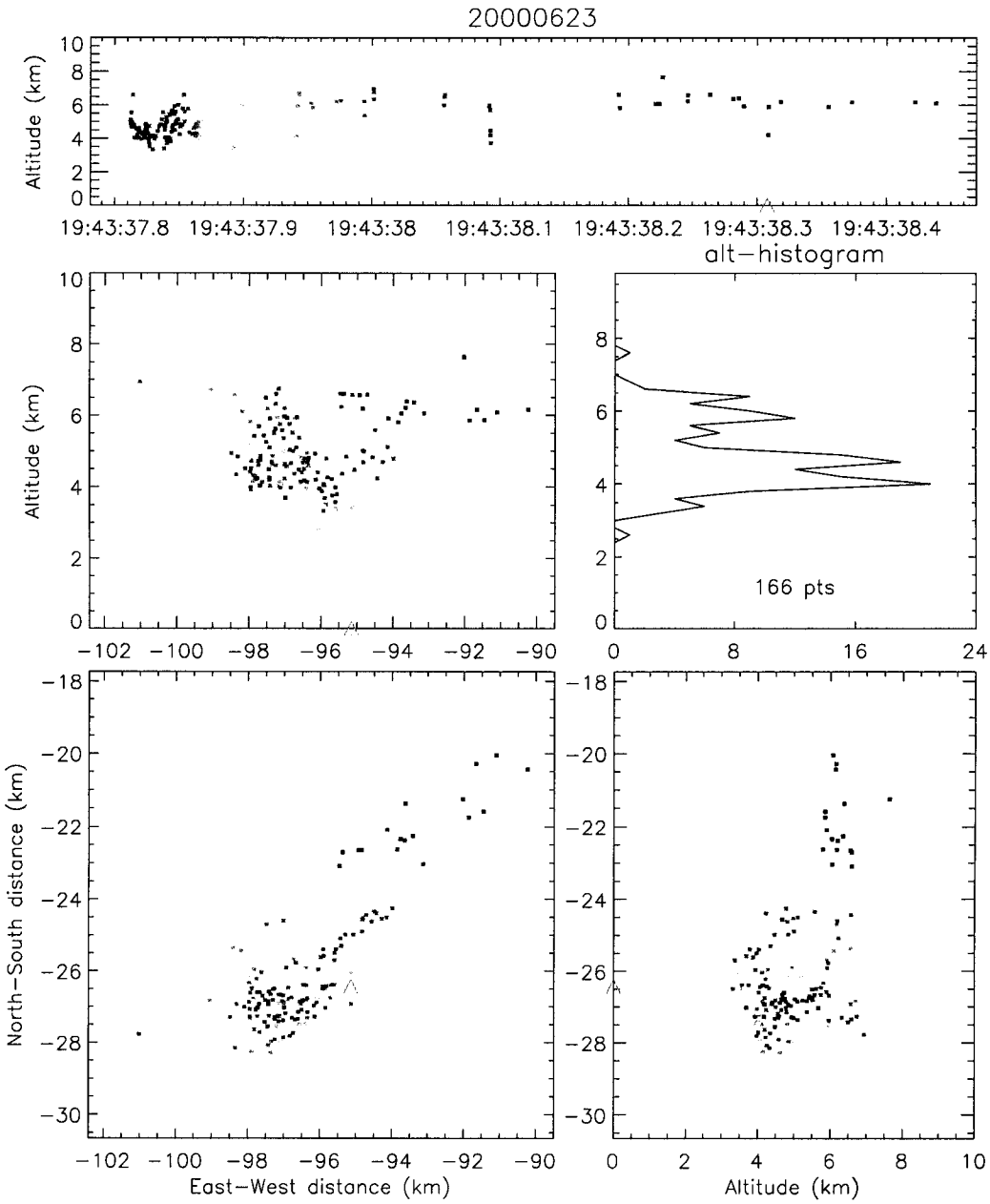

Figure 5.16: Lightning mapping of a typical –CG flash. This one occurred at 1943:37. The sources are color-coded by time.

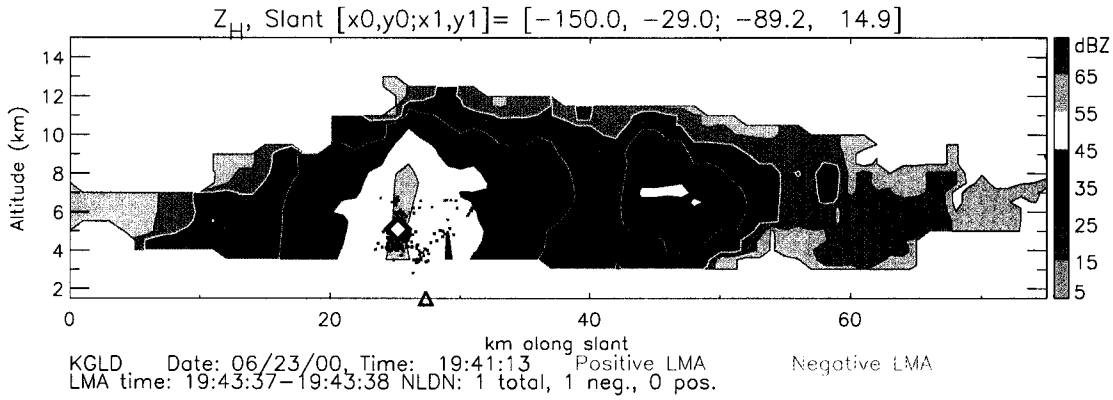

Figure 5.17: Vertical cross-section of horizontal reflectivity from KGLD at 1941 along the same slant path as in Fig. 5.4. The lightning mapping sources from the –CG shown in Fig. 5.16 are overlaid and color-coded by charge. The filled diamond symbol marks the first source of the flash, and the triangle marks the NLDN strike point.

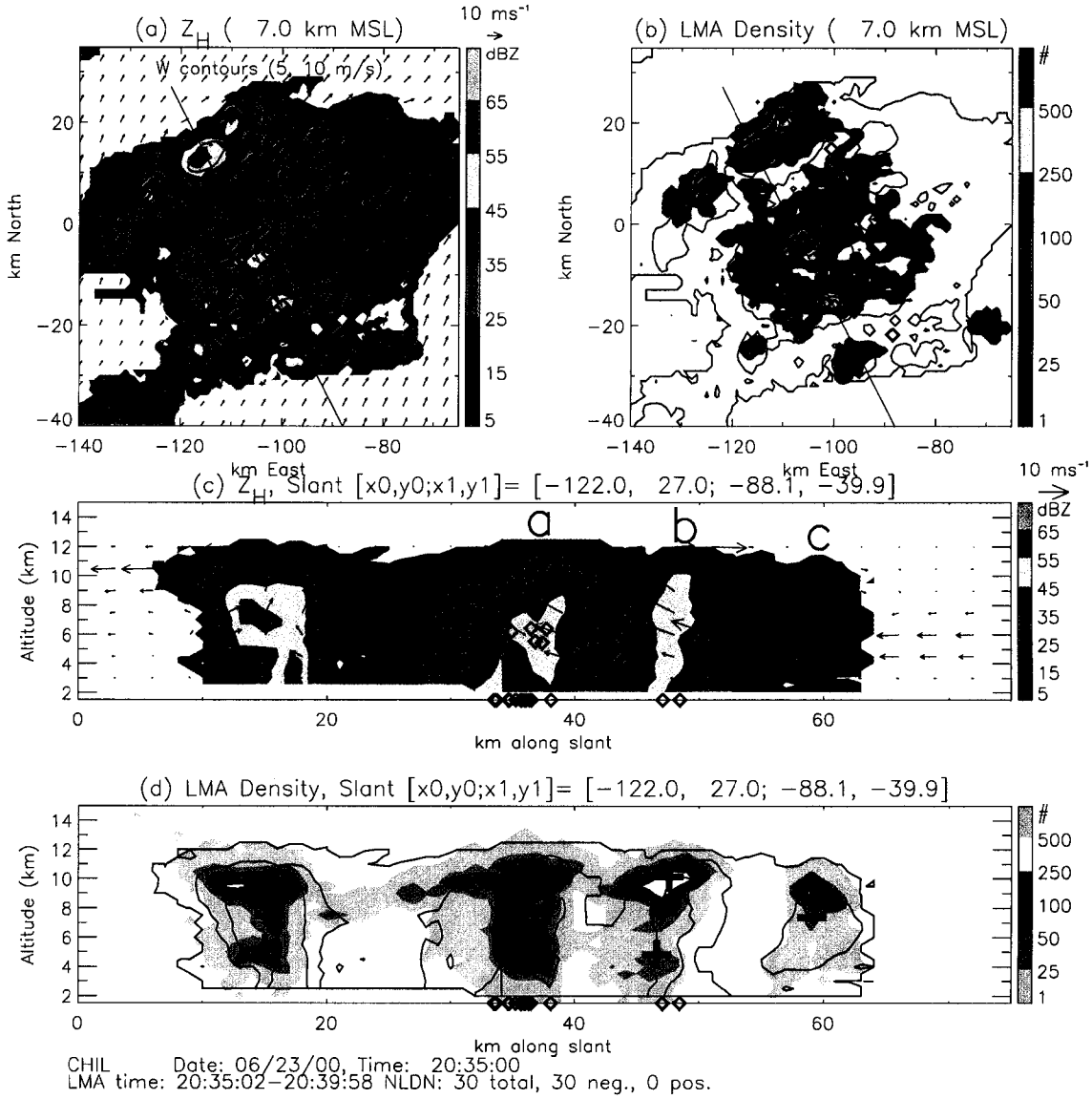

Figure 5.18: Cross-sections at 2035. (a,b) Horizontal cross-sections at 7 km MSL of Z_H and LMA source density, respectively, with diamond symbols marking the strike location of –CG flashes. Additional black updraft contours at 5 and 10 m s^{-1} are shown (a). (c) Vertical cross-section of Z_H along the slant path indicated in (a,b) with Doppler-inferred flow vectors and diamond symbols marking the source and strike locations of –CG flashes. (d) Vertical cross-section of LMA source density (including only those sources within 5 km of the cross-section) with plus and minus symbols indicating the inferred charge structure. The 'a', 'b', and 'c' along the top of the radar echo in panel (c) note the three cells described in the text.

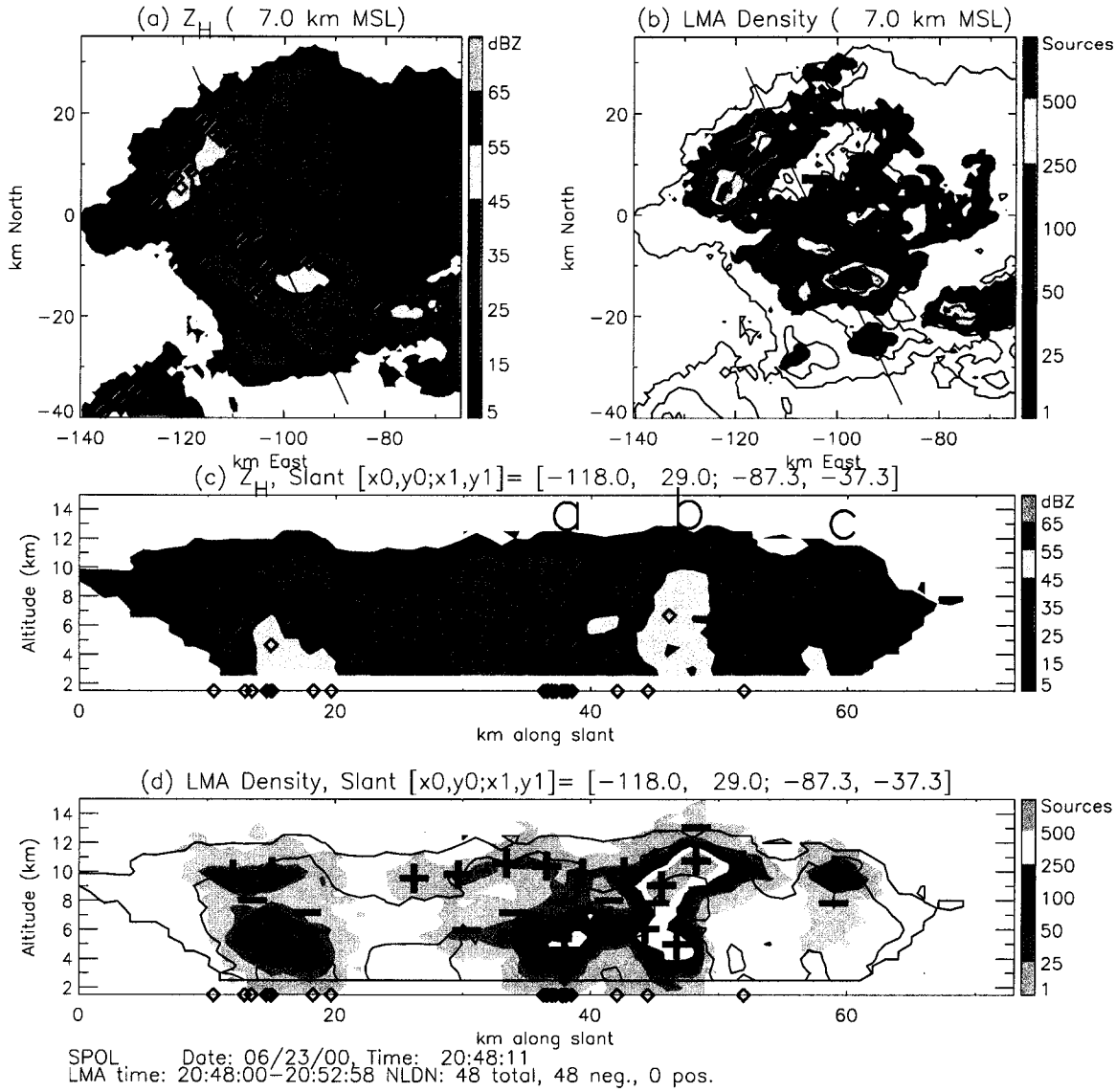

Figure 5.19: As in Fig. 5.18, but for 2048. For clarity, the CG strike points are shown in (a) but not in (b).

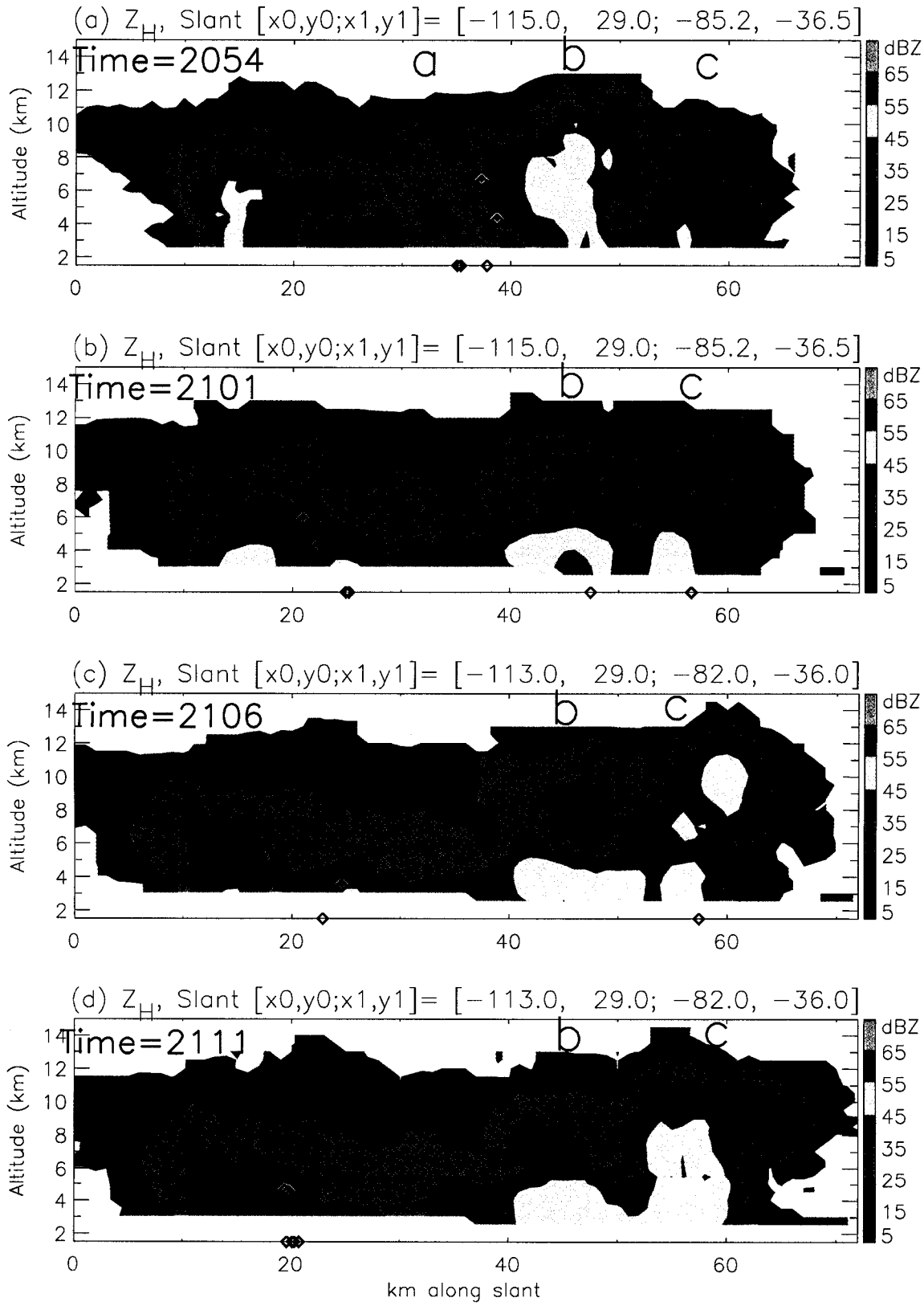

Figure 5.20: Series of vertical radar cross-sections of Z_H from 2054 to 2111 that illustrate the transition to inverted charge structure and +CG flashes.

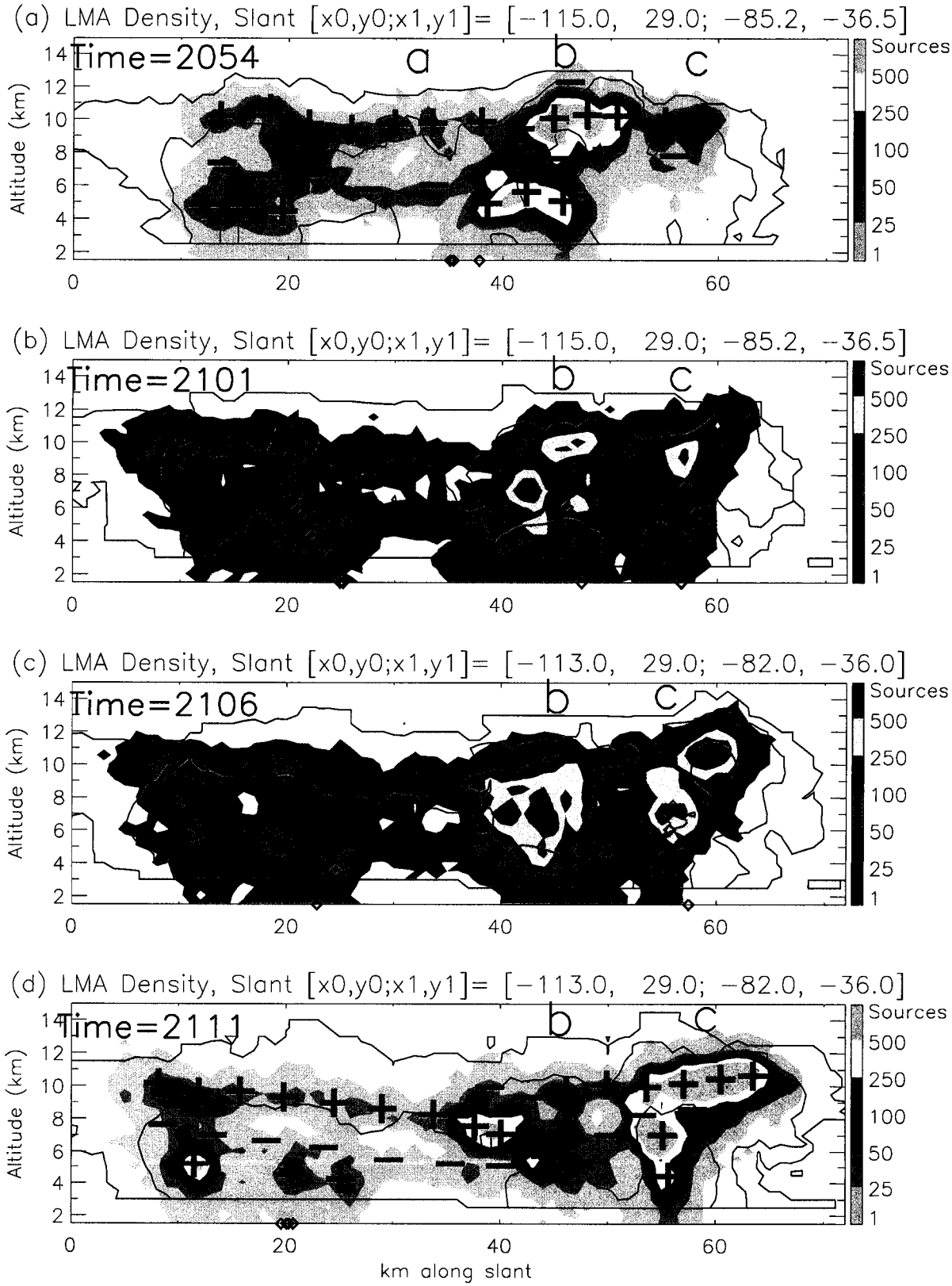

Figure 5.21: As in Fig. 5.20, but for LMA source density, with black line contours of Z_H at 5, 25 and 45 dBZ. Red plus and green minus symbols in (a) and (d) illustrate LMA-inferred charge structure.

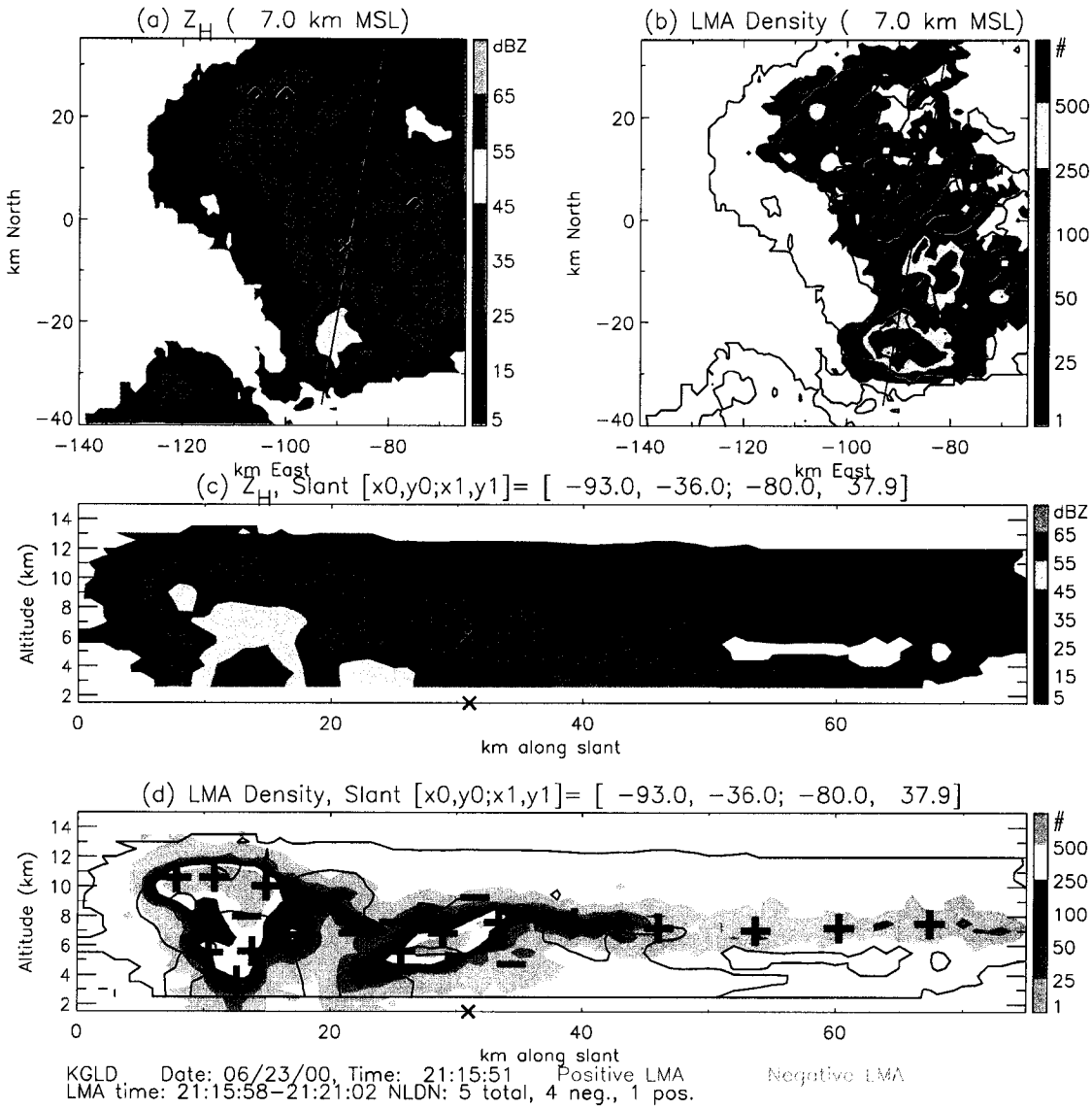

Figure 5.22: As in Fig. 5.18, but for 2116. For clarity, the CG strike points are shown in (a) but not in (b). Only the one +CG strike, indicated by an X, was close enough ($\leq$ 5 km) to the vertical cross-section to be included on (c) and (d).

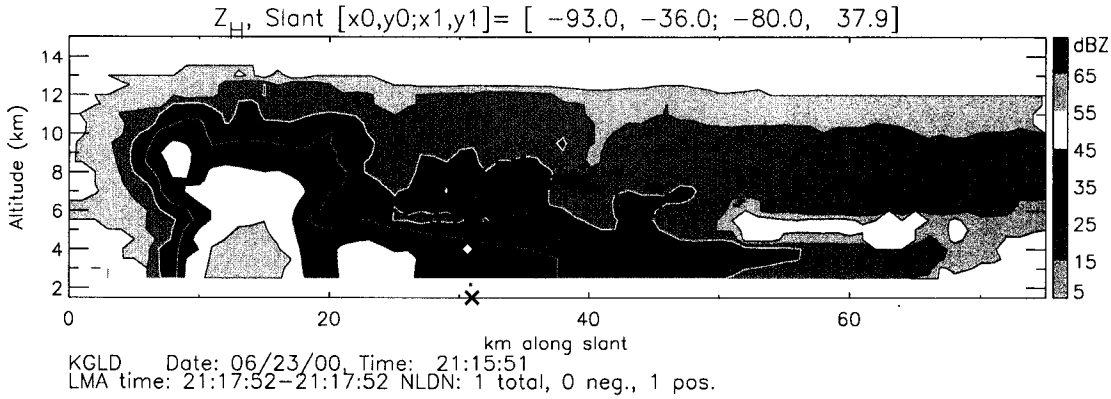

Figure 5.23: Same vertical cross-section as in Fig. 5.22, but with additional blue dots showing the lightning mapping sources from the first +CG flash at 2117:52. The LMA sources are not color-coded by charge. The filled diamond symbol marks the very first LMA source and the red X marks the mean location of the first 10 sources. The black X marks the NLDN strike point.

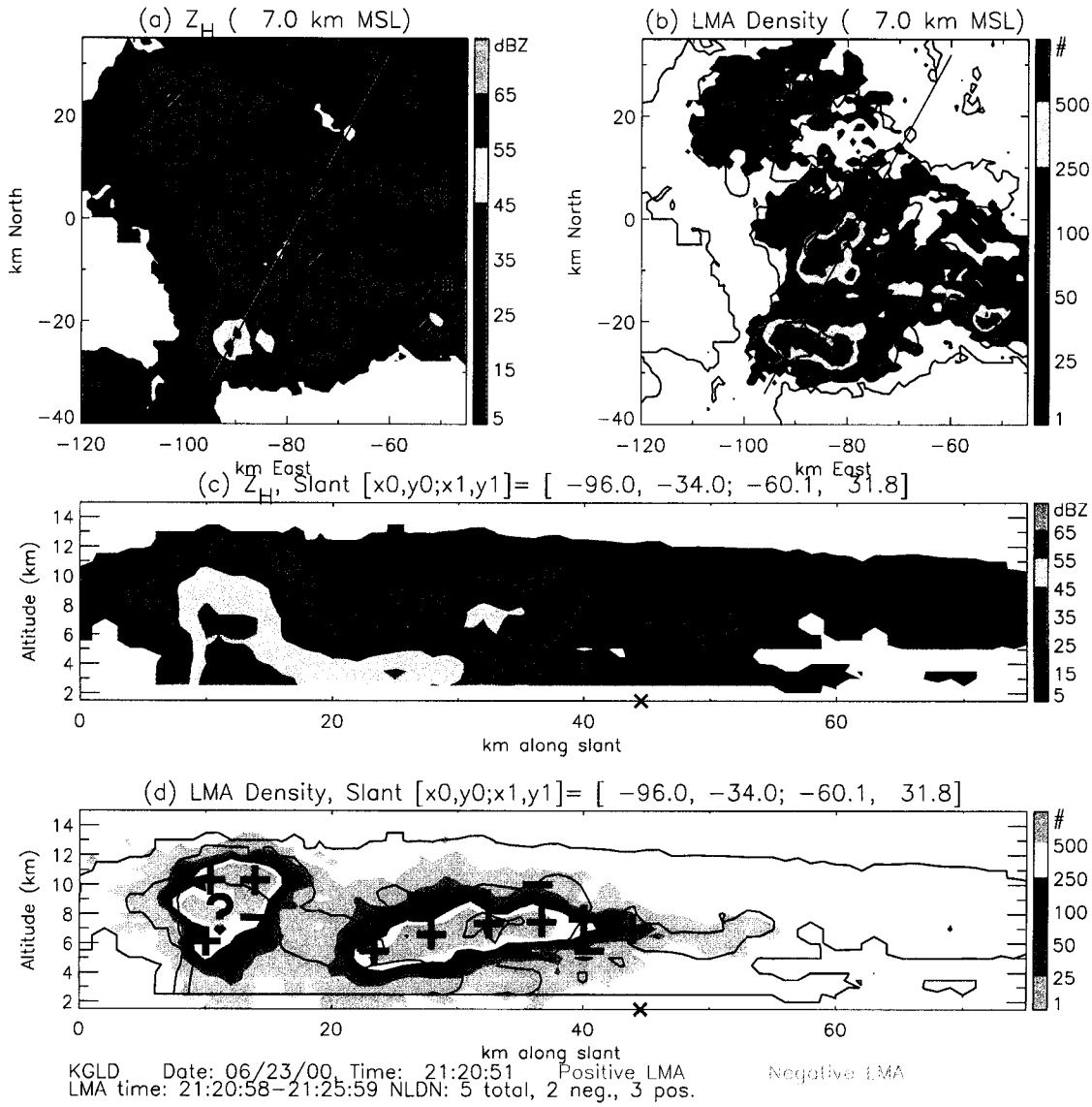

Figure 5.24: As in Fig. 5.18, but for 2121.

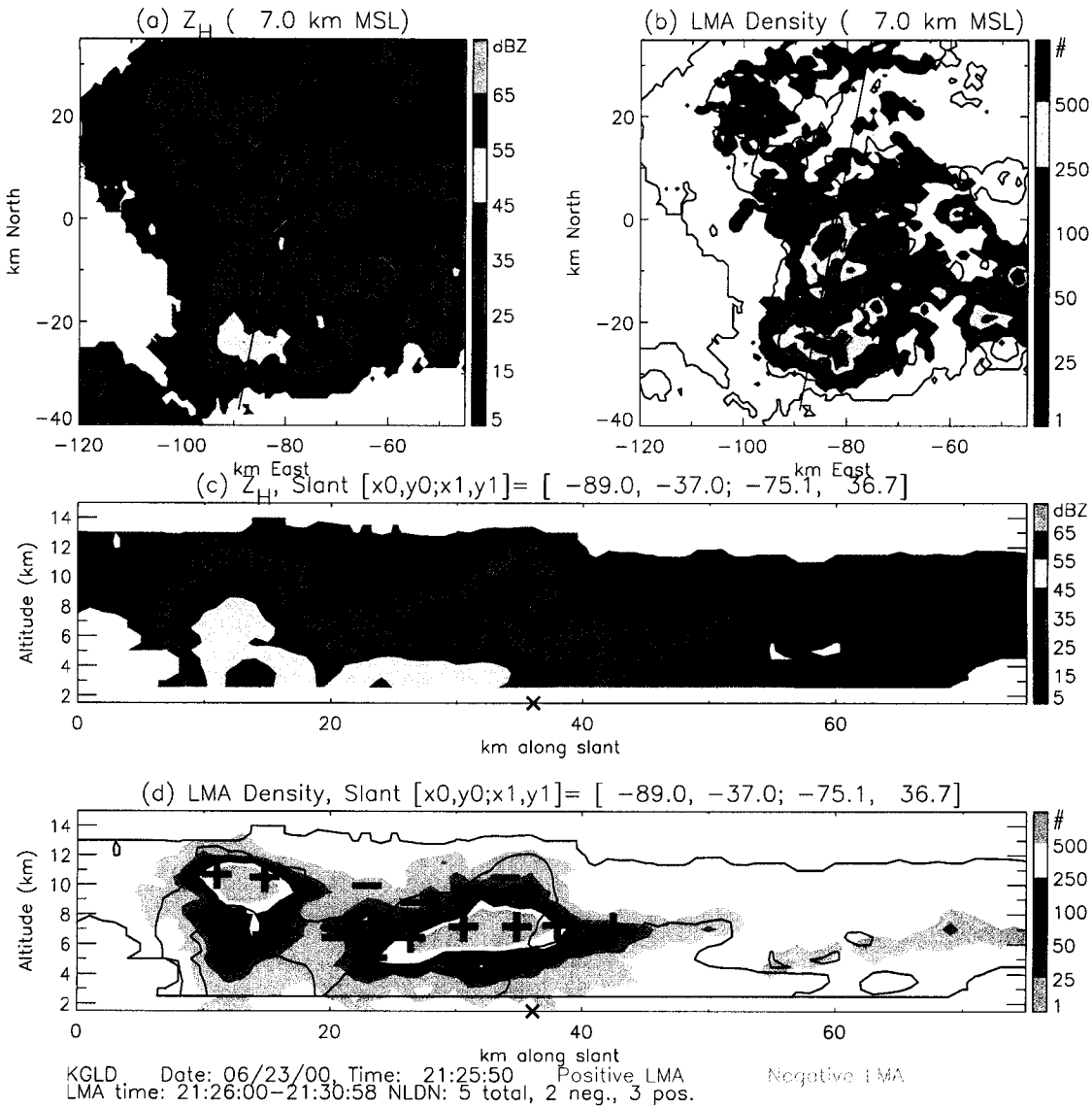

Figure 5.25: As in Fig. 5.18, but for 2126.

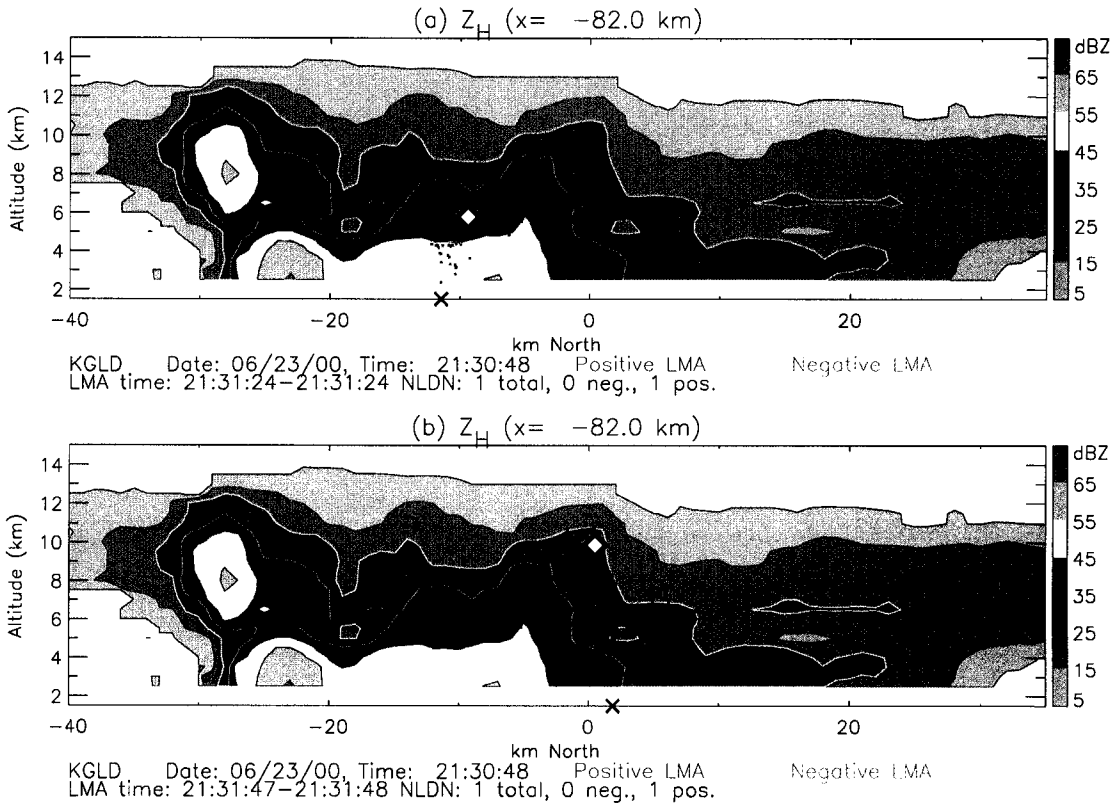

Figure 5.26: Same vertical cross-section as in the right column of Fig. 5.5 with lightning mapping sources from the +CG flashes at 2131:24 and 2131:47 overlaid onto (a) and (b), respectively. Sources are color-coded by inferred charge with red for positive and green for negative. The filled diamond symbols mark the first LMA source in each flash. The black X's mark the NLDN strike points. The +CG flash in (b) was immediately preceded by an inverted IC flash above it. The diamond symbol marks the initiation height of this IC flash and the green-colored points aloft show the negative charge region involved in the flash. Both the IC and +CG tapped the same positive charge region.

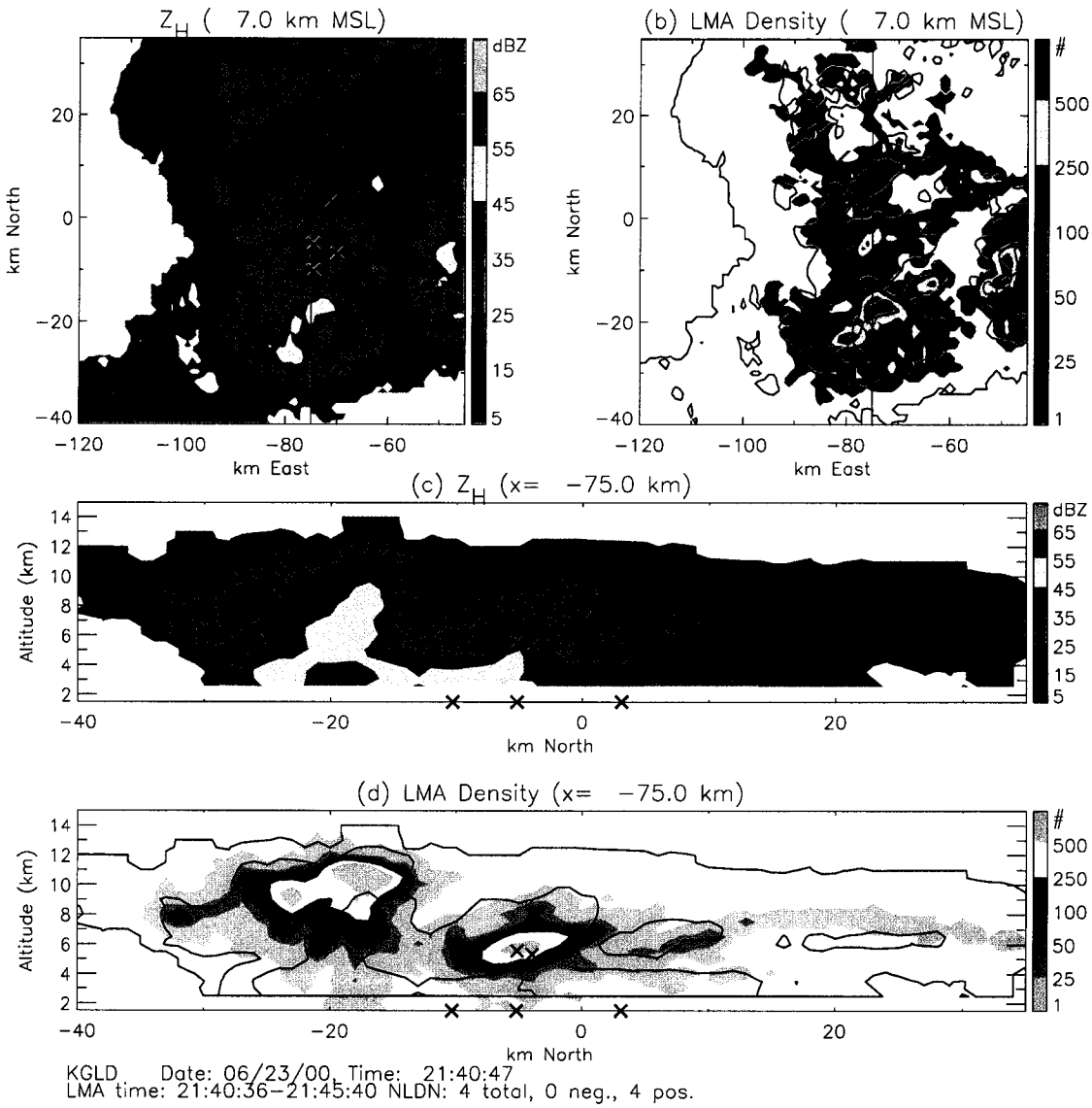

Figure 5.27: As in Fig. 5.18, but for 2141.

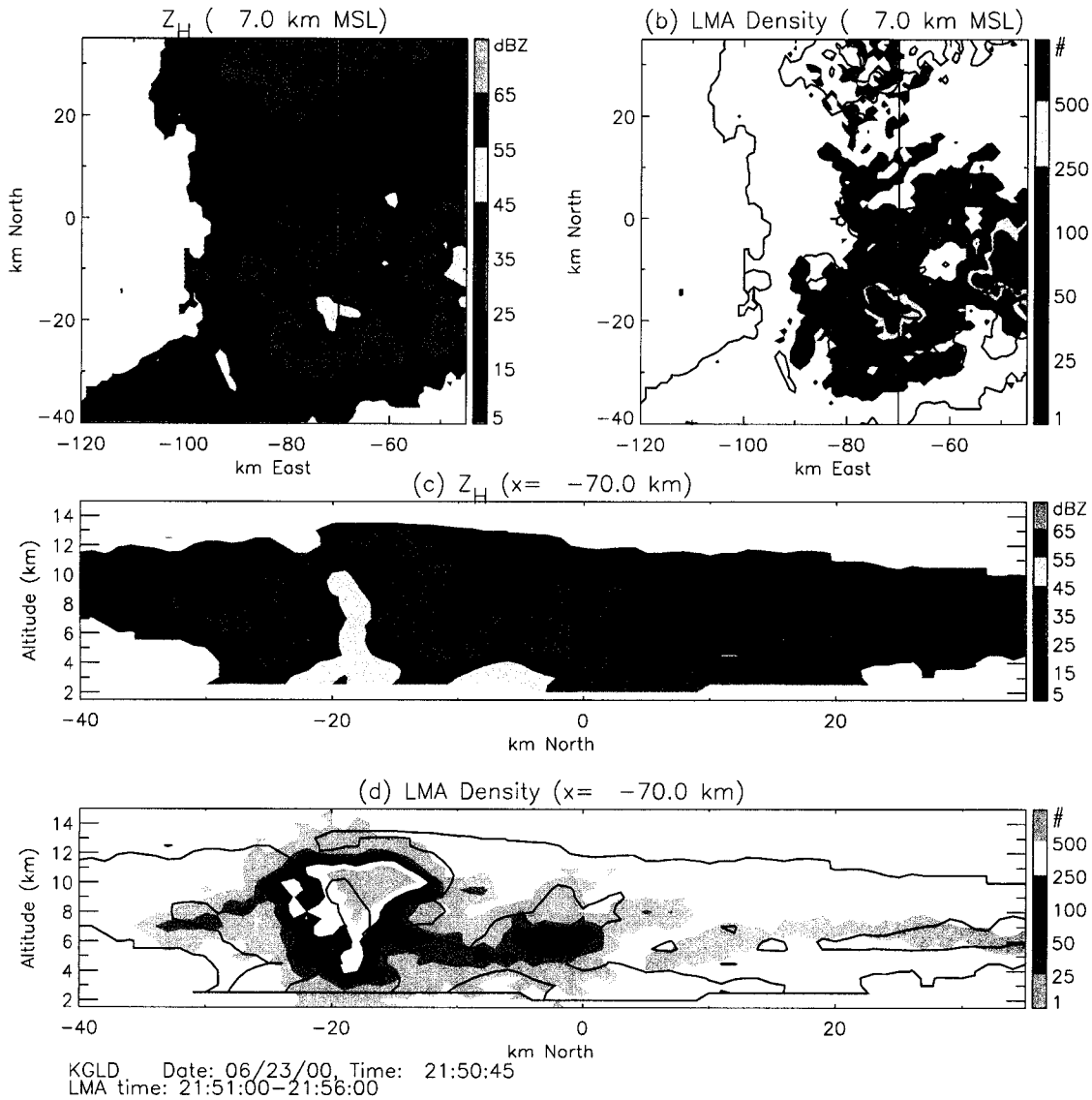

Figure 5.28: As in Fig. 5.18, but for 2151.

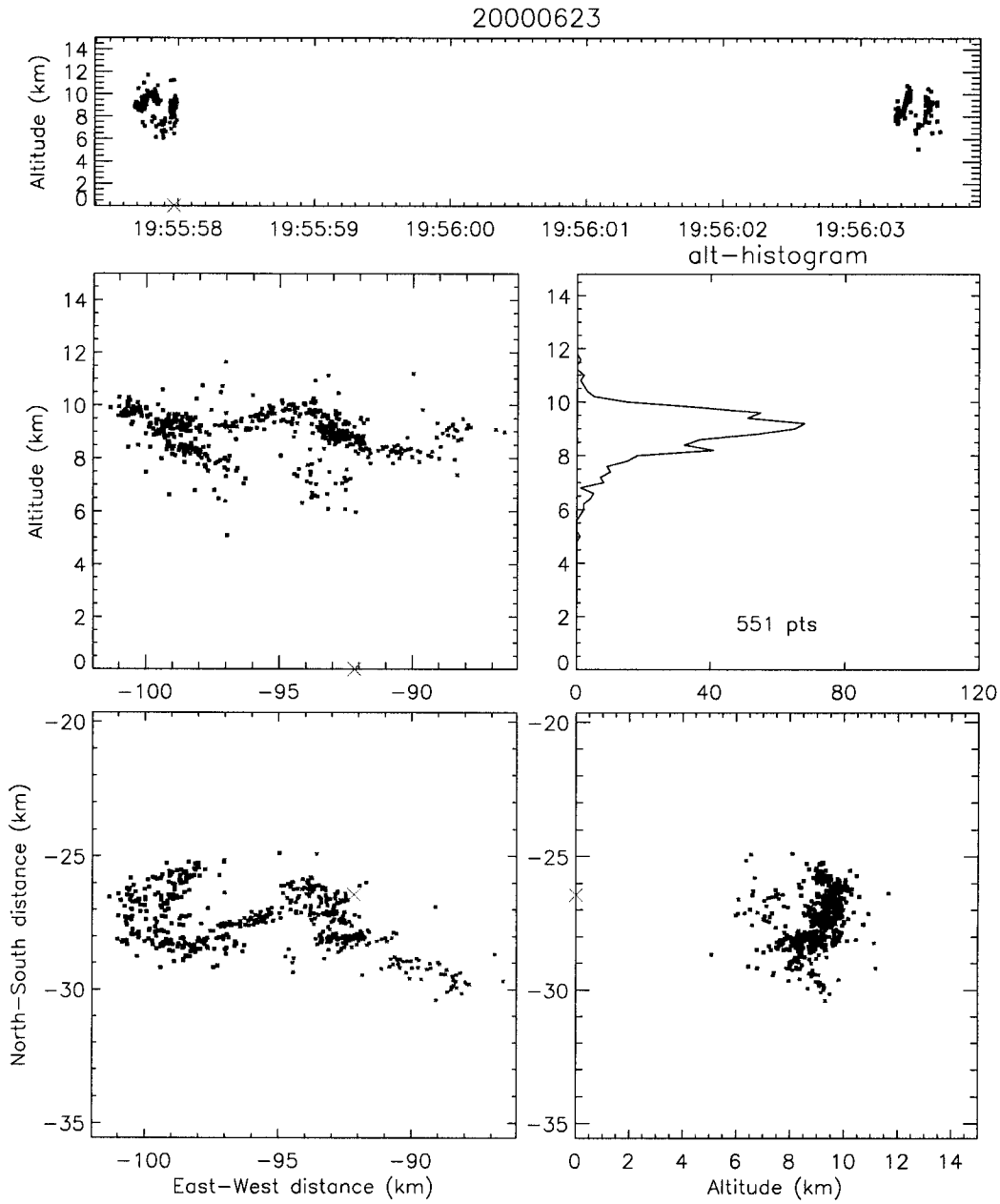

Figure 5.29: Lightning mapping of two flashes around 1956. Sources are color-coded by time. Though both flashes look like normal IC flashes between mid-level negative and upper positive, NLDN associated a +CG with only the first one.

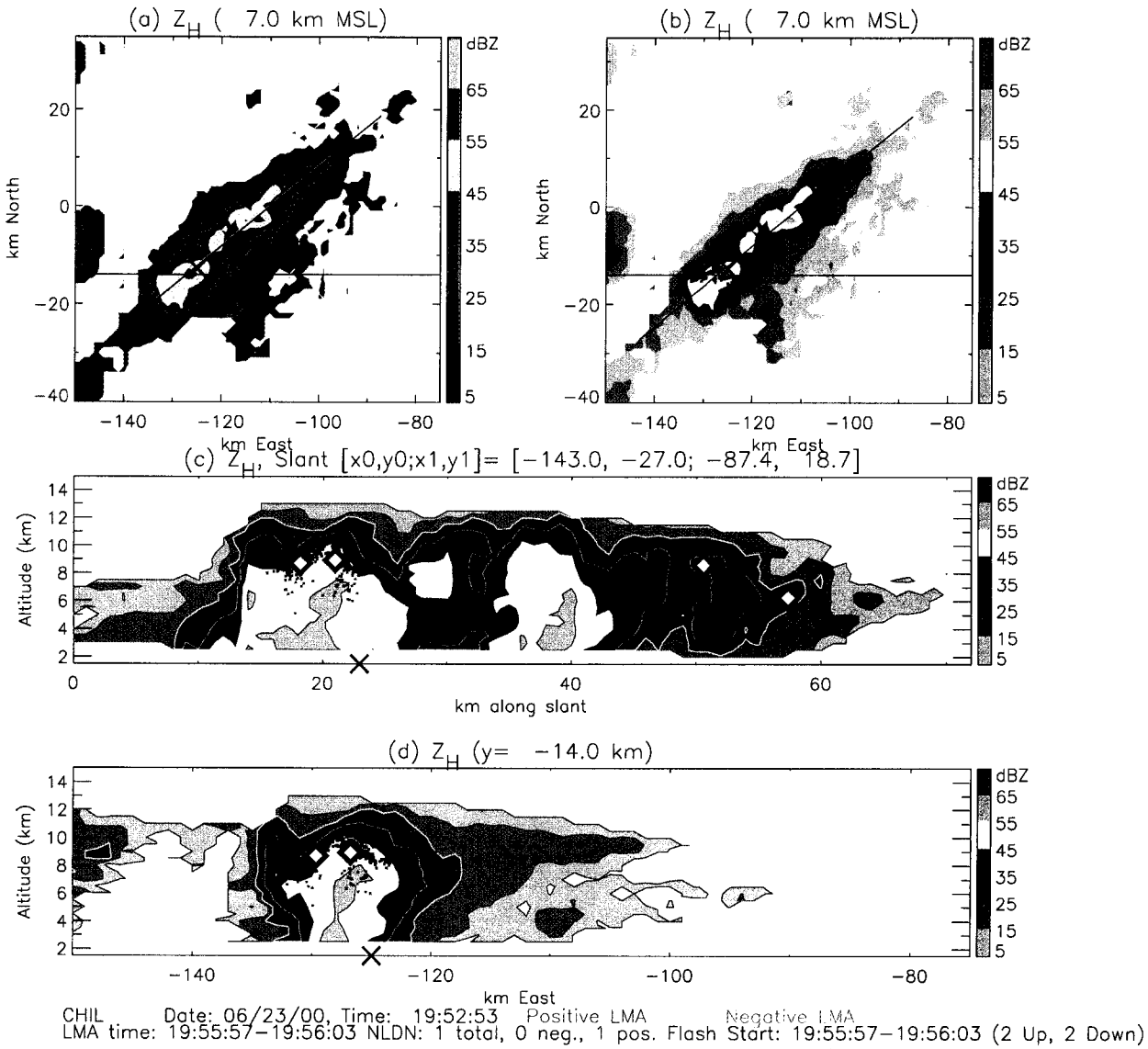

Figure 5.30: CHILL radar cross-sections at 1953, with the two flashes from Fig. 5.29 overlaid and color-coded by charge. Filled diamond symbols mark the first source of each flash, and X symbol marks the NLDN strike point of the suspicious +CG. The vertical cross-section in (c) is along the same slant path as in Fig. 5.4. The vertical cross-section in (d) is along $y = -14$ km.

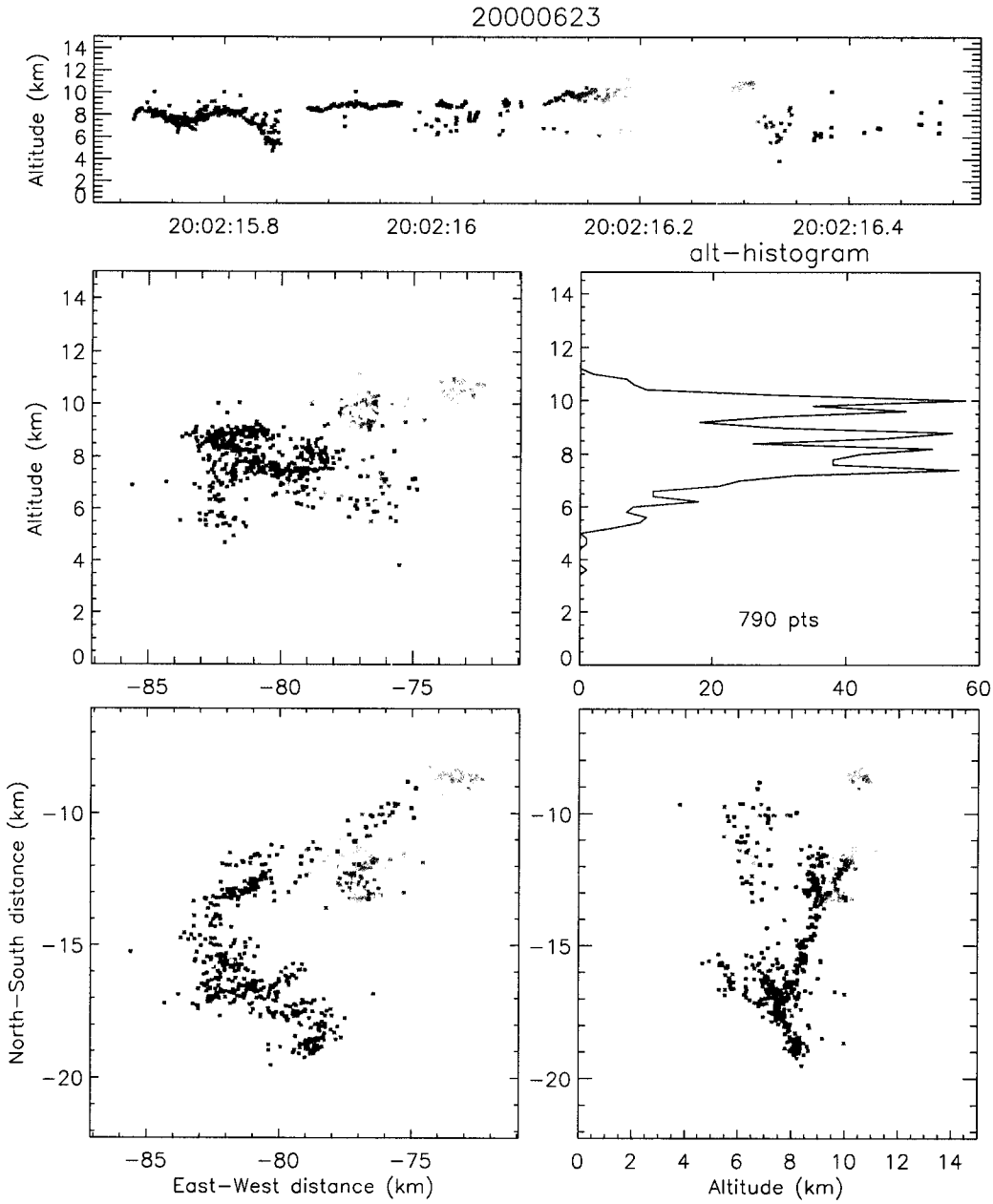

Figure 5.31: Lightning mapping of the suspicious +CG at 2002:16. Sources are color-coded by time.

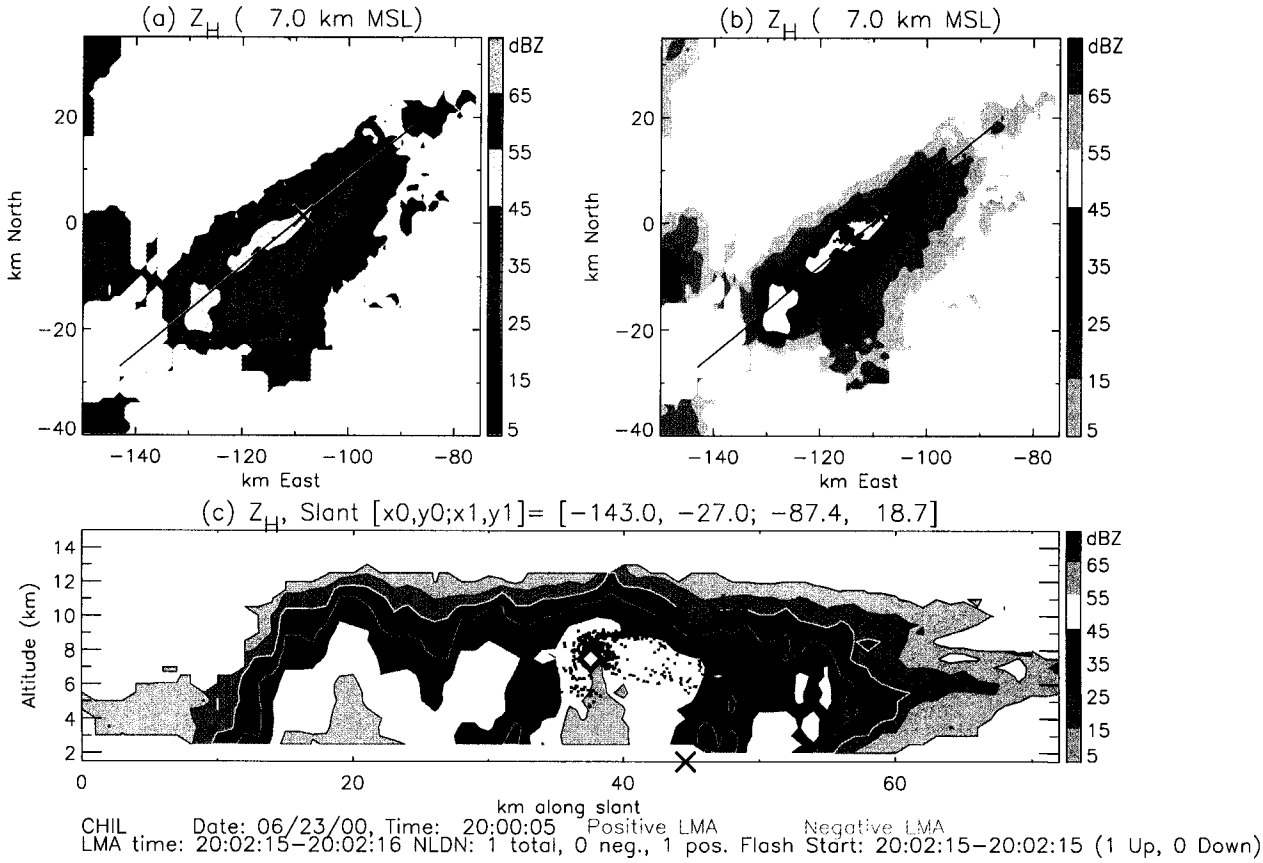

Figure 5.32: As in Fig. 5.30, but for cross-sections at 2000. Lightning mapping sources of the flash from Fig. 5.31 are overlaid and color-coded by charge.

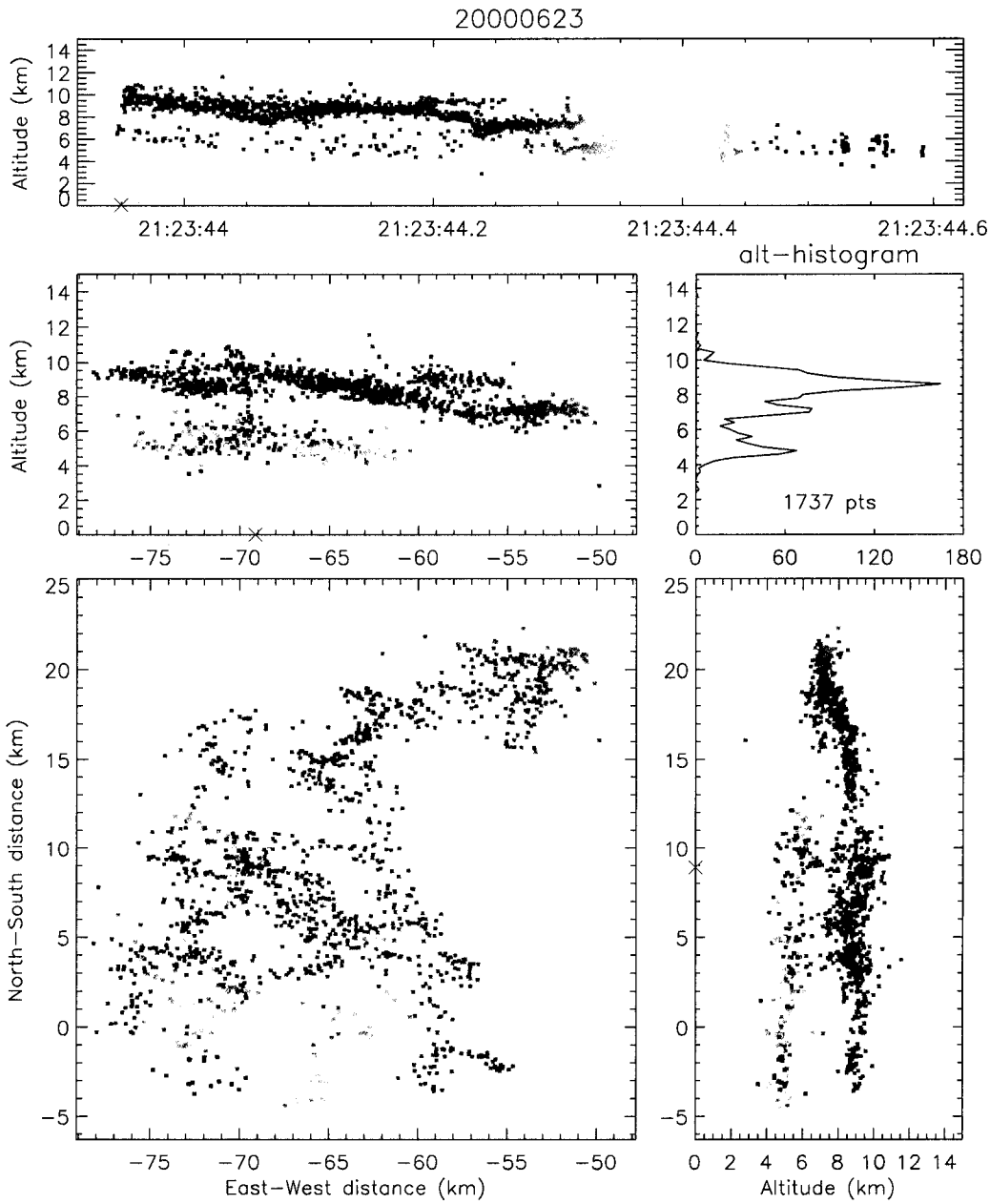

Figure 5.33: Lightning mapping of the +CG in the northern part of storm 1 at 2123:44. Sources are color-coded by time. Peak current is 21.2 kA.

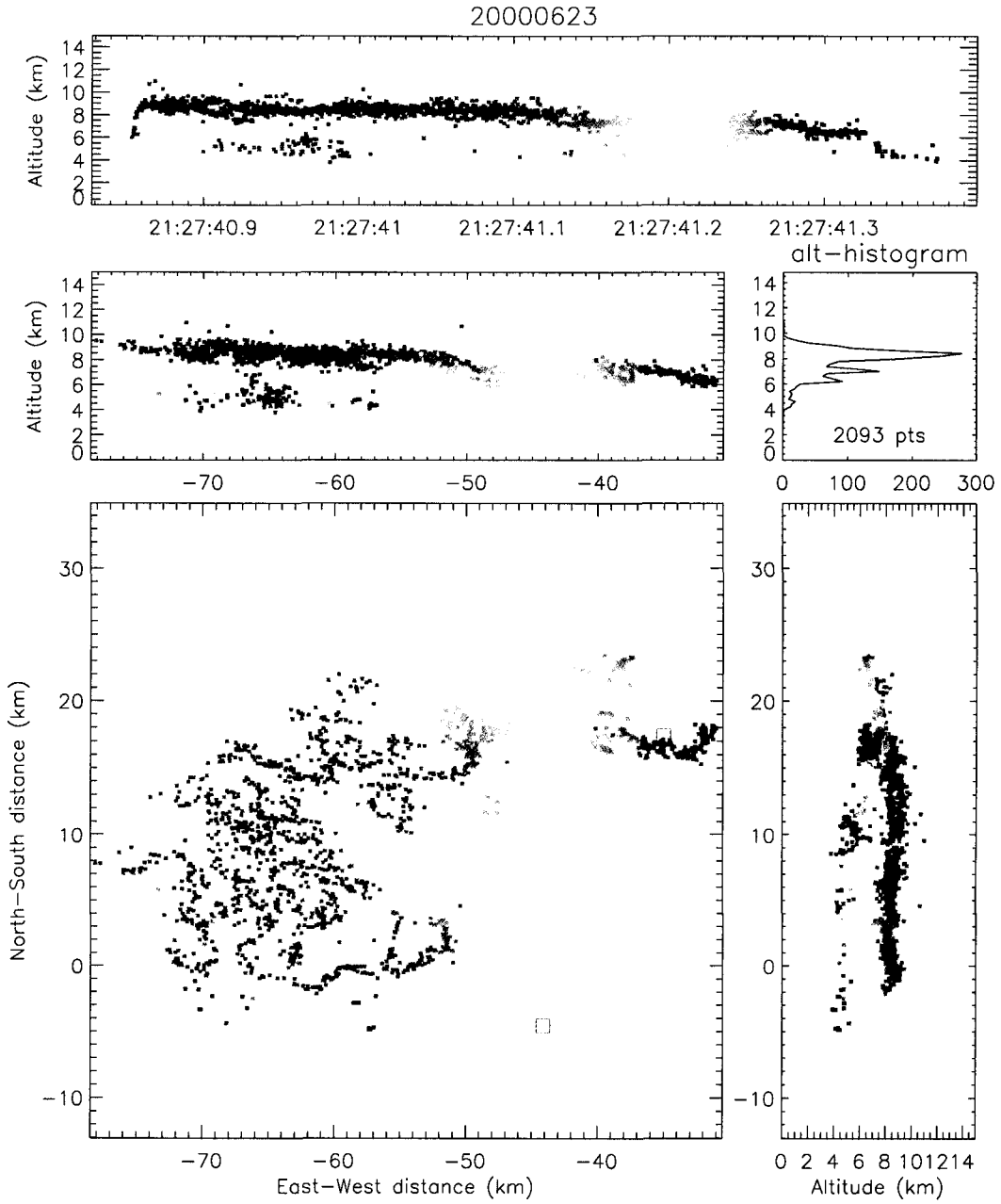

Figure 5.34: Lightning mapping of a normal IC flash in the northern part of storm 1 at 2127:40. Sources are color-coded by time.

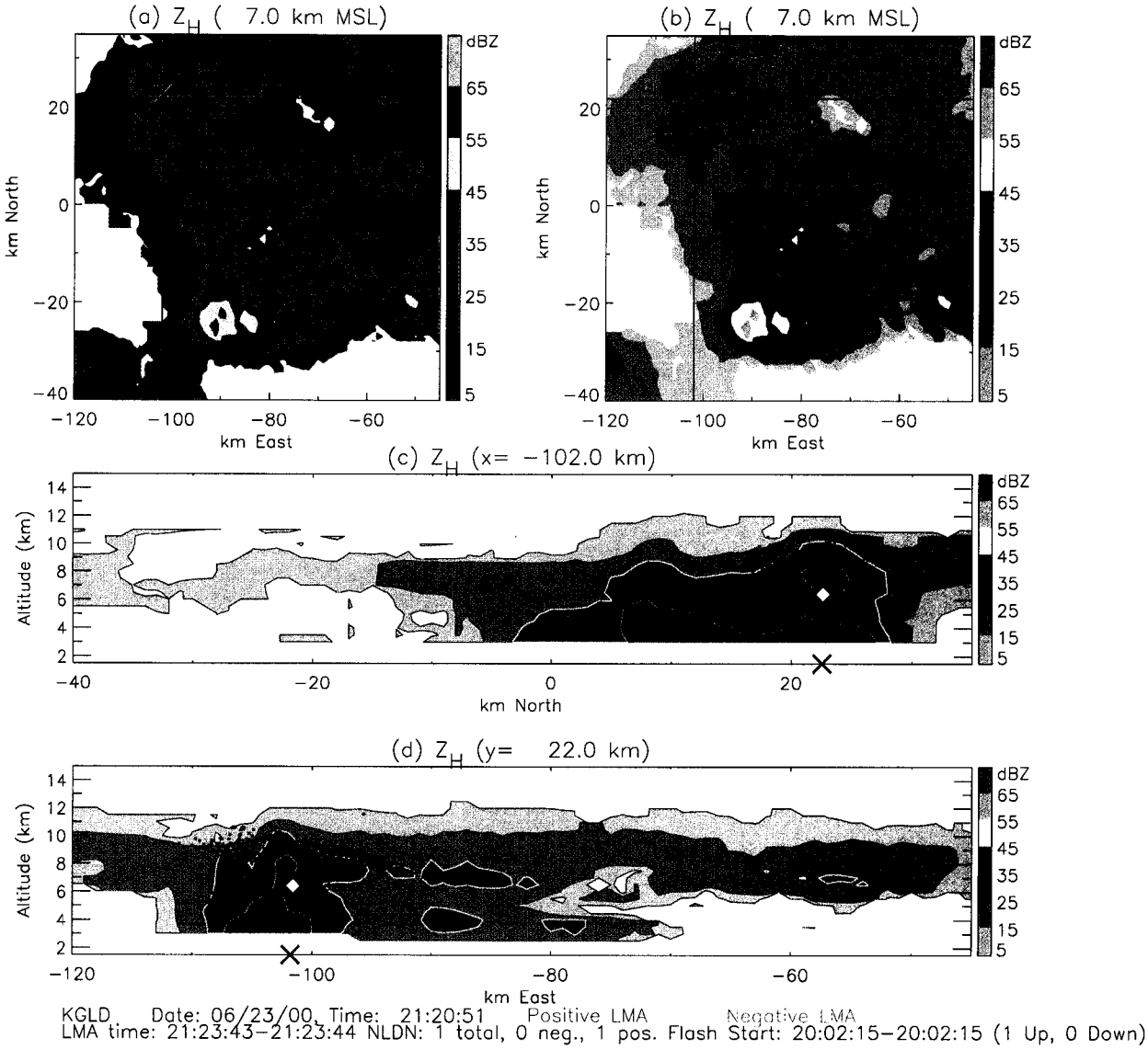

Figure 5.35: KGLD radar cross-sections at 2121 with the LMA sources from Fig. 5.33 overlaid and color-coded by charge.

5.3 Storm 3

This case was chosen because of its +CG-dominance, relative isolation from surrounding convection, and excellent radar coverage. It formed in the center of the STEPS region and was relatively stationary. Polarimetric radar scans began at 2058, and multi-Doppler scans began at 2108. Though this storm was within the polarimetric and multi-Doppler coverage area until midnight UTC, it merged with the eastward-moving "storm 1" around 2230 (see, e.g., Figs. 5.1 and 5.2). The observation period ends at the time of this merger; however, this was a sufficient time period to understand how this storm developed the structure responsible for its +CG-dominance. This was not a supercell storm. However, it did produce a modest amount of large hail for a brief period of time. This marginally severe +CG-dominated storm provides an excellent comparison with the –CG-dominated cells that formed further west in "storm 1" and with the severe +CG-dominated supercell storm of 29 June.

5.3.1 Storm 3 Overview

An MGLASS sounding (Fig. 5.36) was launched from the CHILL site at 2032, in very close proximity to this storm. The temperature profile from this sounding was used in the FHC calculations. In comparison with the 1728 sounding (Fig. 5.3) used to characterize the environment of "storm 1", CAPE at this later time was a little lower (200 vs. 300 J kg^{-1}) and the cloud base a little higher. Overall though, the thermodynamic environment had not changed much in the three hours between the two soundings. Surface winds were still weak southeasterlies. Winds aloft were stronger and from the west-southwest.

As shown in the summary cross-sections of Figs. 5.37 and 5.38, there were two distinct cells in "storm 3". The eastern cell developed within the remnants of the older collapsed convection of "storm 2" (see e.g., Fig. 5.1). The resurgence of this eastern cell, in terms of echo top height and lightning flashes, began around 2100. The eastern cell produced all of the –CG flashes of "storm 3" but only one of the +CG flashes. The western cell formed at 2030 within an echo-free region in the middle

of the STEPS network. This western cell was the stronger and longer-lived of the two and produced no –CG flashes and all but one of the 22 +CG flashes during the observation period.

From 2030 to 2220, the east and west cells remained largely distinct from other surrounding convection and from each other. This permitted isolation of their associated >30 dBZ radar echo and LMA sources for the purposes of computing separate time series of echo volumes and flash rates for each cell. Fig. 5.39 illustrates how this isolation was done. It was not possible to separate the *total* echo volume of each cell (i.e., all echo volume >0 dBZ) because the anvil regions of each cell were indistinct. This problem became even worse as the anvil from "storm 1" moved in from the west. Hence the isolation of each cell in this case really means isolation of the >30 dBZ core of each cell. An unfortunate downside to this is that the echo volume computations do not encompass the entire echo at any time. Hence, unlike the 3 June and 29 June cases, the time series of echo volumes and total flash rate were not "de-trended" from the total storm volume to examine residual correlations. They could have been de-trended, but the time series of total storm volume used in the detrending process would not have been representative of the actual echo volume of the cell, making the whole process meaningless. In any case, Figs. 5.40 and 5.41 show the resultant time series for the western and eastern cells, respectively. Figs. 5.42 and 5.43 show the respective altitude histograms of LMA sources and flash start heights. The following two sections give an overview of the evolution of each cell. More detailed observations follow in Section 5.3.2.

Western Cell

The time series in Fig. 5.40 show physically consistent relationships between the kinematic and microphysical evolution of the western cell. The first hour of the observation period (i.e., from 2100 to 2200) was a period of continuous growth. Peak updrafts were sustained above 10 ms^{-1}, and volume of updraft exceeding 10 ms^{-1} (hereafter, UV_{10}) remained above 50 km^3 (Fig. 5.40d). Correspondingly, the 30, 40,

and 50 dBZ reflectivity echo volumes increased monotonically (Fig. 5.40a–c), and each increase (decrease) in UV_{10} was generally accompanied by an increase (decrease) in echo top heights. There was significant volume of reflectivity exceeding 50 dBZ for the entire observation period, though robust hail growth aloft began only after the sharp increase in UV_{10} at 2125. The FHC identified significant echo volume of large hail only from 2125 to 2145, with hail forming aloft then descending (Fig. 5.40f). In the last ten minutes of the observation period (2210 to 2220), the UV_{10} dropped to near zero, and the $>$ 50 dBZ echo volume decreased in both magnitude and vertical extent.

In comparison with the more isolated cases of 3 and 29 June, the total flash rate of this cell was not as well-correlated with its graupel echo volume and UV_{10}. However, panels (d), (g), and (h) of Fig. 5.40 show good correspondence between the echo top heights and the magnitude (i.e, flash rate) and vertical extent of the lightning activity. During the initial growth of this cell, as echo top heights maximized at 2100, the total flash rates rapidly increased to near 60 min^{-1} and the LMA sources extended to over 12 km altitude. Throughout the remainder of the observation period, there were corresponding maxima (minima) in total flash rate and LMA source height for nearly every maxima (minima) in echo top height. Hence, as in the other cases of this dissertation, the lightning was a reasonably good indicator of convective strength, though the correlations between the time series of flash rates and radar echo volumes were not as clear and robust as they were in the more isolated storms of 3 and 29 June.

During the first hour of lightning, the LMA sources were highly concentrated at 8–10 km altitude, with very little activity at lower levels (Fig. 5.40h). As shown in the the altitude histograms of Fig. 5.42, this dominant upper-level maximum of LMA sources was bracketed by frequent downward flashes above it and relatively less frequent upward flashes below it. This is indicative of an inverted tripole charge structure consisting of positive charge at 8–10 km altitude with negative charge above and below. Though the term "inverted tripole" is a reasonably accurate description,

this terminology may be misleading. Compare the altitude distributions of this storm to those of the normal tripole during the early stages of storm 1 (i.e., compare Fig. 5.42 to Fig. 5.12). The LMA source distributions are actually very similar, as are the locations of maximum upward flashes below the upper positive. Hence, both storm 1 and storm 3 have the upper two charge regions of a normal tripole. The storm 3 histograms also show some indication of a lower positive charge region, with a semblance of a secondary maximum of LMA sources at 6 km altitude and a few downward-initiating flashes near this secondary maximum. The differences between storms 1 and 3 are that

1. The upper positive and negative charge regions are more *elevated* in storm 3.
2. There is very clear indication of an active extreme upper negative charge in storm 3 and less so in storm 1.
3. There is very clear indication of an active lower positive charge in storm 1 and less so in storm 3.

Perhaps "elevated dipole with extreme upper negative and small lower positive" is a less misleading description of the charge structure of storm 3. That's quite a mouthful though. For lack of a better term, we'll stick with "inverted tripole" and hope there's no misunderstanding. From 2130 onward, the LMA source and flash start histograms indicate that a roughly inverted tripole structure persisted, though the upper-level maximum of LMA sources broadened and descended. The downward-initiating flashes between the extreme upper-negative and upper positive remained the most frequent type of flash throughout the duration of the observation period.

There were no CG flashes in the west cell's first hour of lightning activity. Ground flashes began once the upper-level maximum of LMA sources (i.e, positive charge) broadened and descended (see Fig. 5.40g,h). All of the ground flashes produced by the west cell were +CGs[4]. Fig. 5.44 shows histograms of origin height and peak current

[4]The one –CG in Fig. 5.40g was from the eastern cell and should be disregarded.

of the CGs in both the east and west cell. The peak currents of all of the +CGs was above the 10 kA threshold. The +CGs originated from 5–8 km altitude–below or on the lower end of the descending region of concentrated LMA sources. Interestingly, these +CG flashes began during the onset of robust hail growth, much like in the 29 June supercell case.

Eastern Cell

As discussed above, the eastern cell of storm 3 developed within the remnants of an earlier storm. Though there was lofted >30 dBZ echo prior to the start of the time series in Fig. 5.41, there had been no lightning in this echo for almost 20 minutes. The mere presence of precipitation-sized ice was apparently not a sufficient condition for lightning. As the laboratory studies of the NIC mechanism have shown, electrification requires collisions between ice crystals and *actively* riming graupel or hail, which in turn requires dynamic forcing, i.e., updraft. Lightning flashes resumed in the eastern cell once the >30 dBZ echo volumes started to increase aloft, i.e., once active riming growth resumed. Though there is no Doppler-derived updraft right at the start of this resurgence in lightning, the growth in echo volume aloft is a clear manifestation of renewed convective updraft.

In comparison with the western cell, this eastern cell was much smaller and weaker. Echo volumes of >30, 40, and 50 dBZ and UV_{10} were roughly four times less, and peak total flash rates were an order of magnitude less. There is some indication of hail growth aloft, but little indication of *large* hail. As in all the other cases of this dissertation, the total flash rate of this eastern cell was indicative of the convective state of the storm and even generally followed the trends in graupel echo volume. Total flash rates and graupel echo volume both peaked around 2140, just after the prominent spike in UV_{10} around 2135. UV_{10} then fell rapidly to zero, followed by corresponding decreases in graupel echo volume and total flash rate.

The LMA source and flash start altitude histograms indicate a normal tripole charge structure from 2100 to 2110 (first panel of Fig. 5.43), with upper positive

charge at 8–10 km altitude, lower positive charge from 4–6 km, and negative charge between. There were two –CG flashes during this first ten minutes of lightning, both of which originated in the upper portion of the inferred lower positive charge region (Fig. 5.41g,h). Over the next 30 minutes, this cell retained its normal tripole, but flash rates doubled as the upper positive charge became more prominent and elevated. As indicated by the large number of downward flashes in the upper levels, an additional negative charge formed atop the upper positive. There were no CGs of either polarity during this 30 minute period of increased lightning and elevated charge structure. After the absolute peak in flash rates at 2140, the LMA distributions broadened out and descended as the cell dissipated and flash rates plummeted. This cell produced one +CG from 6 km altitude during the rapid collapse of the cell. Interestingly, the time of this lone +CG was also the time of maximum (albeit very small) radar-inferred large hail echo volume. By 2200, the charge structure had collapsed with just one low-level maximum at 5 km altitude, and this cell produced one –CG (originating near 5 km) among its last few flashes.

As an aside, Williams et al. (1999), Hamlin (2004), and others have noted "jumps" in lightning flash rate and dramatic increase in the vertical extent of LMA sources prior to severe weather at the ground. They posit that such lightning "jumps" are manifestations of convective surges. The total flash rates in both the western and eastern cells briefly decreased from 2100 to 2105 then increased rapidly again (Figs. 5.40 and 5.41) This lightning "jump" was especially pronounced in the eastern cell, and as shown in Fig. 5.43 much of this lightning jump was due to onset of downward flashes well aloft, indicating formation of an extreme upper-negative charge. The more vigorous western cell already had an extreme upper-negative charge prior to the lightning jump, but its upper-negative charge also became more active during the jump. The next lightning jump in the eastern cell at 2140 occurred just after a pronounced spike in UV_{10} and also corresponded to increased downward flashes from extreme upper-negative charge. So, the lightning jumps in these cases do appear to be manifestations of convective surges. Perhaps the extreme upper negative charge

is carried by ice crystals that are a by-product of the liquid water rich core of the updraft where NIC studies indicate the larger riming ice charges positively. Collisions in weaker updraft or on the periphery of the stronger updraft grant positive charge to the ice crystals and negative charge to the rimer, forming the usual normal dipole. Collisions in the core of stronger, broader updrafts grant negative charge to the ice crystals which are then quickly transported upward to form the extreme upper negative. Perhaps this explains why only the dynamically stronger storms on this day (and also the 29 June storm) have the extreme upper negative, while weaker storms do not. If NIC mechanisms are the only charging mechanisms operating, then the resultant charge structure pretty much depends only on how strong and broad the updraft is and where the collisions occur relative to the core of the updraft.

5.3.2 Initial Growth and Electrification

The first echo of the western "cell" of storm 3 was at 2036, consisting actually of two or three patches of weak (<35 dBZ) echo aloft that started to grow and descend by 2041 (Fig. 5.45a). Lightning flashes began at 2047, with only six flashes from 2047–2053 (Fig. 5.46). These first few flashes were all normal ICs between negative charge at 6–8 km and positive charge at 8–10 km. As shown in Fig. 5.45b, the inferred negative charge was in the strongest echo of each of the three western cells, with inferred positive charge in weaker echo aloft. The central cell was the most vigorous, with the strongest and most elevated echo. The charge regions were also relatively elevated in the central cell in comparison with the other two cells.

Frequent vertically compact flashes in the upper regions began at 2053 (Fig. 5.46), bringing the flash rate up to tens min^{-1} (Fig. 5.40g). The charge structure of these initial compact flashes was difficult to determine on a flash-by-flash basis; however, the altitude histograms in Fig. 5.42 suggest that the compact upper level flashes were due to the formation of a negative charge region above the pre-existing upper positive charge. It's difficult to interpret the microphysical context of the lightning-active upper region because KGLD was not topping the echo. Presumably, this upper

negative charge was either a screening layer charge or was carried by ice crystals in yet weaker echo further aloft. This upper negative charge participated in the majority of the flashes over the remainder of the observation period, so it's unlikely that it was merely a screening layer.

By the time the polarimetric radar scans began at 2058[5], the middle of the three western cells had become quite vigorous, with lofted 55 dBZ echo and higher echo tops than the surrounding convection (see left column of Fig. 5.37). The lightning was also most active in this central cell, with most of the LMA sources concentrated at 8–11 km altitude, at the apex of the 45 dBZ echo. As indicated by the charge composite in the left column of Fig. 5.37, all three of the western cells had positive charge from 8–11 km with negative charge below. The extreme upper negative charge lay atop this positive, but only above the vigorous central cell. The altitude distributions in Fig. 5.42 show that the vast majority of flashes discharged into the positive charge region at 8–11 km, from both negative charge region above and below the main positive charge region. There were only a few flashes indicating lower positive charge at 4–6 km, and these low flashes were restricted to the strongest (>55 dBZ) low-level echo on the west side of the cells (see, for example, Fig. 5.48).

At 2100, lightning activity resumed in the re-invigorated convection further east. The lighting in the eastern cell described a normal tripole charge structure with two –CGs originating from the mid-level negative charge region. These observations are illustrated more clearly in Figs. 5.47 and 5.48 which show the lightning mapping of these first two –CGs along with a couple dozen other flashes in both the eastern and western "cells" from 2106–2106:45. These first two –CGs originated from the same place in the eastern cell, but they took different paths to ground. The first –CG traveled westward on its way to ground, with a very nicely mapped downward leader through the lower positive charge (Fig. 5.49). The second –CG initiated from the same spot as the first one, but took a more direct vertical path to ground (Fig. 5.50).

[5]CHILL scans started at 2058, and S-Pol scans started at 2108

The NLDN strike point of this second –CG appears to be 8–10 km west of where the lightning mapping indicates that it struck.

Multi-Doppler coverage began with the radar scans at 2108. The addition of this wind flow information greatly aids interpretation of the storm structure. The middle column of Fig. 5.37 shows two updraft cores, one in the main western cell with peak updraft in excess of 15 ms^{-1} and one in the eastern cell with updrafts near 10 ms^{-1}. The storm-relative wind vectors on the vertical cross-section in the middle panel show low-level inflow from the east-southeast and upper-level outflow back to the east-northeast, which is consistent with the MGLASS sounding in Fig. 5.36. The juxtaposition of the echo structure with this wind flow suggests that the larger precipitation forming in the updraft core were falling out directly, while smaller particles were swept up and out to the northeast. As discussed in the next paragraph, the structure of the lightning-mapped charge regions corroborates this interpretation.

The lightning mapping of the flashes from 2114–2119 showed very clear and consistent charge structure in both the east and west cells. The charge density plot in Fig. 5.51 accentuates this consistency. Compare this charge density plot to the echo structure and charge composite in the middle column of Fig. 5.37. In the east cell, the lightning revealed a normal tripole charge structure with upper positive charge near 10 km atop the updraft core and 45 dBZ precipitation shaft, negative charge at 6–8 km within the precipitation shaft, and lower positive charge in the strongest precipitation below 6 km. The two upper charge regions also slanted downward to the northeast, following the Doppler-inferred wind flow. The lower positive charge, however, was restricted to the precipitation core on the southwest side, again suggesting that the largest precipitation was carrying positive charge and that this precipitation was falling out directly on the western edge of the cell. The LMA altitude histogram (Fig. 5.43) for the eastern cell from 2110–2220 is consistent with this charge structure. The LMA source maxima at 5 and 10 km altitude correspond to the lower and upper positive charge, respectively. The upward and downward flash start maxima at 6 and 8 km altitude nicely bracket the mid-level negative charge. Note also in Fig. 5.43

the maximum of downward flashes near 11 km indicating an extreme upper negative charge in the eastern cell that is absent in the charge density plot of Fig. 5.51. The flash-by-flash analysis did, in fact, show such frequent downward flashes from an extreme upper negative charge, but these flashes ceased almost entirely by 2114 and hence are not included in the charge density plot. The western cell had an overall charge structure similar to the eastern cell, but with more horizontally extensive mid-level-negative and upper-positive charge regions and an additional extreme upper negative charge (again refer to Fig. 5.51 and the middle column of Fig. 5.37). Flashes within the lower positive charge of the western "cell" occurred only to the extreme southwest. As described above, there was really more than one convective cell in the western "cell", so the term "cell" is imprecise and clumsy. In any case, it's clear in Fig. 5.37 that the more collapsed cell (hereafter, the small cell) on the extreme southwest was the only source of flashes indicating lower positive charge at this time. The main central cell had no flashes indicating a lower positive charge region, despite a very well-developed precipitation shaft. As with the eastern cell, the altitude histogram for the western cell (Fig. 5.42) agrees with the manual flash-by-flash analysis summarized in Fig. 5.51. Downward flashes between the extreme upper negative and upper positive were the most frequent type of flash.

Over the next 15 minutes (2120 to 2130), the echo and charge structure remained roughly the same in both the east and west cell, though the upper charge regions became more horizontally extensive and there was more indication of extreme upper negative charge in the eastern cell (Fig. 5.52). There were also a few flashes that initiated in the western cell and branched across to both the upper and lower positive charge regions of the eastern cell.

5.3.3 Intensification, Hail Growth, and Clustered +CGs

The UV_{10} in both the east and west cells increased dramatically around 2130, leading to increased formation of >50 dBZ echo aloft and a robust signal of large hail growth in the western "cell" (Figs. 5.40 and 5.41). By 2134, the small cell

on the extreme southwest edge of the domain had completely dissipated while the main western and eastern cells had very deep 55 and 45 dBZ precipitation shafts, respectively (see the right column of Fig. 5.37). The lightning in both of these cells continued as before, though the mid-level negative and upper positive charge regions in the western cell sloped downward even more drastically to the northeast, and the lower positive charge was squarely within the western cell's precipitation core. The upper-positive charge remained the most lightning-active charge region in both cells, participating in frequent flashes initiating from the negative charge regions both above and below.

Additionally, a separate stronger updraft developed due east of the western cell, with peak updraft exceeding 15 ms^{-1}. This new updraft region is not along the path of the slanted vertical cross-section Fig. 5.37, but is quite clear in the east-west vertical cross-section in Fig. 5.53. This new convection to the near east was still in development with its strongest echo residing aloft. The initial lightning in the new convection revealed an inverted tripole charge structure, with the lower negative charge extending as low as 4 km MSL. The flashes between the mid-level positive and lower negative in this new convection were very clear (e.g., Figs. 5.54 and 5.55). One can't help but think that the outflow from the heavy precipitation of the main western cell played some part in the initiation of this new convection and that the formation of the inverted tripole structure in this new convection was influenced by the pre-existing cell to the west of it. Perhaps the northeastward-sloping charge regions induced by the wind-flow supplied the lower negative charge of the new cell simply by advection. As the new cell grew, it maintained an inverted tripole structure. Perhaps inductive processes played some role to reinforce the charge structure that the older cell initially granted it.

From 2140 to 2150, things became more complex as the new updraft on the east edge of the main western cell started to confuse things. As the cross-sections in Fig. 5.56 show, there was some semblance of a mid-level BWER and lightning hole associated with this updraft. The charge structure on the western side of the western

cells was still tripolar with upper negative charge. The lofted echo in the newer convection to near northeast had instead a lower negative and an overall inverted tripole charge structure. Along the north-south cross-sections in Fig. 5.57, the juxtaposition of the updraft, inflow, and charge structure suggests that an elevated inverted tripole formed (or was maintained) in the stronger updraft on the upwind (south) side, while lower positive formed within the strongest precipitation growing in this updraft. This precipitation fell out, carrying the positive charge with it, leaving only the mid-level positive and lower negative charge further downwind.

The first +CG flash initiated amidst the inverted tripole north of the main updraft (as indicated by the magenta X's in Fig. 5.57). Figs. 5.58–5.60 show the details of this first +CG flash. It was immediately preceded by an inverted IC down through the lower positive in the strongest echo further south. The leader to ground then proceeded northeastward through the lower negative of the inverted tripole. The post-strike breakdown tapped the mid-level positive charge of the inverted tripole and also discharged through inferred sloping positive charge further northeast. The second +CG occurred in the far eastern cell and was also immediately preceded by an inverted IC flash (Figs. 5.61–5.62). This was the only +CG flash in the eastern cell, and *unlike almost every other +CG flash documented in this dissertation, this one occurred in the apparent absence of a lower negative charge.* The +CG was the first flash to suggest any such lower negative charge. If there were, in fact, a lower negative charge involved in this +CG flash, perhaps it was advected there from the cell to its southwest. The wind flow and slope of the charge regions suggest this may have been the case. Positive ground flashes continued for the next 30 minutes at an average rate of $\sim$1 min^{-1}. Fig. 5.63 shows the strike locations of all of the CGs from 2140 to 2220 in the context of the radar data. Fig. 5.64 shows the lightning mapping of a few representative CG flashes overlaid onto vertical radar cross-sections. Of the 22 +CGs that occurred from 2140 to 2200, 14 of them struck in a cluster within or very near the precipitation core of the western cell.

The flash rates almost tripled from 2150 to 2200, peaking near 150 min^{-1} at

2200. The +CGs also began in earnest. The western cell(s) were very vigorous during this time, with a very deep and broad precipitation core (see the left column of Fig. 5.38). The LMA density cross-section at 2153 in Fig. 5.38 shows a very deep region of concentrated LMA sources extending from 5 to 10 km altitude within the precipitation core. As suggested by the corresponding charge composite, the lightning and charge structure in these cells was *very* complex in the mid- and upper-levels, possibly because of intermingling of the charge regions resulting from collisions in the two updraft cores. Note also the descent and broadening of the the distribution of LMA sources from 2130 to 2150 in Figs. 5.40h and 5.42. As discussed earlier, this descent of the bulk of the LMA sources was coincident with the formation and descent of large hail. This coincidence strongly indicates that the hail was either carrying positive charge and hence bringing the positive down with it and/or that the descent of this hail caused large-scale descent via precipitation-loading of the updraft. The +CGs during this hail descent all originated from about the same place and showed structure similar to the first +CG in Fig. 5.60. They generally initiated near 7 km MSL between the deep mid-level positive charge and lower negative charge on the downwind (north) edge of the updraft and hail shaft. After contacting ground in (or on the northern edge of) the hail shaft, they tapped positive charge both in the precipitation core and and in weaker echo to the northeast. Fig. 5.64a,b show two representative examples.

5.3.4 Dissipation and Dispersal of +CGs

By 2200, most of the large hail had fallen out, and the altitude distribution of LMA sources in the western cell(s) recovered a more sharply peaked maximum near 9 km MSL (Fig. 5.42). Meanwhile, the far eastern cell dissipated rapidly and produced one very extensive –CG among its last few flashes. Fig. 5.64c shows the lightning mapping of this –CG flash (green sources) in comparison with another of the clustered +CGs (red sources) in the western cell. The remaining +CG flashes were also not as clustered near the precipitation core of the western cell, though those

that did continue to cluster there were still quite similar in structure to the examples discussed above.

Over the next 20 minutes (2200 to 2220), the western cell also dissipated while other cells popped up to the west and south of it (see the last two columns of Fig. 5.38 and 5.63). The cell to the west was very weak, and its location relative to the surrounding convection suggests that it may have been kicked off by convergence of outflow from both the main western cell and the oncoming cells of "storm 1" further west. This small, weak cell produced two +CGs that were nearly identical to each other but quite different from the preceding examples. Fig. 5.64d shows one of these +CGs. The new cell to the south was much stronger, and by 2220 this southern cell was the most lightning-active cell of the domain (right columnn of Fig. 5.38). The sharp increase in total flash rates at the end of the observation period (see Fig. 5.40) was due mostly to the development of this new southern cell. Like the cell that developed just east of the western cell at 2130, this new southern cell also had very lofted echo, initially formed an inverted tripole structure, and produced a handful of +CGs (see the right column of Fig. 5.38). Fig. 5.65 shows the lightning mapping of one of these +CGs. The extensive and horizontally stratified structure of this +CG made it the charge classification very easy. As you can see in the radar overlay of Fig. 5.66, this +CG initiated nearer the new southern cell but struck ground in between the old western cell and new southern cell. It tapped a horizontally stratified region of positive charge extending both north and south at 8–9 km MSL. The lower negative charge was also extensive and horizontally stratified at 4–6 km.

5.3.5 Discussion of Storm 3

How did the inverted structure that produced the clustered +CG flashes form? The electrification process on the south and west side of the west cell (i.e., upwind side) formed a four-layer charge structure: positive charge at 8–10 km, negative charge above and below, and an additional lower positive charge at the very bottom. However, the lower positive charge was restricted to the upwind side of the precipitation

core, suggesting that the precipitation carrying this lower positive charge was falling out directly, while the three upper charge regions in the weaker echo aloft extended further downwind, sloping downward further from the updraft (e.g, Fig. 5.51). Hence, the charge structure transitioned from a four-layer structure on the upwind side to an inverted tripole structure (the four-layer structure minus the lower positive) on the downwind side. This charge structure was persistent throughout the storm. However, this did not produce any CG flashes of either polarity for the first hour of lightning activity. The lack of –CG flashes may have been due to the restriction of the lower positive charge within the precipitation core on the western edge. In other words, the charge regions were not vertically stacked enough to provide the negative charge with a suitable positive charge conduit to ground (e.g., Lopez and Aubagnac, 1997). Another explanation is that the IC flashes involving the mid-level negative and upper-positive charge were frequent enough to relieve the electrical stress (i.e., reduce the electric field), thus precluding the need for ground flashes from the negative charge region. There were no +CG flashes during the first hour perhaps because the lower negative charge of the inverted tripole charge structure was a substantial amount of charge (as opposed to a small pocket of charge analogous to the lower positive of a normal tripole) or that the whole structure was too elevated above ground, making IC flashes between the positive and lower negative of the tripole more favorable than +CG flashes. Indeed, the +CG flashes began only after the growth and descent of large hail around 2140, which apparently led to large scale subsidence of the entire charge structure not only within the hail core but also downwind (see, for example, Fig. 5.57). This resulted in a less elevated tripole structure downwind from which the majority of the +CG flashes originated. These +CG flashes tapped the positive charge both within the descending hail core and within the downward sloping positive charge of the inverted tripole downwind (e.g,. Figs. 5.60 and 5.64).

This interpretation of the previous paragraph is an oversimplification, as there were certainly other complicating factors. For example, the formation of new convective cells around the periphery of the main +CG-producing cell may have exerted

some influence on the charge structure evolution. On the whole though, formation and descent of an inverted tripole structure is a concise and reasonably accurate description of the events leading to the clustered +CG flashes.

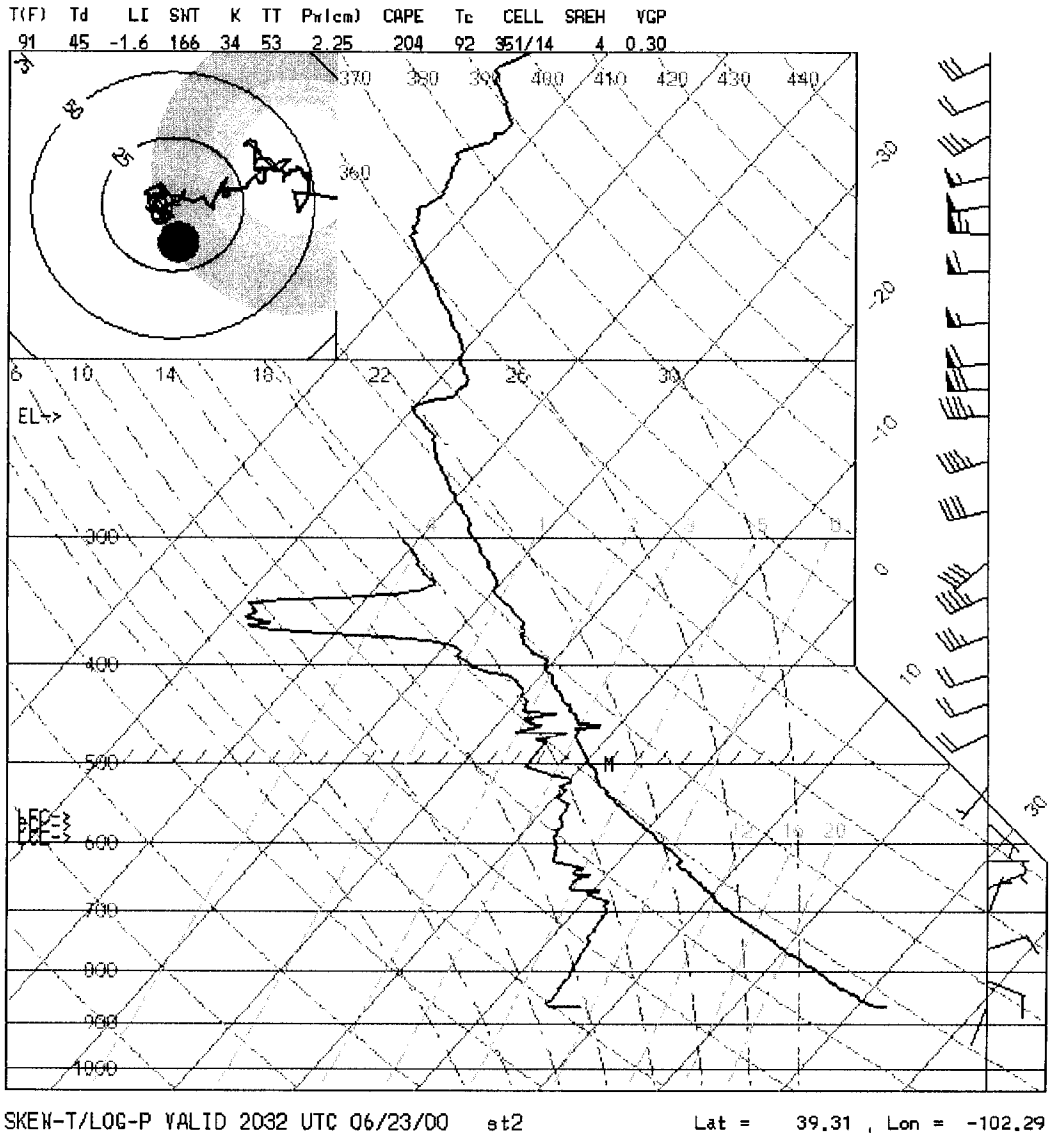

Figure 5.36: MGLASS sounding used for 23 June, storm 3. This sounding was launched from the CHILL radar site at 2032 UTC. Its trajectory is indicated in the third panel of Fig. 5.1.

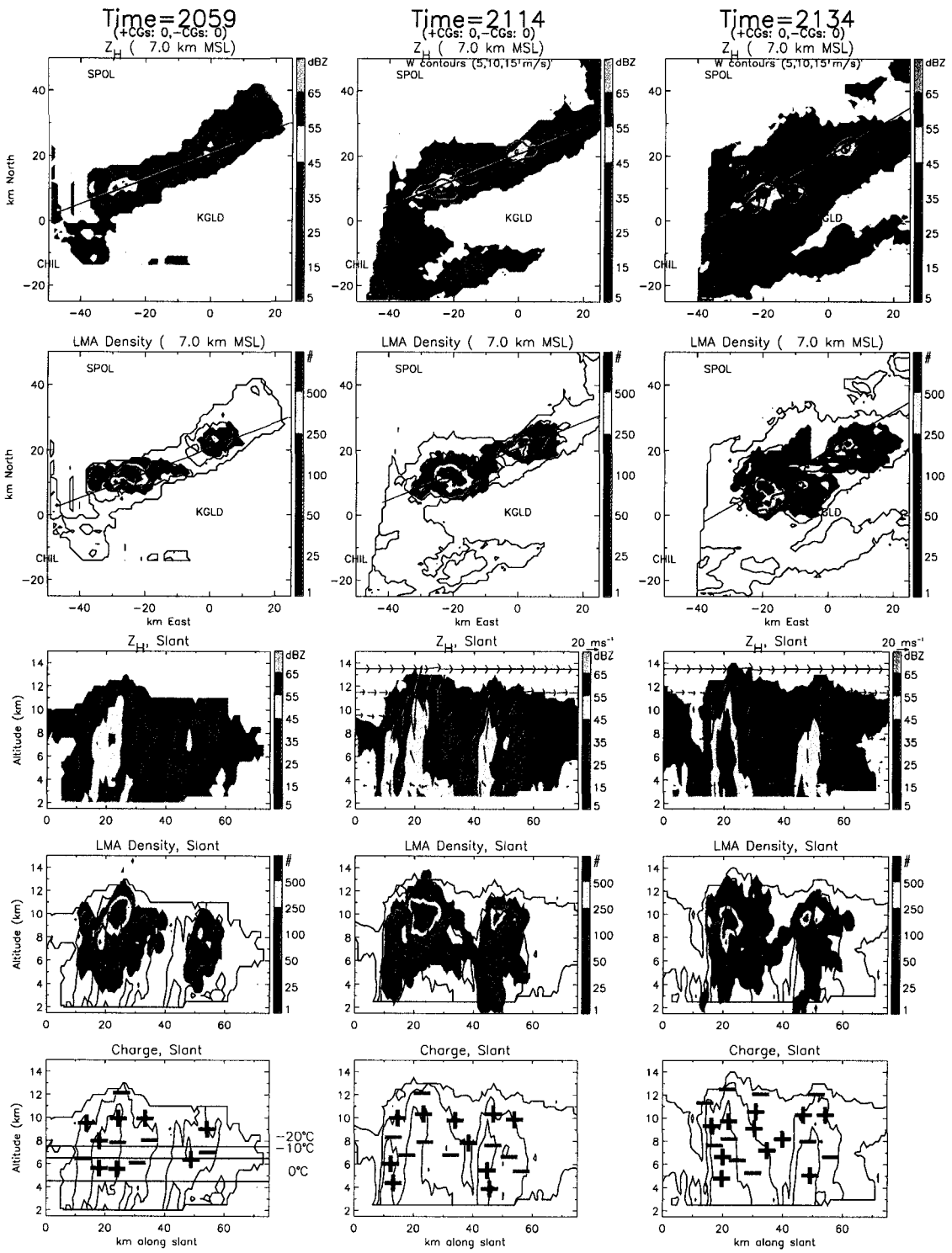

Figure 5.37: Representative cross-sections of storm 3 on 23 June at 2059, 2114 and 2134. Each column corresponds to the same time. From top to bottom: Horizontal cross-sections at 7 km altitude of radar reflectivity (Z_H) and LMA density (5 minute cumulative) followed by vertical cross-sections of Z_H, LMA density and composite charge structure along the line indicated in the horizontal cross-sections. Contours of Z_H at 5, 25, and 45 dBZ are repeated on the LMA density and charge composites. Black and green diamonds (black and red X's) are NLDN strike locations and origin locations of –CG (+CG) strikes, respectively.

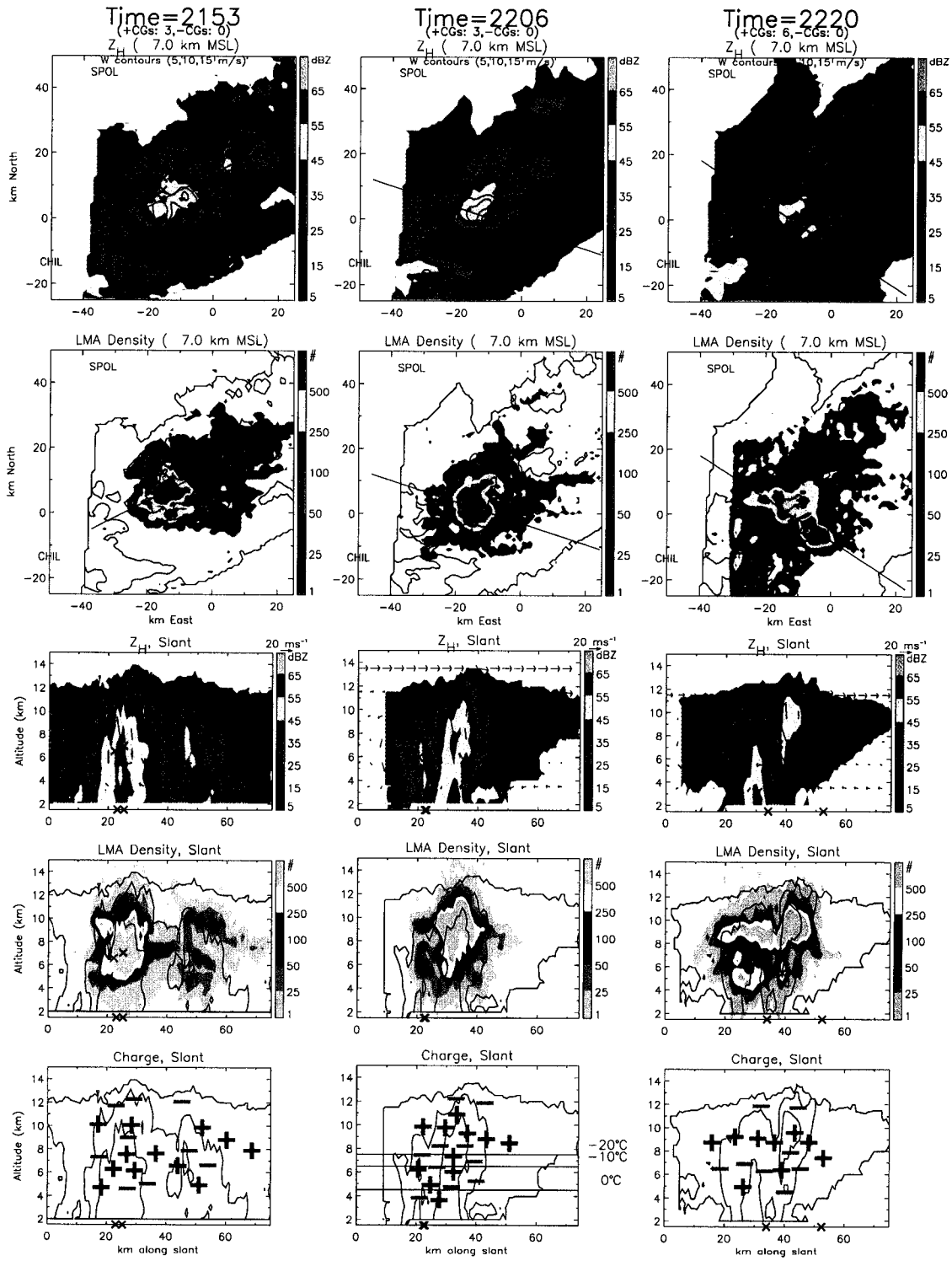

Figure 5.38: As in Fig. 5.37, but for volume scans beginning at 2153, 2206, and 2220. The LMA density vertical cross-sections are contoured in gray scale to accentuate the origin locations of the +CG flashes indicated by the red X's.

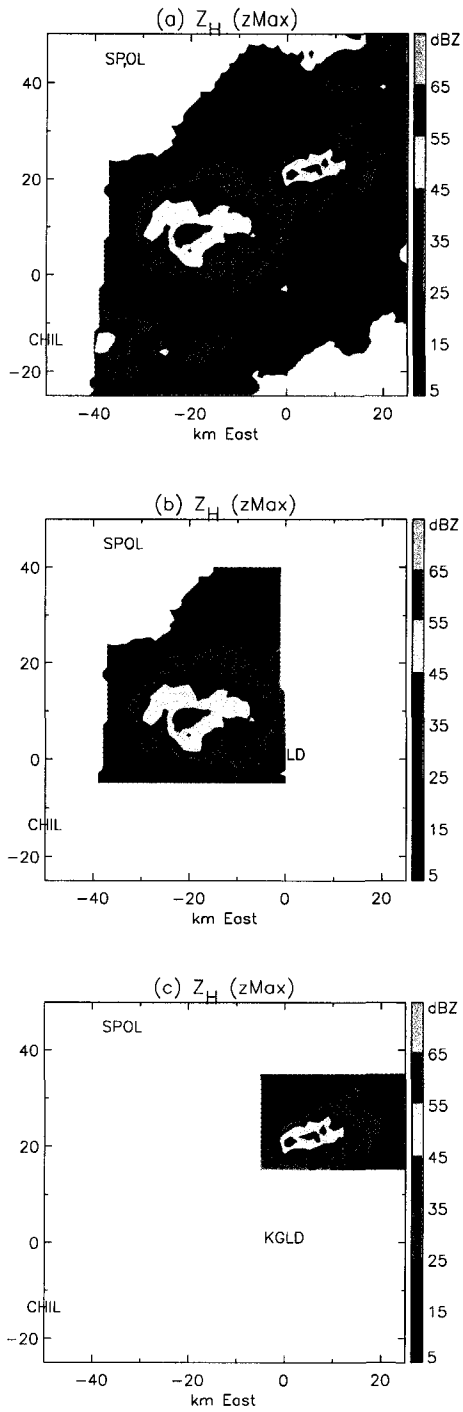

Figure 5.39: Example of how the east and west cells of storm 3 on 23 June were isolated in software for computing separate time series of their echo volumes and flash rates. (a) All echo during the 2134 volume scan. (b) Echo used for the western cell. (c) Echo used for the eastern cell.

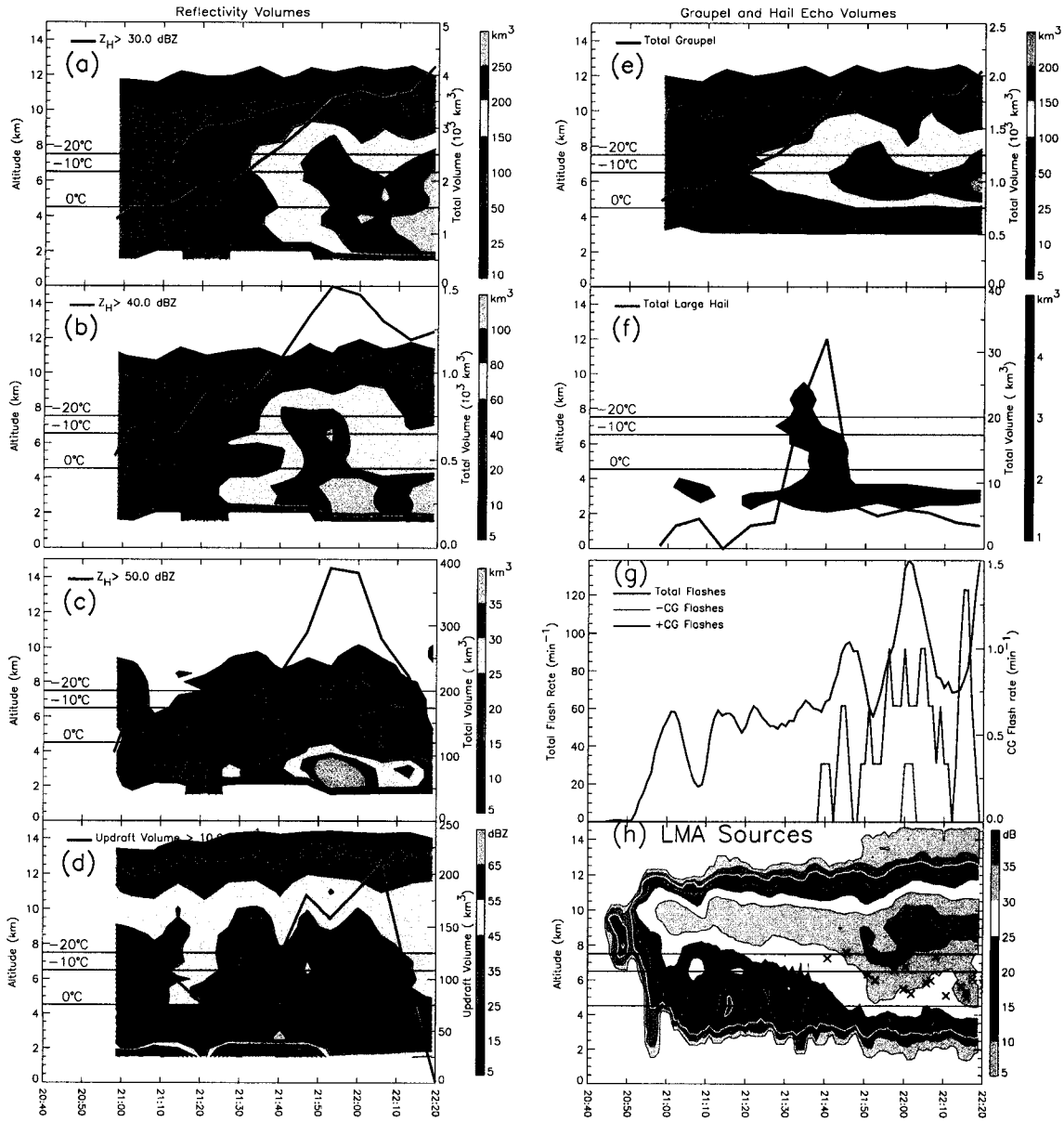

Figure 5.40: Time series summary of the west cell of storm 3 on 23 June. (a–c) Contours of reflectivity (Z_H) volumes >30, >40, >50 dBZ, respectively, with units of $km^3/0.5$ km. The total (height-integrated) volume is shown as a thick black line in each case with units given on the right ordinate. (d) Contours of maximum Z_H with volume of updraft (> 10 ms^{-1}) overlaid as thick black line. (e–f) Contours of graupel and large hail echo volumes. (g) Total and CG flash rates. Ignore the lone –CG, as it was from the eastern cell. (h) Contours of total LMA sources in logarithmic units with +CG mean origin heights overlaid as the red X's.

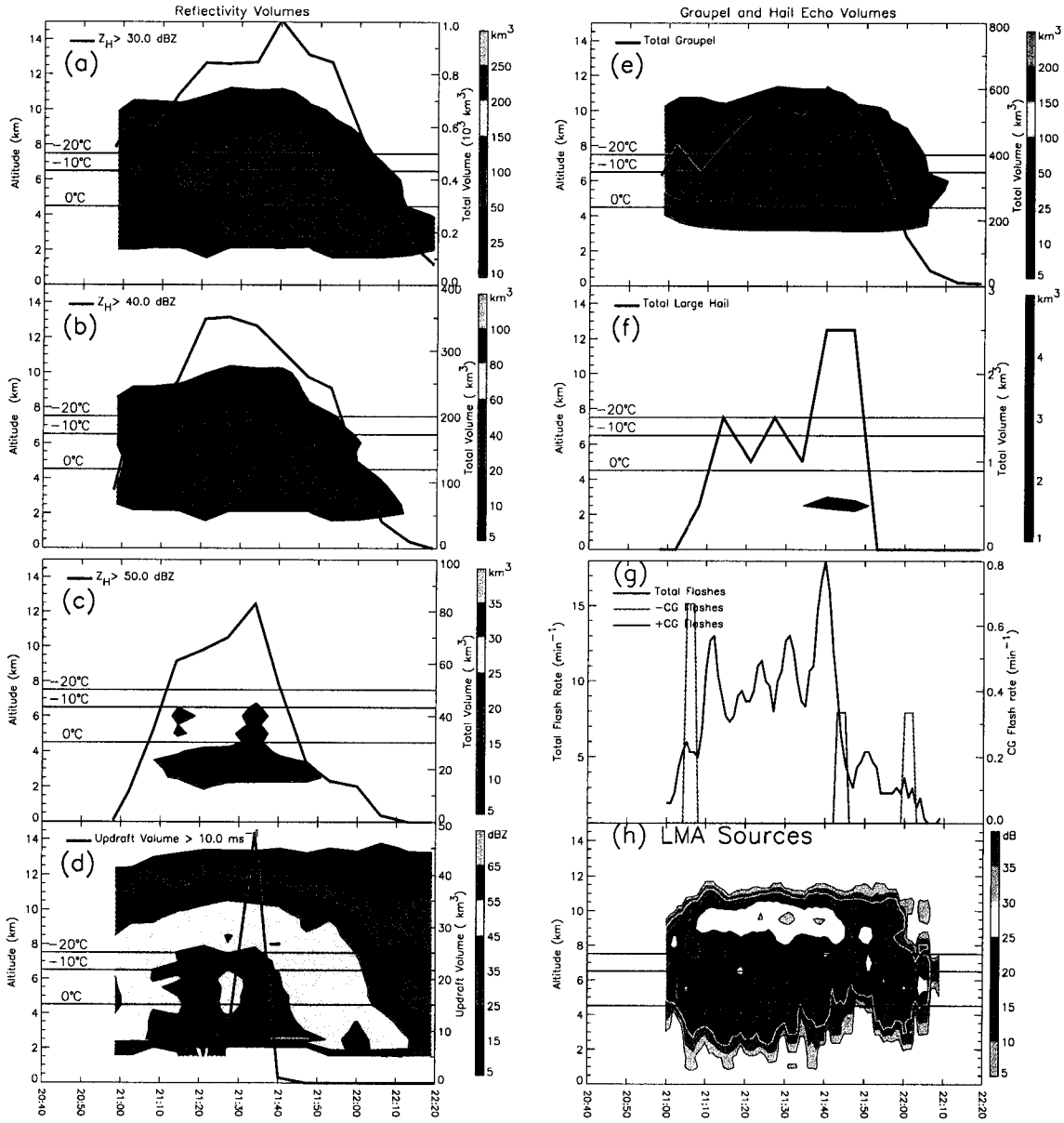

Figure 5.41: As in Fig. 5.40, but for the east cell of storm 3 on 23 June.

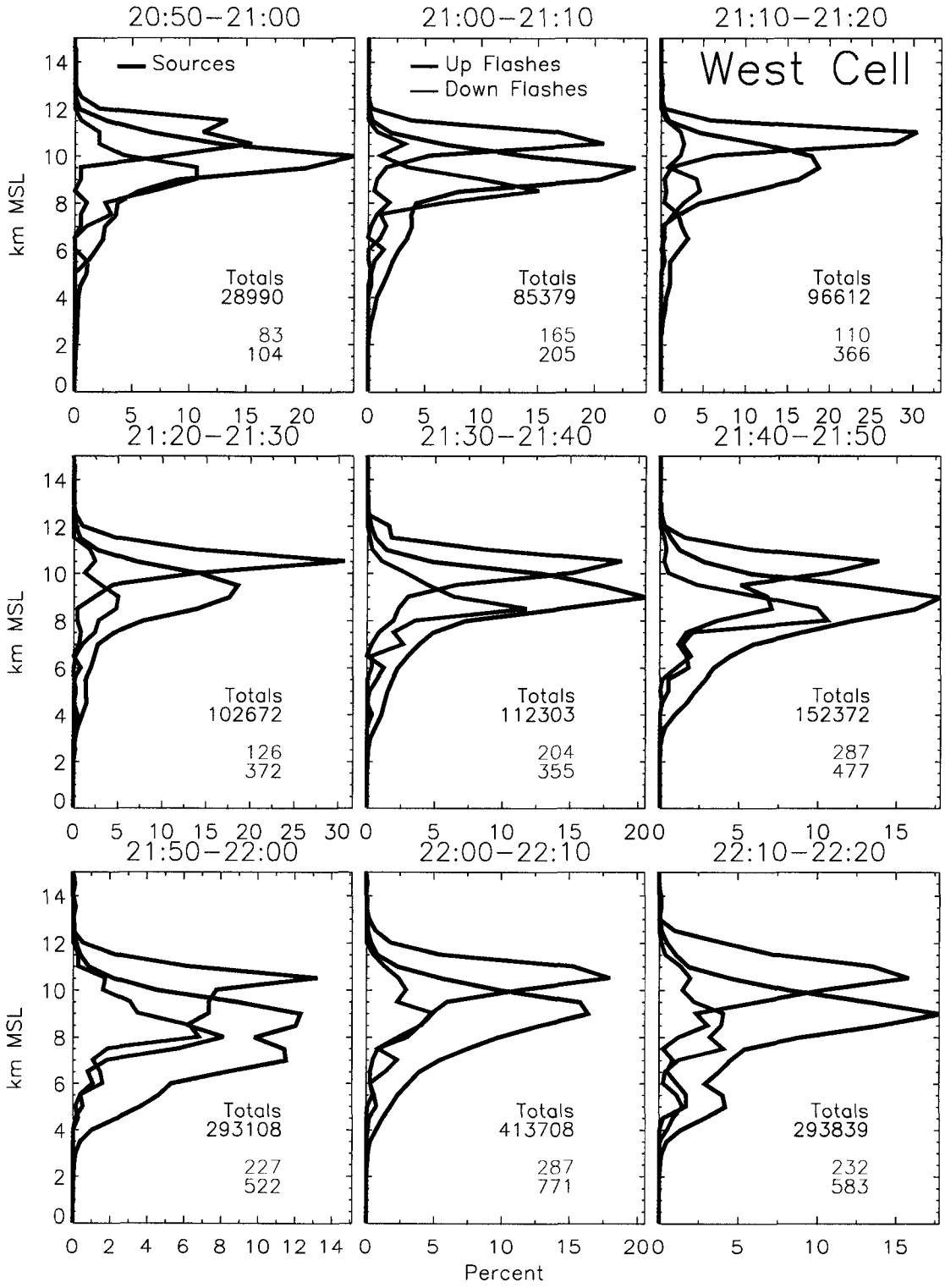

Figure 5.42: Altitude histograms of LMA sources (black) and total flash origins (red) for the western cell of storm 3 on 23 June. The blue and green curves are flash origins corresponding to the flashes that initiated upward and downward, respectively. Each panel shows 10 minutes of data, plotted as percentage of the total for that 10 minutes. Numbers in bottom-right of each panel give the total number of sources and flashes during each 10 minute interval.

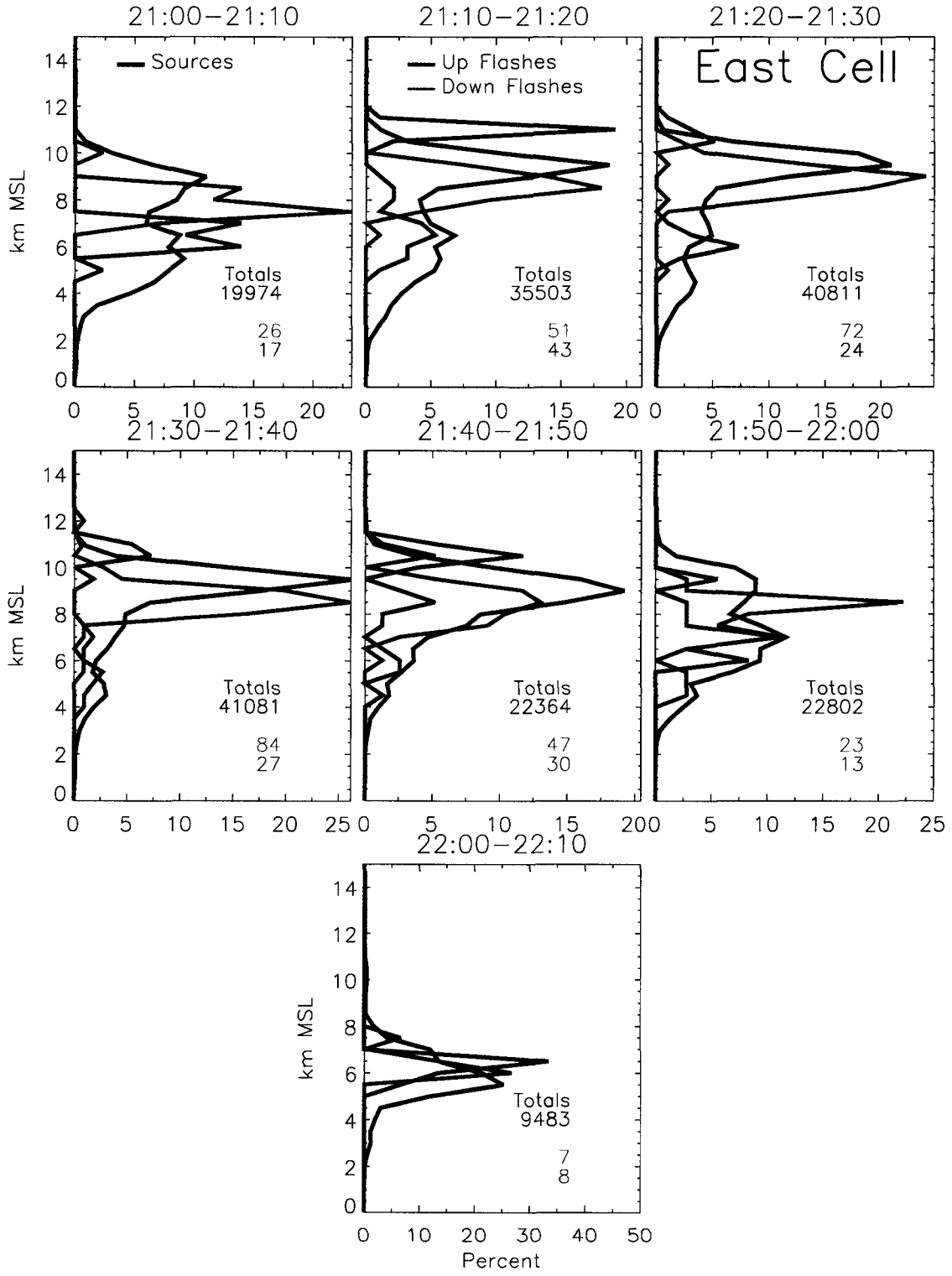

Figure 5.43: Altitude histograms of LMA sources (black) and total flash origins (red) for the eastern cell of storm 3 on 23 June. The blue and green curves are flash origins corresponding to the flashes that initiated upward and downward, respectively. Each panel shows 10 minutes of data, plotted as percentage of the total for that 10 minutes. Numbers in bottom-right of each panel give the total number of sources and flashes during each 10 minute interval.

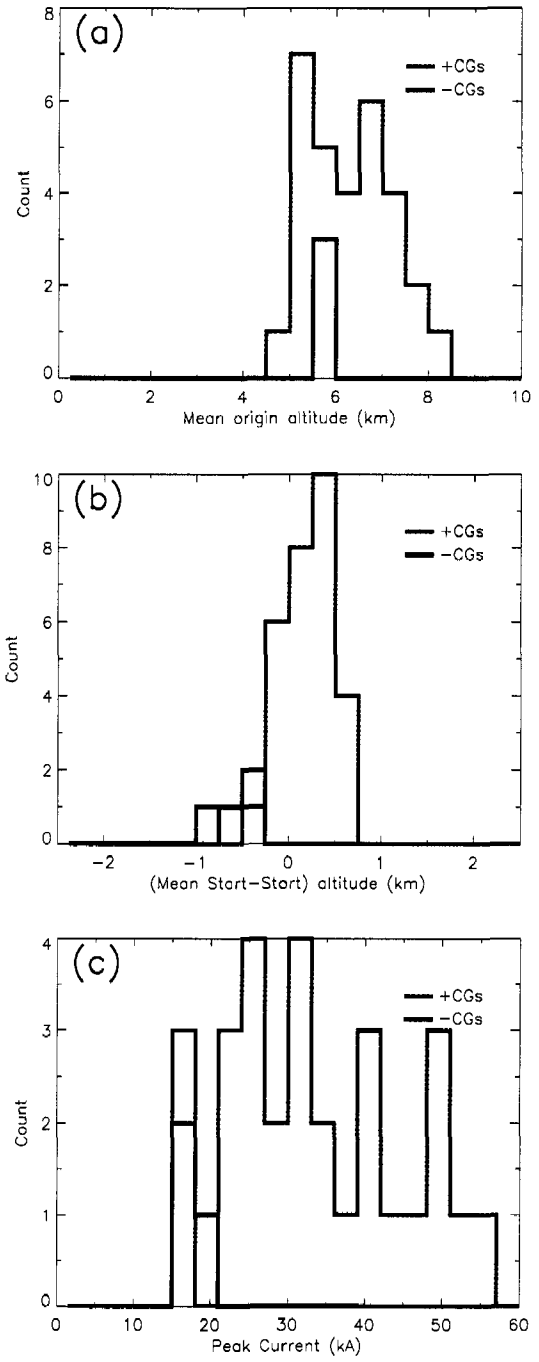

Figure 5.44: CG flash histograms for 23 June, storm 3. Includes CGs in both the east and west cell from 2040 to 2230 UTC. (a) Mean origin height. (b) Difference between height of first source and height of the mean of the first 10 sources, i.e., if positive, then first source was lower than the mean of the first 10 sources and flash initiated upward. (c) Peak current.

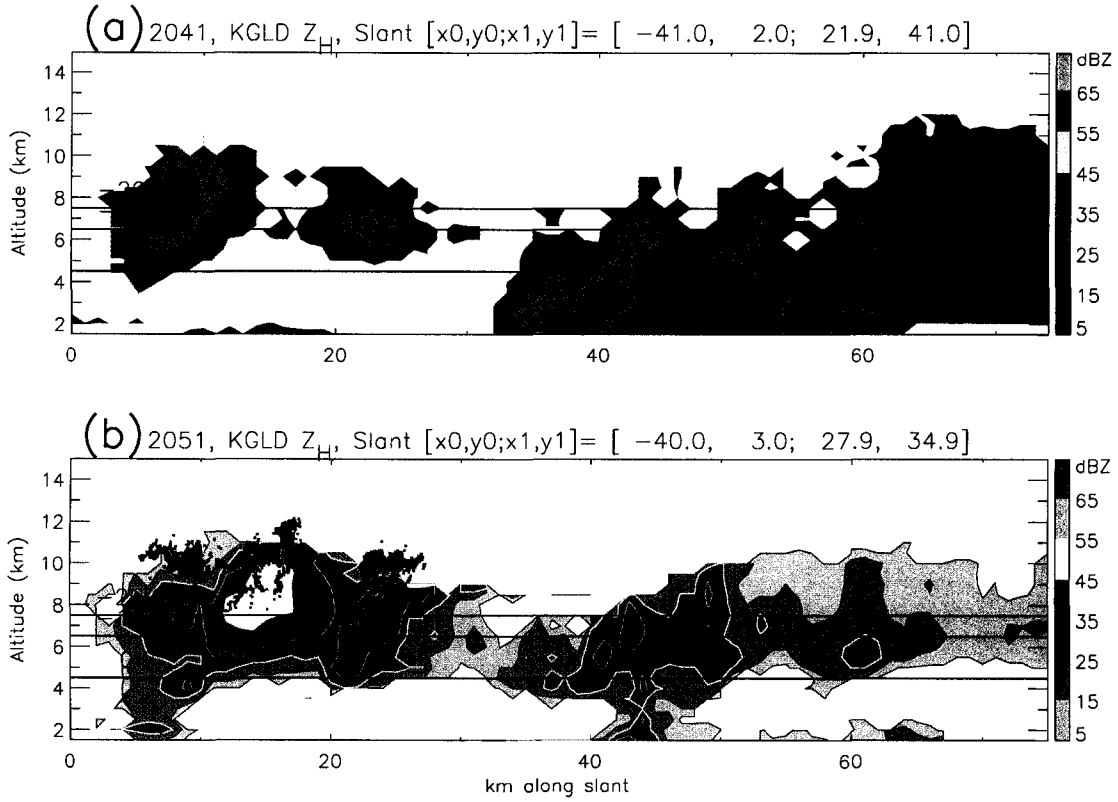

Figure 5.45: Vertical cross-sections of horizontal reflectivity (Z_H) from KGLD at (a) 2041 and (b) 2051. The orientations of these vertical cross-sections are similar to the ones in the left column of Fig. 5.37. The LMA sources from 2051–2056 in Fig. 5.46 are overlaid in (b) and color-coded by inferred charge region (red for positive, green for negative and magenta for undetermined). There was no lightning activity within five minutes of the radar cross-section in (a).

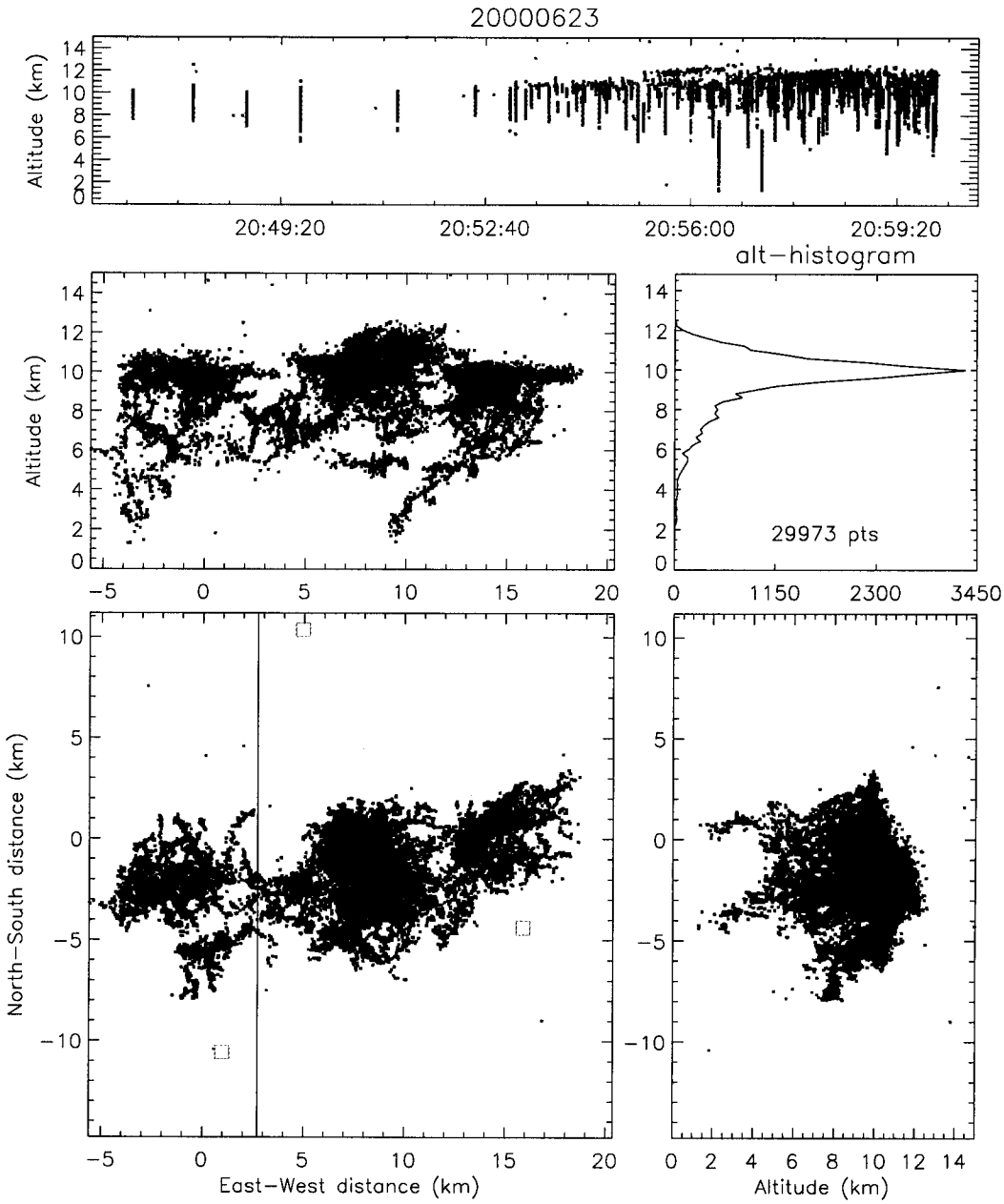

Figure 5.46: Lightning mapping of the first ~15 minutes of lightning in storm 3 on 23 June. Sources are color-coded by inferred charge region (red for positive, blue for negative, green for undetermined).

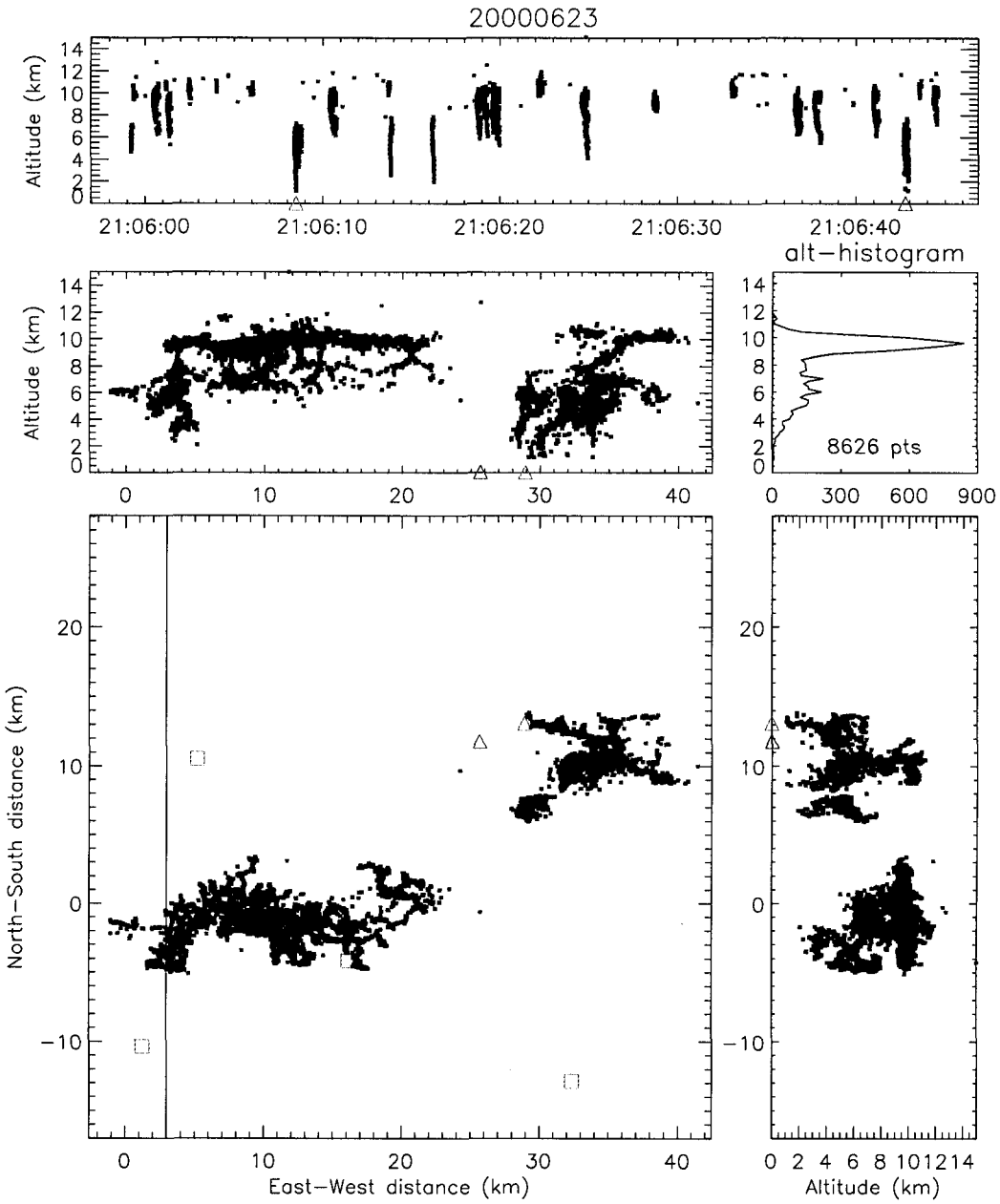

Figure 5.47: Lightning mapping of flashes from 2106 to 2106:45. Sources are color-coded by charge as in Fig. 5.46.

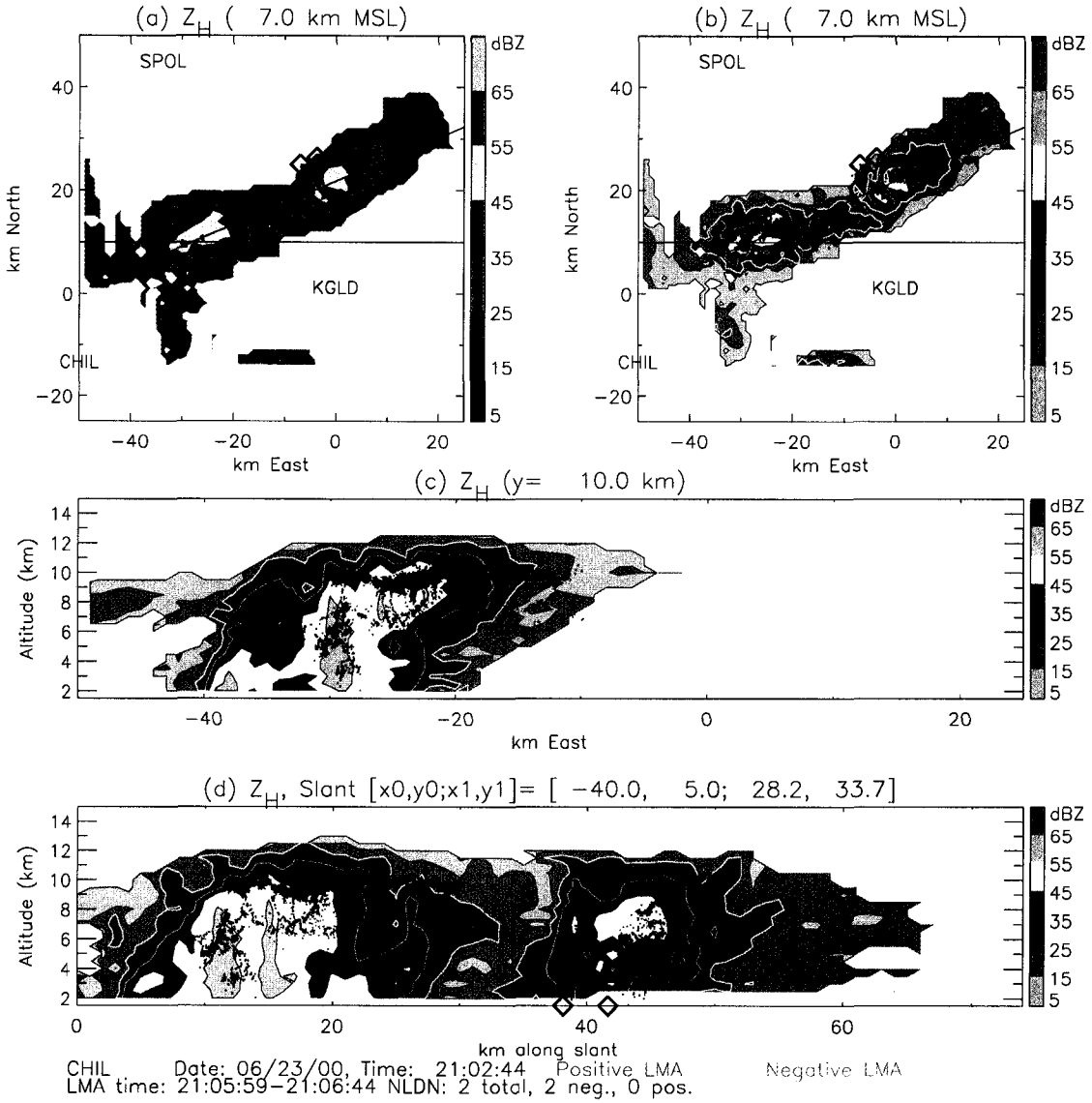

Figure 5.48: CHILL radar cross-sections from the 2103 volume scan, with the LMA sources from Fig. 5.47 overlaid and color-coded by charge (red for positive, green for negative). The black diamond symbols mark the NLDN strike points of the two –CGs. The blue diamond symbols in (d) mark the mean origin locations of these two –CGs.

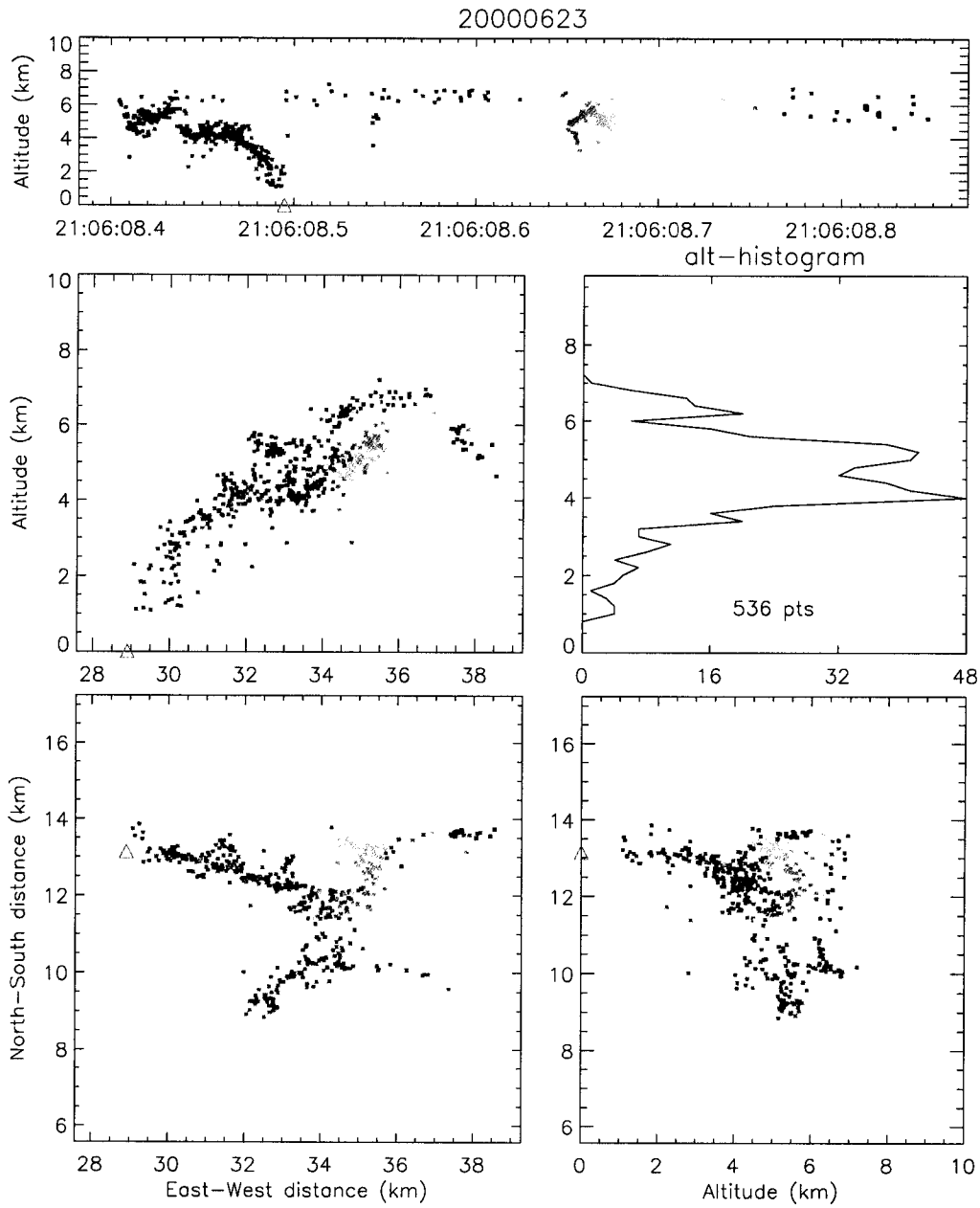

Figure 5.49: Lightning mapping of the first –CG at 2106:08. LMA sources are color-coded by time.

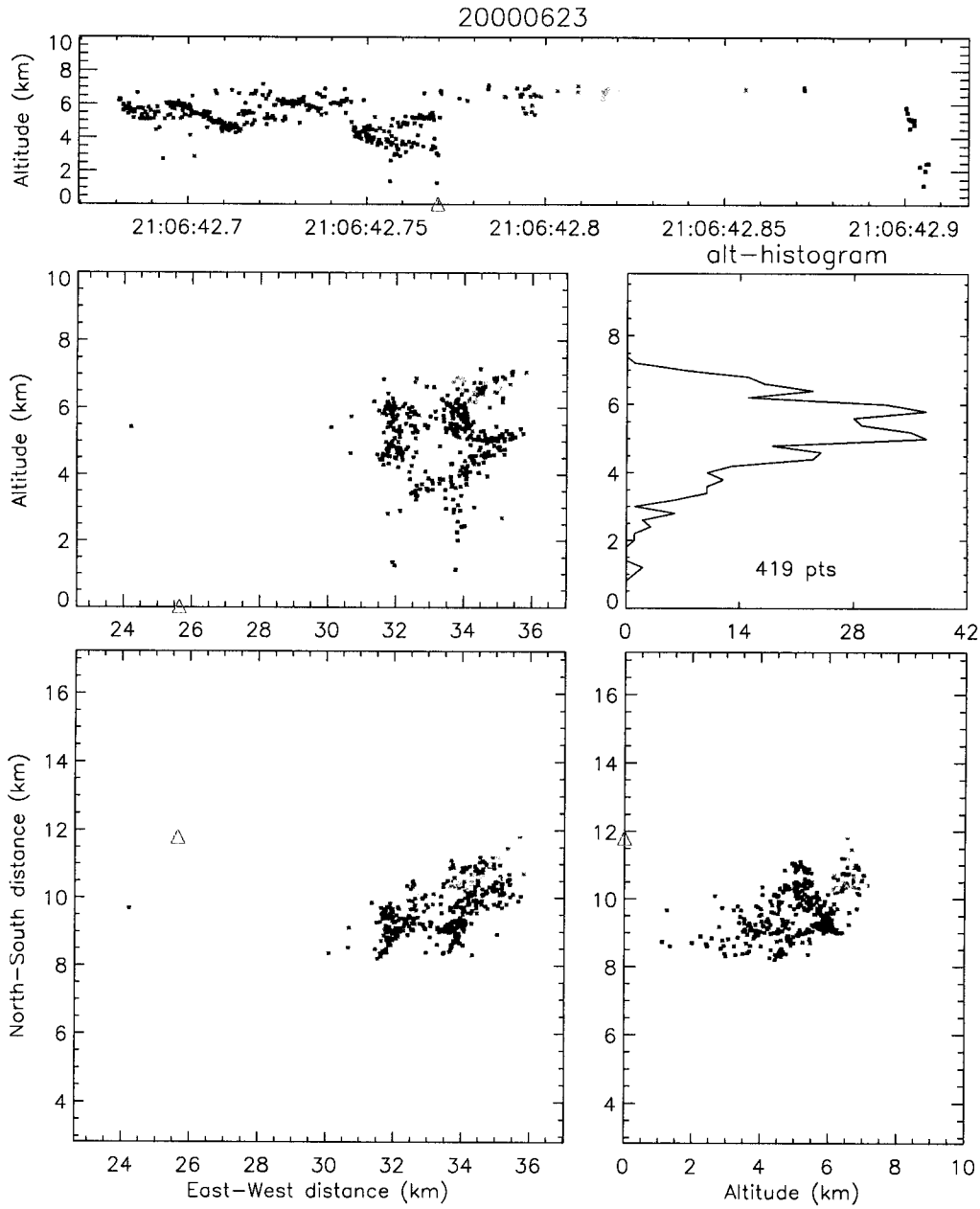

Figure 5.50: Lightning mapping of the second –CG at 2106:42. LMA sources are color-coded by time.

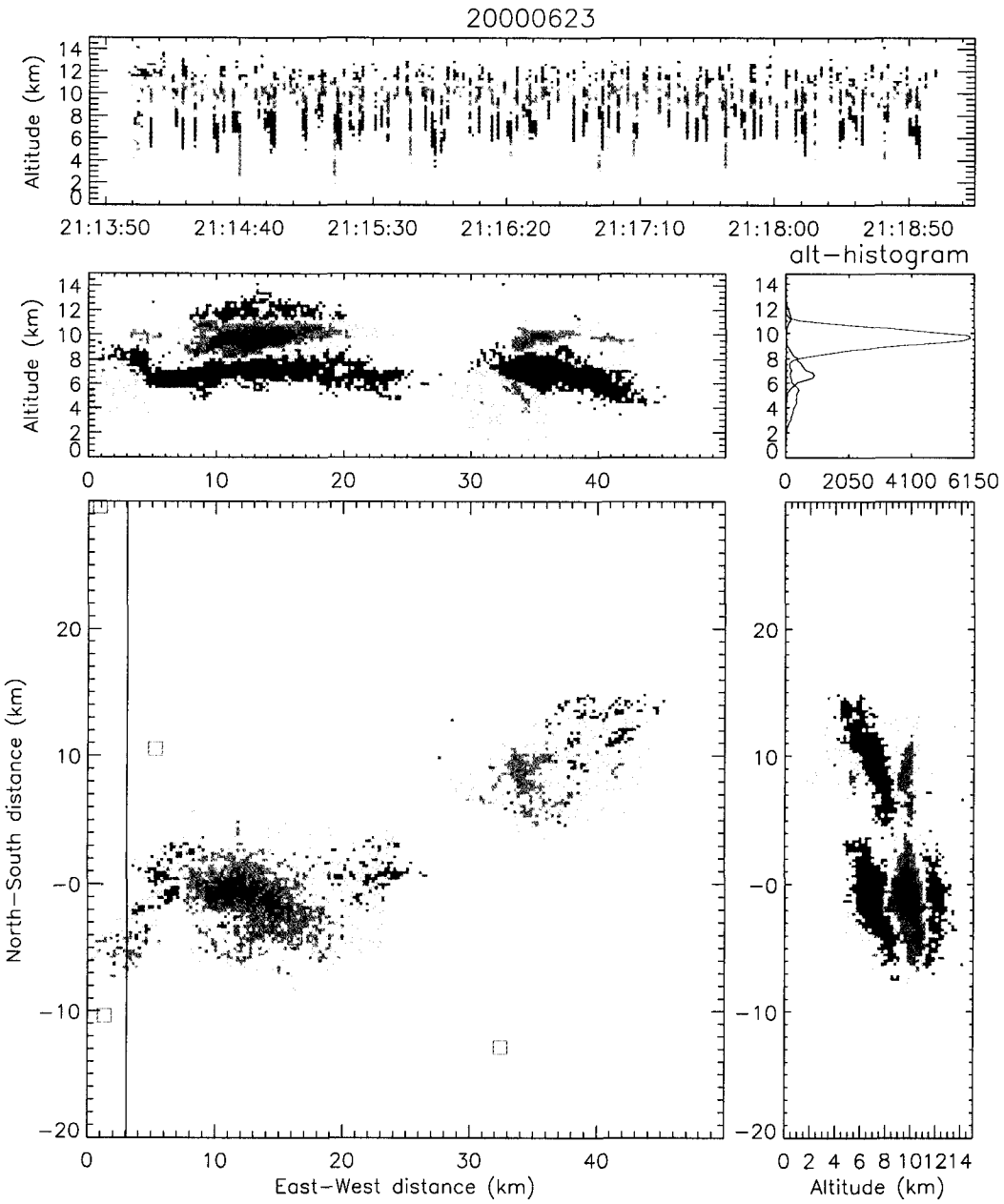

Figure 5.51: Lightning mapping "charge density" from 2114–2119. Redder (bluer) colors indicate greater number of LMA sources in inferred positive (negative) charge regions.

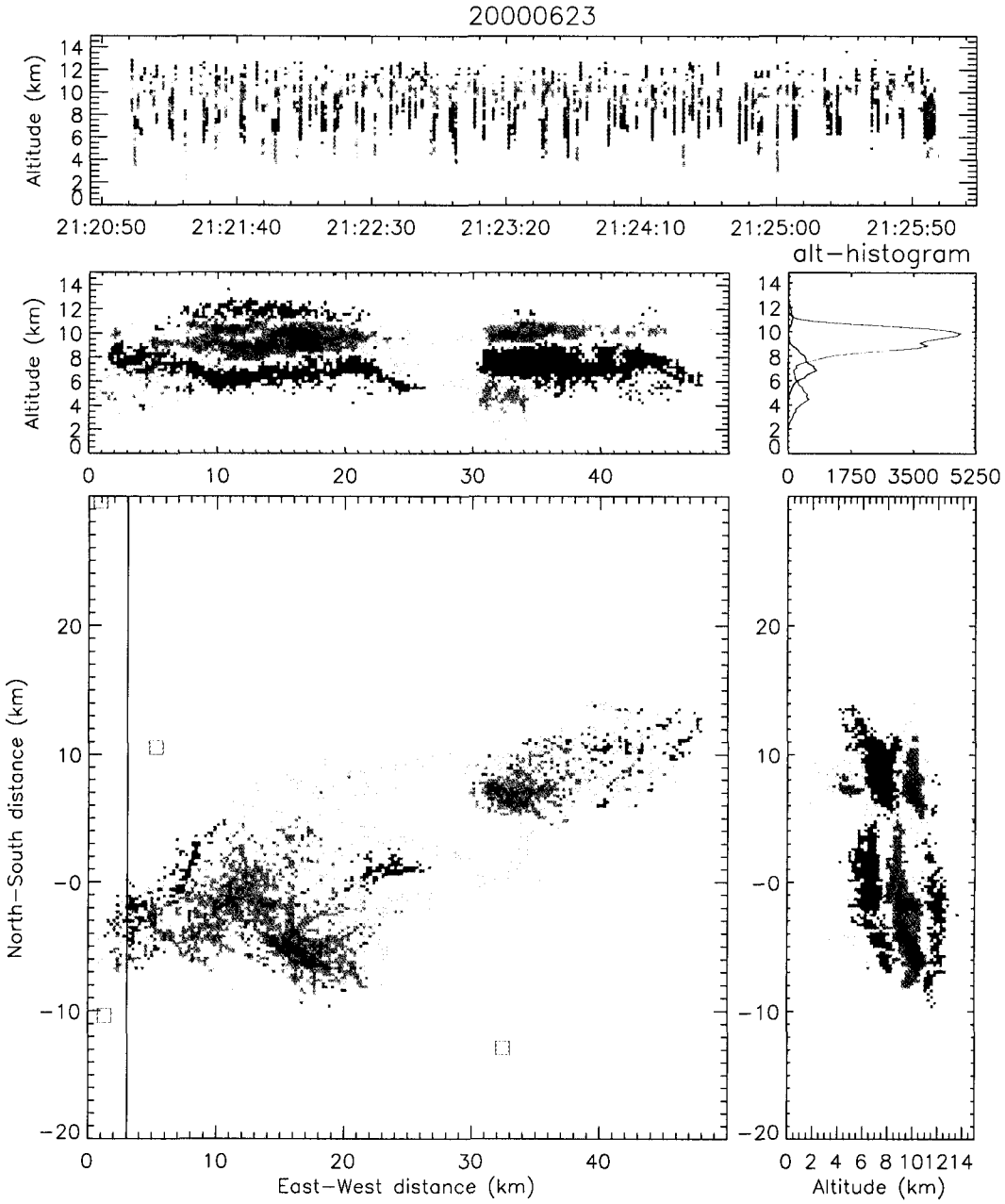

Figure 5.52: As in Fig. 5.51, but for 2121–2126.

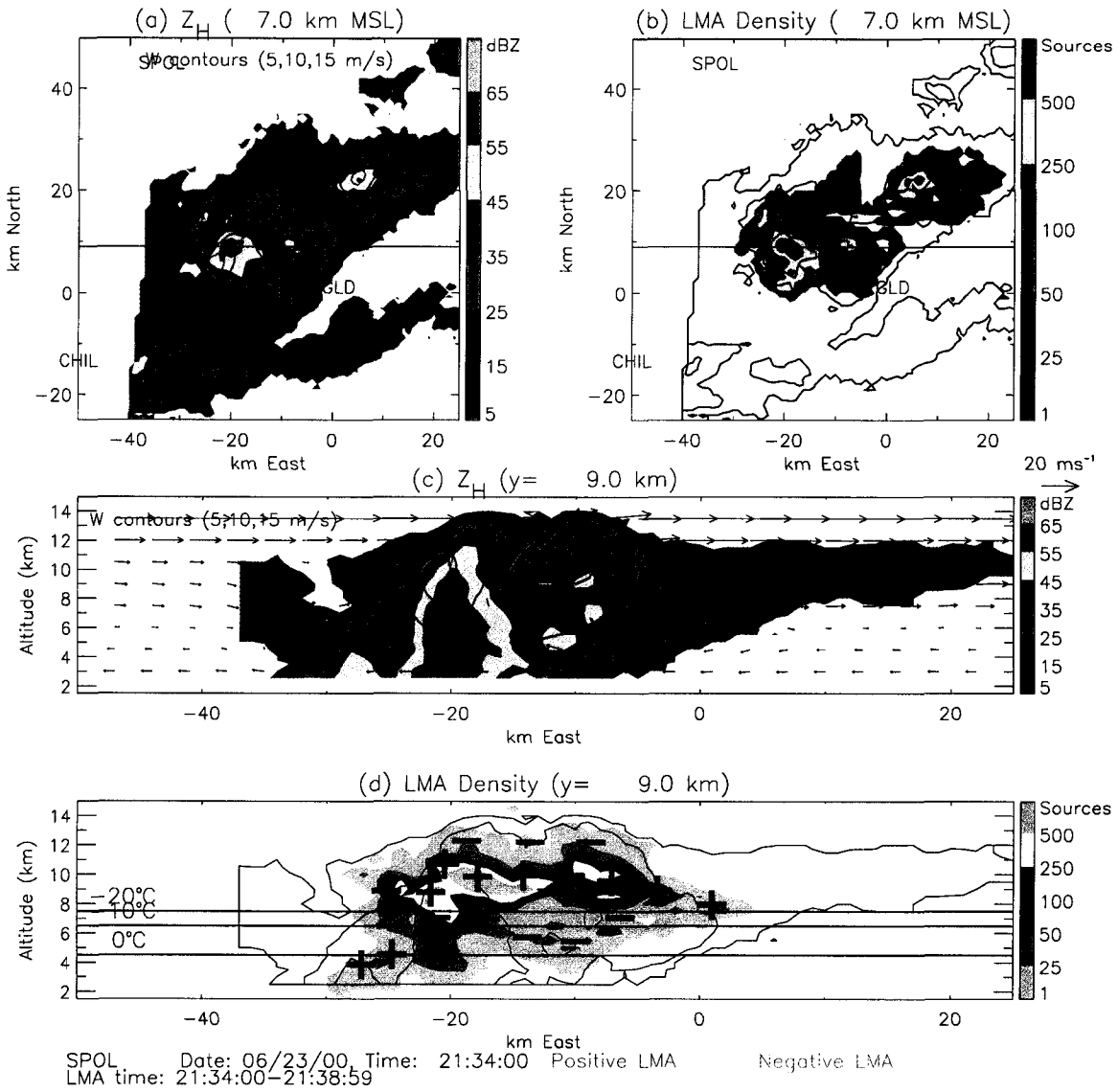

Figure 5.53: Radar cross-sections from the volume scan beginning at 2134. The horizontal cross-sections in (a) and (b) are the same as in the right column of Fig. 5.37, but the vertical cross-sections are along an east-west line at $y = 9km$, as indicated in (a) and (b). The vertical cross-section in (d) has additional black contours of updraft speed at 5, 10, and 15 ms^{-1}.

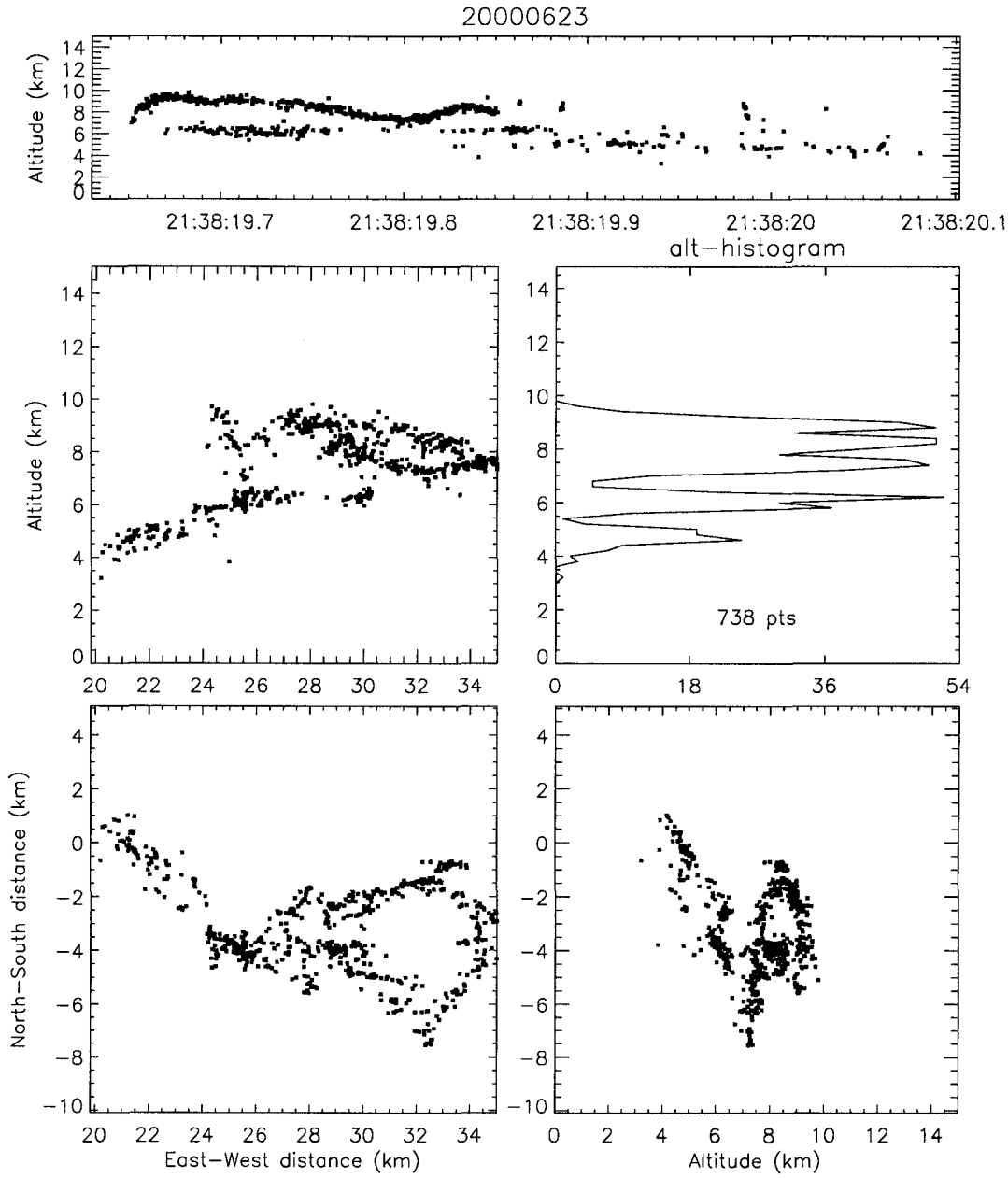

Figure 5.54: Lightning mapping of one of the first flashes in the new convection just east of main western cell at 2138. This is a normal IC flashes that initiated upward from negative charge into positive charge. Sources are color-coded by inferred ambient charge (red for positive, blue for negative).

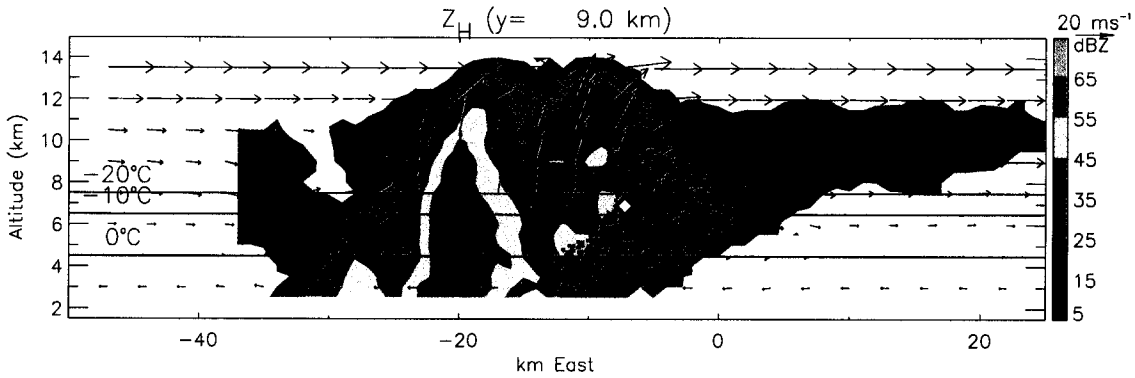

Figure 5.55: Same vertical cross-section as Fig. 5.53c with overlaid LMA sources from the flash shown Fig. 5.54. Sources are color-coded by charge (red for positive, black for negative). The filled diamond symbol marks the first source of the flash.

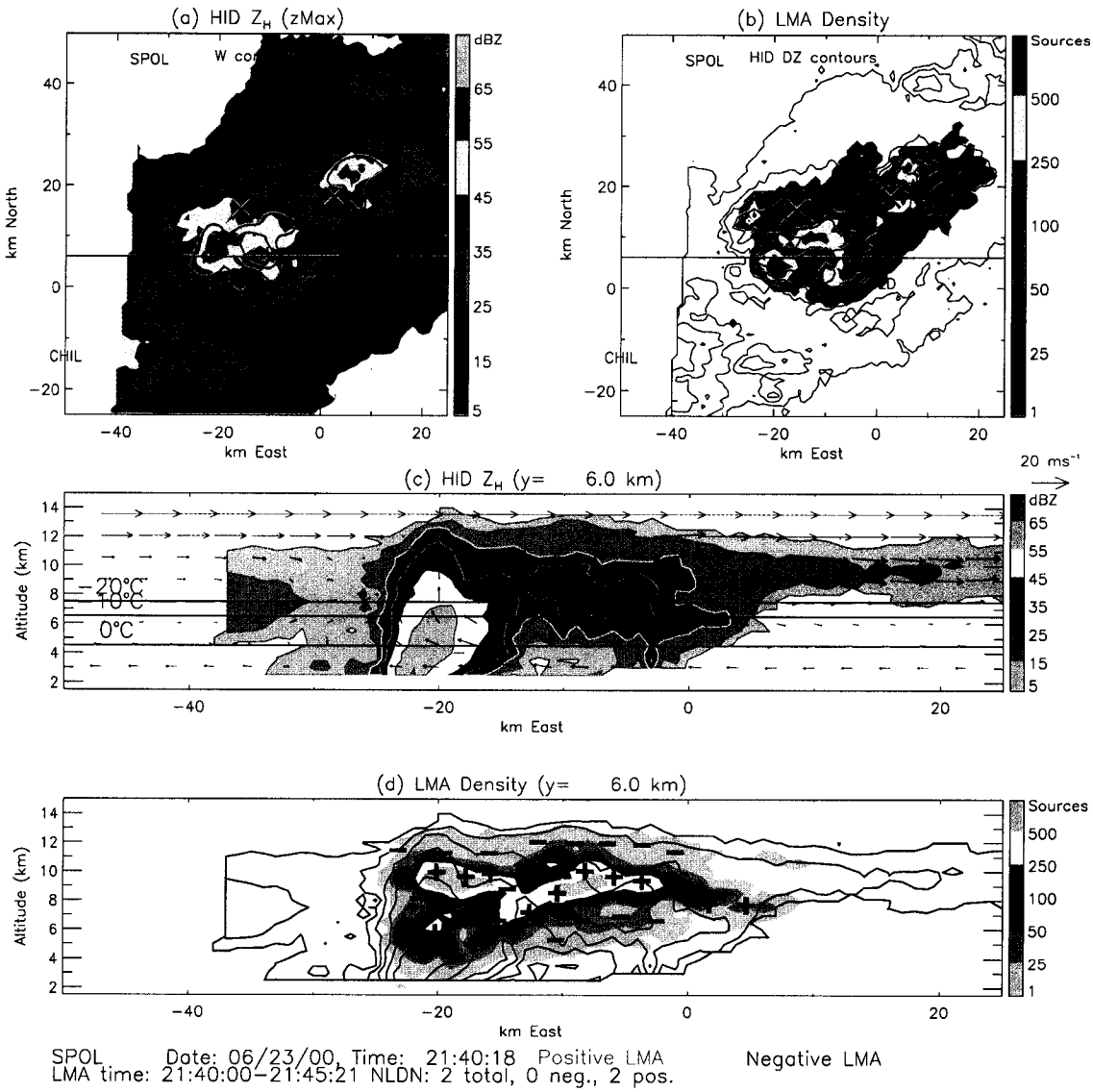

Figure 5.56: As in Fig. 5.53, but for the volume scan beginning at 2140. The two black X's in (a) and (b) mark the NLDN strike points of +CG flashes. These strikes are not indicated on the vertical cross-sections of (c) and (d) because they are too far away.

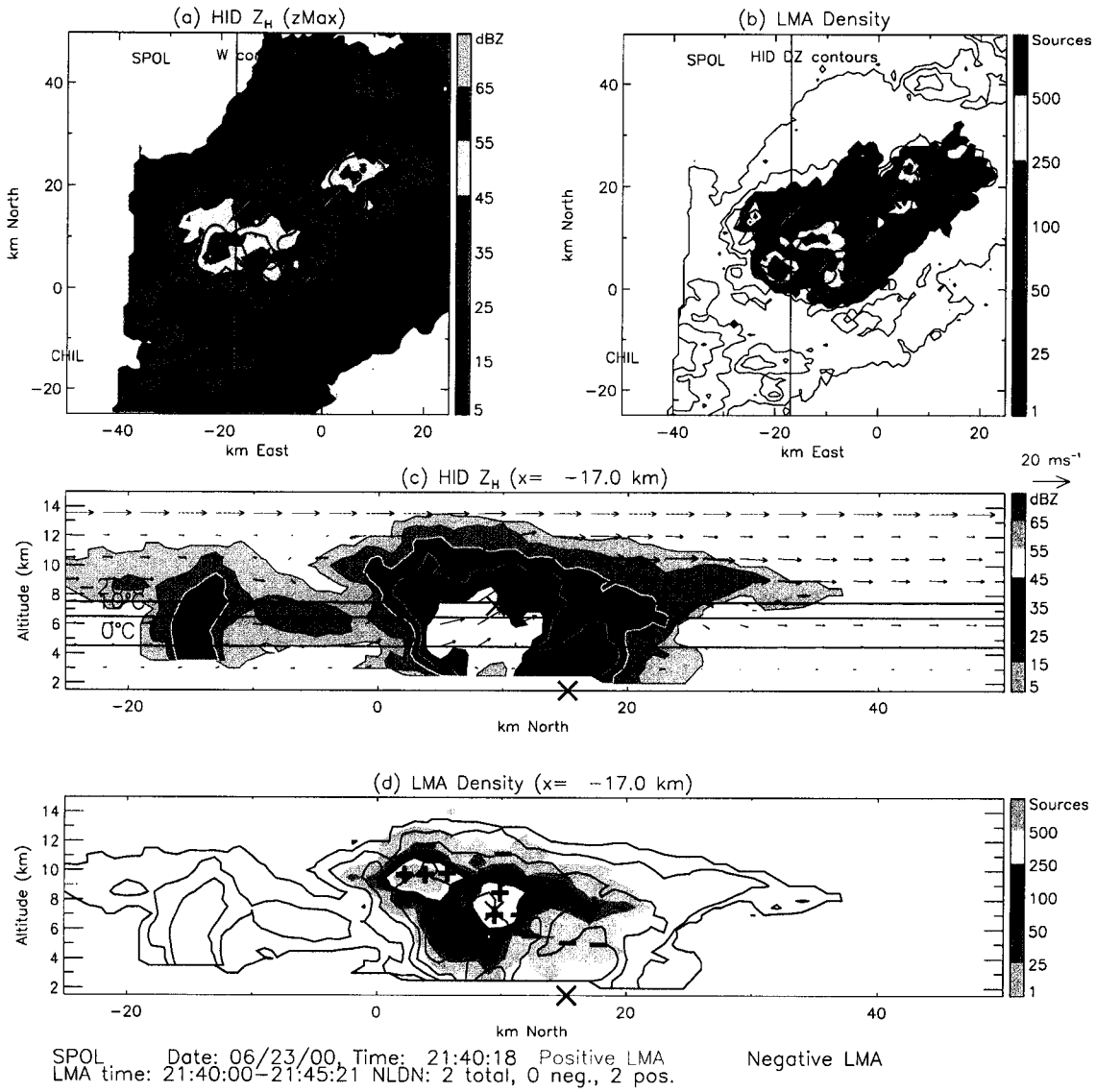

Figure 5.57: As in Fig. 5.56, but along a north-south vertical cross-section. The magenta X's aloft in the vertical cross-sections of (c) and (d) mark the origin location of the western +CG flash.

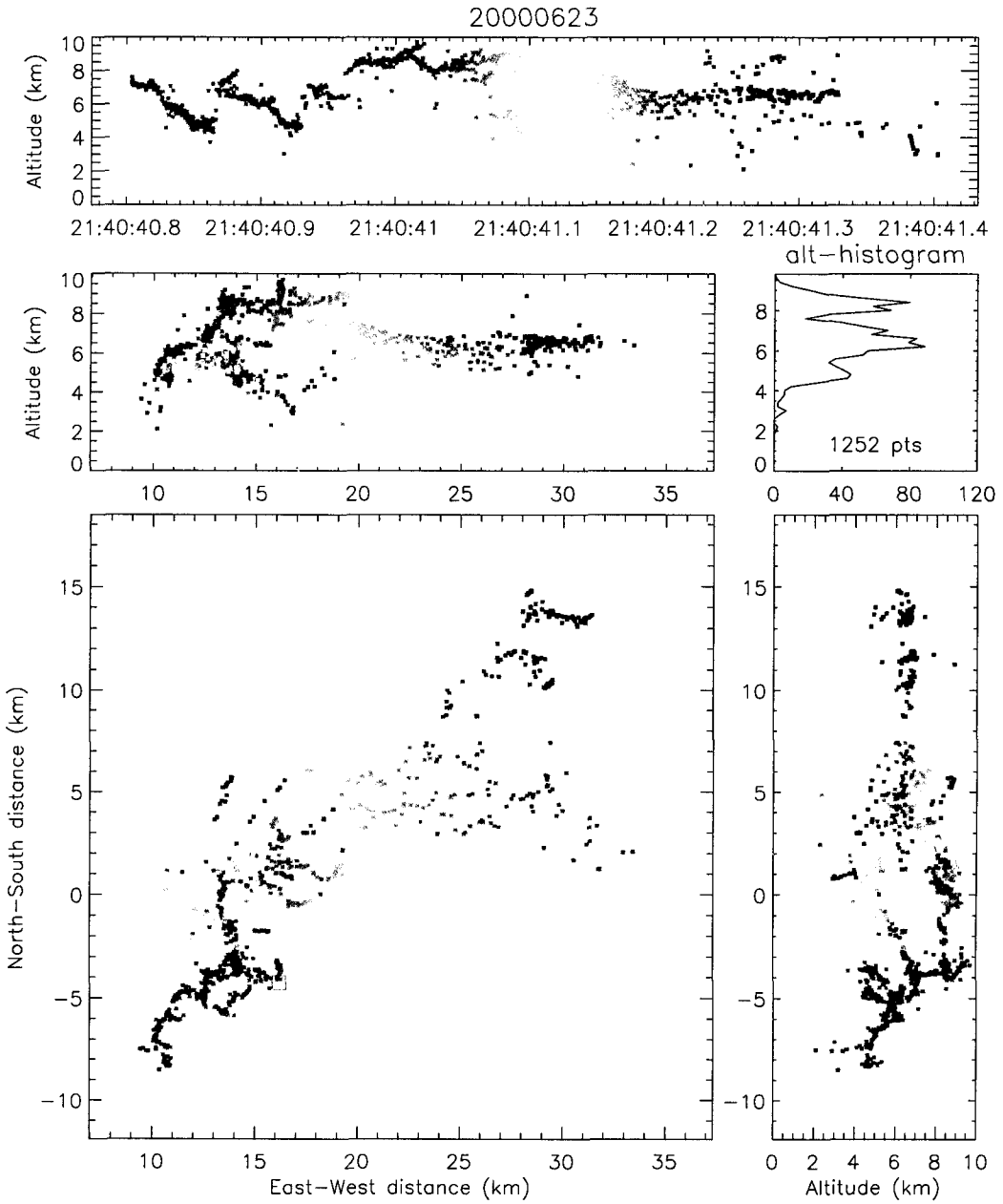

Figure 5.58: Lightning mapping of the first +CG at 2140:41. Sources are colored-coded by time. The flash was a "hybrid", meaning that the +CG flash was immediately preceded by an IC flash. The initial IC flash started downward from 7.5 km altitude at (x=13, y=−4km) and traveled through lower positive on the southern end of the domain. The leader to ground then proceeded downward and northward from the same initiation region, while negative breakdown proceeded upward then northward through the upper positive. The sequence of events is clearer in the lower-right panel, and clarified further in Fig. 5.59. 259

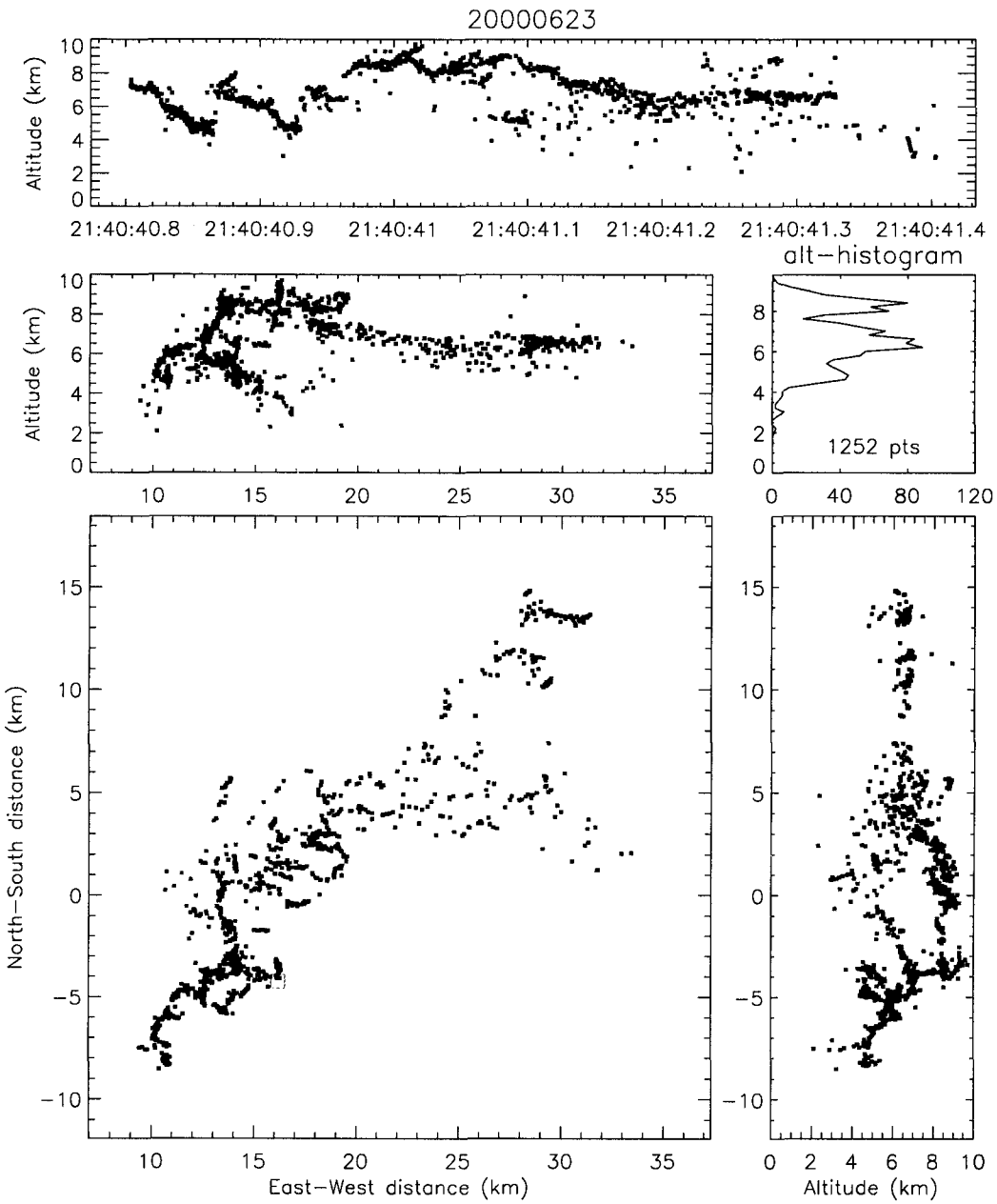

Figure 5.59: As in Fig. 5.58, but here the sources are color-coded by charge.

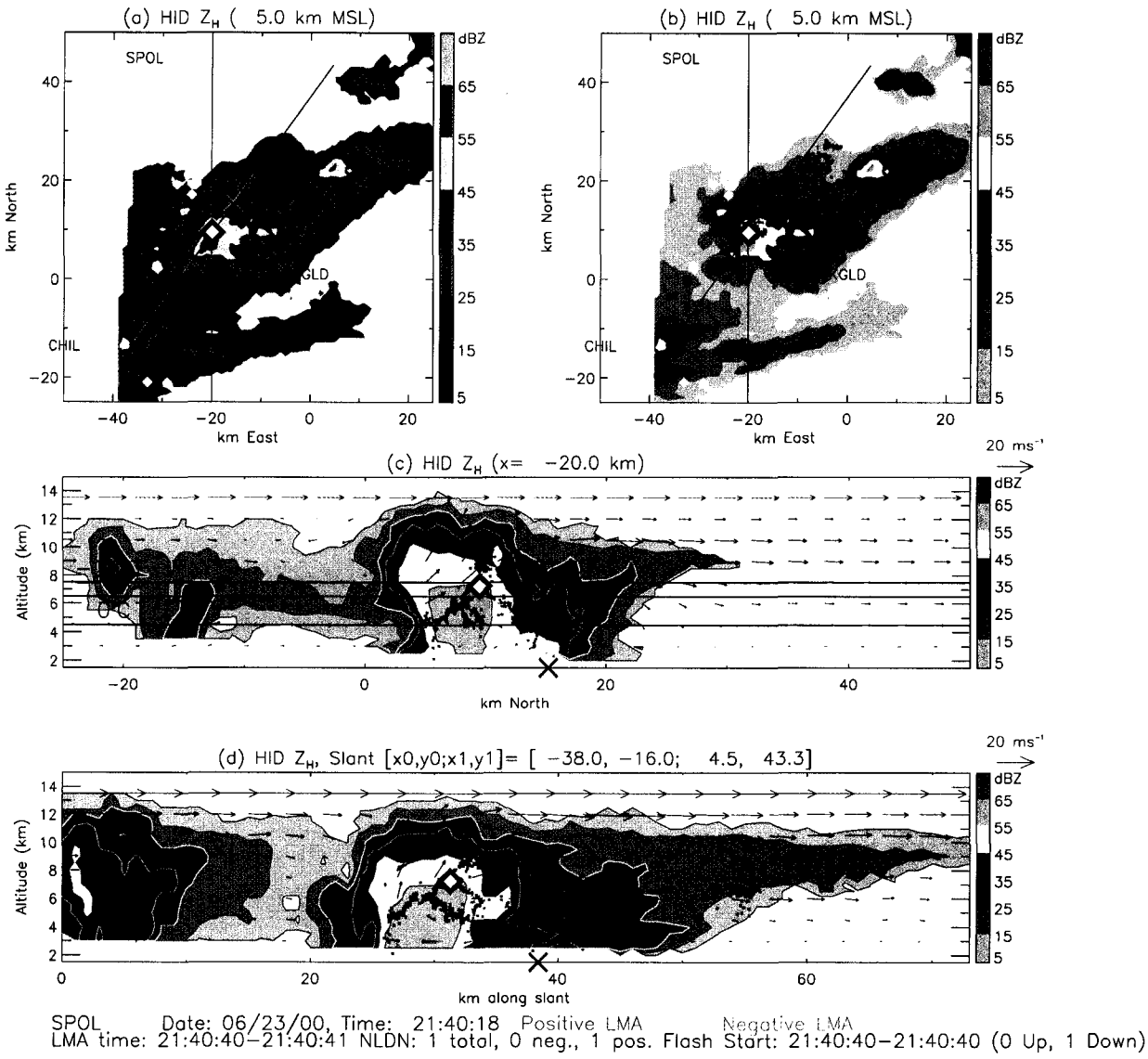

Figure 5.60: Radar cross-sections at 2140 with overlaid lightning mapping sources from the +CG flash shown in Figs. 5.58 and 5.59. Filled diamond symbol marks the initiation point, and X marks the strike point.

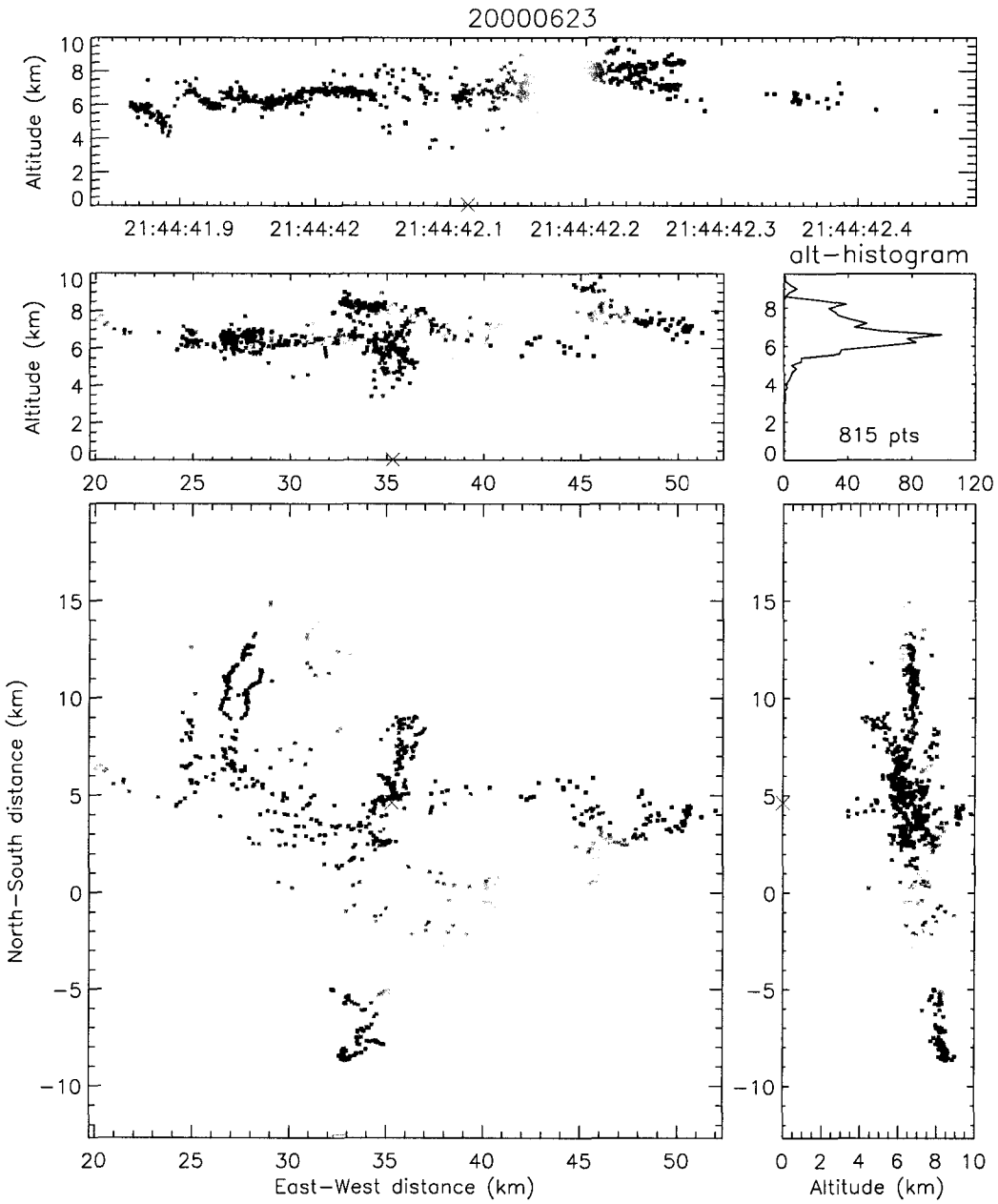

Figure 5.61: Lightning mapping of the second +CG at 2144:42. Sources are colored-coded by time. The flash was also a "hybrid", initiating downward and northward from 6 km altitude at (x=35, y=5 km). This flash was extremely complex, though the leader to ground is clear in the lower right panel. The leader to ground descended from essentially the same spot as the very first source of the whole flash, but the leader went straight down, without a northward component.

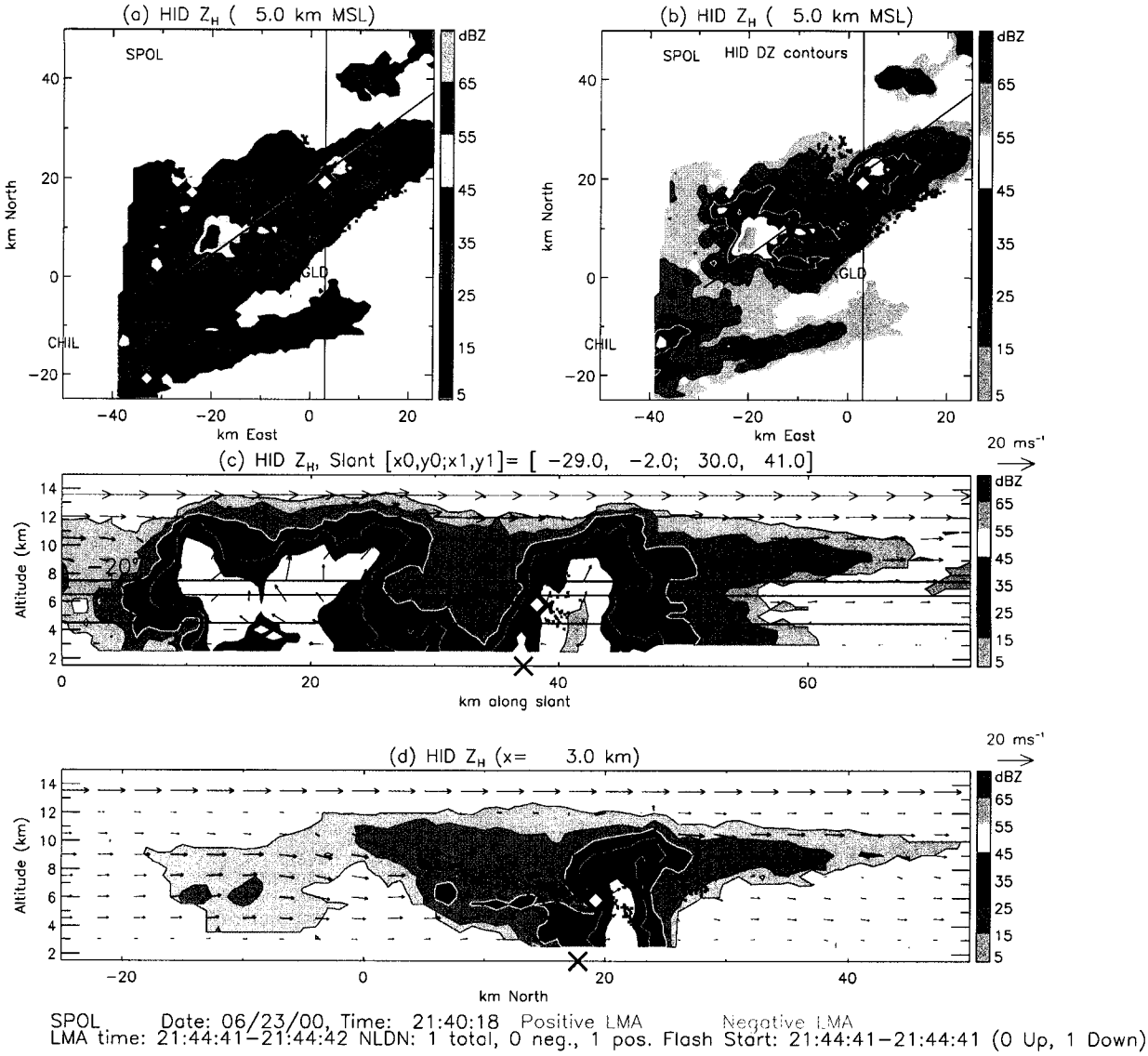

Figure 5.62: Radar cross-sections at 2140 with overlaid lightning mapping sources from the +CG flash shown in Fig. 5.61. Filled diamond symbol marks the initiation point, and X marks the strike point. Though the LMA sources are color-coded, they do not represent specific charge regions, per se. The green sources are the leader to ground. The rest are unclassified, but most of them are likely within positive charge.

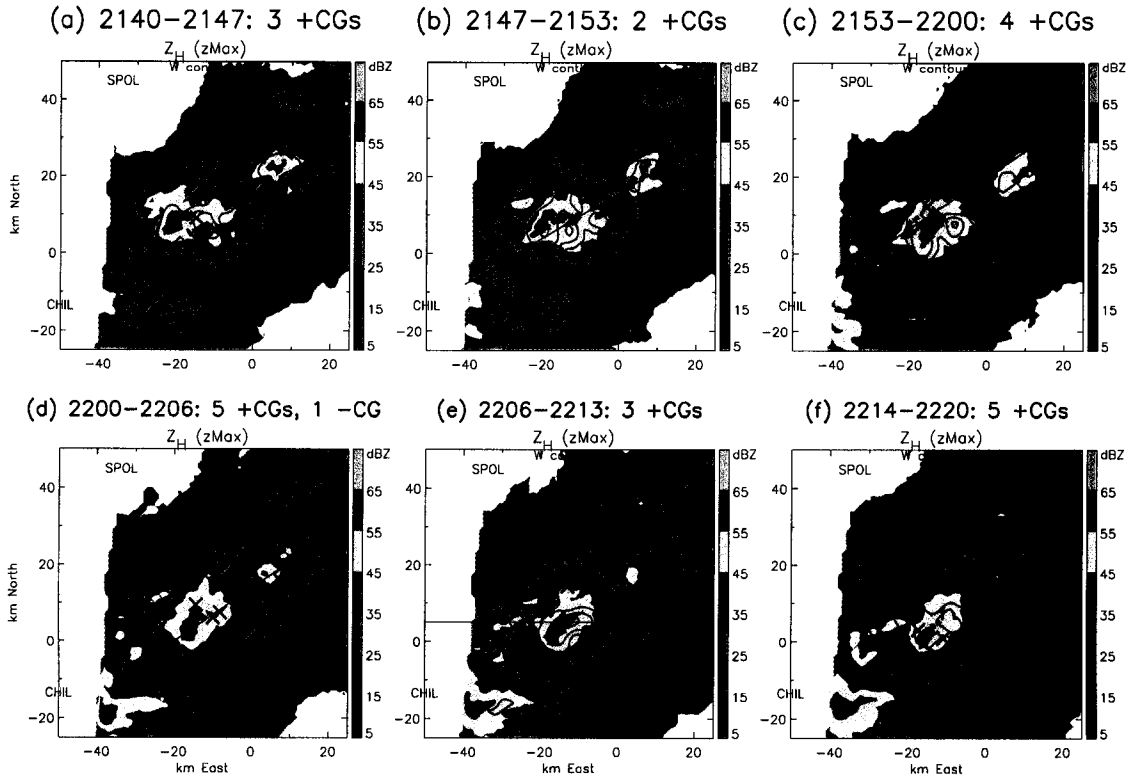

Figure 5.63: Horizontal cross-sections of column-max horizontal reflectivity (Z_H, see color bars) and column-max updraft in intervals of 5 ms^{-1} for each volume scan from 2140 to 2114. The X (diamond) symbols mark the NLDN strike points for all the +CGs (−CGs) from the start of one volume scan to the start of the next volume scan. The time intervals are listed above each panel. The straight lines show the orientation of the vertical cross-sections show in Fig. 5.64.

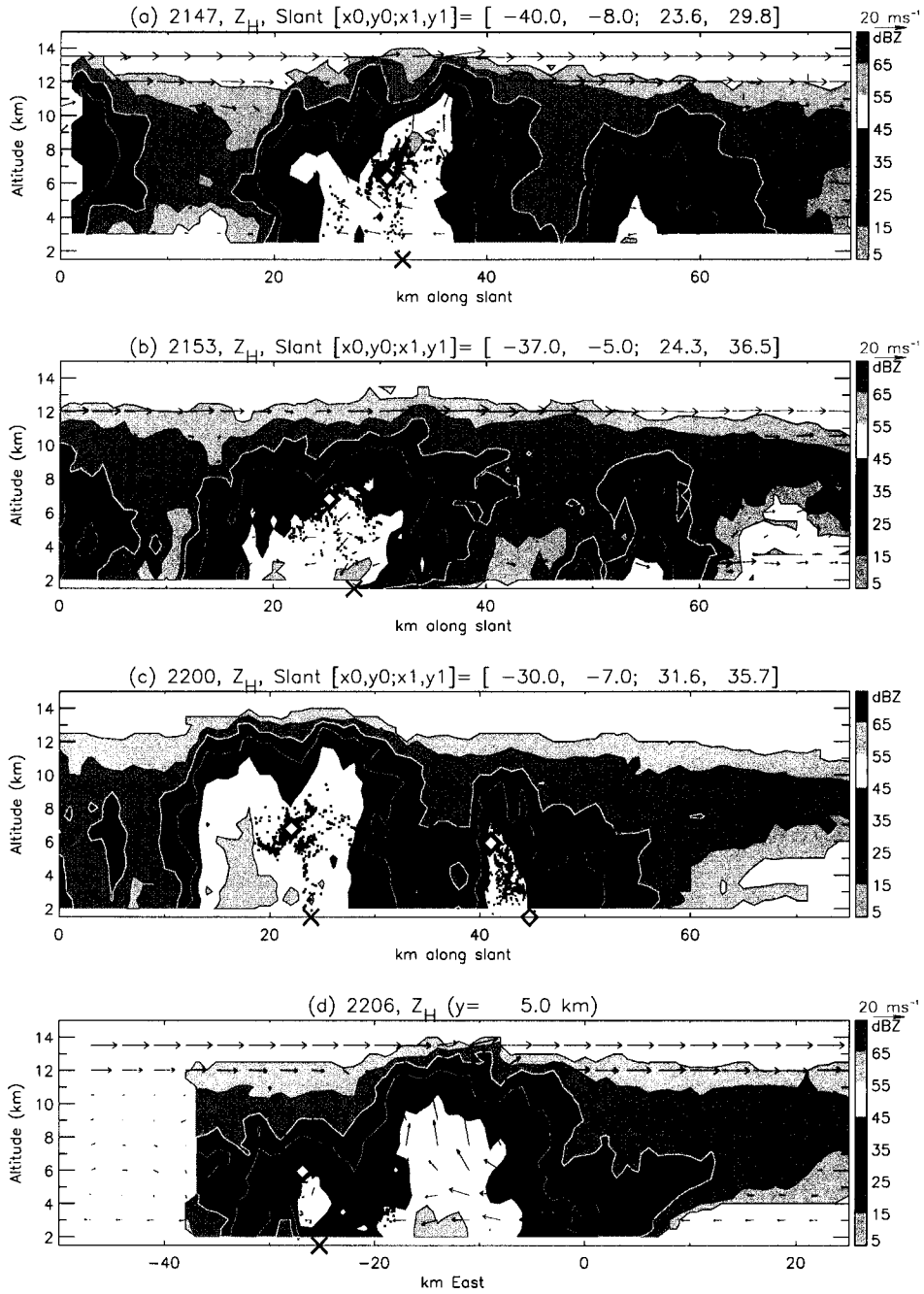

Figure 5.64: Representative +CGs overlaid onto radar vertical cross-sections at (a) 2147, (b) 2153, (c) 2200, (d) 2206. LMA sources are color-coded by charge (red for positive, green for negative), except in (c) where the red sources correspond to all the sources of the +CG flash and the green sources correspond to all the sources of the –CG flash. Filled diamond symbols mark the first source in each flash, and X's (diamonds) along the ground mark the NLDN strike points of the +CGs (–CGs). See the corresponding times in Fig. 5.63 for the orientation of the cross-sections. Multi-Doppler synthesis was not possible for the cross-section in (c).

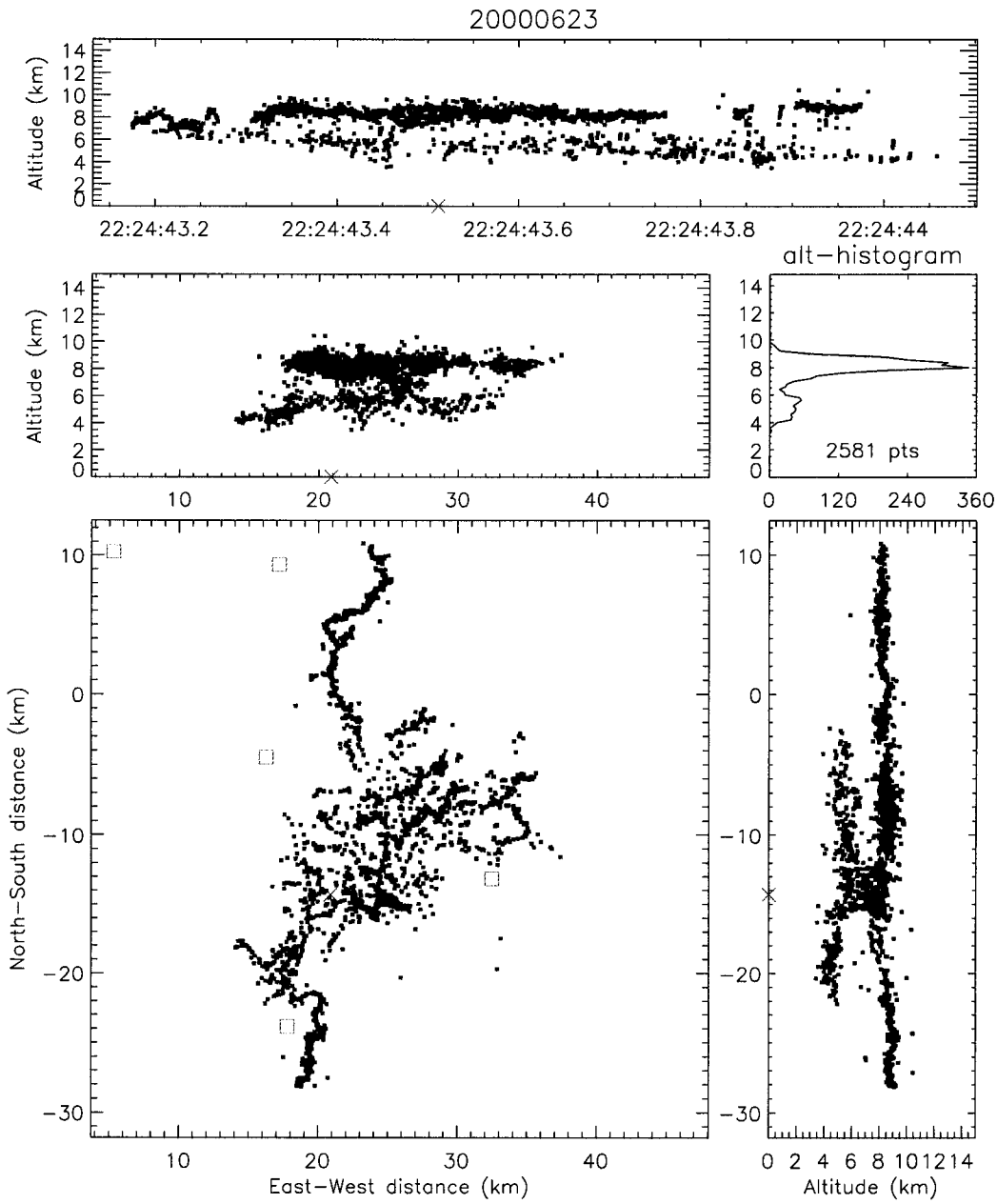

Figure 5.65: Lightning mapping of the +CG at 2224:43. Sources are color-coded by charge.

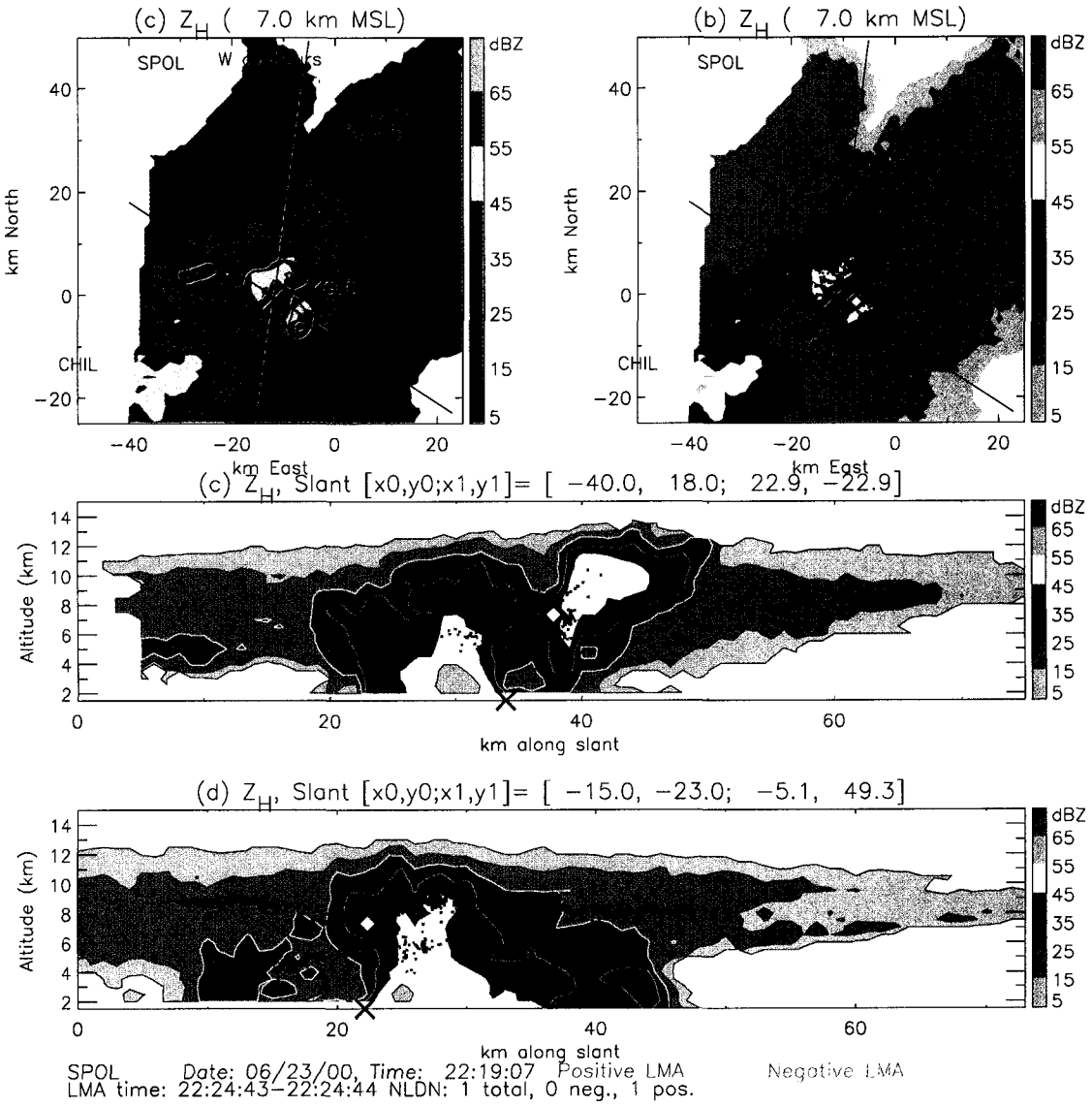

Figure 5.66: Radar cross-sections at 220 with overlaid lightning mapping sources from the +CG flash shown in Fig. 5.65. LMA sources are color-coded by charge and the filled diamond symbol marks the first source of the flash. The vertical cross-section in (c) is along the same slant path as the vertical cross-sections in the right column of Fig. 5.38.

CHAPTER 6

SUMMARY OF RESULTS

The objective of this dissertation was to investigate the kinematic, microphysical and electrical characteristics of several storms observed during STEPS, with a focus on determining what is different and/or unique about those storms which are dominated by +CG flashes. The set of case studies included the +CG-dominant supercell on 29 June, multicellular storms of varying severity on 23 June that experienced a shift from –CG-dominance to +CG-dominance, and an isolated storm on 3 June that produced no CG flashes of either polarity despite frequent intra-cloud lightning. Specific questions to be addressed included:

1. What are the charge structures of these storms and how do these structures develop, evolve, and differ?

2. Do +CG-dominated storms have charge structure that is consistently different from –CG-dominated storms?

3. What are the source charge regions of +CG and –CG flashes and how do these source regions compare with the overall charge structure?

4. Are there any kinematic/microphysical differences between +CG-dominated and –CG-dominated storms, and if so, can these differences explain the differing CG production?

5. To what extent do the observations of charge structure agree with laboratory charging studies?

6. To what extent do the observations agree with hypothesized explanations for +CG-dominated storms?

7. Do total lightning flash rate and CG-polarity have any utility as indicators or predictors of severe weather?

These questions were addressed in the previous chapters which are summarized here.

6.1 Charge Structure and CG Polarity

In the simplest vertical sense, –CG flashes resulted from a normal tripole structure, and +CG flashes resulted from an inverted tripole structure (e.g., Fig. 6.1). With little exception, +CG flashes originated between the mid-level positive and lower negative charge regions of an inverted tripole charge structure and tapped the mid-level positive charge. The -CG flashes originated between the mid-level negative and lower positive charge regions of a normal tripole charge structure and tapped the mid-level negative charge. Neither polarity of ground flash occurred without the presence of a lower charge region (lower positive charge in the case of –CG flashes, and lower negative charge in the case of +CG flashes). These vertical descriptions of the charge structure are gross simplifications, however, as the charge structure of each storm varied greatly in the horizontal and with time. The following paragraphs summarize the evolution of the charge structure and lightning activity of each storm in this study.

The evolution of the +CG-dominated 29 June supercell storm is illustrated schematically in Fig. 3.24. The first 20 minutes (2130–2150) of lightning in this storm showed only mid-level negative and lower positive charge (e.g., Fig. 3.14) which could be described as an inverted dipole structure. However, these two charge regions also correspond to the two lower charge regions of a normal tripole configuration. Following a burst of updraft, additional charge regions developed above the pre-existing low inverted dipole, resulting in an overall 5-layer charge structure, alternating in polarity with positive charge nearest the ground (e.g., Fig. 3.15). During the severe

stage of the 29 June storm (2330–0115), lightning near the strong updraft revealed an elevated inverted dipole structure, while further downwind the charge was roughly an inverted tripole with negative charge nearest the ground (e.g., Fig. 6.2 top). This charge structure supported frequent +CG flashes and persisted for nearly three hours. The +CG flashes originated between the mid-level positive and lower negative charge on the downwind side of the precipitation core and tapped positive charge within the precipitation core and (more often) mid-level positive charge extending further downwind of the precipitation core (see, for example, the schematic in Fig. 6.5 top).

The –CG-dominated cells in the early stages of storm 1 on 23 June followed the typical normal tripole archetype. They began with with only IC flashes between mid-level negative and upper positive charge (i.e., a normal dipole structure) and no –CG flashes. As precipitation grew and descended, the lower positive charge formed within the strongest precipitation, thus completing the tripole. –CG flashes began only after the formation of the lower positive charge, and the –CG flashes originated between the mid-level negative and lower positive charge (e.g, Fig. 6.3, top). In the later stages of storm 1, convective collapse apparently led to descent of the charge regions and formation of an inverted tripole structure (e.g., Fig. 6.3, bottom). During this collapse, –CG flashes ceased and +CG flashes began. All of the +CG flashes originated between the mid-level positive and lower negative charge regions of the inverted tripole in the collapsed cell. This transition from -CG to +CG flashes seems to fit with the precipitation unshielding hypothesis and/or an EOSO, but with some qualifications (see discussion in Section 5.2.6).

In many ways the structure and evolution of the west cell of storm 3 on 23 June was similar to the later stages (i.e, after 2200) of the 29 June supercell. Storm 3 on 23 June initially electrified with very active lightning between a positive charge region near 10 km MSL and negative charge above and below, with relatively infrequent flashes between mid-level negative and lower positive charge (e.g., Fig. 6.4, top). In both the 23 June and 29 June cases, inverted IC flashes between the upper positive and extreme upper negative dominated the lightning activity. In both cases, no CG

flashes occurred in the first hour of lightning activity. Frequent clustered +CG flashes began during large scale descent and/or deepening of the dominant upper positive charge region, apparently caused by growth and descent of hail. The +CG flashes originated from a roughly inverted tripole charge structure, tapped positive charge both within the precipitation core and further downwind, and went to ground on the downwind side of the main precipitation core (e.g., Fig. 6.4, bottom).

Finally, there was the storm on 3 June, which was the oddball of the bunch in that it produced no CG flashes of either polarity. The charge structure of this storm was relatively simple (as inferred from both the LMA and an EFM balloon sounding), consisting of a vertically thin negative charge region at 10–12 km altitude, and a deep (or multi-layered) positive charge below (Fig. 6.2, bottom). The 3 June storm was thus structurally similar to "storm 3" on 23 June and to the 29 June storm, but with one important difference: There was never any LMA indication of a lower negative charge region in the 3 June storm. This lack of a lower negative charge is apparently the reason why the 3 June storm produced no +CG flashes despite its inverted structure.

6.2 Thermodynamic and kinematic influences on charge structure

Assuming that non-inductive collisional charging (NIC) is primarily responsible for thunderstorm electrification, how then did these storms develop such different charge structures? According to laboratory experiments, the sign and magnitude of the charge transferred depends on temperature (T), liquid water content (LWC), and impact velocity (or equivalently, on T and riming rate; see Figs. 1.3 and 1.4). These parameters depend largely on the size and strength of the updraft, and on where the collisions occur relative to the core of this updraft. The following paragraphs *speculate* on how the NIC mechanism (in combination with thermodynamic and kinematic influences) could explain the different charge structures in the storms of this study.

It's reasonable to expect that charge-separating collisions occur across the updraft, not just in the core. Thus, these collisions occur over a wide range of the

T/LWC parameter space (Fig. 6.6). The core of the updraft would likely have the largest LWC, as it is more protected from entrainment, so collisions within the core of the updraft (and/or at warmer temperatures) would grant positive charge to the rimer. This positive charging region would extend deeper (i.e., to colder temperatures) for cases with stronger, broader updrafts (e.g., 3 June and 29 June. See Figs. 6.5 and 6.6). Collisions on the periphery of the updraft core (or equivalently in a weaker, narrower updraft) would restrict positive charging of the rimer to warmer temperatures and grant negative charge to the rimer over a broader range of temperatures (e.g., the early stages of storm 1 on 23 June. See Figs. 6.5 and 6.6). Hence, to first-order, *the differences in the size and strength of the updraft may explain the differing charge structure in the storms of this study.*

In the 3 June and 29 June cases, the stronger, deeper updraft led to enhanced positive charging of the rimer and enhanced negative charging of ice crystals, resulting in an inverted dipole structure near the core of the updrafts (Fig. 6.5). Indeed, evidence of a stronger updraft leading to inverted charge structure can also be found in the comparatively weaker storms on 23 June. In these cases the term "inverted" is perhaps not appropriate. Rather, a stronger updraft led to formation of extreme upper negative charge carried by ice crystals, apparently due to collisions in the LWC-rich core of these strong updrafts. For example, in the case of storm 1 on 23 June, note the increase in total flash rates and echo top heights at 2040, 2100, and 2150 (Fig. 5.6). Each of these was accompanied by dramatic increase in the number of downward flashes aloft (Fig. 5.12), indicating formation of extreme upper negative charge. In the case of the western cell of storm 3, the extreme upper negative charge was a persistent feature of the flash histograms (Figs. 5.42 and 5.43), but was much more active and pronounced in the stronger western cell. In all of these cases, the appearance (or enhancement) of the extreme upper negative charge was accompanied by decreases in –CG flashes. In the more extreme cases of 3 June, 29 June, and storm 3 on 23 June, there were essentially no –CG flashes at all. One interpretation of these observations is that the increased updraft led to a deeper region of "lower"

positive charge on the riming ice and a corresponding increase of negative charging of ice crystals above the deep "lower" positive charge. Negative CG flashes would then be suppressed because the "lower" positive is a dominant charge region (as opposed to the more frequently observed small pocket of charge), so that IC flashes between the upper negative and deep lower positive are energetically favored relative to –CG flashes and are more effective than –CG flashes at relieving the electrical strain between the two charge regions.

In addition to the differences in the strength and size of the updraft, *what also seemed to set the no-CG and +CG-dominated storms apart from the –CG-dominated storms is the difference in horizontal flow structure, i.e., shear.* Note the pronounced vaulted echo structure of the 3 June and 29 June storms in Figs. 6.2 and 6.5). The lightning mapping indicated an inverted dipole structure atop these updrafts, with larger ice particle getting positive charge in collisions, even at the colder temperatures within the vaulted echo structures. Following the schematic of Fig. 6.6 and the arguments of Williams et al. (2004), the rimer gets positive charge because of the large LWC in the undiluted cores of these updrafts. In addition, Williams et al. proposed that storms with higher cloud base and stronger updraft should tend to have greater LWC not only because of the strength of the updraft but also because collision and coalescence processes have little chance to remove any of the liquid water below the freezing level. Following this line of reasoning, a stronger updraft and higher CBH allows for more liquid water in the mixed phase region of the storm which enhances (and/or deepens the region of) positive rimer charging. Now factor in the affect of shear which forces the precipitation forming within the updraft to fall out downwind, thus offsetting the precipitation cores from updraft cores. This serves to maintain the high CBH associated with the strong updraft which sustains the high LWC and enhanced positive rimer charging within the updraft. In the case of the 29 June and storm 3 on 23 June, charging in the LWC-rich updraft granted positive charge to the rimer (hail) and negative charge to ice crystals (as indicated by the thick red arrow in Fig. 6.6). The positively charged hail growing in the strong updraft fell out directly

(as indicated in Fig. 6.5top) leaving an inverted charge structure downwind. The upper negative charge region downwind in Fig. 6.5(top) may have been due simply to advection of the ice crystals that charged negatively in the core of the updraft. The mid-level positive and lower negative charge regions downwind may have formed due to collisions in the LWC-deficient periphery of the updraft which imparted negative charge to graupel and positive charge to ice crystals (as indicated by the thin red arrow in Fig. 6.6). The +CG flashes traveled through the lower negative charge to ground and tapped the positive charge in both the heavy precipitation adjacent to the updraft and the mid-level positive charge further downwind. In contrast, the 3 June storm showed no evidence of a lower negative charge (Fig. 6.5 middle). Hence, as indicated by the blue arrow in Fig. 6.6, perhaps all of the collisions were restricted to the core of the updraft such that all collisions granted positive charge to the rimer.

In contrast to these no-CG and +CG-dominated storms, the –CG dominated cells of storm 1 on 23 June were more upright, meaning their updrafts were nearly co-located with their precipitation cores (Fig. 6.5bottom). This co-location of updraft and precipitation maintained a lower cloud base associated with the updraft core. Collision and coalescence processes could thus remove more of the liquid water below the freezing level, and this effect combined with weaker and narrower updrafts would restrict positive charging of the rimer to warmer temperatures and allow for a deeper region of negative rimer charging (as indicated by the green arrow in Fig. 6.6) . In addition, because the shear was less, the upper charge regions (specifically the negative charge region) were not displaced relative to the lower positive charge. This allowed for the negative charge region to discharge downward through the lower positive in the form of –CG flashes (e.g., Jacobson and Krider, 1976; Lopez and Aubagnac, 1997).

In summary, the hypothesized explanation for the differing charge structures in these storms is as follows:

- The stronger, broader updraft of no-CG and +CG-dominated storms allowed for near adiabatic LWC in the core of the updraft. This deepened the region

of positive rimer charging, effectively resulting in an inverted charge structure: low-to-mid-level positive charge carried by the riming ice, upper negative charge carried by ice crystals.

- The no-CG and +CG-dominated storms also had higher CBH associated with their main updrafts, and, because of shear, their updrafts were offset from their precipitation cores. The higher CBH prevented loss of liquid water to collision-coalescence processes and allowed for higher LWC (more positive rimer charging) in the mixed-phase region. The offset of the precipitation cores relative to the updrafts allowed these updrafts to maintain high CBH and maintain positive charging of the rimer.

- Weaker and/or narrower updraft combined with lower CBH of the –CG-dominated storms led to loss of liquid water to collision-coalescence and reduced LWC in the mixed-phase region. This restricted positive rimer charging to warmer temperatures and led to a deeper region of negative rimer charging, formation of a normal tripole charge structure, and –CG flashes.

- Weaker shear in the –CG-dominated storms prevented offset of the updraft from the precipitation core. This maintained the lower CBH and allowed for continued collision-coalescence processes below the mixed-phase region, thus maintaining the normal tripole structure.

Of course, the NIC mechanism may not have been the only electrification mechanism operating. Other mechanisms such as inductive charging, advection of charge, and charge deposition by lightning may have had some influence.

6.3 Flash rates and storm severity

All of the cases in this study showed a clear relationship between total flash rate (TFR) and convective development. In the case of the 29 June storm, the TFR showed a robust correlation with volumes of updraft exceeding 10 ms^{-1} (UV_{10}), and especially

with inferred graupel echo volume (GEV). This latter correlation highlights the importance of charge-separating collisions involving actively riming ice. The robustness of these correlations in the 29 June case is quite surprising considering the many sources of uncertainty involved. The other cases did not show such clear mathematical correlations between TFR and GEV, which may have been due to the relatively poorer quality of the radar coverage. However, even when the correlations were less robust, the TFR clearly increased with each increase in convective development (as indicated by surges in updraft and/or increases in echo top heights).

Williams et al. (1999), Hamlin (2004), and others have noted "jumps" in TFR and dramatic increases in the vertical extent of LMA sources prior to severe weather at the ground. They posit that such lightning "jumps" are manifestations of convective surges. Numerous instances of lightning "jumps" occurred in the storms of this study. In most cases, these jumps were accompanied by vertically elevated LMA sources. For example, the total flash rates in both the western and eastern cells of storm 3 on 23 June briefly decreased from 2100 to 2105 then increased rapidly again (Figs. 5.40 and 5.41). This lightning "jump" was especially pronounced in the eastern cell, and as shown in Fig. 5.43 much of the jump was due to onset of downward flashes well aloft, indicating formation of an extreme upper-negative charge. The more vigorous western cell already had an extreme upper-negative charge prior to the lightning jump, but its upper-negative charge also became more active during the jump (e.g, compare first three panels of Fig. 5.42). The next lightning jump in the eastern cell at 2140 (Fig. 5.41g) occurred just after a pronounced spike in UV_{10} and also corresponded to increased downward flashes from extreme upper-negative charge (see '21:40-21:50' panel in Fig. 5.43). In the 29 June case there were instances of lightning jumps (Fig. 3.3c) accompanied by lightning "holes" (e.g., see the left and right columns of Fig. 3.10). These lightning holes were coincident with bounded weak echo regions (BWERs), with vaulted radar echo structures and vertically elevated LMA sources above the BWERs and lightning holes. These lightning jumps and holes occurred during vigorous growth of hail aloft. In their LMA observations of tornadic storms

in Oklahoma, Krehbiel et al. (2000a) noted similar lightning "holes" in otherwise volume-filling lightning activity. Hence, there is little doubt that, like BWERs, such lightning holes are indicators of strong, broad updrafts and have some value as an indicator of severe weather.

6.4 Why are +CG storms concentrated in the STEPS region?

As shown in Fig. 1.1c, the +CG-dominant corridor lies near a climatological ridge of surface equivalent potential temperature (θ_e). This θ_e ridge is due to warm, moist flow from the Gulf of Mexico. Surface θ_e is often used a proxy for the Convective Available Potential Energy (CAPE) and thus as a proxy for the threat of very strong thunderstorm activity. Note, however, that θ_e is much stronger in the Southeast part of the United States, yet there is very little +CG activity there. Furthermore, the highest concentration (climatologically speaking) of severe storm reports lies on the southern end of the +CG maximum in regions of yet higher θ_e.

Apparently, the relationship between θ_e (or CAPE) and polarity of ground flash activity is not a simple one. This is exemplified by the study of Smith et al. (2000), in which they investigated the relationships between θ_e and ground flash polarity for 57 thunderstorms during three tornadic outbreaks in the Great Plains. They found that storms that were initially +CG-dominated tended to initiate in regions of strong surface θ_e gradient, while storms that were initially –CG-dominated usually initiated in regions of weak surface θ_e gradients. Furthermore, when storms crossed a maximum of surface θ_e, the dominant ground flash polarity switched from positive to negative. Figure 6.7 shows a schematic of this behavior. This led Smith et al. to suggest that "the polarity reversals were influenced by changes in intensity of the storms' updrafts as brought about by changes in the buoyancy of ingested surface and/or boundary layer air." They also noted that, in their sample, initial +CG-dominant behavior "would have been a good indicator of severe weather whether or not a polarity reversal did eventually take place."

Carey et al. (2003b) extended the θ_e-lightning polarity analysis of Smith et al.

to larger temporal and spatial scales. For the entire contiguous U.S., over the 10 warm seasons (Apr–Sept) of 1989–1998, they gridded the number of severe storm reports and counted how many of these reports were associated with +CG-dominant and –CG-dominant storms. Then for each month of each warm season, they averaged gridded surface θ_e from only those days which had a high flash density +CG-dominant event[1] and examined the resulting monthly mean patterns of surface θ_e and severe storm lightning polarity. Their results were in broad agreement with the Smith et al. (2000) conceptual model. For each month, the maxima of +CG-dominant severe storm reports were generally located to the north and west (dry side) of the θ_e ridge in a strong θ_e gradient. The –CG-dominant severe storm reports were systematically further south and east of the +CG-dominant feature, closer to the θ_e ridge, and in higher mean values of θ_e. Furthermore, this pattern tracked the θ_e ridge as it progressed to the northeast from April to September.

Severe hailstorms are not always dominated by +CG flashes, so there is still something unique about the STEPS region that the observations have yet to reveal. Williams et al. (2004) suggest that large Convective Available Potential Energy (CAPE) combined with the elevated cloud base height (CBH) of storms in the STEPS region may be the answer. Such conditions would tend to inhibit warm rain processes, allowing for "superlative" (i.e, near-adiabatic) supercooled liquid water contents in the resulting broad, strong updrafts. This could lead to enhanced riming growth of graupel and hail and would also have implications for electrification and lightning. The higher CBH (and attendant strong, broad updraft) would elevate the charge-bearing hydrometeors, invigorate the electrification, and increase the total flash rate and ratio of intra-cloud to cloud-to-ground flashes. With little liquid water lost to coalescence below elevated CBH, the supercooled liquid water may reach near-adiabatic (or "superlative" in the parlance of Williams et al.) values in the broad updrafts, resulting

[1]Despite this restriction on the data, there were still almost 8 times as many –CG-dominant events as +CG-dominant events, so the resulting statistics held a sizable population of both types of storms.

in an extended zone of positive charging of graupel and hail via the NIC mechanism. The results of Lang and Rutledge (2002) offer some support to this hypothesis. Their study included 11 storms which spanned a wide range of severity. In general, they found that –CG production decreased with increased updraft and hail production. The two storms of their study which had the strongest, broadest updrafts and greatest hail production, also produced predominantly +CG flashes.

The present study found that the stronger storms (in terms of CAPE and updraft width) and higher CBH storms were, indeed, +CG-dominated. However, the CBH was significantly higher only when the updraft was displaced from the precipitation core. Hence, the *shear* of the +CG-dominated storms also played an important role in their electrification and ground flash production.

6.5 Suggestions for Future Research

The observations of this study (particularly the LMA observations) provided significant insight into the electrification of thunderstorms. However, due to the labor-intensive nature of these detailed case studies, the sample included only a handful of storms, all of which were within a specific geographical region. There are numerous other well-observed storms in the STEPS data set, and analysis would provide valuable comparisons with the storms of this study. Three cases in particular deserve attention:

1. Two other cells developed in the same region as the 29 June supercell. One of which (cell 'B' in Fig. 3.1) even developed at the same time as the supercell, but did not become severe and was not +CG-dominated.

2. The most intense storm on 23 June was "storm 4" (see, for example, Fig. 5.1). This storm was +CG-dominated and produced significant amounts of hail. Unfortunately, time constraints precluded a detailed analysis of this storm.

3. The –CG-dominated storms on 19 June were well-positioned within the STEPS network and would serve as a nice comparison to the storms of this study.

The LMA was an invaluable resource for this study. Lightning mapping arrays are now positioned in other areas around the United States. Similarly detailed studies (using at least Dual-Doppler radar and lightning mapping) in these other geographical regions are needed to really understand and contrast with the storms in the STEPS region.

Flash-by-flash charge structure analysis of the LMA data was tedious. Though it would be difficult to accomplish, it would be a great boon if automated routines could be developed to do this. As an alternative, the altitude histograms of LMA sources and flash start heights provided a very revealing and useful way to summarize and comprehend the charge structure. In general, these histograms were quite consistent with the results of the flash-by-flash analysis. Hence, in lieu of the flash-by-flash analysis, it may be more feasible to rely on such histograms (and other simple LMA plots, like source density cross-sections) to give a rough interpretation of charge structure for a larger sample of storms. However, for detailed studies, charge determination via flash-by-flash analysis should be employed.

Finally, it would be worthwhile to do more direct comparisons of lightning mapping with in situ measurements (e.g., EFM balloons) along the lines of Coleman et al. (2003) to further validate and refine the charge structure inferences made from the lightning mapping. This would give greater confidence in the qualitative fully three-dimensional and time resolved LMA-inferred charge structure of thunderstorms.

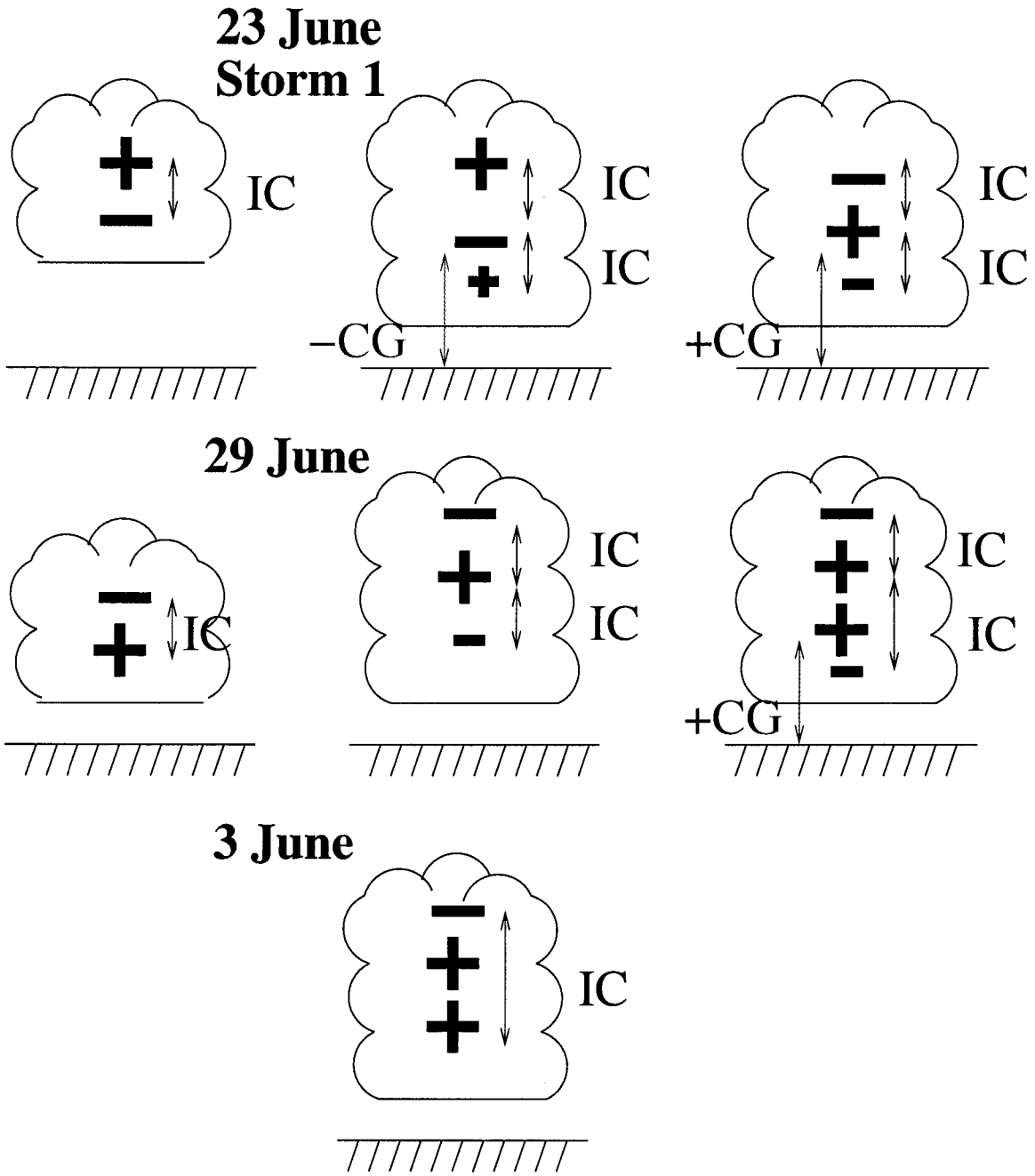

Figure 6.1: Simplified conceptual diagrams of the evolution of charge structure and lightning for the storms of this study.

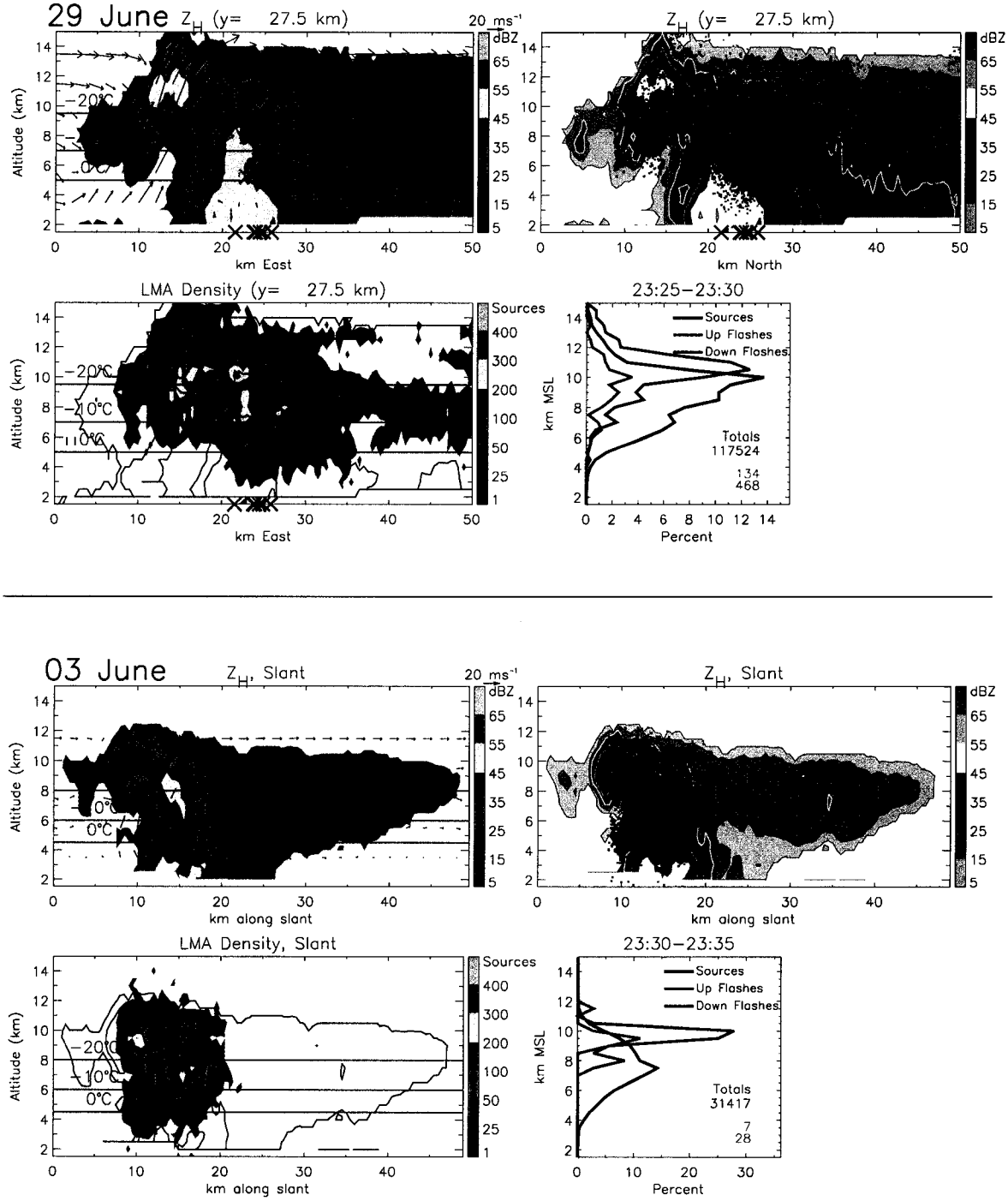

Figure 6.2: Representative cross-sections and LMA histograms for the storms on 3 and 29 June. Each set of four panels shows (clockwise from top-left) cross-section of horizontal reflectivity (Z_H) wind Doppler-inferred wind flow, Z_H again but in gray scale with LMA sources color-coded by charge, altitude histograms of LMA sources and flash start heights, cross-section of LMA source density with black Z_H contours at 5, 25, and 45 dBZ. The X (diamond) symbols mark origin and strike locations of +CG (-CG) flashes.

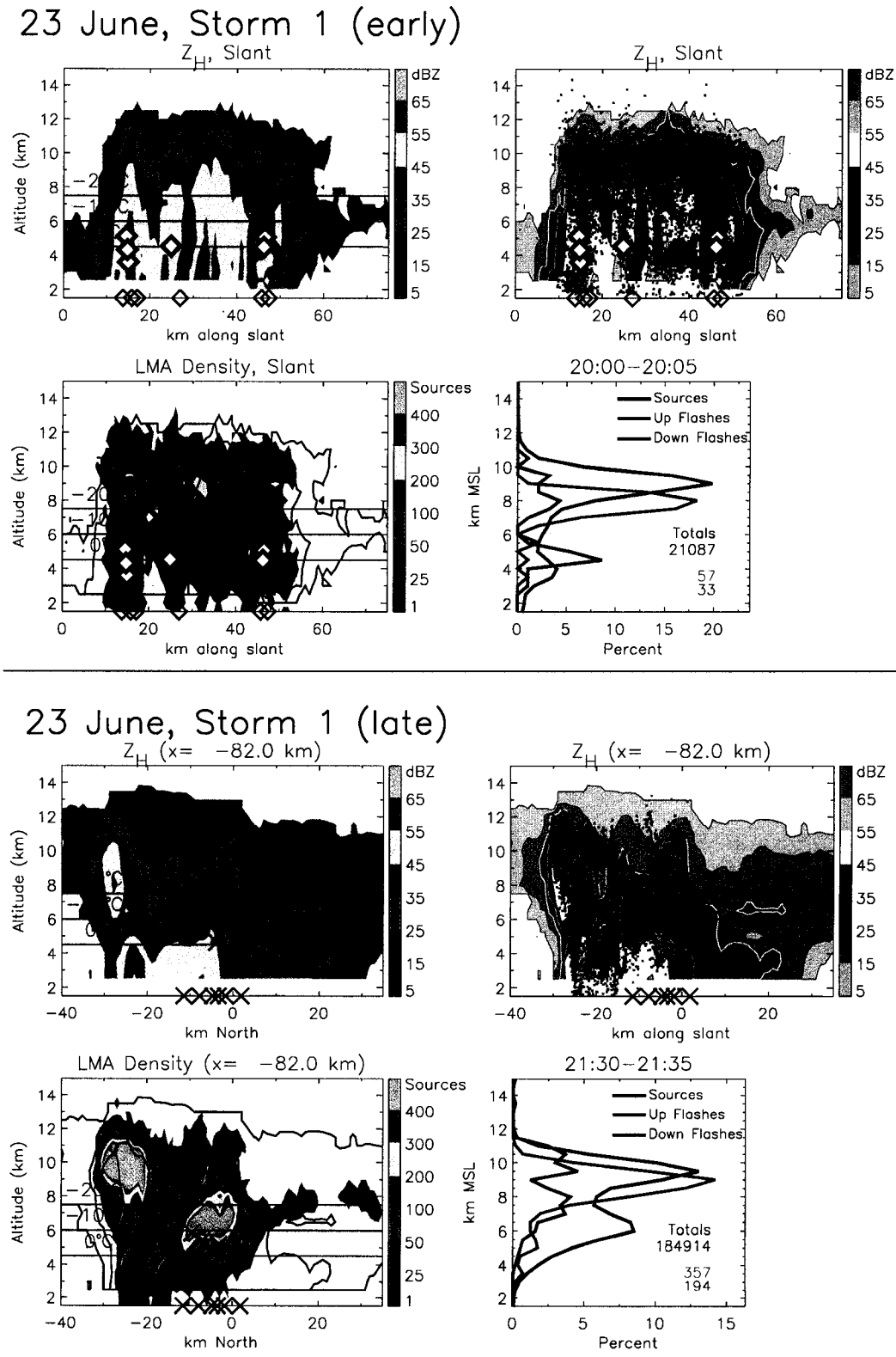

Figure 6.3: Representative cross-sections and LMA histograms for the early –CG-dominated and later +CG-dominated stages of storm 1 on 23 June. Format is the same as in Fig. 6.2, except that there was no multi-Doppler coverage for this storm and hence no wind vectors.

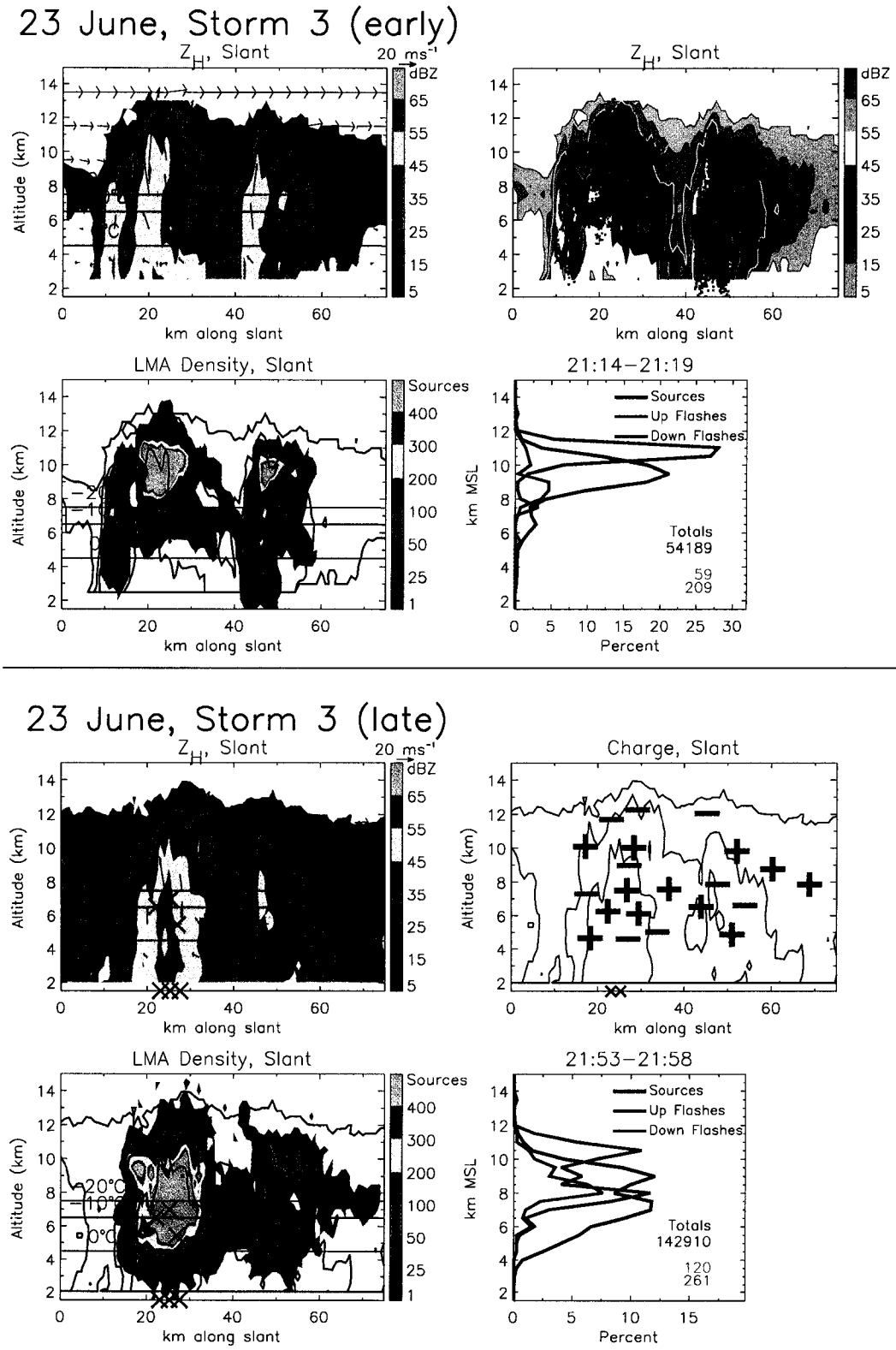

Figure 6.4: Representative cross-sections and LMA histograms for the early no-CG and later +CG-dominated stages of storm 3 on 23 June. Format is the same as in Fig. 6.2, except that the top-right panel for the later phase shows a charge composite instead of actual LMA sources. The histograms include only the LMA sources and flashes of the western (left) cell.

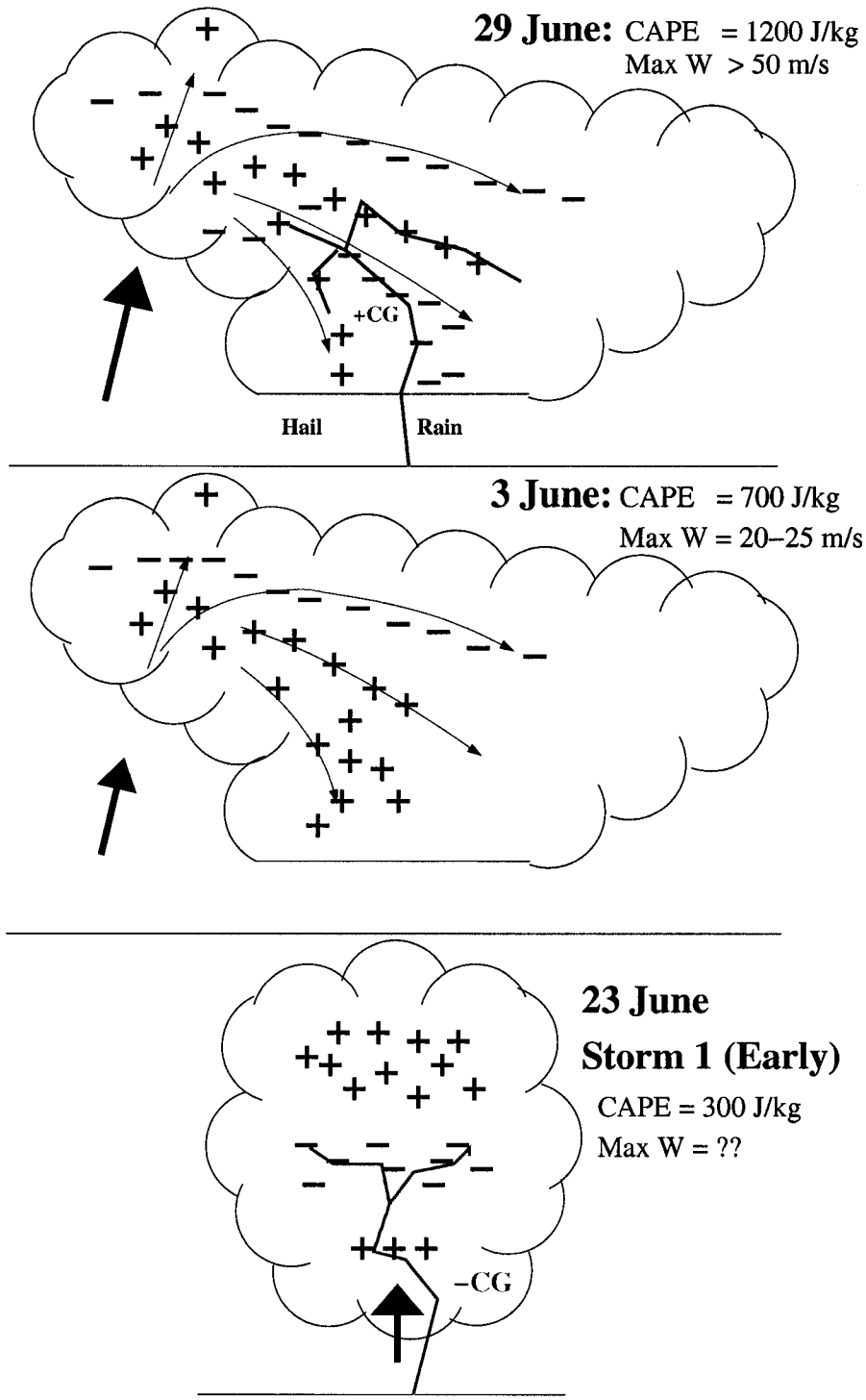

Figure 6.5: Conceptual diagram illustrating representative storm and charge structures of the 29 June, 3 June, and 23 June ("storm 1") storms. Thick blue arrows show main updraft. Thin blue arrows indicate air flow. Red disjointed lines indicate a +CG discharge. Green disjointed lines indicate a –CG discharge.

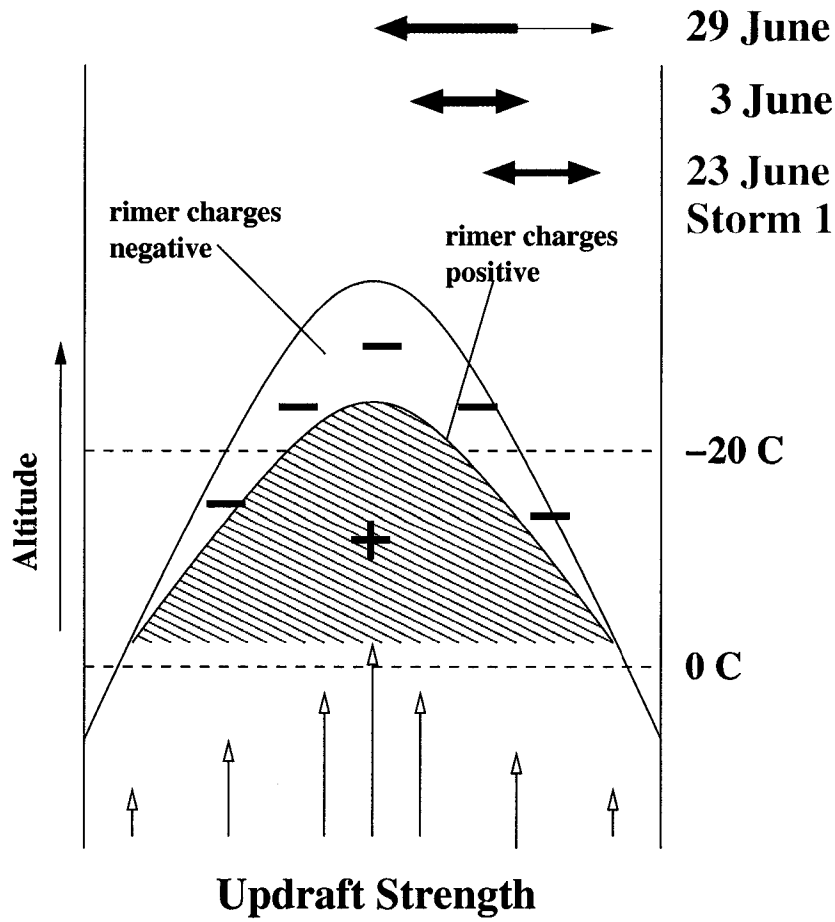

Figure 6.6: Conceptual diagram of collisional charging in thunderstorms. The parabolic envelope represents the width of the updraft and amount of liquid water content (LWC), with stronger updrafts and greater LWC in the center. Collisions in the core of strong updraft have larger LWC which extends the positive rimer charging to colder temperatures. The colored arrows at the top represent the assumed range of LWC within which charge-separating collisions are occurred for the indicated storms. For the 29 June case, the thicker part of the arrow represents collisions in the core of the updraft and thinner part of the arrow represents collisions in the periphery of the updraft.

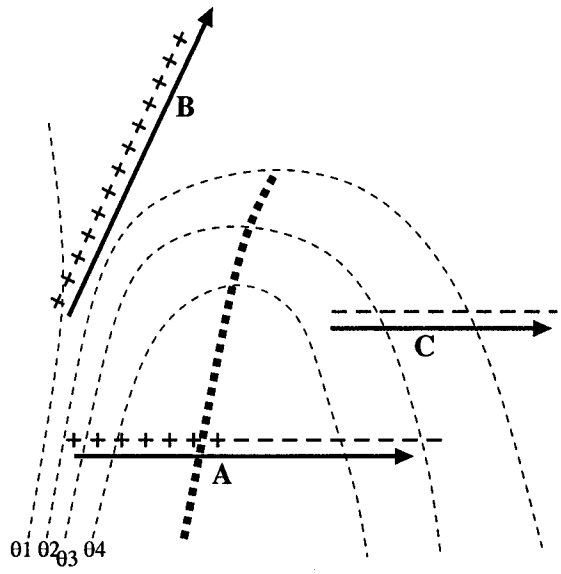

Figure 6.7: Schematic diagram of the conceptual model of dominant lightning polarity as a function of storm location relative to a surface θ_e ridge. Thin dashed lines are contours of surface θ_e, and thick dashed line indicates the θ_e ridge. Arrows indicate storm tracks. Storm track A is a reversal storm, B a +CG-dominated storm, and C a –CG-dominated storm. Adapted from Figure 9 of Smith et al. (2000).

REFERENCES

Aydin, K., T. A. Seliga, and V. Balaji, 1986: Remote sensing of hail with a dual linear polarization radar. *J. Climate and Appl. Meteor.*, **25**, 1475–1484.

Aydin, K., Y. Zhao, and T. A. Seliga, 1990: A differential reflectivity radar hail measurement technique: Observations during the denver hailstorm of 13 june 1984. *J. Atmos. Oceanic Technol.*, **7**, 104–113.

Baker, B., M. B. Baker, E. R. Jayaratne, J. Latham, and C. P. R. Saunders, 1987: The influence of diffusional growth rates on the charge transfer accompanying rebounding collisions between ice crystals and soft hailstones. *Quart. J. Roy. Meteor. Soc.*, **113**, 1193–1215.

Baker, M. B. and J. G. Dash, 1994: Mechanism of charge transfer between colliding ice particles in thunderstorms. *J. Geophys. Res.*, **99**, 10,621–10,626.

Barnes, S. L., 1980: Report on a meeting to establish a common Doppler radar data exchange format. *Bull. Amer. Meteor. Soc.*, **61**, 1401–1404.

Berdeklis, P. and R. List, 2001: The ice crystal-graupel charging mechanism of thunderstorm electrification. *J. Atmos. Sci.*, **58**, 2751–2770.

Bevington, P. R., 1969: *Data Reduction and Error Analysis for the Physical Sciences.* McGraw-Hill.

Bringi, V. N. and V. Chandrasekar, 2001: *Polarimetric Doppler Weathern Radar. Principles and Applications.* Cambridge University Press.

Bringi, V. N., K. Knupp, A. Detwiler, L. Liu, I. J. Caylor, and R. A. Black, 1997: Evolution of a Florida thunderstorm during the Convection and Precipitation / Electrification Experiment: The case of 9 August 1991. *Mon. Wea. Rev.*, **125**, 2131–2160.

Bringi, V. N., J. Vivekanandan, and J. D. Tuttle, 1986: Multiparameter radar measurements in Colorado convective storms. Part ii: Hail detection studies. *J. Atmos. Sci.*, **43**, 2564–2577.

Brook, M., M. Nakano, P. Krehbiel, and T. Takeuti, 1982: The electrical structure of the Hokuriku winter thunderstorms. *J. Geophys. Res.*, **87**, 1207–1215.

Carey, L. D., W. A. Petersen, and S. A. Rutledge, 2003a: The relationship between

severe storm reports and cloud-to-ground lightning polarity in the contiguous United States from 1989 to 1998. *Mon. Wea. Rev.*, **131**, 1211–1228.

— 2003b: Evolution of cloud-to-ground lightning and storm structure in the Spencer, South Dakota, tornadic supercell of 30 May 1998. *Mon. Wea. Rev.*, **131**, 1811–1831.

Carey, L. D. and S. A. Rutledge, 1996: A multiparameter radar case study of the microphysical and kinematic evolution of a lightning producing storm. *Meteorol. Atmos. Phys.*, **59**, 33–64.

— 1998: Electrical and multiparameter radar observations of a severe hailstorm. *J. Geophys. Res.*, **103**, 13,979–14,000.

Coleman, L. M., T. Marshall, M. Stolzenburg, T. Hamlin, P. Krehbiel, W. Rison, and R. J. Thomas, 2003: Effects of charge and electrostatic potential on lightning propagation. *J. Geophys. Res.*, **108**, doi:10.1029/2002JD002718.

Conway, J. W. and D. S. Zrnic, 1993: A study of the embryo production and hail growth using dual-doppler and multiparamter radars. *Mon. Wea. Rev.*, **121**, 2511–2528.

Cummins, K. L., M. J. Murphy, E. A. Bardo, W. L. Hiscox, R. B. Pyle, and A. E. Pifer, 1998: A combined TOA/MDF technology upgrade of the U.S. National Lightning Detection Network. *J. Geophys. Res.*, **103**, 9035–9044.

Curran, E. B. and W. D. Rust, 1992: Positive ground flashes produced by low-precipitation thunderstorms in Oklahoma on 26 April 1984. *Mon. Wea. Rev.*, **120**, 544–553.

Dash, J. G., B. L. Mason, and J. S. Wettlaufer, 2001: Theory of charge and mass transfer in ice-ice collisions. *J. Geophys. Res.*, **106**, 20,395–20,402.

Depue, T. K., 2003: *Ground Truth and Modeling Verification of the Hail Quadrature Parameter*. Master's thesis, Colorado State University.

Dolan, B., 2004: *An Integrated Display and Analysis Tool for Multi-varialbe Radar Data*. Master's thesis, Colorado State University, 161 pp.

Gal-Chen, T., 1982: Errors in fixed and moving frames of reference. Applications for conventional Doppler radar analysis. *J. Atmos. Sci.*, **39**, 2279–2300.

Hall, M. . P. M., J. W. F. Goddard, and S. M. Cherry, 1984: Identification of hydrometeors and other targets by dual-polarization radar. *Radio Sci.*, **19**, 132–140.

Hamlin, T., 2004: *The New Mexico Tech Lightning Mapping Array*. Ph.D. thesis, New Mexico Institute of Mining and Technology, 164 pp.

Herzegh, P. H. and A. R. Jameson, 1992: Observing precipitation through dual-polarization radar measurements. *Bull. Amer. Meteor. Soc.*, **73**, 1365–1374.

Hubbert, J. and V. N. Bringi, 1995: An iterative technique for the analysis of copolar differential phase and dual-frequency radar measurements. *J. Atmos. Oceanic Technol.*, **12**, 643–648.

Illingworth, A. J., J. W. F. Goddard, and S. M. Cherry, 1987: Polarization radar studies of precipitation development in convective storms. *Quart. J. Roy. Meteor. Soc.*, **113**, 469–489.

Jacobson, E. A. and E. P. Krider, 1976: Electrostatic field changes produced by Florida lightning. *J. Atmos. Sci.*, **33**, 103–117.

Jameson, A. R., 1985: Deducing the microphysical character of precipitation from multi-parameter radar polarization measurements. *J. Climate Appl. Meteor.*, **24**, 1037–1047.

Jayaratne, E. R., 1993: The heat balance of a riming graupel pellet and the charge separation during ice-ice collisions. *J. Atmos. Sci.*, **50**, 3185–3193.

Kasemir, H. W., 1960: A contribution to the electrostatic theory of lightning discharge. *J. Geophys. Res.*, **65**, 1873–1878.

Kennedy, P. C., V. N. Bringi, D. A. Brunkow, S. A. Rutledge, and N. J. Doesken, 2001: Hail characterization via the joint utilization of reflectivity, differential reflectivity, and linear depolarization ratio data. *30th Intl. Conf. Radar Meteor.*, Amer. Meteor. Soc., 433–435.

Krehbiel, P. R., 1986: The electrical structure of thunderstorms. *The Earth's Electrical Environment*, National Academy Press, Washington, D. C., 90–113.

Krehbiel, P. R., M. Brook, and R. A. McCrory, 1979: An analysis of the charge structure of lightning discharges to ground. *J. Geophys. Res.*, **84**, 2432–2456.

Krehbiel, P. R., R. J. Thomas, W. Rison, T. Hamlin, J. Harlin, and M. Davis, 2000a: Lightning mapping observations in central Oklahoma. *EOS*, **81**, 22–25.

Krehbiel, P. R., R. J. Thomas, W. Rison, T. Hamlin, J. Harlin, M. Stanley, J. Lombardo, and D. Shown, 2000b: Inverted polarity lightning in STEPS. *Eos Trans., Fall Meet. Suppl*, AGU, San Francisco, volume 81.

Kuhlman, K. M., 2004: *Numerical Simulations of the 29 June 2000 STEPS Tornadic Supercell: Microphysics, Electrification, and Lightning*. Master's thesis, Univ. of Okla., Norman, 72 pp.

Kuhlman, K. M., E. R. Mansell, C. L. Ziegler, D. R. MacGorman, and J. M. Straka, 2003: Charging and lightning in simulations of the 29 June 2000 STEPS supercell. *Proc. 12th Int. Conf. Atmos. Elec., Versailles, France, June 2003*.

Lang, T. J., L. J. Miller, M. Weisman, S. A. Rutledge, L. J. B. III, V. N. Bringi, V. Chandrasekar, A. Detwiler, N. Noesken, J. Helsdon, E. Rasumssen, W. Rison, W. D. Rust, and R. J. Thomas, 2004a: The Severe Thunderstorm Electrification and Precipitation Study. *Bull. Amer. Meteorol. Soc.*, doi:10.1175/BAMS-85-8-1107.

Lang, T. J. and S. A. Rutledge, 2002: Relationships between convective storm kinematics, precipitation, and lightning. *Mon. Wea. Rev.*, **130**, 2492–2506.

Lang, T. J., S. A. Rutledge, and K. C. Wiens, 2004b: Origins of positive cloud-to-ground lightning in the stratiform region of a mesoscale convective system. *Geophys. Res. Letts.*, **31**, doi:10.1029/2004GL019823.

Larson, H. R. and E. J. Stansbury, 1974: Association of lightning flashes with precipitation cores extending to height 7 km. *J. Atmos. Terr. Phys.*, **36**, 1547–1553.

Lim, S., 2001: *Fuzzy Logic System for Hydrometeor Classification from Polarimetric Radar Measurements*. Master's thesis, Colorado State University, 97 pp.

Liu, H. and V. Chandrasekar, 2000: Classification of hydrometeors based on polarimetric radar measurements: Development of fuzzy logic and neuro-fuzzy systems and in situ verification. *J. Atmos. Oceanic Technol.*, **17**, 140–164.

Lopez, R. E. and J. Aubagnac, 1997: The lightning activity of a hailstorm as a function of changes in its microphysical characteristics inferred from polarimetric radar observations. *J. Geophys. Res.*, **102**, 16,799–16,813.

MacGorman, D. R. and D. W. Burgess, 1994: Positive cloud-to-ground lightning in tornadic storms and hailstorms. *Mon. Wea. Rev.*, **122**, 1671–1697.

MacGorman, D. R., D. W. Burgess, V. Mazur, W. D. Rust, W. L. Taylor, and B. C. Johnson, 1989: Lightning rates relative to tornadic storm evolution on 22 May 1981. *J. Atmos. Sci.*, **46**, 221–250.

MacGorman, D. R. and W. D. Rust, 1998: *The Electrical Nature of Storms*. Oxford University Press, 422 pp.

MacGorman, D. R., W. D. Rust, P. Krehbiel, E. Bruning, and K. Wiens, 2004: The electrical structure of two supercell storms during STEPS. *Mon. Wea. Rev.*, in Review.

Mansell, E. R., 2000: *Electrification and Lightning in Simulated Supercell and Non-supercell Thunderstorms*. Ph.D. thesis, Univ. of Oklahoma, Norman, OK, 211 pp.

Mansell, E. R., D. R. MacGorman, C. Ziegler, and J. M. Straka, 2002: Simulated three-dimensional branched lightning in a numerical thunderstorm model. *J. Geophys. Res.*, **107**, doi:10.1029/2000JD00244.

Marsh, S. J. and T. C. Marshall, 1993: Charge precipitation measurements before the first lightning flash in a thunderstorm. *J. Geophys. Res.*, **98**, 16,605–16,611.

Marshall, T. C. and B. Lin, 1992: Electricity in dying thunderstorms. *J. Geophys. Res.*, **97**, 9913–9918.

Marshall, T. C. and S. J. Marsh, 1993: Negatively charged precipitation in a new mexico thunderstorm. *J. Geophys. Res.*, **98**, 14,909–14,916.

Marshall, T. C., W. D. Rust, W. P. Winn, and K. E. Gilbert, 1989: Electrical structure of two thunderstorm anvil clouds. *J. Geophys. Res.*, **94**, 2171–2181.

Marshall, T. C. and M. Stolzenburg, 2002: Electrical energy constraints on lightning. *J. Geophys. Res.*, **107**, doi:10.1029/2000JD000024.

Marshall, T. C. and W. P. Winn, 1982: Measurements of charged precipitation in a new mexico thunderstorm: Lower positive charge centers. *J. Geophys. Res.*, **87**, 7141–7157.

Mason, B. L. and J. G. Dash, 2000: Charge and mass transfer in ice-ice collisions: Experimental observations of a mechanism in thunderstorm electrification. *J. Geophys. Res.*, **105**, 10,185–10,192.

Mazur, V. and L. Ruhnke, 1993: Common physical processes of natural and artificially triggered lightning. *J. Geophys. Res.*, **98**, 12 913–12 930.

Miller, L. J., C. G. Mohr, and A. J. Weinheimer, 1986: The simple rectification to Cartesian space of folded radial velocities from Doppler radar sampling. *J. Atmos. Oceanic. Technol.*, **3**, 162–174.

Mohr, C. G., L. J. Miller, R. L. Vaughn, and H. W. Frank, 1986: On the merger of mesoscale data sets into a common Cartesian format for efficient and systematic analysis. *J. Atmos. Oceanic. Technol.*, **3**, 143–161.

Mohr, C. G. and R. L. Vaughn, 1979: An economical approach for Cartesian interpolation and display of reflectivity factor data in three-dimensional space. *J. Appl. Meteor.*, **18**, 661–670.

Moller, A. R., C. A. D. III, M. P. Foster, and G. R. Woodall, 1994: The operational recognition of supercell thunderstorm environments and storm structure. *Wea. Forecasting*, **9**, 327–347.

Moore, C. B. and B. Vonnegut, 1977: The thundercloud. *Lightning. Vol I: Physics of Lightning*, R. H. Golde, ed., Academic Press, San Diego, 64–98.

O'Brien, J. J., 1970: Alternative solutions to the classical vertical velocity problem. *J. Appl. Meteor.*, **9**, 197–203.

Orville, R. E. and G. R. Huffines, 2001: Cloud-to-ground lightning in the United

States: NLDN results in the first decade, 1989-98. *Mon. Wea. Rev.*, **129**, 1179–1193.

Rhodes, C. T., X. M. Shao, P. R. Krehbiel, R. J. Thomas, and C. O. Hayenga, 1994: Observations of lightning phenomena using radio interferometry. *J. Geophys. Res.*, **99**, 13,059–13,082.

Rison, W., R. J. Thomas, P. R. Krehbiel, T. Hamlin, and J. Harlin, 1999: A GPS-based three-dimensional lightning mapping system: Initial observations in central New Mexico. *Geophys. Res. Lett.*, **26**, 3573–3576.

Rust, W. D., 1989: Utilization of a mobile laboratory for storm electricity measurements. *J. Geophys. Res.*, **94**, 13,305–13,311.

Rust, W. D. and D. R. MacGorman, 2002: Possibly inverted-polarity electrical structures in thunderstorms during STEPS. *Geophys. Res. Lett.*, **29**, doi:10.1029/2001GL014303.

Rust, W. D., D. R. MacGorman, E. C. Bruning, S. A. Weiss, P. R. Krehbiel, R. J. Thomas, W. Rison, T. Hamlin, and J. Harlin, 2004: Inverted-polarity electrical structures in thunderstorms in the Severe Tunderstorm Electrification and Precipitation Study (STEPS). *Submitted to special issue of Atmos. Res., Intn'l. Conf. Atmos. Elec., Versailles 2003*.

Ryzhkov, A. V. and D. S. Zrnic, 1998: Polarimetric rainfall estimation in the presence of anomalous propagation. *J. Atmos. Oceanic. Technol.*, **15**, 1320–1330.

Saunders, C. P. R., W. D. Keith, and R. P. Mitzeva, 1991: The effect of liquid water content on thunderstorm charging. *J. Geophys. Res.*, **96**, 11,007–11,017.

Saunders, C. P. R. and S. L. Peck, 1998: Laboratory studies of the influence of the rime accretion rate on charge transfer during graupel/crystal collisions. *J. Geophys. Res.*, **103**, 13,949–13,956.

Scott, R. D., P. R. Krehbiel, and W. Rison, 2001: The use of simultaneous horizontal and vertical transmissions for dual-polarization radar meteorological observations. *J. Atmos. Oceanic Technol.*, **18**, 629–648.

Shao, X. M. and P. R. Krehbiel, 1996: The spatial and temporal development of intracloud lightning. *J. Geophys. Res.*, **101**, 26 641–26 668.

Smith, S. B., J. G. LaDue, and D. R. MacGorman, 2000: The relationship between cloud-to-ground lightning polarity and surface equivalent potential temperature during three tornadic outbreaks. *Mon. Wea. Rev.*, **128**, 3320–3328.

Stolzenburg, M., 1994: Observations of high ground flash densities of positive lightning in summertime thunderstorms. *Mon. Wea. Rev.*, **122**, 1740–1750.

Stolzenburg, M. and T. C. Marshall, 2002: Two simultaneous charge structures in thunderstorm convection. *J. Geophys. Res.*, **107**, 4352, doi:10.1029/2001JD000904.

Stolzenburg, M., W. D. Rust, , and T. C. Marshall, 1998b: Electrical structure in thunderstorm convective regions 2. Isolated storms. *J. Geophys. Res.*, **103**, 14,079–14,096.

— 1998c: Electrical structure in thunderstorm convective regions 3. Synthesis. *J. Geophys. Res.*, **103**, 14,097–14,108.

Stolzenburg, M., W. D. Rust, B. F. Stull, and T. C. Marshall, 1998a: Electrical structure in thunderstorm convective regions 1. Mesoscale convective systems. *J. Geophys. Res.*, **103**, 14,059–14,078.

Straka, J. M., D. S. Zrnic, and A. V. Ryzhkov, 2000: Bulk hydrometeor classification and quantification using polarimetric radar data: Synthesis of relations. *J. Appl. Meteor.*, **39**, 1341–1372.

Takahashi, T., 1978: Riming electrification as a charge generation mechanism in thunderstorms. *J. Atmos. Sci.*, **35**, 1536–1548.

Tessendorf, S. A., 2003: *Kinematic and Microphysical Evolution of the 29 June Supercell Observed during STEPS*. Master's thesis, Colorado State University, 102 pp.

Tessendorf, S. A., L. J. Miller, K. C. Wiens, and S. A. Rutledge, 2004a: The 29 June 2000 supercell observed during STEPS. Part I: Kinematics and microphysics. *J. Atmos. Sci.*, in Review.

Tessendorf, S. A., K. C. Wiens, and S. A. Rutledge, 2004b: Lightning and radar observations of two storms observed during STEPS. *22nd Conf. Severe Local Storms*, Amer. Met. Soc., Hyannis, Mass., abstract P14.2.

Thomas, R. J., P. R. Krehbiel, W. Rison, J. Harlin, T. Hamlin, and N. Campbell, 2003: The LMA flash algorithm. *Proc. 12th Int. Conf. Atmos. Elec., Versailles, France, June 2003*.

Thomas, R. J., P. R. Krehbiel, W. Rison, S. J. Hunyady, W. P. Winn, T. Hamlin, and J. Harlin, 2004: Accuracy of the Lightning Mapping Array. *J. Geophys. Res.*, **109**, doi:10.1029/2004JD004549.

Wiens, K. C., S. A. Rutledge, and S. A. Tessendorf, 2004: The 29 June supercell observerd during STEPS. Part II: Lightning and charge structure. *J. Atmos. Sci.*, in Review.

Willams, E. R., C. M. Cooke, and K. A. Wright, 1985: Electrical discharge propagation in and around space charge clouds. *J. Geophys. Res.*, **90**, 6059–6070.

Williams, E. R., 1989: The tripole structure of thunderstorms. *J. Geophys. Res.*, **94**, 13,151–13,167.

— 2001: The electrification of severe storms. *Severe Convective Storms*, C. A. D. III,

ed., Amer. Meteor. Soc., volume 50 of *Meteor. Monogr.*, 527–561.

Williams, E. R., B. Boldi, A. Matlin, M. Weber, S. Hodanish, D. Sharp, S. Goodman, R. Raghaven, and D. Buechler, 1999: The behavior of total lightning activity in severe Florida thunderstorms. *Atmos. Res.*, **51**, 245–264.

Williams, E. R., V. Mushtak, D. Rosenfeld, S. Goodman, and D. Boccippio, 2004: Thermodynamic conditions favorable to superlative thunderstorm updraft, mixed phase microphysics and lightning flash rate. *Submitted to special issue of Atmos. Res., Intn'l. Conf. Atmos. Elec., Versailles 2003.*

Williams, E. R., M. E. Weber, and R. E. Orville, 1989b: The relationship between lightning type and convective state of thunderclouds. *J. Geophys. Res.*, **94**, 13,213–13,220.

Williams, E. R., R. Zhang, and D. Boccippio, 1994: Microphysical growth state of ice particles and large-scale electrical structure of clouds. *J. Geophys. Res.*, **99**, 10,787–10,792.

Winn, W. P. and I. L. G. Byerley, 1975: Electric field growth in thunderclouds. *Q. J. Roy. Meteor. Soc.*, **101**, 979–994.

Winn, W. P., C. B. Moore, and C. R. Holmes, 1981: Electric field structure in an active part of a small, isolated thundercloud. *J. Geophys. Res.*, **86**, 1187–1193.

Winn, W. P., C. B. Moore, C. R. Holmes, and I. L. G. Byerley, 1978: Thunderstorm on July 16, 1975, over Langmuir Laboratory: A case study. *J. Geophys. Res.*, **83**, 3079–3092.

Zajac, B. A. and S. A. Rutledge, 2001: Cloud-to-ground lightning activity in the contiguous United States from 1995 to 1999. *Mon. Wea. Rev.*, **129**, 999–1019.

Zhang, Y., P. R. Krehbiel, T. Hamlin, J. Harlin, R. Thomas, and W. Rison, 2001: Electrical charge structure and cloud-to-ground lightning in thunderstorms during STEPS. *Eos Trans. AGU, 82(47), Fall Meet. Suppl, Abstract AE12A-0079.*

Zrnic, D. S., A. Ryzhkov, J. Straka, Y. Liu, and J. Vivekanandan, 2001: Testing a procedure for automatic classification of hydrometeor types. *J. Atmos. Oceanic. Technol.*, **18**, 892–913.

Zrnic, D. S. and A. V. Ryzhkov, 1999: Polarimetry for weather service radars. *Bull. Amer. Meteor. Soc.*, **80**, 389–406.